

RICE UNIVERSITY

**Synthesis, Structure and Properties of Various Carbon
Nanomaterials**

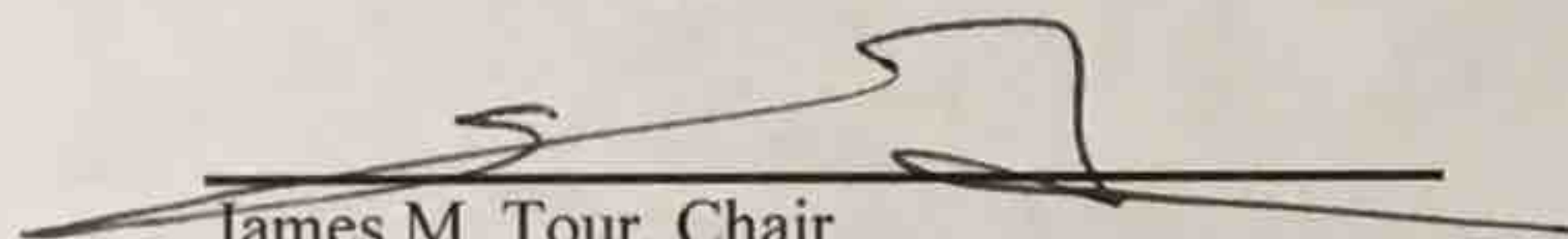
by

Yilun Li

A THESIS SUBMITTED
IN PARTIAL FULFILLMENT OF THE
REQUIREMENTS FOR THE DEGREE

Doctor of Philosophy

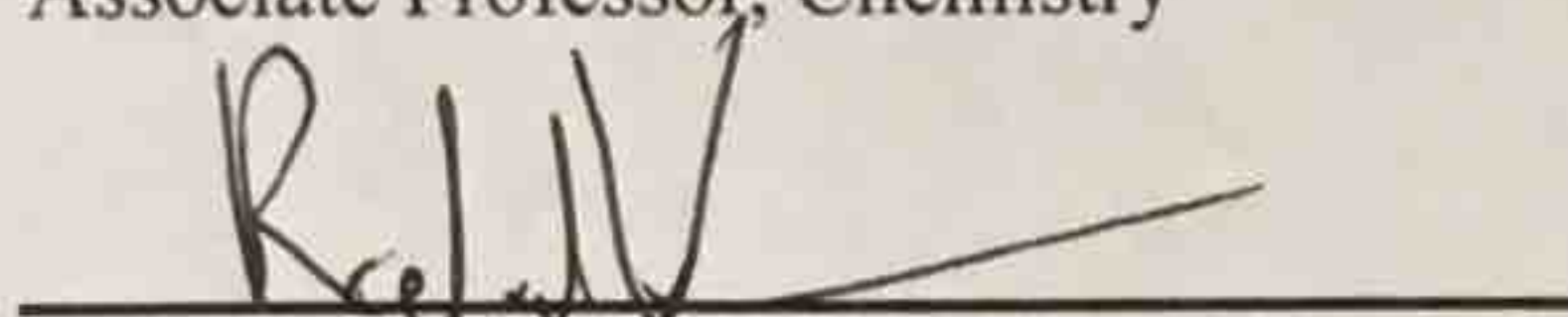
APPROVED, THESIS COMMITTEE



James M. Tour, Chair
T. T. and W. F. Chao Professor, Chemistry



Angel Marti
Associate Professor, Chemistry



Rafael Verduzco
Associate Professor, Chemical and
Biomolecular Engineering

HOUSTON, TEXAS
July 2017

RICE UNIVERSITY

**Synthesis, Structure and Properties of Various Carbon
Nanomaterials**

by

Yilun Li

A THESIS SUBMITTED
IN PARTIAL FULFILLMENT OF THE
REQUIREMENTS FOR THE DEGREE

Doctor of Philosophy

APPROVED, THESIS COMMITTEE

James M. Tour, Chair
T. T. and W. F. Chao Professor, Chemistry

Angle Marti
Associate Professor, Chemistry

Rafael Verduzco
Associate Professor, Chemical and
Biomolecular Engineering

HOUSTON, TEXAS
July 2017

ABSTRACT

Synthesis, Structure and Properties of Various Carbon Nanomaterials by

Yilun Li

Carbon nanomaterials can have a unique place in the field of nanotechnology thanks to their exceptional electrical, optical, chemical, and mechanical properties, and thus they have become promising for a diverse array of applications. More importantly, the properties of a specific carbon nanomaterial are often determined by the structure of the material itself, which further traces back to its synthesis. Accordingly, it is of great interest and importance to understand the relationship between the synthesis, structure, and properties of the carbon nanomaterials.

My thesis begins with the chemical vapor deposition (CVD) synthesis and investigation of various graphene/nanotube (NT) hybrid structures in **Chapter 1**, including rebar graphene from functionalized boron nitride nanotubes (BNNTs), growing carbon nanotubes (CNTs) from both sides of graphene, and the selective growth and transfer of seamless three-dimensional (3D) graphene/CNT hybrids. Then, **Chapter 2** discusses the fabrication of laser-induced graphene (LIG) materials in controlled atmospheres. Next, **Chapter 3** describes the 3D printed graphene foams. Finally, **Chapter 4** introduces biochar as a renewable source for high-performance CO₂ porous carbon sorbent.

Acknowledgments

First of all, I give my most sincere thanks to Prof. James M. Tour, the mentor of my thesis and also an outstanding role model for my career. Ever since the first day I came to Rice University, Prof. Tour has been teaching me what it takes to be a responsible scientist and as well as a successful person. As one of the world's most cited researcher, Prof. Tour usually has a heavily occupied schedule, but he has always been available in the office or through the email whenever I seek instruction or discussion. Prof. Tour's passion and enthusiasm towards chemistry and science has always been a strong motivation for me to face and overcome the challenges during my graduate studies. Without his timely supervision and discussion, this thesis would not have been accomplished.

I also want to thank Dr. Dustin K. James and Dr. Paul Cherukuri, the lab managers of the Tour group. They are always the first readers of my manuscripts. Their revisions and comments on my writings and research have been extremely valuable towards my every publication. I truly appreciate their time and work.

Special thanks to Prof. Angel Marti and Prof. Rafael Verduzco, who are so generous to serve as my committee members, and to provide insightful suggestion and valuable comments towards my PhD thesis.

Great thanks to my parents, Baoji Li and Fang Liu, who have always been supporting me to finish my PhD. I am also deeply grateful to my fiancée, Lei Lei. Her love and care have always been the strongest power behind me.

I would also like to express my gratitude to the senior researchers, peers, and collaborators who have been very influential and helpful during my PhD studies. Among them are: Prof. Pulickel M Ajayan, Prof. Jun Lou, Prof. Miguel Jose-Yacamán, Prof. Jian Lin, Prof. Jinlong Jiang, Prof. Xiujun Fan, Prof. Yang Yang, Prof. Christopher J. Arnusch, Prof. Almaz S. Jalilov, Prof. Xinlu Li, Prof. Jian Tian, Prof. Yonghao Zheng, Dr. Bo Chen, Dr. Gang Liang, Dr. Wenhua Guo, Dr. Zheng Yan, Dr. Zhiwei Peng, Dr. Nam Dong Kim, Dr. Gedeng Ruan, Dr. Lei Li, Dr. Pei Dong, Dr. Huilong Fei, Dr. Swatantra P. Singh, Dr. Chih-Chau Hwang, Dr. Rodrigo V. Salvatierra, Dr. Seoung-Ki Lee, Dr. Yongsung Ji, Dr. Changsheng Xiang, Dr. Caitian Gao, Dr. Gunuk Wang, Dr. Jason A Mann, Dr. Abdul-Rahman O. Raji, Carter Kittrell, Junwei Sha, Ruquan Ye, Andrew Metzger, Lizanne G. Nilewski, Duy Xuan Luong, Jibo Zhang, Tuo Wang, Chenhao Zhang, and Gladys A. L. Silva among many others. It has been a very fruitful four years for me because of your support and friendship.

Contents

Acknowledgments.....	iii
Contents	v
List of Figures	vii
List of Tables	xii
List of Equations	xiii
List of Videos.....	xiv
Nomenclature	15
Graphene/Nanotube Hybrid Structures	18
1.1. Introduction.....	18
1.2. Rebar Graphene from Functionalized BNNTs	22
1.2.1. Experimental Section	22
1.2.2. Result and Discussion	26
1.2.3. Conclusion.....	46
1.3. Growing CNTs from Both Sides of Graphene	47
1.3.1. Experimental Section	47
1.3.2. Result and Discussion	50
1.3.3. Conclusion.....	68
1.4. Growth and Transfer of Seamless 3D Graphene/CNT Hybrids	69
1.4.1. Experimental Section	69
1.4.2. Result and Discussion	71
1.4.3. Conclusion.....	85
1.5. Experimental Contributions	86
Laser-Induced Graphene Materials	87
2.1. Introduction.....	87
2.2. Laser-Induced Graphene in Controlled Atmospheres.....	89
2.2.1. Experimental Section	89
2.2.2. Result and Discussion	95
2.2.3. Conclusion.....	124

2.3. Experimental Contributions	125
Three-Dimensional Graphene Foams	126
3.1. Introduction.....	126
3.2. Three-Dimensional Printed Graphene Foams.....	128
3.2.1. Experimental Section	128
3.2.2. Result and Discussion	130
3.2.3. Conclusion.....	150
3.3. Experimental Contributions	151
Porous Carbon for CO₂ Capture.....	152
4.1. Introduction.....	152
4.2. Biochar as a Renewable Source for High-Performance CO ₂ Sorbent	155
4.2.1. Experimental Section	155
4.2.2. Result and Discussion	158
4.2.3. Conclusions	178
4.3. Experimental Contributions	178
References	180

List of Figures

Figure 1-1. The synthesis, Raman spectra, and photograph of RGBNNT.....	28
Figure 1-2. Photograph of raw BNNTs.	29
Figure 1-3. Photographs and TEM images of functionalized BNNTs solutions.	29
Figure 1-4. Raman spectra of RGBNNT on Cu foils.	30
Figure 1-5. Raman mapping of graphene and RGBNNT.....	32
Figure 1-6. Raman spectra of BNNTs on Cu.....	33
Figure 1-7. Photographs of RGBNNT floating on water.	34
Figure 1-8. SEM and TEM characterizations of RGBNNT.....	36
Figure 1-9. SEM images of RGBNNT.	37
Figure 1-10. TEM images of RGBNNT.	37
Figure 1-11. EELS elemental mapping of RGBNNT.	38
Figure 1-12. AR-STEM images of a RGBNNT film (method 3).	40
Figure 1-13. A BF-STEM image of RGBNNT (method 3), same image as Figure 1-12a but without filter.....	41
Figure 1-14. The XPS spectra of RGBNNT (method 1).....	42
Figure 1-15. The XPS spectra of RGBNNT (method 2).....	43
Figure 1-16. The XPS spectra of RGBNNT (method 3).....	43
Figure 1-17. The XPS spectra of RGBNNT (method 4).....	43
Figure 1-18. Optical and electrical properties of RGBNNT.....	45
Figure 1-19. Scheme for the synthesis of graphene/B-CNT and T-CNT/graphene/B-CNT structures.....	52
Figure 1-20. Characterization of the graphene/B-CNT structure.	54

Figure 1-21. The deconvoluted Raman spectra of graphene/B-CNT (Figure 1-20).	55
Figure 1-22. SEM and Raman spectra of typical B-CNT structure, with the composition of Si/Al₂O₃/Fe/CNTs (from bottom to top).	55
Figure 1-23. Scheme for growth mechanisms.	58
Figure 1-24. SEM and Raman spectra of typical T-CNT structure, with the composition of Cu/graphene/CNTs/Fe/Al₂O₃ (from bottom to top).	59
Figure 1-25. Characterization of the T-CNT/graphene/B-CNT structure.	61
Figure 1-26. SEM and TEM analysis of T-CNT/graphene/B-CNT structures with different CNTs growth times.	62
Figure 1-27. TEM images of T-CNT/graphene/B-CNT structure (a-c) and graphene/B-CNT structure (d-f).	64
Figure 1-28. Additional TEM images.	65
Figure 1-29. Electrical measurement between sub-structures.	67
Figure 1-30. Schematic illustration for fabrication and transfer of a patterned 3D GCNT hybrid structure.	72
Figure 1-31. Selective growth of VA-CNTs on patterned GRs.	74
Figure 1-32. VA-CNT growth on graphene pattern of 30 μm width with different thicknesses of catalyst supports (Al₂O₃ layer).	75
Figure 1-33. Polymer-free transfer of patterned GCNT structures.	78
Figure 1-34. Photo of collapsed interdigitated pattern.	79
Figure 1-35. SEM images of transferred and collapsed GCNT structures after drying under atmospheric conditions.	80
Figure 1-36. SEM images of transferred GCNT.	81
Figure 1-37. XPS analysis for Al and Fe before and after the catalyst etching process by BOE or 1 M HCl solution.	82

Figure 1-38. Electric property characterization of a transferred GCNT structure.....	83
Figure 1-39. Electrical property measurements of transferred GCNT.....	85
Figure 2-1. Scheme and SEM images of LIG in controlled atmospheres.	91
Figure 2-2. The top view and side view drawings of the home-built controlled atmosphere chamber.....	92
Figure 2-3. Additional SEM images of LIG in controlled atmospheres.	93
Figure 2-4. LIG made with N₂ in the chamber.	94
Figure 2-5. Additional SEM images of LIG in H₂ and O₂.....	97
Figure 2-6. TEM of carbon nanoparticles on the surface of LIG.....	98
Figure 2-7. TEM images of LIG made under different gas atmosphere.	99
Figure 2-8. Film of LIG that was scraped from the PI surface and prepared through vacuum filtration.....	101
Figure 2-9. Rastering directions and hydrophobicity.....	102
Figure 2-10. Contact angles of LIG samples prepared under different gas atmospheres with different laser duty cycles.....	104
Figure 2-11. XPS and Raman spectra of LIG in controlled atmospheres.	106
Figure 2-12. Additional XPS spectra for LIG in H₂ and Ar.	108
Figure 2-13. Captive bubble contact angels for LIG.	109
Figure 2-14. Characterization of LIG made with an atmosphere of SF₆ in the chamber.....	112
Figure 2-15. SEM and TEM images of LIG prepared with SF₆ (chamber).....	113
Figure 2-16. XPS depth profile for LIG in SF₆.....	114
Figure 2-17. Additional XPS data for LIG in SF₆.....	115
Figure 2-18. Stability of the superhydrophilic/superhydrophobic LIG samples.	117

Figure 2-19. Hysteresis in water contact angle for LIG.....	118
Figure 2-20. Oil/water separation of LIG.....	120
Figure 2-21. Anti-icing properties of LIG.	121
Figure 2-22. Performance of microsupercapacitors prepared from LIG with O₂ in the chamber vs air in the chamber.	123
Figure 2-23. Additional data for LIG supercapacitors.....	124
Figure 3-1. The synthesis of 3D GF.....	132
Figure 3-2. ATR-IR spectra of Ni powder, sucrose, and Ni/sucrose hybrid powder.....	133
Figure 3-3. SEM images of 3D printed GFs with Ni scaffold prepared using 100P.	136
Figure 3-4. Low magnification SEM images of 3D printed GFs with Ni scaffold prepared using 100P.	137
Figure 3-5. SEM images of 3D printed GFs with Ni scaffold prepared using 5S.	138
Figure 3-6. Raman spectra of 3D printed GFs with Ni scaffold.....	140
Figure 3-7. SEM and TEM images of 3D printed GFs after removing Ni.	142
Figure 3-8. Additioanl characterizations for the 3D GF.....	144
Figure 3-9. Electrical testing for 3D GF.....	145
Figure 3-10. Mechanical properties of 3D GF.....	147
Figure 3-11. Additional control experiments.	148
Figure 3-12. 3D printed sample with fiber laser.....	150
Figure 4-1. Calculation of absolute gas uptake.	157
Figure 4-2. The scheme of synthesis and SEM/TEM images of B-PC.	159
Figure 4-3. Textural properties of B-PC characterized by BET measurements.	161

Figure 4-4. CO₂ uptake properties of B-PC.	164
Figure 4-5. Relationship between excess CO₂ uptake and different textural propertes.....	165
Figure 4-6. Additional CO₂ uptake properties of B-PC.	168
Figure 4-7. Comparison of excess gravimetric (25 °C) and volumetric (23 °C) CO₂ uptake for B-PC.....	169
Figure 4-8. Excess CO₂ and CH₄ uptake of B-PC at different temperatures.....	172
Figure 4-9. Properties of B-PC synthesized from biochar made from different biosources.....	175

List of Tables

Table 3-1. Room temperature damping capacities reported in the literature.	
.....	147
Table 4-1. Summary of B-PC synthesized under different activation conditions^a.	
.....	162
Table 4-2. Detailed pore volumes of B-PC synthesized under different activation conditions^a.	
.....	165
Table 4-3. Summary of CO₂ uptakes from B-PC and other porous carbons....	166
Table 4-4. Comparison of working capacity of B-PC and various porous carbons.	170
Table 4-5. Properties of B-PC synthesized from different biosources^a.	176

List of Equations

Equation 1-1. Calculation of RGBNNT FET mobilities.	25
Equation 3-1. Calculation of the porosity of 3D printed GFs.....	141
Equation 3-2. Calculation for damping capacity.	146
Equation 4-1. Calculation of absolute gas uptake. ^{167, 168, 186}	156

List of Videos

Video 2-1. A superhydrophilic LIG surface patterned inside a superhydrophobic LIG frame, and water rolls off the superhydrophobic LIG surface but is trapped at superhydrophilic LIG surface domains.....	104
Video 2-2. Water droplet bouncing on the surface of LIG with SF ₆ in the chamber.....	113
Video 2-3. Oil filter in performance.....	121

Nomenclature

1D	One-dimensional
2D	Two-dimensional
3D	Three-dimensional
a-H	Atomic hydrogen
A-PC	Asphalt-derived porous carbon
AR-STEM	Atomic resolution scanning transmission electron microscope
B-CNT	Base-grown carbon nanotube
B-PC	Biochar-derived porous carbon
BE	Binding energy
BET	Brunauer-Emmett-Teller
BF	Bright field
BN	Boron nitride
BNNT	Boron nitride nanotube
BOE	Buffered oxide etchant
CNT	Carbon nanotube
CPD	Critical point drying
CVD	Chemical vapor deposition
DF	Dark field
DI	Deionized

EELS	Energy loss spectroscopy
FET	Field effect transistor
GCNT	Graphene/CNT
GF	Graphene foam
GNR	Graphene nanoribbon
HTP	High temperature pressure
LIG	Laser-induced graphene
MOF	Metal-organic framework
NLDFT	Non-local density functional theory
NT	Nanotube
ORR	Oxygen reduction reaction
PET	Poly(ethylene terephthalate)
PI	Polyimide
PMMA	Poly(methylmethacrylate)
RBM	Radial breathing mode
RIE	Reactive ion etch
RGBNNT	Rebar graphene with BNNTs
RPM	Revolutions per minute
SAED	Selected area electron diffraction
SEM	Scanning electron microscope
STEM	Scanning transmission electron microscope
T-CNT	Tip-grown carbon nanotube

TEM	Transmission electron microscope
VA-CNT	Vertically aligned carbon nanotube
XPS	X-ray photoelectron spectroscopy

Chapter 1

Graphene/Nanotube Hybrid Structures

This chapter was entirely copied from references.¹⁻³

1.1. Introduction

Carbon nanotubes (CNTs)^{4, 5} and graphene^{6, 7} are both important members of the family of carbon nanomaterials with hexagonal aromatic structures. With outstanding properties such as good mechanical strength,^{8, 9} high carrier mobility,¹⁰⁻¹² high thermal conductivity,^{13, 14} and large surface area,^{15, 16} CNTs and graphene are promising candidates for use in a host of materials ranging from energy storage,¹⁷⁻¹⁹ transistor devices,^{10, 20, 21} and sensors.^{22, 23} The combination between graphene and CNTs, however, has the potential to extend the original 2D/1D structures into versatile 3D structures, and provides further varied performance.²⁴⁻³²

A 1:1 mixture of boron and nitrogen (boron nitride, BN) is isoelectronic to carbon and can also form hexagonal low dimensional nanomaterials including 2D *h*-BN and 1D BN nanotubes (BNNTs), which share an atomic structure similar to graphene and carbon nanotubes (CNTs).^{33, 34} The BN nanomaterials are similar to or more transparent, thermally stable, and thermally conductive than carbon nanomaterials, yet 2D *h*-BN is insulating with a bandgap up to 5.9 eV.³⁵ Due to its having similar hexagonal structures, B-N and C-C bonds tend to segregate in BCN systems.³⁶ Much research has been directed to the study of hybridized hexagonal BCN structures as they provide a new approach to tailor the physical and chemical properties of 2D nanomaterials.³⁷⁻⁴¹ Interesting applications include high-performance oxygen reduction reaction (ORR) catalysts,⁴⁰ bandgap modifications of BN-doped graphene,^{39, 42} and as active layers in field effect transistors (FETs).⁴¹ However, current studies of BCN structures have been limited to the hybridization between 2D graphene and 2D *h*-BN, or doping of carbon/BN nanomaterials by B, N or C atoms; yet the hybridization between 2D graphene and 1D BNNTs remains unstudied.

Recently, the Tour group reported the synthesis of a 2D hybrid structure of 2D graphene and 1D CNTs, called rebar graphene, *via* an annealing and growth protocol that produces graphene with enhanced mechanical strength due to the reinforcement effect of the CNTs.³¹ Characterization showed that the CNTs were partially unzipped and merged into the graphene layer to generate covalent connections between the two materials. Similarly, taking advantage of this concept

of rebar graphene and the shared hexagonal structure of BNNTs and graphene, **section 1.2** reports a 2D hybrid BCN structure of 2D graphene and 1D BNNTs, namely rebar graphene with BNNTs (RGBNNT). This rebar film was synthesized from functionalized or wrapped BNNTs, where the covalent bonding between partially unzipped BNNTs and graphene enhanced the mechanical strength of the 2D sheet enabling transfer of the sheet to another substrate without polymer adhesion.

Regarding the 3D CNTs/graphene hybrid structures, the Tour group reported a seamless graphene/CNT (GCNT) hybrid structure where the vertically aligned CNT carpets were grown directly from large-area chemical vapor deposition (CVD) graphene through a tip-growth process.²⁸ The covalent bonding and ohmic contact between graphene and CNTs were experimentally confirmed through atomic scale aberration-corrected scanning transmission electron microscope (STEM) and electrical measurements. Yet, only one kind of GCNT hybrid structure (CNT carpets on top of graphene) from one type of catalyst design (Fe/Al₂O₃ on top of graphene) was achieved. And before being able to prepare seamless graphene/CNT structures with further complicated 3D configurations, questions remained whether a top-graphene/bottom-CNT structure could be realized or whether CNT carpets could grow simultaneously from both sides of a graphene layer to form the CNT/graphene/CNT sandwich structure.

In **section 1.3**, with a carefully designed catalyst deposition protocol, we are able to grow vertically aligned CNT carpets beneath graphene through a base-

growth mechanism (B-CNT), which lifts the graphene off the substrate surface, thereby creating a graphene/B-CNT structure. With an additional layer of catalyst, we can simultaneously grow vertically aligned CNT carpets on the top surface of the graphene through a tip-growth mechanism (T-CNT) in addition to the B-CNT, which further generates a sandwich structure of T-CNT/graphene/B-CNT. The good electrical contact between the top and bottom CNT carpets suggests an efficient junction through the hybrid structure. These large-area graphene/CNT hybrids could provide a more complex design for 3D CNT/graphene hybrids, and have applications in the fields of energy storage and nanomanufacturing.

In addition, micro-patterning of the original GCNT hybrid structure could provide further benefits and produce a more versatile platform structure.^{43, 44} Several methods have been developed to prepare patterned CNT arrays. These include either a bottom-up approach by patterning of catalyst for CNT growth using various lithography processes,⁴³⁻⁴⁶ or a top-down approach by micromachining of existing dense vertically aligned CNT (VA-CNT) carpets using focused ion beams or lasers.^{47, 48} Patterned GCNT structures have been developed in the Tour group, showing high AC line filtering performance in micro-supercapacitors.³⁰ Other designs showed excellent field emission properties.⁴⁹

However, fabricating patterned GCNT structures has been much more difficult because of the need for several photolithographic processes, with delicate catalyst aligning steps, on the graphene pattern. This complicated GCNT structure patterning is a tedious process with much room for improvement.

In **section 1.4**, a straightforward methodology is disclosed to fabricate patterned GCNT structures. Using this method, the number of processes is reduced to a single patterning step without the need for additional catalyst aligning and patterning. This patterned GCNT structure is transferred to other substrates without the need for a polymer support. As a result, the transferred GCNT pattern is without contamination from other materials, which increases Ohmic contact through the structure.

1.2. Rebar Graphene from Functionalized BNNTs

1.2.1. Experimental Section

RGBNNT synthesis. A standard 1-inch quartz tube was used as the reaction chamber and temperatures were pre-calibrated using a k-type thermocouple probe (Omega Engineering, Inc.). The typical synthesis process was as follows. A 25- μm -thick 10 cm \times 10 cm Cu foil (99.8% purity, Alfa Aesar) was first pretreated using the electrochemical polishing method as described.⁵⁰ The pretreated Cu foil was cut into 1 cm \times 1 cm pieces and coated with a BNNT solution using a spin-coater. See below for concentrations and spin rates. Then, the Cu foil was loaded into the furnace that served as both an annealing system and as a CVD chamber and the reaction chamber (temperature was increased to 1077 °C before the loading) was evacuated to \sim 16 mTorr. For graphene growth with CH₄, 500 sccm H₂ was introduced into the system and the Cu foil was moved into the hot region of the furnace by a magnetic rod and the foil was annealed for 5 min. Then an additional 1 sccm CH₄ was introduced into

the system for 15 min for the graphene growth. Afterwards, the Cu foil was quickly removed from the hot region using a magnetic rod and permitted to cool to the room temperature. For graphene growth without CH₄, 50 sccm H₂ and 500 sccm Ar were introduced into the system and the Cu foil was then moved into the hot region of the furnace by a magnetic rod and the foil was annealed for 20 min. After the annealing, the Cu foil was quickly removed from the hot region using a magnetic rod and permitted to cool to the room temperature.

Preparation of functionalized BNNTs. Highly crystalline, long, few-walled BNNTs synthesized by a catalyst-free high temperature pressure (HTP) laser heating method were used as raw materials.⁵¹ For RCO₂-functionalized BNNTs, BNNTs (10 mg) were sonicated with HNO₃ (15 mL, 70%) for 12 h, and the reaction mixture was then filtered under vacuum and washed with 20 mL H₂O and then with 20 mL acetone, both H₂O and acetone washes were repeated three times to yield 5.0 mg of HO-BNNTs.⁵² The as-produced HO-BNNTs were then reacted with 2-ethylhexanoyl chloride (5 mL, excess) at 100 °C for 120 h, and the reaction mixture was filtered under vacuum and washed with 20 mL H₂O and then with 20 mL acetone, both H₂O and acetone washes were repeated three times to yield 3.5 mg of RCO₂-BNNTs.⁵³ The as-produced RCO₂-BNNTs were dissolved in CHCl₃ at a concentration of 2 mg/mL. For Pluronic/BNNTs, BNNTs (2 mg) were dispersed together with Pluronic F127 (10 mg, Sigma-Aldrich) in DI water (10 mL). The solution was then tip sonicated (Misonix Sonicator 3000) at 30 W for 1 min to generate a homogeneous solution.

Dispersion of functionalized BNNTs onto Cu foil. For RCO₂-BNNTs solution, 100 μ L RCO₂-BNNTs CHCl₃ solution was deposited on the surface of the pretreated Cu foil (1 cm \times 1 cm) by spin coating at 500 rpm for 10 s, and the procedure was repeated 10 times. For Pluronic/BNNTs solution, the spin-coating was conducted at 1000 rpm for 40 s, and the procedure was repeated 10 times.

Polymer-free transfer of RGBNNT sheets on target substrates. The transfer protocol used was similar to the literature protocol.³¹ (1) The Cu foil was etched in 100 mL 0.1 M aqueous (NH₄)₂S₂O₈ with 1% butanol by volume overnight, resulting in the rebar graphene film being lifted from the surface of the Cu and floating to the top of the etchant solution; (2) submerging a clean glass slide into the etchant and picking up the floating film with the glass slide, followed by transferring the film from the glass slide into 100 mL H₂O containing 1% butanol by volume overnight to wash away remaining etchants; (3) dipping a target substrate into the water and butanol solution, and picking up the film; (4) leaving the sample overnight in the air, and then drying at 60 °C overnight at 130 Torr.

Device fabrication and measurement. RGBNNT FETs were fabricated on SiO₂ (300 nm)/highly doped p-type Si wafers. Six-terminal electrode leads were defined with photolithography followed by the sputter deposition of Au (20 nm) and lift-off. A six-probe station (Desert Cryogenic TT-probe 6 system) was used to measure the electrical properties under a pressure of 10⁻⁵-10⁻⁶ Torr under room temperature using an Agilent B1500A Semiconductor Device Analyzer. The

mobilities of the FET devices were calculated based on the slope of current variation against gate voltage using **Equation 1-1**:

$$\mu = \left(\frac{\Delta I_{ds}}{\Delta V_{gs}} \right) / \left(\frac{C_g W V_{ds}}{L} \right)$$

Equation 1-1. Calculation of RGBNNT FET mobilities.

where I_{ds} and V_{ds} are the source–drain current and voltage, respectively, V_{gs} is the back-gate source voltage, L and W are the effective channel length and width, respectively, and C_g is the gate capacitance of the FET device.

Calculations for using RCO₂ functional group and Pluronic F127 as carbon source for graphene growth. The surface area of single layer graphene is 2965 m²/g (both sides).¹⁶ Then, for a 1 cm × 1 cm Cu foil, the mass of graphene (mass of C atoms) is 7 × 10⁻⁸ g. For method 2 (RCO₂-BNNTs), the concentration of the solution is 2 mg/mL, the mass percentage of C atoms is ~ 40% as determined by X-ray photoelectron spectroscopy (XPS) analysis. If only 10 µL of the solution stays on the Cu after spin coating (100 µL, 10 times), the mass of C left is 8 × 10⁻⁶ g, over 100 times larger than the amount needed. Similarly, for method 4 (Pluronic/BNNTs), the concentration of the solution is 12 mg/mL and the mass percentage of C atoms is ~ 30% as determined by XPS analysis. If only 10 µL of the solution stays on the Cu after spin coating (100 µL, 10 times), the mass of C left is 5 × 10⁻⁶ g, over 500 times larger than the amount needed. In conclusion, there should be

enough C from RCO₂ functional groups or Pluronic F127 to serve as the carbon source for graphene growth.

Characterizations. The Raman spectra were recorded with a Renishaw Raman RE01 scope. Scanning Electron Microscope (SEM) images were taken using a JEOL 6500F Scanning Electron Microscope. Transmission Electron Microscope (TEM) characterizations were performed using a 200-kV JEOL FE2100 TEM. STEM images were collected with a JEOL JEM-ARM200F operated at 80 kV equipped with a Cs probe corrector. A six-probe station (Desert Cryogenic TT-probe 6 system) was used to measure the electrical properties under a pressure of 10⁻⁵-10⁻⁶ Torr at room temperature using an Agilent B1500A Semiconductor Device Analyzer. XPS was performed on a PHI Quantera SXM scanning X-ray microprobe with 100 μm beam size and 45° takeoff angle, and calibrated using C 1s at 284.5 eV.

1.2.2. Result and Discussion

The synthesis scheme of the rebar graphene with BNNTs (RGBNNT) is shown in **Figure 1-1a**. Highly crystalline, long, few-walled BNNTs synthesized by a catalyst-free high temperature pressure (HTP) laser heating method (**Figure 1-2**) were used as starting materials.⁵¹ Functionalized BNNT solutions were prepared using two approaches. In the first approach, 2-ethylhexanoyl functionalized-BNNTs (RCO₂-BNNTs) were prepared by sonicating BNNTs with HNO₃ to introduce hydroxyl groups (HO-BNNTs),⁵² followed by reaction with 2-ethylhexanoyl chloride for 120 h to form the 2-ethylhexanoyl esters.⁵³ Surfactant (Pluronic F127) dispersed BNNTs

(Pluronic/BNNTs) were prepared by tip-sonicating BNNTs with Pluronic F127 solution for 1 min. Digital photos of the functionalized BNNT solutions and TEM images of single RCO₂-BNNT and Pluronic/BNNT tubes are shown in Supporting **Figure 1-3**. The functionalized BNNT solutions (0.2 mg/mL) were spin-coated onto pre-treated Cu foils (1 cm ×1 cm).⁵⁴ The synthesis of rebar graphene was then performed in a tubular furnace with and without CH₄ as the carbon source. When using CH₄ as the carbon source, the Cu foils were loaded into a CVD furnace at 1077 °C, annealed with 500 sccm H₂ at 7 Torr for 5 min, and then an additional 1 sccm CH₄ was introduced for 15 min. When not using CH₄ as the carbon source, the Cu foils were loaded into a furnace at 1077 °C, and then annealed with 500 sccm Ar and 50 sccm H₂ at 7 Torr for 20 min. In this case, the RCO₂-functional groups or the wrapped Pluronic surfactant served as the carbon sources for the graphene growth. To simplify, the synthesis of RGBNNT using RCO₂-BNNTs and CH₄ is denoted as method 1; the synthesis of RGBNNT using RCO₂-BNNTs without CH₄ is denoted as method 2; the synthesis of RGBNNT with Pluronic/BNNTs with CH₄ is denoted as method 3; and the synthesis of RGBNNT with Pluronic/BNNTs without CH₄ is denoted as method 4. All growth methods afforded nearly identical 2D-film products.

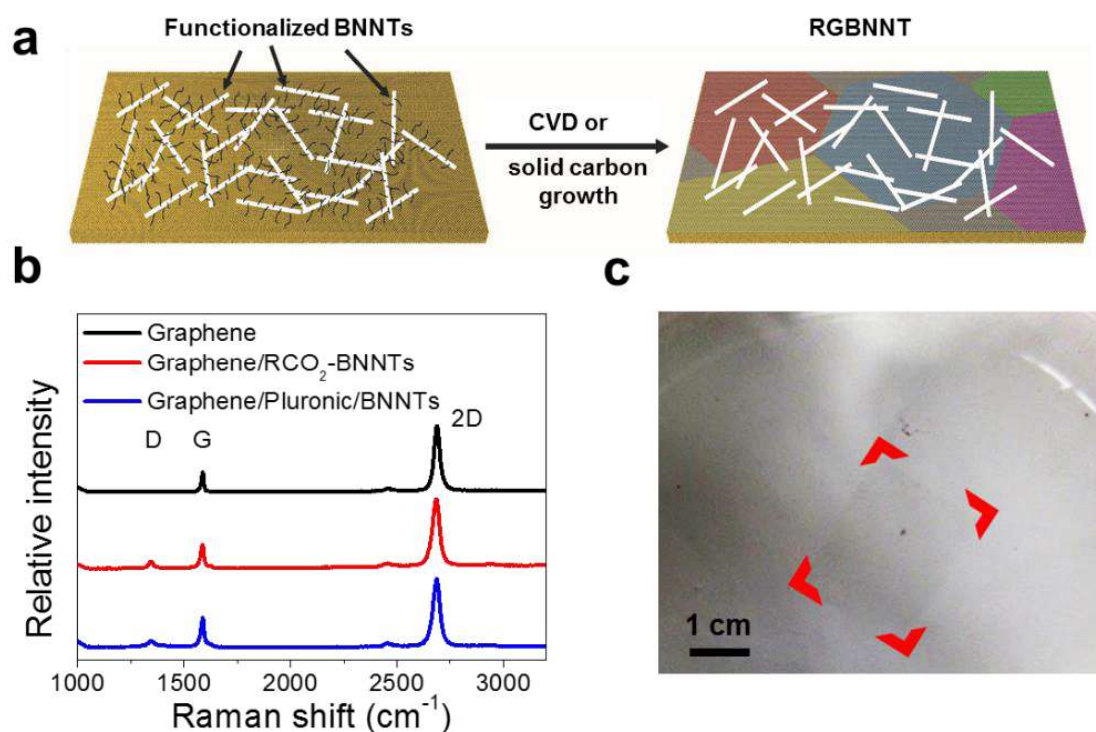


Figure 1-1. The synthesis, Raman spectra, and photograph of RGBNNT.

(a) The synthesis of RGBNNT was accomplished by first depositing functionalized BNNTs onto Cu foil, and then conducting the CVD or solid carbon source process for graphene growth. (b) Raman spectra (excited with 514 nm laser) of as-grown RGBNNT on a SiO₂/Si substrate, showing that single-layer graphene sheets were synthesized using method 1 and method 3. (c) Photograph of free-floating RGBNNT synthesized using method 1. Red highlights are used to enhance visualization of the high-transparency rectangular film.



Figure 1-2. Photograph of raw BNNTs.

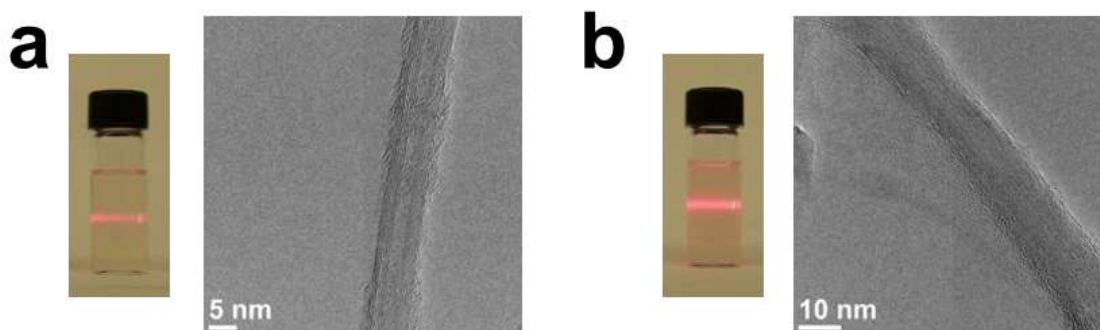


Figure 1-3. Photographs and TEM images of functionalized BNNTs solutions.
(a) Photograph of RCO₂-BNNTs solution (with a laser light passing through the solution) and TEM image of an isolated nanotube. (b) Photograph of Pluronic/BNNTs solution (with a laser light passing through the solution) and TEM image of an isolated nanotube.

To investigate the formation of graphene after annealing or CVD growth, Raman spectra were taken of the product on the Cu foils (**Figure 1-4**). For all four methods, the representative Raman spectra show a G band at $\sim 1585 \text{ cm}^{-1}$ and a 2D band at $\sim 2690 \text{ cm}^{-1}$, similar to those of graphene synthesized using the CVD reaction with CH_4 as the carbon source but without any BNNTs. As the ratio between the intensity of the 2D band and the G band in Raman spectra has been widely used to determine the number of layers of graphene,^{55, 56} the as-grown RGBNNT was found to be single-layer graphene with a 2D/G intensity ratio of ~ 3 , similar to that from rebar graphene made using CNTs.³¹

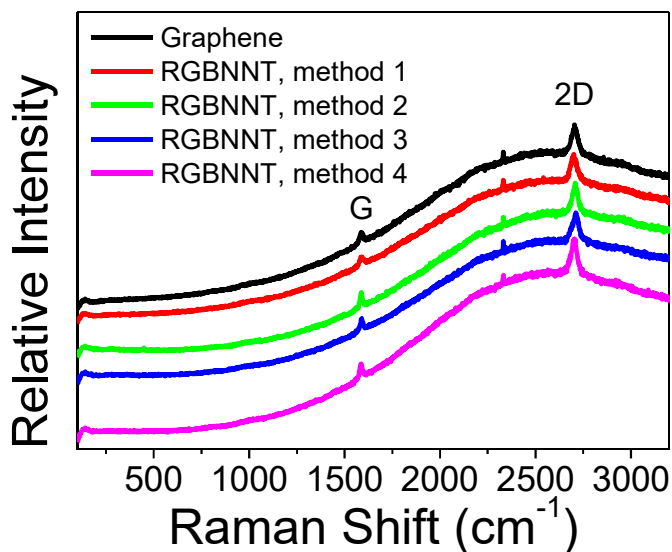


Figure 1-4. Raman spectra of RGBNNT on Cu foils.

Raman spectra (excited with 514 nm laser) of as-grown RGBNNT on Cu. The black curve is the control of graphene synthesized without BNNTs; the red curve is RGBNNT synthesized using method 1; the green curve is RGBNNT synthesized using method 2; the blue curve is RGBNNT synthesized using method 3; the pink curve is RGBNNT synthesized using method 4.

Interestingly, while an external gas flow (CH_4 for instance) is often used as the primary carbon source for graphene growth,⁵⁷ here monolayer graphene was also synthesized without introducing CH_4 (method 2 and method 4), as shown in **Figure 1-4**. In this case, the RCO_2 -BNNTs functional groups or the Pluronic surfactant in the Pluronic/BNNTs were alternative carbon sources for graphene growth.³¹ This CH_4 -free approach, similar to the use of solid carbon sources for graphene growth,⁵⁸⁻⁶¹ provides another method for the synthesis of RGBNNT.

To eliminate the influence of Cu fluorescence and obtain better resolution for the Raman analyses, the synthesized RGBNNT and graphene produced without BNNTs were transferred onto SiO₂/Si substrates followed by Raman analyses. From **Figure 1-1b**, compared to the control (single-layer graphene), the RGBNNT made from method 1 and method 3 both showed weak but higher D band ($\sim 1345\text{ cm}^{-1}$) and D' band ($\sim 1620\text{ cm}^{-1}$, shoulder peak) signal, which originate from the distortion in the graphene lattice.⁶² In addition, from the Raman mapping data shown in **Figure 1-5**, RGBNNT made from all four methods show higher D/G ratios in a 100 μm^2 area when compared with single-layer graphene, yet with a relatively constant range for 2D/G ratios. These increased distortion peaks within RGBNNT were caused by graphene/BN hybridization,^{39, 41} yet the single-layer characteristic of graphene is well-retained. Although the distribution of the D/G ratio is not perfectly uniform throughout the mapped area, this variation is probably not a good correlation with the position of the BNNTs, as the size of BNNTs, with a diameter of 5 to 10 nm, is much smaller than the size of the Raman laser spot, with a diameter of 1 to 2 μm . The Raman spectra of spin-coated BNNTs on Cu foils are shown in **Figure 1-6**, with a weak peak at $\sim 1370\text{ cm}^{-1}$, corresponding to the hexagonal BN structure.^{63, 64} After graphene growth, however, these weak peaks were no longer observed (**Figure 1-1b**, **Figure 1-6**), indicating the damage of the BNNT structure, as induced by the interaction between graphene and BNNTs which share the hexagonal structure.

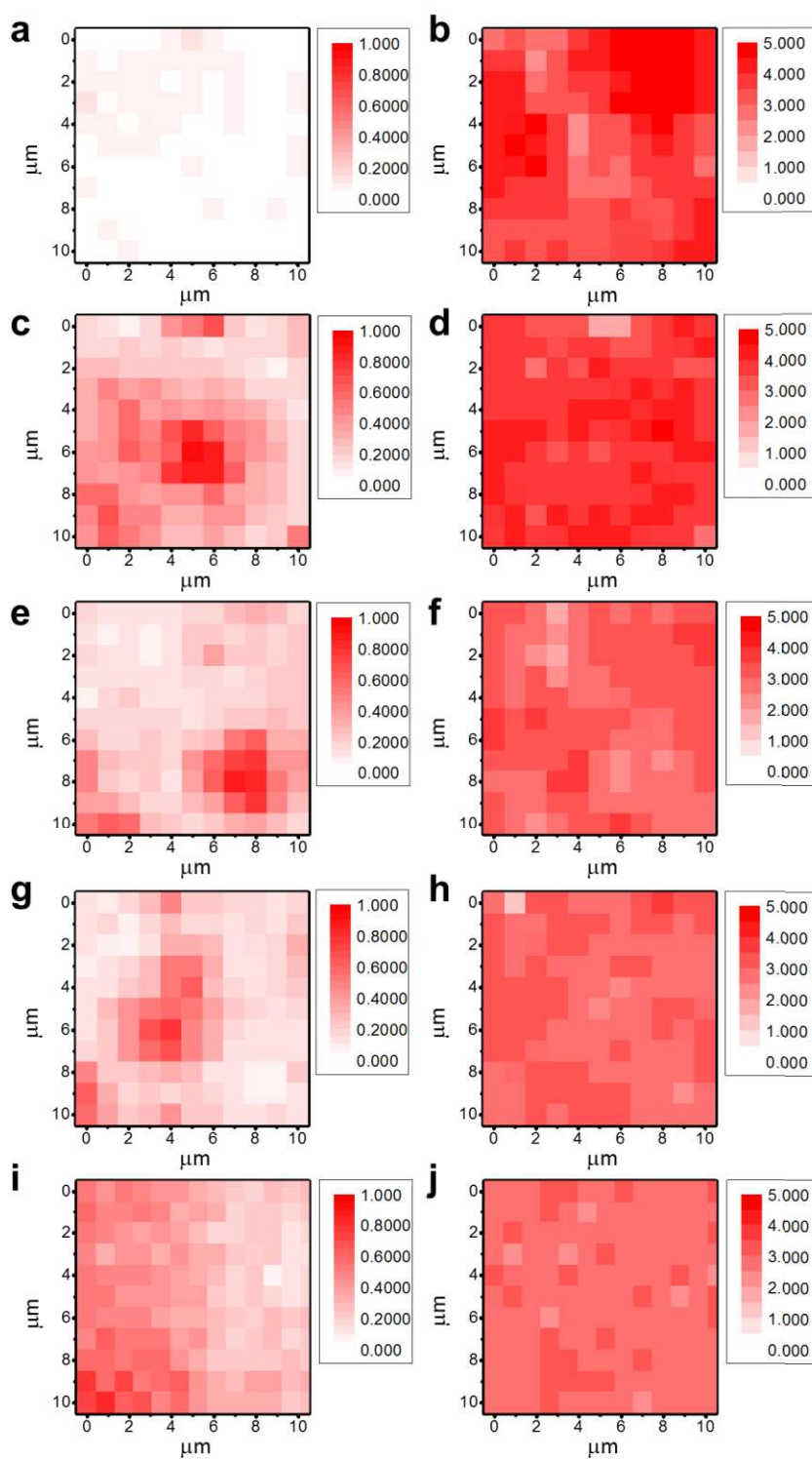


Figure 1-5. Raman mapping of graphene and RGBNNT.

Raman mapping (excited with 514 nm laser) of (a,b) graphene and RGBNNT made from (c,d) method 1; (e,f) method 2; (g,h) method 3; and (i,j) method 4; on SiO₂/Si substrate. (a,c,e,g,i) show the ratio between the intensity of the D peak over the G peak (D/G). (b,d,f,h,j) show the ratio between the intensity of the 2D peak over the G peak (2D/G).

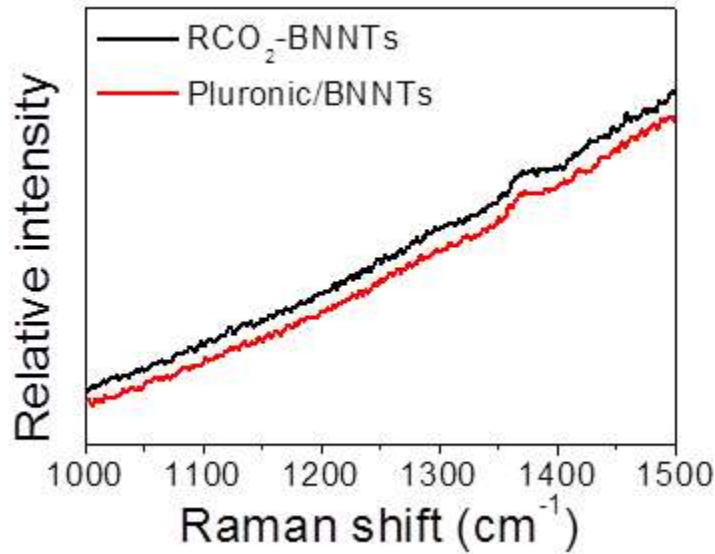


Figure 1-6. Raman spectra of BNNTs on Cu.

Raman spectra (excited with 514 nm laser) of spin-coated RCO₂-BNNTs and Pluronic/BNNTs on Cu before graphene growth.

For most conventional methods, the use of a polymer to assist transfer is required when graphene^{65, 66} or graphene-like 2D materials^{67, 68} are transferred onto other substrates after growth. To test the mechanical strength and ability to transfer without assistance from a polymer, the RGBNNT on Cu foil (method 1) was etched in (NH₄)₂S₂O₈/H₂O/C₄H₉OH without PMMA protection to dissolve the Cu

substrate. The remaining RGBNNT floated on 1% butanol in H₂O without any breakage (**Figure 1-1c** and **Figure 1-7a**); this was also the case for RGBNNT grown using methods 2 to 4 (**Figure 1-7b-d**). As a control experiment, a graphene film grown on a Cu substrate without BNNTs was also tested for transferring without PMMA protection. Interestingly, this sample (not shown) broke apart when floated on a water/butanol surface. Admittedly this test is not a quantitative measurement for robustness determination. Based on this result, BNNTs also form a rebar network within the monolayer graphene film and in turn the mechanical strength of the 2D film was enhanced.

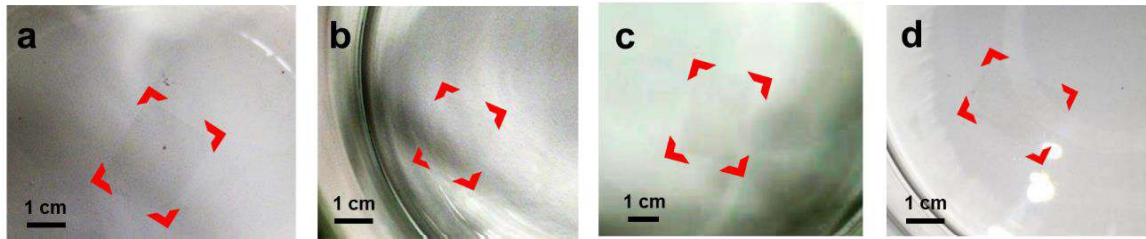


Figure 1-7. Photographs of RGBNNT floating on water.
Photographs of free-floating RGBNNT on 1% butanol in H₂O. (a) Method 1; (b) method 2; (c) method 3; and (d) method 4. To aid visualization, the rectangular RGBNNT is highlighted in red at the corners.

To examine the formation of BNNT networks within the graphene layer, scanning electron microscope (SEM) images of RGBNNT transferred to a SiO₂/Si substrate are shown in **Figure 1-8a** and **Figure 1-9**; almost no obvious BNNT bundles are observed, indicating the formation of a 2D hybrid sheet similar to rebar graphene with CNTs.³¹ The as-produced RGBNNT was transferred onto a

transmission electron microscope (TEM) grid for further characterization. From a representative TEM image (**Figure 1-8b**), a BNNT network could be observed on the continuous 2D sheets. The existence of the underlying graphene sheet was examined by selected area electron diffraction (SAED) (**Figure 1-8c**), and the hexagonal crystalline structure of graphene could be confirmed.⁵⁴ From a higher resolved TEM image (**Figure 1-8d** and **Figure 1-10**), the partial unzipping of a BNNT is observed with the disappearance of part of the sidewall of the BNNT, suggesting the covalent interaction between BNNT sidewalls and the graphene sheet, as it is widely reported that BN atoms can covalently network with CNTs^{37, 38} or graphene^{40, 41} based on the shared hexagonal structure to generate the BCN structure. Further evidence of BCN hybridization is provided by electron energy loss spectroscopy (EELS) elemental mapping shown in **Figure 1-11**. It is observed that B and N atoms are mostly distributed along the BNNT, with some diffusion into the graphene layer, as a result of the BCN hybridization. The C atoms, on the other hand, are uniformly distributed within the image area. The covalent BCN hybridization should in turn cause the increase of D band in the Raman spectra of RGBNNT as the atomic structure of graphene is influenced by BN introduction.^{39, 41}

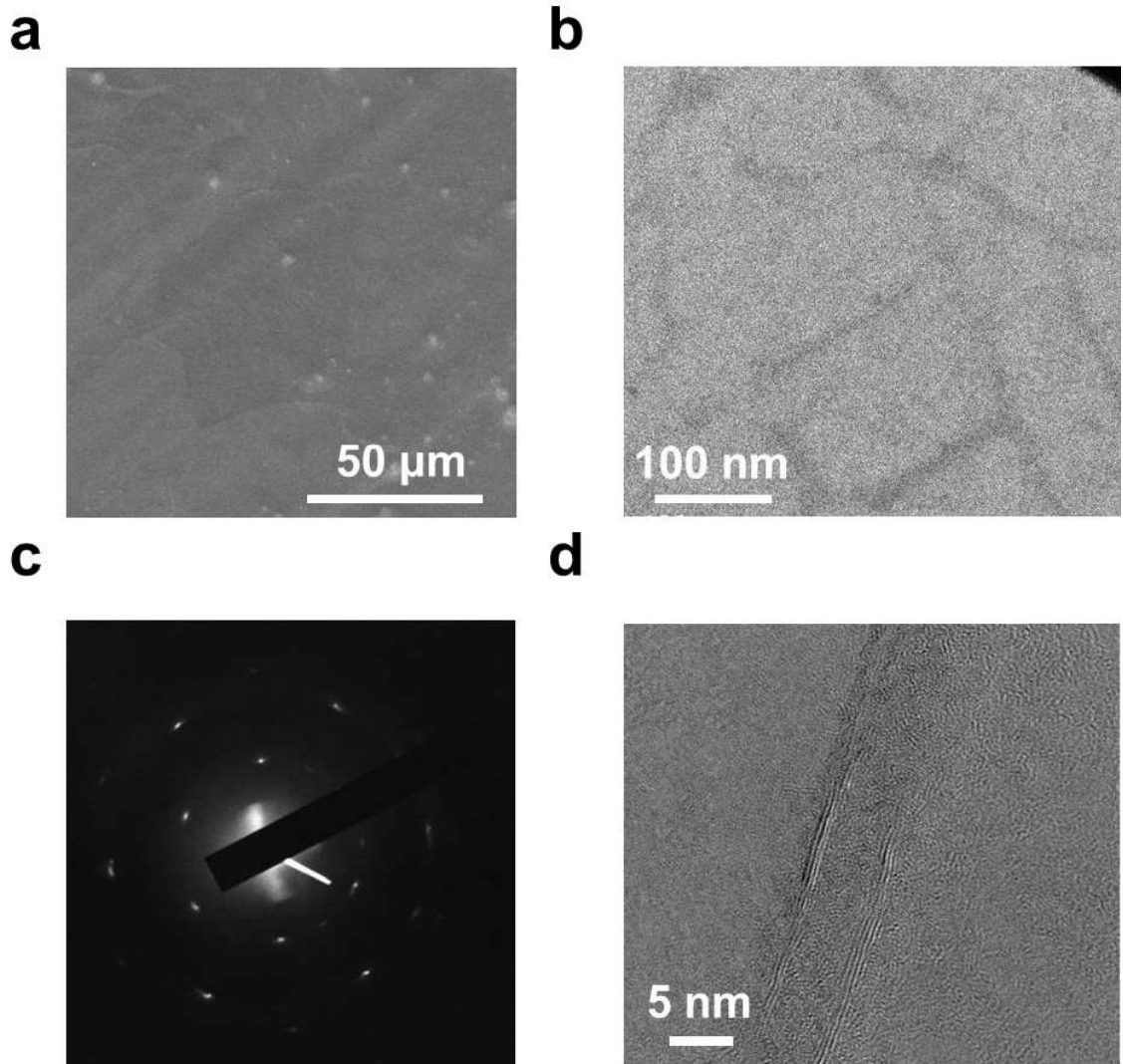


Figure 1-8. SEM and TEM characterizations of RGBNNT.

(a) Typical SEM image of transferred RGBNNT (method 1) on a SiO₂/Si substrate; very few obvious BNNT bundles were observed. **(b)** Typical TEM image of BNNT networks within a RGBNNT (method 3) layer. **(c)** SAED pattern of a RGBNNT film (method 3) on a TEM grid; the hexagonal pattern corresponds to the hexagonal structure of the graphene sheet. **(d)** A TEM image of partially unzipped BNNTs within the RGBNNT film (method 3).

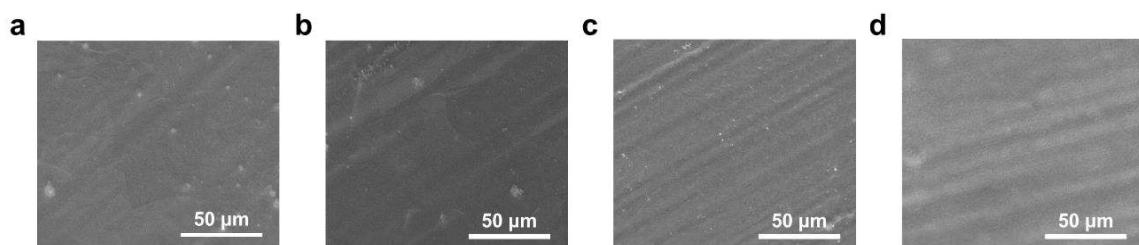


Figure 1-9. SEM images of RGBNNT.

SEM images of RGBNNT prepared from (a) method 1; (b) method 2; (c) method 3; and (d) method 4. Very few BNNT bundles were observed.

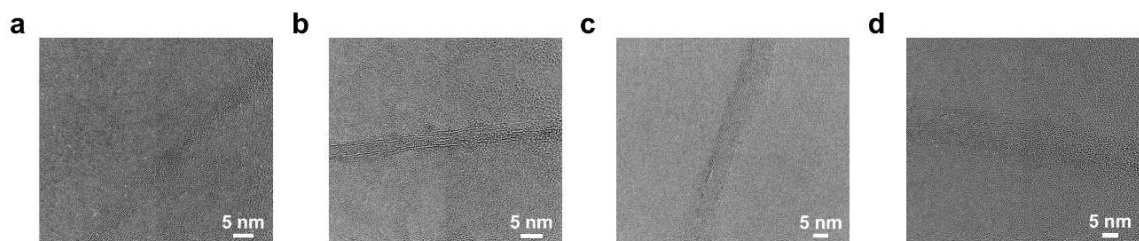


Figure 1-10. TEM images of RGBNNT.

TEM images of a BNNT within RGBNNT prepared from (a) method 1; (d) method 2; (c) method 3; and (d) method 4.

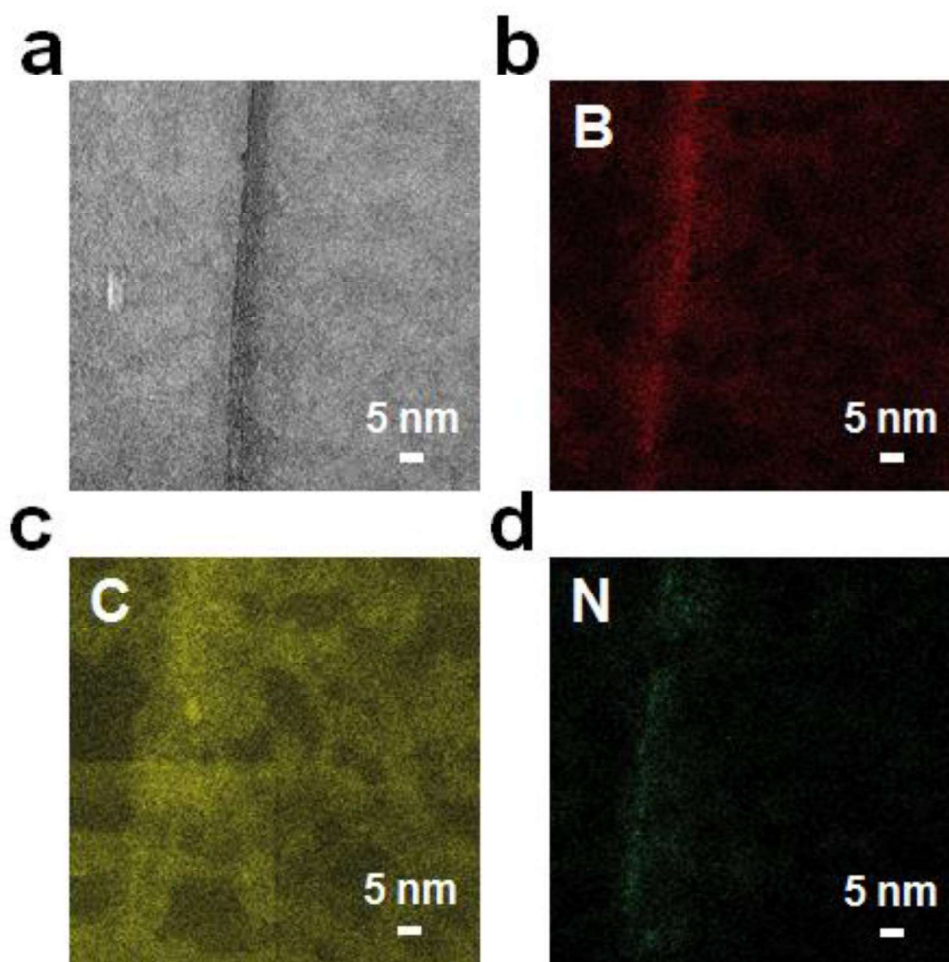


Figure 1-11. EELS elemental mapping of RGBNNT.

EELS elemental mapping of a BNNT within RGBNNT prepared from method 1. (a) TEM image of the BNNT and graphene. (b-d) Elemental distribution of B, C, N, respectively. The mismatch in BNNT position comes from the image drift during TEM imaging.

To further characterize the behavior of BNNTs within the monolayer graphene sheet, atomic resolution scanning transmission electron microscopy (AR-STEM, **Figure 1-12**) images of RGBNNT (method 3) were taken. To confirm the hexagonal structure of graphene, an AR-STEM image was first taken on a graphene

sheet without any appearance of BNNTs. From **Figure 1-13** (without filter) and **Figure 1-12a** (with filter), the hexagonal atomic structure of the graphene sheet is observed, and the distorted direction of the hexagons indicates the graphene sheet is polycrystalline with the existence of grain boundaries.⁶⁹ **Figure 1-12b**, d-f are the bright field (BF) AR-STEM images, and **Figure 1-12c**, g-i are the dark field (DF) AR-STEM images of BNNTs within the graphene layer. **Figure 1-12b,c** are two interconnected BNNTs with an intersection angle of $\sim 90^\circ$; these two BNNTs are part of the BNNT network that strengthens the underlying 2D layer. **Figure 1-12d,g** show a BNNT with a section of the sidewall gone that unzipped and merged with the graphene forming BCN hybrid. **Figure 1-12e,h** are a BNNT where the left side of the sidewall remains intact while the right side of the wall is completely decomposed. **Figure 1-12f,i** are a BNNT with both sidewalls gone, which could be defined as a BN nanoribbon instead of a BNNT. Interestingly, from these images, the BNNTs have partially unzipped and the atoms have merged into the graphene layer, resulting in a BCN hybrid structure.

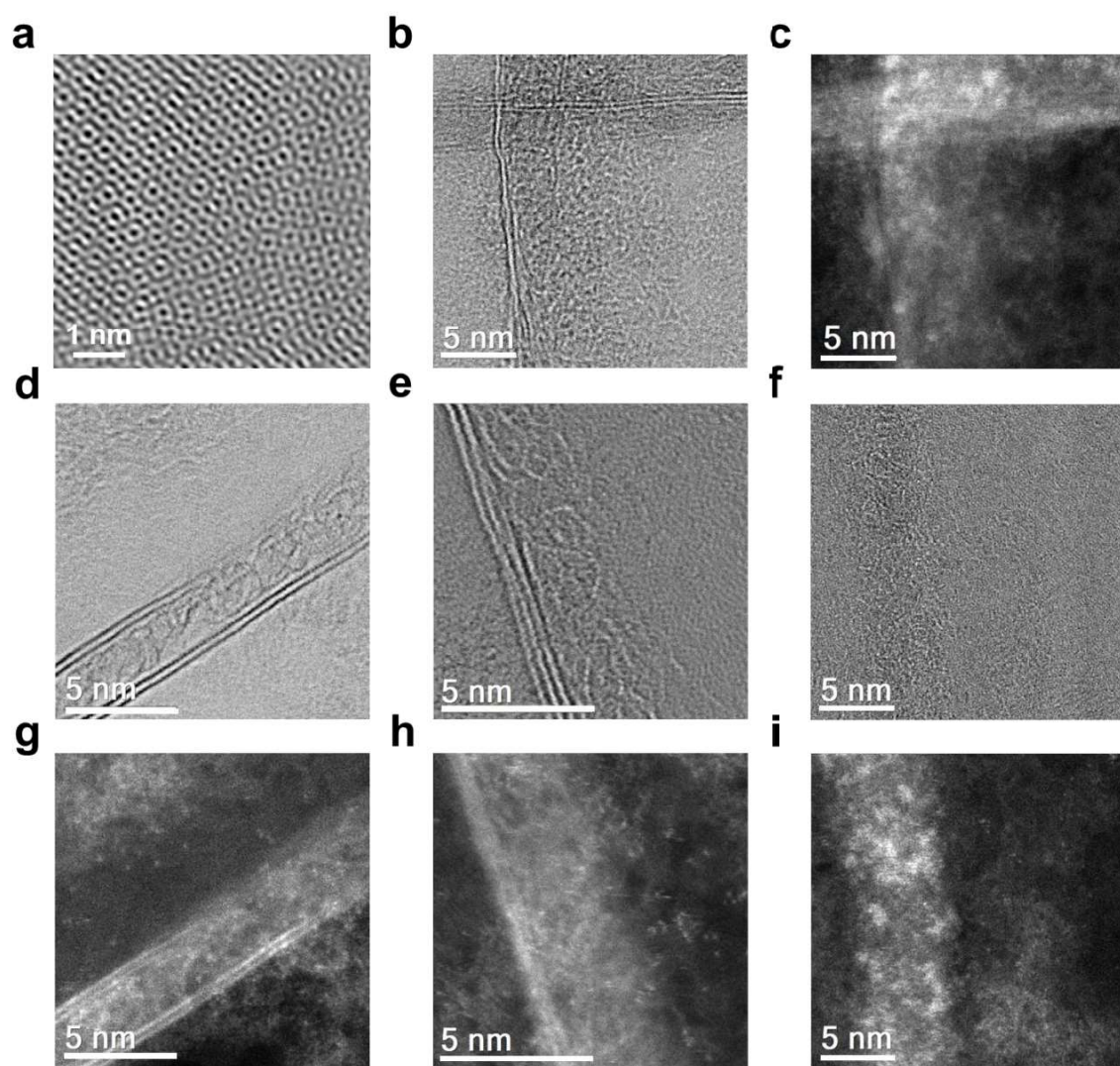


Figure 1-12. AR-STEM images of a RGBNNT film (method 3).

(a) A BF AR-STEM image of RGBNNT with filter applied. **(b, d-f)** BF AR-STEM and **(c, g-i)** DF AR-STEM images of BNNTs within the RGBNNT film. **(b-c)**: two interconnected BNNTs. **(d)** and **(g)**: a BNNT with a section of the sidewall gone (unzipped). **(e)** and **(h)**: a partially unzipped BNNT with the walls at one side merged into the graphene film. **(f)** and **(i)**: a completely unzipped BNNT with walls on both sides merged into the graphene film.

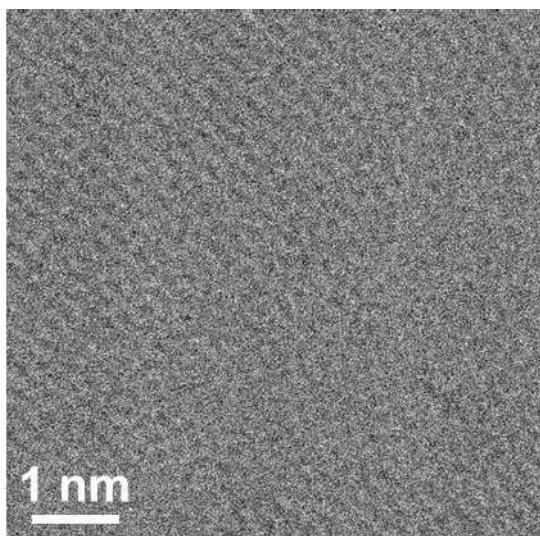


Figure 1-13. A BF-STEM image of RGBNNT (method 3), same image as Figure 1-12a but without filter.

Because two types of interaction, non-covalent interaction and covalent bonding, could exist between the graphene and BNNTs, a control experiment was designed to demonstrate that the enhanced mechanical strength of RGBNNT results primarily from the covalent bonding between graphene and BNNT domains. A graphene film grown on Cu was spin-coated with BNNTs, and then etched without PMMA protection in the same way as the RGBNNT sample. This control sample, with only non-covalent interaction between the spin-coated BNNTs and graphene, broke into pieces in 1% butanol in H₂O. Hence, the covalent reinforcement is required for increased mechanical strength.

To analyze the elemental composition of the RGBNNT, X-ray photoelectron spectroscopy (XPS) spectra were taken of the as-grown RGBNNT on the Cu foils

(Figure 1-14, Figure 1-15, Figure 1-16, Figure 1-17). Since the RGBNNT is mainly composed of graphene, the position of 284.5 eV for sp^2 C 1s peak is used as standard to shift all other peaks.^{31, 70} After calibration, the B 1s peak is located at 189.8 eV, and the N 1s peak is located at 397.5 eV; both energies are similar to the values reported for *h*-BN⁷¹ or other BCN hybrid structures.^{39, 41} Interestingly, a side peak of N 1s is observed at 400.2 eV, corresponding to the N-C bond as is reported with N-doped graphene,⁷² which provides further evidence towards the covalent interaction between partially unzipped BNNT and graphene sheet; no obvious side peak of B 1s is observed due to the low S/N ratio. The concentrations of B and N atoms within RGBNNT were found to be 2 to 3%, indicating carbon is the dominant part of the 2D hybrid film.

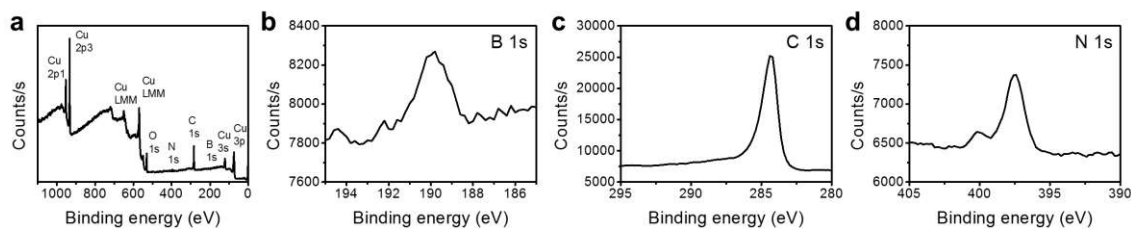


Figure 1-14. The XPS spectra of RGBNNT (method 1). (a) Survey, (b) B 1s, (c) C 1s, (d) N 1s.

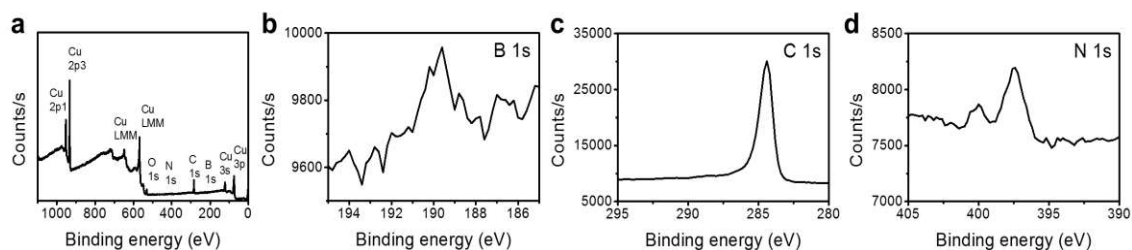


Figure 1-15. The XPS spectra of RGBNNT (method 2).

(a) Survey, (b) B 1s, (c) C 1s, (d) N 1s.

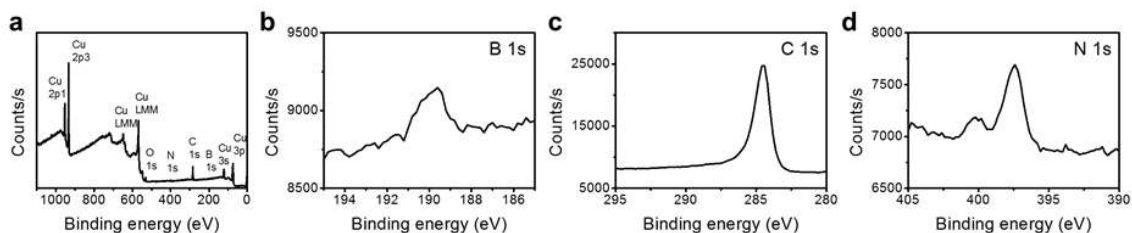


Figure 1-16. The XPS spectra of RGBNNT (method 3).

(a) Survey, (b) B 1s, (c) C 1s, (d) N 1s.

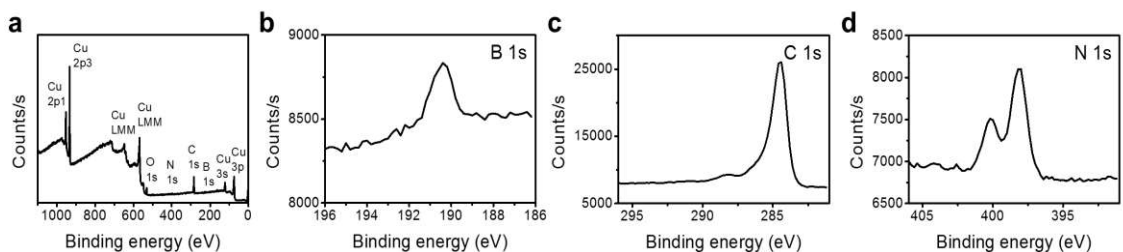


Figure 1-17. The XPS spectra of RGBNNT (method 4).

(a) Survey, (b) B 1s, (c) C 1s, (d) N 1s.

To further characterize the properties of RGBNNT, the as-grown RGBNNT films were transferred onto glass slides, using the polymer-free method, for

transmittance and conductivity measurements (**Figure 1-18a,b**). For RGBNNT made from method 1, the transmittance at 550 nm was 97.0% with a sheet resistance of 36 k Ω /□ . For RGBNNT made from method 3, the transmittance at 550 nm was 98.1% with a sheet resistance of 24 k Ω /□ . The resistance of RGBNNT is significantly higher than that of monolayer graphene (~ 1 k Ω /□)⁶⁶ or rebar graphene with CNTs (0.6 k Ω /□);³¹ this is a result of the impregnation of graphene by insulating BNNTs. A non-covalent interaction should not significantly lower the electrical conductivity of an intact graphene layer, further suggesting the hybridization through covalent interaction in the RGBNNT. As for optical transmittance, RGBNNT has the same transmittance value as monolayer graphene (97.4%)⁶⁶ at 550 nm; BNNTs absorb little light in the visible region,³³ while the high optical absorbance of CNTs makes rebar graphene with CNTs (95.6%)³¹ slightly darker.

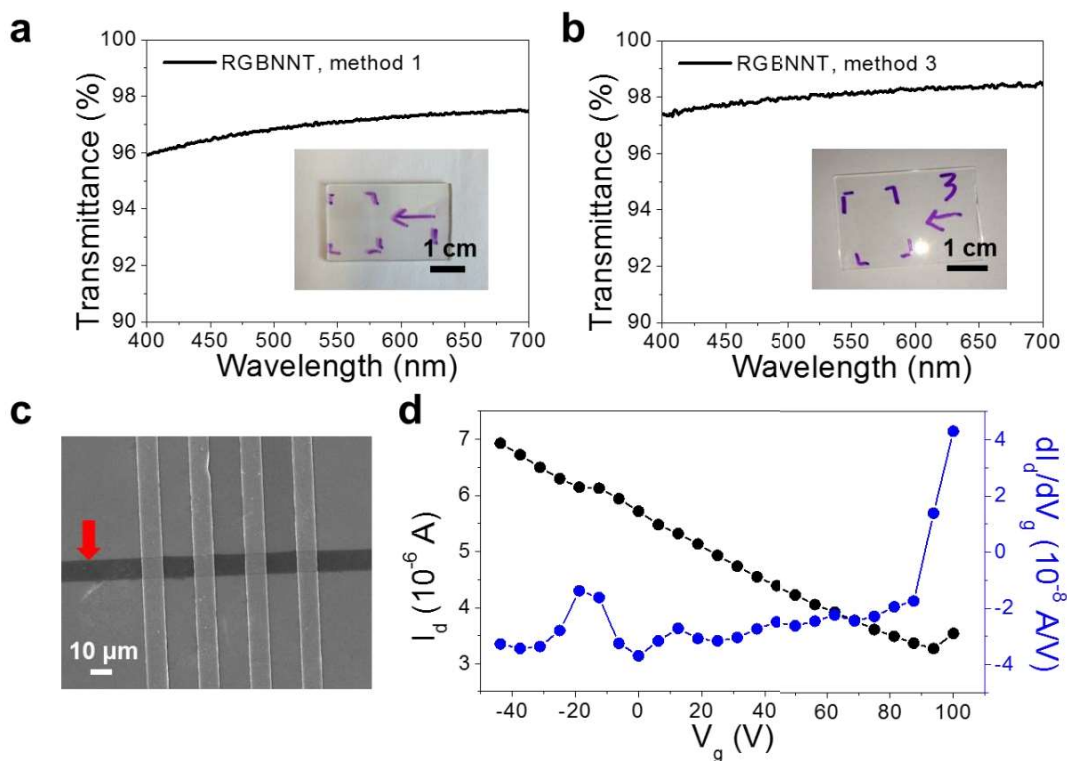


Figure 1-18. Optical and electrical properties of RGBNNT.

UV-Vis spectra of RGBNNT films transferred onto glass slides without the assistance of a polymer. (a) RGBNNT made from method 1, the transmittance at 550 nm was 97.0% with a sheet resistance of 36 k Ω /□ (insert is a photograph of the film on glass). (b) RGBNNT made from method 3, the transmittance at 550 nm was 98.1% with a sheet resistance of 24 k Ω /□ (insert is a photograph of the film on glass). (c) A SEM image of the fabricated RGBNNT (method 1) FET on 300 nm SiO₂/highly doped p-type Si substrate; the red arrow is pointed at the RGBNNT nanoribbon with a width of 10 μm. The four Au electrodes with a separation distance of 14 μm are 90° to the RGBNNT. (d) The drain current as a function of the voltage applied to the back (bottom) gate of the device shown in (c). And the derivative of the drain current vs the back gate voltage. The source-drain voltage was 1 V.

In order to investigate the electrical properties of RGBNNT, a FET was fabricated on a lithography-cut strip of the RGBNNT (method 1). The strip was on

SiO₂ (300 nm)/highly doped p-type Si with four electrodes and tested at 10⁻⁵-10⁻⁶ Torr at room temperature, as shown in **Figure 1-18c**. **Figure 1-18d** shows the V_g - I_d curve with the back-gate voltage ranging from -40 to 100 V at $V_d = 1$ V. The RGBNNTs shows an ambipolar semiconducting behavior (typical of CVD graphene^{66, 73, 74}) with a charge-neutrality point at ~ 95 V, which indicates highly p-doped material due to the BNNT hybridization on the graphene grain boundaries, in agreement with other BCN hybrid structures.^{39, 41, 75} The carrier mobility of the RGBNNT FET device was $\sim 20 \text{ cm}^2 \text{ V}^{-1} \text{ s}^{-1}$ based on the slope of I_d variation with back-gate voltages. This is much smaller than the mobility reported for rebar graphene with CNTs ($1500\text{-}2200 \text{ cm}^2 \text{ V}^{-1} \text{ s}^{-1}$)³¹ or single layer graphene ($2000\text{-}4000 \text{ cm}^2 \text{ V}^{-1} \text{ s}^{-1}$)^{66, 73, 74} on SiO₂. This can be attributed to the scattering of electrons at the interfaces or boundaries between the graphene and BNNT domains, similar to that seen in CVD hexagonal BCN FET devices ($5\text{-}20 \text{ cm}^2 \text{ V}^{-1} \text{ s}^{-1}$).³⁹ These results are consistent with the RGBNNT components being covalently bonded rather than having solely a BNNT/graphene stacking structure. The ON/OFF ratio of this FET device was ~ 2.5 , similar to that seen in single-layer graphene (1-5),^{66, 73, 74} and also similar to CVD h-BCN devices (1-2).³⁹

1.2.3. Conclusion

RGBNNT was successfully synthesized using functionalized BNNTs. Similar to rebar graphene with CNTs, BNNTs formed a rebar network within the graphene layer, and enhanced the mechanical strength of graphene, making it possible to transfer the layer to another substrate without assistance from a polymer. The

BNNT-graphene interface was investigated using AR-STEM, and it was shown that BNNTs were partially unzipped and merged into the graphene layer to generate a BCN hybrid structure, which resulted in an increased D band in the Raman spectra and an increased sheet resistance. The electronic properties of the RGBNNT were measured using a FET. The synthesis of this new kind of 2D hybrid provides an alternative and easy approach towards the hybridization between C and BN nanostructures, while the extension into other graphene-like 2D hybrid structures is foreseeable.

1.3. Growing CNTs from Both Sides of Graphene

1.3.1. Experimental Section

Graphene synthesis. A standard 1-inch quartz tube in a CVD furnace was used as the reaction chamber and the temperature was pre-calibrated using a k-type thermocouple probe (Omega Engineering, Inc.). The typical synthesis process was as follows.⁵⁵ A 25 μm thick $10\times 10\text{ cm}^2$ Cu foil (99.8% purity, Alfa Aesar) was first pretreated using the electrochemical polishing method previously described.⁵⁰ The pretreated Cu foil was cut into $1\times 1\text{ cm}^2$ pieces and then loaded into the reaction chamber and the quartz tube was evacuated to $\sim 16\text{ mTorr}$. The temperature of the tube furnace was then increased to $1000\text{ }^\circ\text{C}$, and the Cu foil was annealed with 300 sccm H_2 for 10 min at 350 Torr controlled by a needle vacuum valve. For graphene growth, 10 sccm CH_4 was introduced to the reaction chamber for 15 min (the flow rate of H_2 was kept at 300 sccm, and the total pressure was at 360 Torr). After

growth, the Cu foil was quickly removed from the hot region and permitted to cool to room temperature under a H₂ atmosphere.

Graphene/B-CNT synthesis. The buffer layer (10-nm-thick Al₂O₃) was deposited on a Si wafer by e-beam evaporation. The catalyst (1-nm-thick Fe) was deposited on top of the Al₂O₃ layer by e-beam evaporation. The as-grown few-layer graphene was then transferred as previously described on top of the Fe/Al₂O₃/Si after etching away the Cu substrate with an aqueous (NH₄)₂S₂O₈ solution to complete the substrate preparation.^{1,31} A water-assisted hot filament furnace was then used for the CNT carpet growth.⁷⁶ With 2 sccm of C₂H₂ and 210 sccm of H₂ (among which 200 sccm was used for water bubbling), the substrate was annealed at 25 Torr for 30 s during which a tungsten filament was activated at 30 W to reduce the catalyst and to start CNT growth. Then the pressure was reduced to 5 Torr and the hot filament was turned off immediately to extend CNT carpet growth for an additional minute.

T-CNT/graphene/B-CNT synthesis. On top of the graphene/Fe/Al₂O₃/Si substrate, another layer of catalyst (1-nm-thick Fe) was deposited by e-beam evaporation, followed by another buffer layer of 3-nm-thick Al₂O₃. The substrate was then carried through the same CNT carpet growth protocol with an anneal time of 30 s followed by a growth time of 1 min.

Characterizations. Raman spectra were recorded with a Renishaw Raman RE01 microscope. SEM images were taken using a JEOL 6500F SEM. TEM characterizations were performed using a 200-kV JEOL FE2100 TEM.

Device fabrication and measurement. The as-grown T-CNT/graphene/B-CNT structure was transferred (upside down) on to an Au/PET substrate by etching with HF aqueous solution. A six-probe station (Desert Cryogenic TT-probe 6 system) was used to measure the electrical properties with an Agilent 4155C semiconductor parameter analyzer. The probe tips used are LakeShore ZN50R-25-W (tip radius 25 μm , Tungsten). The measurement was conducted at room temperature and atmospheric condition. For Au to Au contact, both probe tips directly touched the Au substrate; for Au to B-CNT contact, one probe tip contacted the Au substrate, while the other probe tip contacted the B-CNT component; for B-CNT to B-CNT contact, two probe tips were in contact with two different areas of the B-CNT component.

Graphene transfer. The transfer protocol used was similar to a literature report.^{1, 31} First, the Cu foil was etched in 100 mL 0.1 M aqueous $(\text{NH}_4)_2\text{S}_2\text{O}_8$ with 1% butanol by volume overnight, resulting in a graphene film being lifted off from the surface of the Cu and floating on the top of the etchant solution. Next, a clean glass slide was submerged into the etchant which picked up the floating film with the glass slide, followed by transferring the film from the glass slide into 100 mL H_2O containing 1% butanol by volume overnight to wash away remaining etchants. Finally, dipping a target substrate into the water and butanol solution picks up the film and the sample was left overnight in air.

TEM sample preparation. The as-grown graphene/B-CNT or T-CNT/graphene/B-CNT was scratched off from the substrate and sonicated in chloroform for 5 to 20 min. The suspension was then dropped onto a Cu grid and dried at room temperature.

Typical B-CNT synthesis. The synthesis protocol used was similar to a literature report.⁷⁷ The buffer layer (10-nm-thick Al₂O₃) was deposited on a Si wafer by e-beam evaporation. The catalyst (1-nm-thick Fe) was deposited on top of the Al₂O₃ layer by e-beam evaporation. The substrate was then carried through the same CNT carpets growth protocol with a growth time of 1 min.

Typical T-CNT synthesis. The synthesis protocol used was similar to a literature report.^{28, 76} On top of the as-grown graphene/Cu substrate, catalyst layer (1-nm-thick Fe) was deposited with e-beam evaporation, followed by e-beam evaporation of another buffer layer (3-nm-thick Al₂O₃). The substrate was then carried through the same CNT carpets growth protocol with a growth time of 10 min.

1.3.2. Result and Discussion

The synthesis schemes for graphene/B-CNT and T-CNT/graphene/B-CNT structures are shown in **Figure 1-19**. Few-layer graphene was grown on a Cu substrate using a previously reported CVD method with CH₄/H₂ at 1000 °C.⁵⁵ Thin films of Fe/Al₂O₃ catalysts (1 nm/10 nm thick) were deposited on a Si substrate by e-beam evaporation. The few-layer graphene was then transferred onto the Fe/Al₂O₃/Si substrate after etching away the Cu substrate with an aqueous

(NH₄)₂S₂O₈ solution with 1% butanol.^{1, 31} The as-prepared graphene/Fe/Al₂O₃/Si then went through a previously reported CNT carpets growth protocol using C₂H₂/H₂/H₂O at 750 °C,^{28, 76} and the vertically aligned base-grown CNT carpets then lifted the top graphene layer to yield a graphene/B-CNT structure. The sandwich structure of T-CNT/graphene/B-CNT was obtained by e-beam depositing another layer of Fe (1 nm thick) and then Al₂O₃ (3 nm thick) on top of the graphene/Fe/Al₂O₃/Si substrate. This was followed by a CNT carpet growth process, where vertically aligned base-grown CNT carpets were generated beneath graphene and tip-grown CNT carpets were generated on top of graphene. For comparison, typical base-grown CNT carpets and tip-grown CNT carpets were synthesized using previously reported methods.^{28, 76, 77}

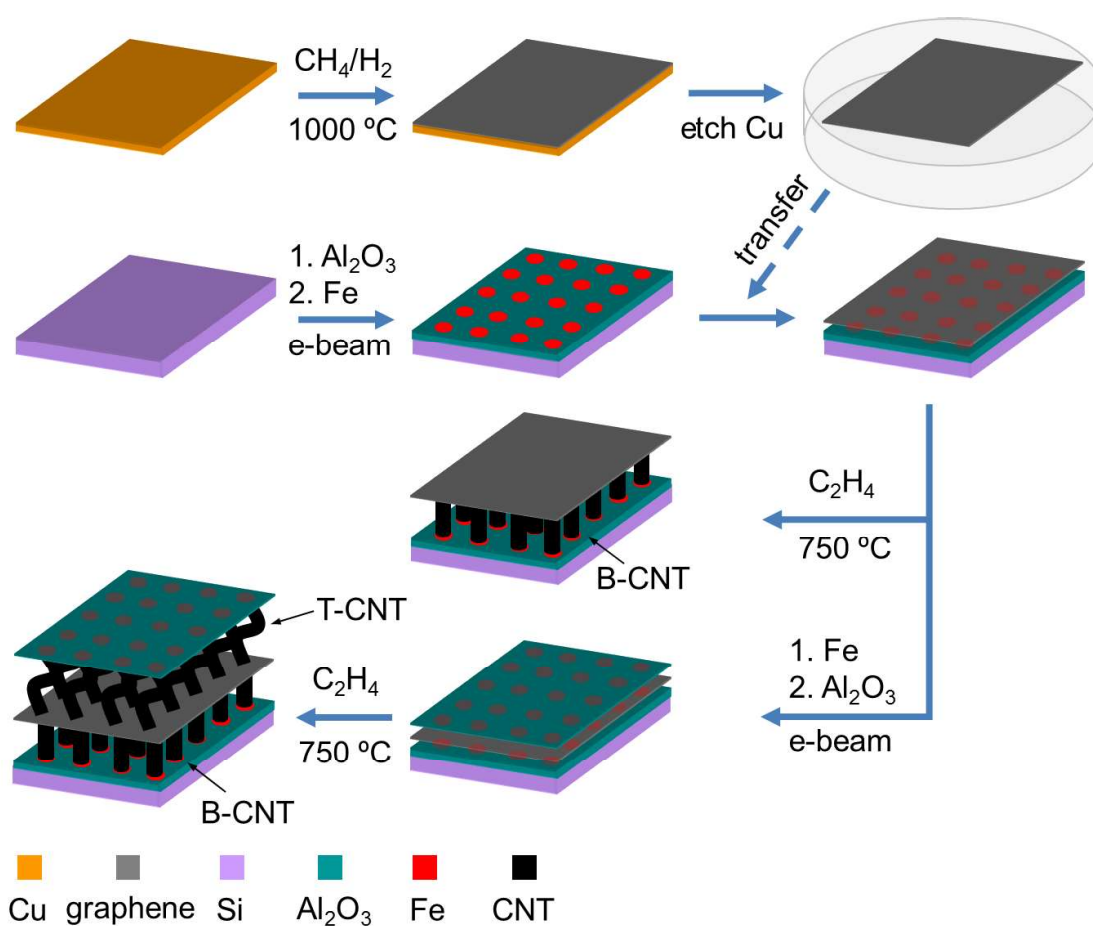


Figure 1-19. Scheme for the synthesis of graphene/B-CNT and T-CNT/graphene/B-CNT structures.

CNT carpets can grow below graphene to raise up the graphene. Or CNT carpets can grow both below and above the graphene.

To characterize the formation of base-grown CNT carpets underneath graphene, scanning electron microscope (SEM) images were taken of the graphene/B-CNT sample. **Figure 1-20a** shows the top-view SEM image of the graphene/B-CNT structure, where the sheet-like graphene structure is visible with breakages homogenously distributed among the entire graphene layer, creating

individual graphene flakes with an average dimension of $\sim 5 \times 5 \mu\text{m}^2$. **Figure 1-20b** shows the close-up top-view SEM image of one of the graphene flakes. With higher magnification, vertically aligned CNTs become recognizable between the edges of different graphene flakes, and partially masked CNTs are observed through the graphene flake on top. Apparently during CNT carpets growth, the graphene sheet is lifted up by the growing CNT carpets, and this mechanical force results in graphene breakages. In addition, as some part of the graphene layer could be etched by the $\text{H}_2/\text{H}_2\text{O}$ gas flow,⁷⁸⁻⁸⁰ the induced defects could further contribute to the observed breakages. Meanwhile, the decomposed carbon species could dissolve in the Fe catalyst, and act as an additional carbon source for CNT carpet growth.⁸¹ A side-view SEM image of the graphene/B-CNT structure is shown in **Figure 1-20c**. Underneath the broken graphene flakes, the vertically aligned CNTs with a height of $\sim 15 \mu\text{m}$ are identified. The CNTs under the graphene are mostly straight with no bending despite the graphene on top, resembling the features of a typical base-grown CNT carpets prepared with the same catalyst composition but without the graphene layer (**Figure 1-22a,b**).

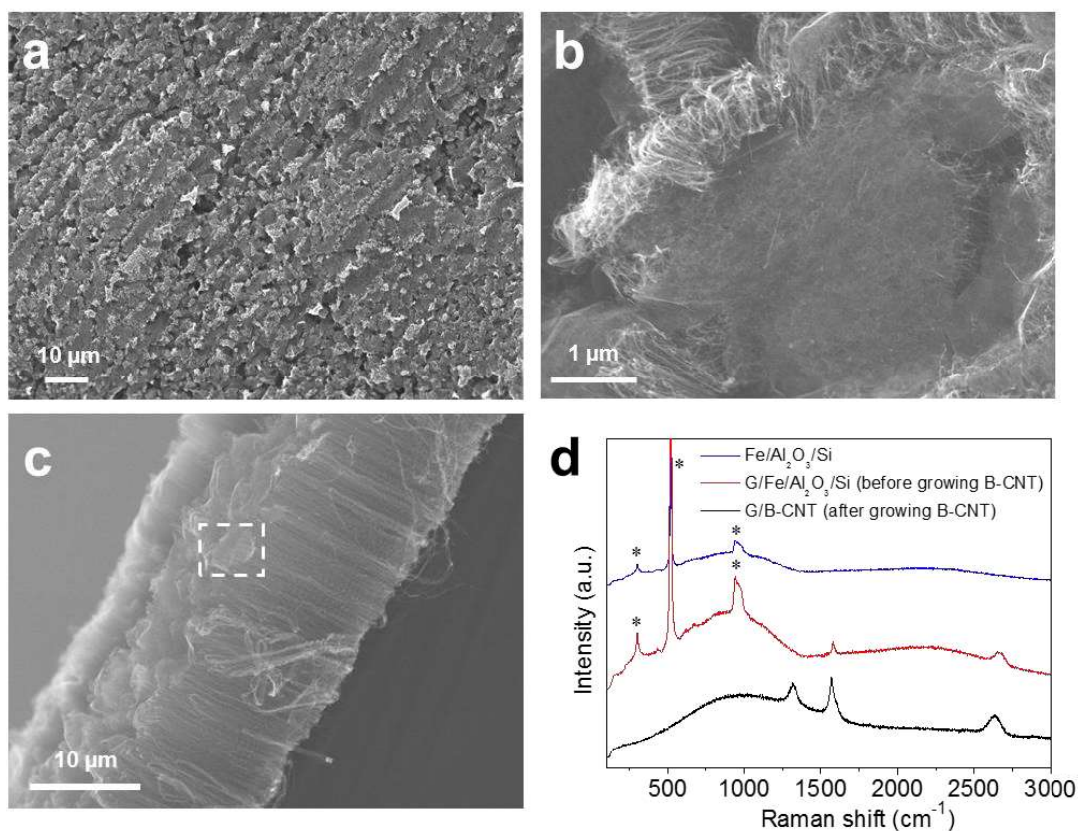


Figure 1-20. Characterization of the graphene/B-CNT structure.

(a,b) Top-view SEM image. (c) Side-view SEM image. Both CNTs and graphene components could be observed from these images. Part of the graphene is marked by a rectangle (dashed). (d) Raman spectra of Fe/Al₂O₃/Si (blue), graphene/Fe/Al₂O₃/Si before growth (red), and graphene/B-CNT after growth (black), excited with a 633 nm laser. The deconvoluted spectrum of G/B-CNT is shown in Figure 1-21. *Raman signals of the Si substrate.

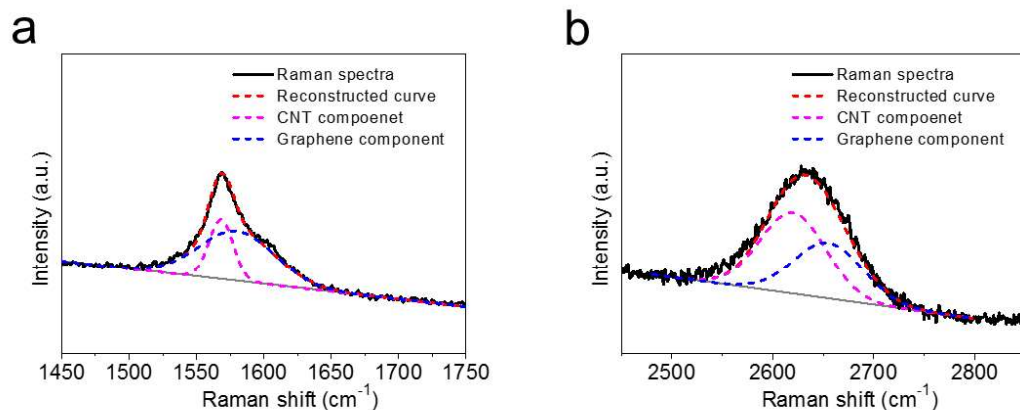


Figure 1-21. The deconvoluted Raman spectra of graphene/B-CNT (Figure 1-20).

(a) Deconvoluted G peak. (b) Deconvoluted 2D peak.

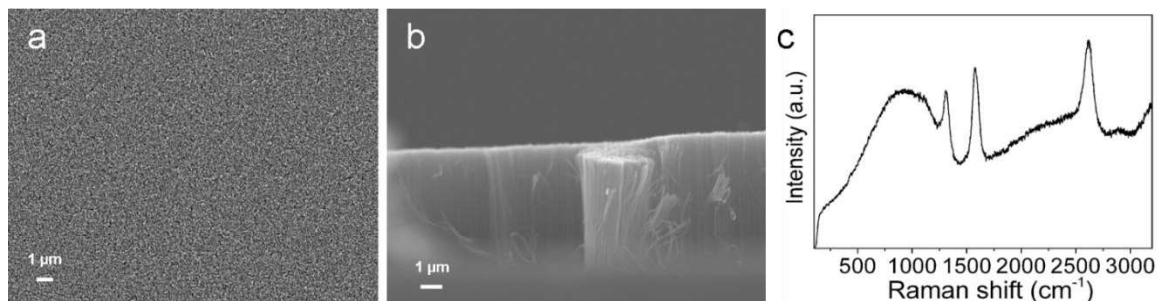


Figure 1-22. SEM and Raman spectra of typical B-CNT structure, with the composition of Si/Al₂O₃/Fe/CNTs (from bottom to top).

(a) Top-view SEM image. (b) Side-view SEM image. (c) Raman spectra excited with 633 nm laser. D band: 1310 cm⁻¹, G band: 1570 cm⁻¹, 2D band: 2620 cm⁻¹, RBM: not observed.

Raman spectroscopy was used to further characterize the graphene/B-CNT structure before and after CNT carpets growth. As shown in **Figure 1-20d**, with only Fe/Al₂O₃ catalyst on a Si substrate, Si peaks and broad metal fluorescence

background are present. After the CVD-grown graphene was transferred atop the Fe/Al₂O₃ layer, the G peak (1578 cm⁻¹) and 2D peak (2654 cm⁻¹) could be easily observed. The intensity ratio between the G peak and 2D peak is normally used to identify the number of graphene layers; here, with a 2D/G ratio of ~ 0.7 , the graphene should be few-layered.^{55, 56} After CNT carpet growth, Si peaks were no longer measurable due to the thick CNT carpet layer ($\sim 15\ \mu\text{m}$). Interestingly, both CNT and graphene Raman signals could be found after deconvolution of the peaks, as shown in **Figure 1-21**. For the G peak, the position of the graphene component was found to be 1580 cm⁻¹ (close to that of the transferred few-layer graphene before growth). The much sharper CNT component was at 1568 cm⁻¹, which is very close to the 1570 cm⁻¹ measured with typical B-CNT (**Figure 1-22c**). Similarly, the 2D peak of graphene/B-CNT could be separated into 2655 cm⁻¹ for graphene and 2620 cm⁻¹ for CNT; both deconvoluted peak positions are in accordance with the individual graphene and B-CNT structure. As the D band results from the distortion of the graphitic structure,⁶² the relatively high D peak in graphene/B-CNT should result from the defects of CNTs and graphene, as the H₂/H₂O gas flow could etch and damage graphene-based carbon materials,⁷⁸⁻⁸⁰ plus the potential covalent connection at the graphene/B-CNT interface. No radial breathing mode (RBM) Raman peaks could be observed for either graphene/B-CNT and typical B-CNT with a 633 nm laser, as the chiralities for those CNTs might be away from the resonance window of the Raman laser,^{82, 83} yet the existence of CNTs is certain as shown by the SEM images.

A well-designed catalyst composition is crucial for the fabrication of CNT/graphene hybrid structures. In the previous report of seamless CNT/graphene hybrid structures, the Fe catalyst was deposited on top of the graphene, the Al_2O_3 was further deposited on top of Fe to act as a floating buffer layer, and a tip-growth process⁷⁶ occurred during CNT carpet growth as the entire $\text{Al}_2\text{O}_3/\text{Fe}$ layer was lifted by the CNT carpets, yielding $\text{Al}_2\text{O}_3/\text{Fe}/\text{T-CNT}/\text{graphene}$ (**Figure 1-23a**).²⁸ In the graphene/B-CNT structure, however, the Al_2O_3 buffer layer was deposited under the Fe catalyst layer beneath graphene, where CNTs gradually formed on the Fe catalyst to the contrary side of the Al_2O_3 buffer layer, i.e. following the base-growth mechanism,^{77, 84} yielding $\text{graphene}/\text{B-CNT}/\text{Fe}/\text{Al}_2\text{O}_3$ (**Figure 1-23b**). Interestingly, in both cases, CNT carpets are formed in contact with graphene from the interface between the Fe catalyst and graphene, and the Fe catalyst always remain in contact with the Al_2O_3 buffer due to the strong interaction between the two layers;⁸⁵ hence, in order to obtain CNT carpets in contact with graphene from both sides, it requires tip-growth CNT carpets on top of the graphene and base-growth CNT carpets underneath graphene ($\text{Al}_2\text{O}_3/\text{Fe}/\text{T-CNT}/\text{graphene}/\text{B-CNT}/\text{Fe}/\text{Al}_2\text{O}_3$, from top to bottom), the catalyst/buffer structure is designed as $\text{Al}_2\text{O}_3/\text{Fe}/\text{graphene}/\text{Fe}/\text{Al}_2\text{O}_3$, where T-CNT and B-CNT can grow simultaneously during the CNT carpet growth process, as shown in **Figure 1-19**. Interestingly, based on the SEM characterizations for typical B-CNT (**Figure 1-22**) and typical T-CNT (**Figure 1-24**), it is found that most T-CNTs are curved (tip catalysts are separated during growth while being lifted up by the CNTs) but most B-CNTs remain upright and well-ordered (base

catalysts remain connected on the surface of the substrate).⁸⁵ These features help to distinguish the T-CNT component and the B-CNT component within the sandwich structure.

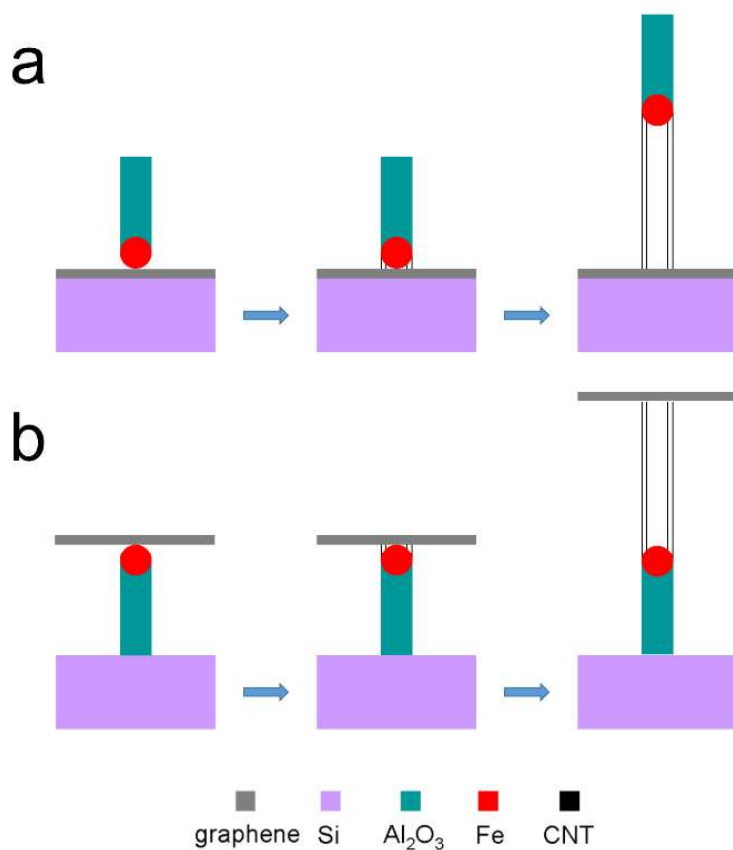


Figure 1-23. Scheme for growth mechanisms.

(a) Tip-growth yielding T-CNT/graphene, (b) base-growth CNT carpets yielding graphene/B-CNT.

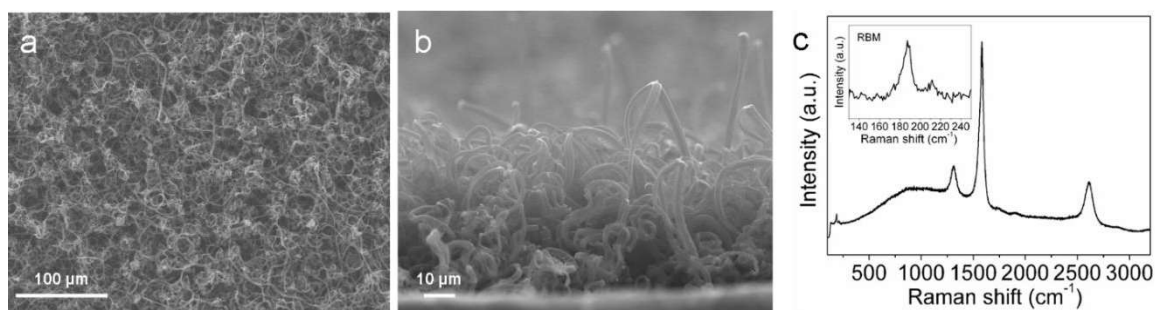


Figure 1-24. SEM and Raman spectra of typical T-CNT structure, with the composition of Cu/graphene/CNTs/Fe/Al₂O₃ (from bottom to top). (a) Top-view SEM image. (b) Side-view SEM image. (c) Raman spectra excited with 633 nm laser, inset is the enlarged RBM region. D band: 1312 cm⁻¹, G band: 1582 cm⁻¹, 2D band: 2611 cm⁻¹, RBM: 188 cm⁻¹ and 212 cm⁻¹.

With the designed catalyst composition, SEM images are used to characterize the formation of the T-CNT/graphene/B-CNT structure after CNT carpet growth. **Figure 1-25a,b** shows the top-view SEM images of the as-grown T-CNT/graphene/B-CNT structure on a Si substrate after 30 s annealing and 1 min CNT carpet growth. Significantly different from the base-grown CNT carpets, the CNTs on top of the sandwich structure were obviously curved rather than upright, similar to the typical T-CNT shown in **Figure 1-24a,b**. This curving feature along with the residual Fe/Al₂O₃ catalyst (white particles in the **Figure 1-25a,b**) on the tip of the CNTs further confirms the T-CNT component was grown through a tip-growth mechanism.^{76, 85} While the inner graphene layer's appearance could not be clearly judged from these top-view images, **Figure 1-25d** shows a side-view SEM image of the sandwich structure, and the magnified side-views are shown in **Figure 1-25e,f**. In addition to the clear interface between the curved T-CNT (length ~ 30 μm) and

the straight B-CNT (length $\sim 30\ \mu\text{m}$), the graphene layer could be observed as a sheet-like structure highlighted by the rectangle (dashed) in **Figure 1-25f**. The duration of the CNT carpet growth should have significant impact on the morphology of the graphene sheet as the graphene layer tends to break apart during CNT carpet growth; images of T-CNT/graphene/B-CNT structures with different annealing and growth times are shown in **Figure 1-26**. When the sample was only annealed for 5 s without further growth (**Figure 1-26a-c**), both T-CNT and B-CNT are upright with lengths of $\sim 200\ \text{nm}$. And the in-between graphene layer could be clearly observed, especially from the side-view transmission electron microscope (TEM) image (**Figure 1-26c**), where the positions of the residual catalyst (Fe, dark particles) also helps to identify the tip/base-growth mechanisms on different sides of the graphene sheet. As the annealing time was gradually increased to 10 s and 30 s without further growth (**Figure 1-26d-i**), the top T-CNT components start to curve; the length of the T-CNT increased from $\sim 2.5\ \mu\text{m}$ to $\sim 12\ \mu\text{m}$, and the length of the B-CNT increased from $\sim 1.2\ \mu\text{m}$ to $\sim 12\ \mu\text{m}$. The interfaces are clearly observable in these cases, while high-resolution images (**Figure 1-26f,i**) show the existence of the in-between graphene sheets. When the CNT carpets were grown for 10 min after a 30 s anneal (**Figure 1-26j-l**), the T-CNT component was significantly curved (length $\sim 75\ \mu\text{m}$) while the B-CNT still remained straight (length $\sim 100\ \mu\text{m}$). Although the T-CNT/B-CNT interface is still clearly visible, no graphene sheets could be found as the broken graphene flakes may be too small after the 10 min growth, or may be buried deep inside the junction between T-CNT and B-CNT.

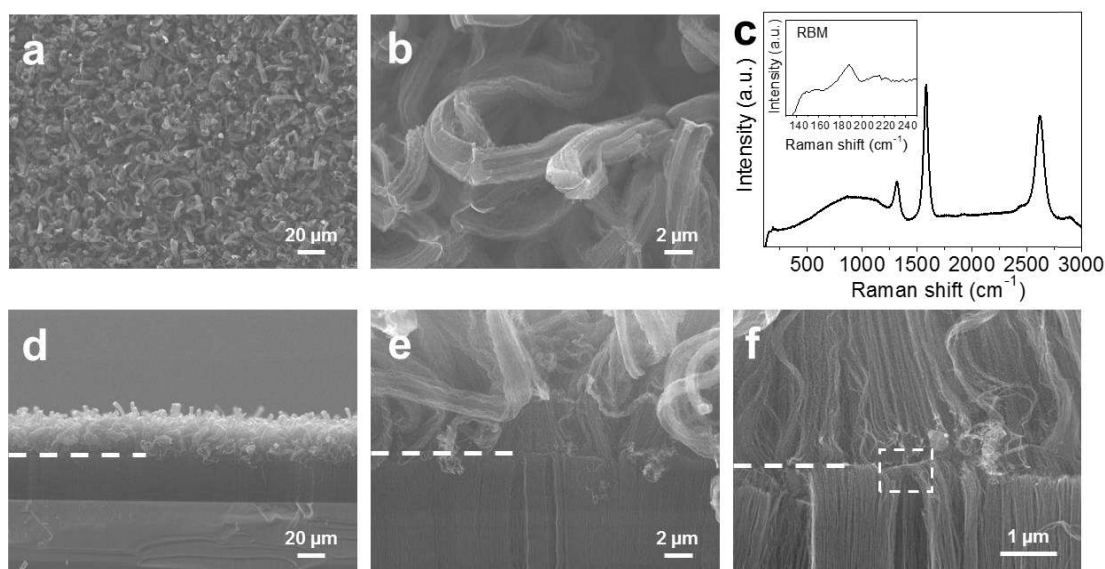


Figure 1-25. Characterization of the T-CNT/graphene/B-CNT structure.
(a,b) Top-view SEM image. (c) Raman spectra of T-CNT/graphene/B-CNT after growth, excited with a 633 nm laser. Inset is the enlarged RBM region. (d-f) Side-view SEM image. Curved T-CNT and straight B-CNT components could be observed from these images. A partial white dashed line is drawn in d-f at the top/bottom interface point where the graphene layer resides. Part of the graphene component is marked by a dashed rectangle in f.

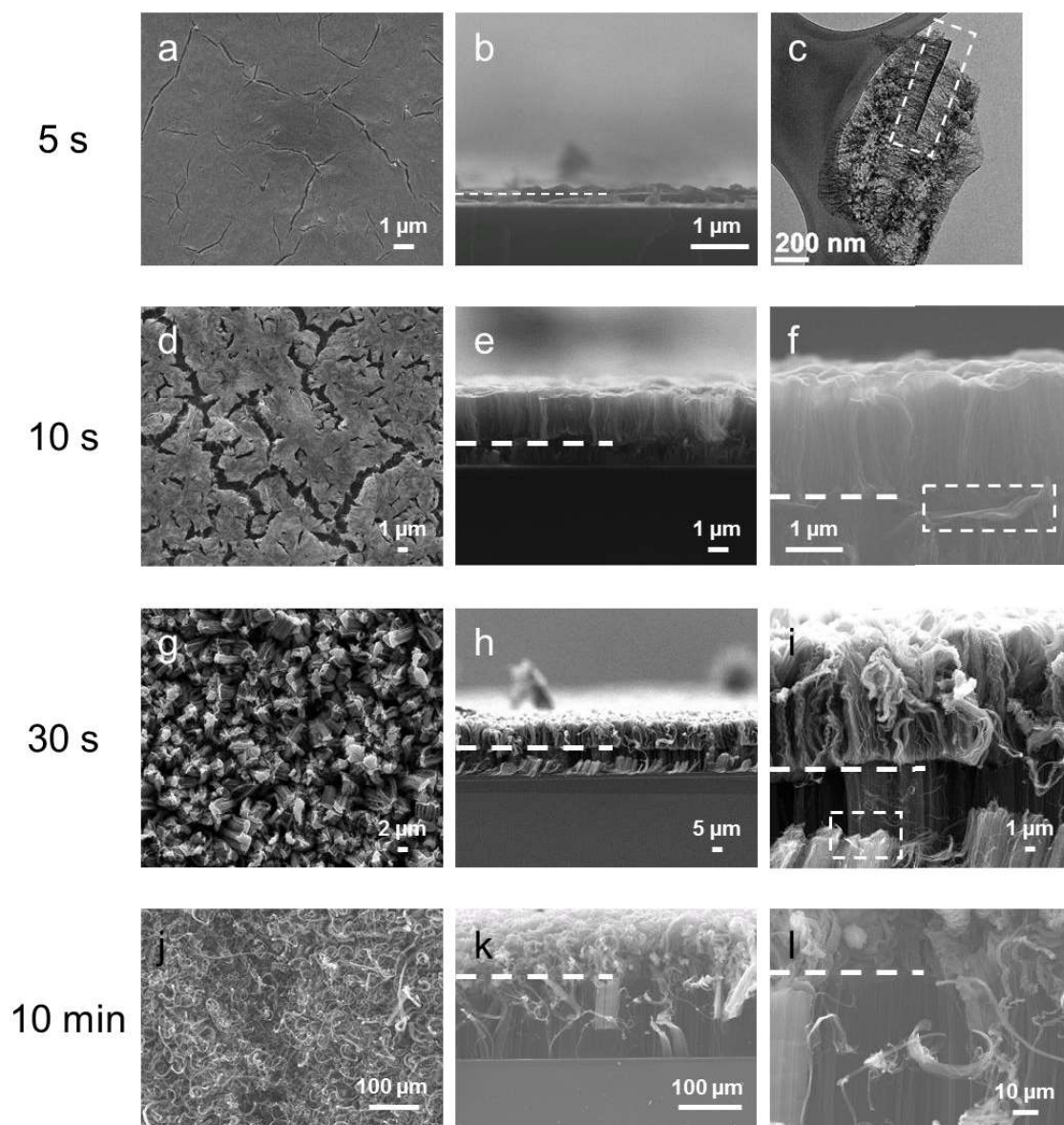


Figure 1-26. SEM and TEM analysis of T-CNT/graphene/B-CNT structures with different CNTs growth times.

(a-c) After 5 s anneal. (d-f) After 10 s anneal. (g-i) After 30 s anneal. (j-l) After 30 s anneal followed by 10 min CNT carpets growth. (a,d,g,j) Top-view SEM images. (b,e,f,h,i,k,l) Side-view SEM images. (c) Side-view TEM image. Partial white dashed lines are drawn at the top/bottom interfaces point where the graphene layer resides. (c,f,i) Some of the separated graphene components are marked by dashed white rectangles. (c) The black particles are the residual Fe catalysts.

Raman analysis was performed on the T-CNT/graphene/B-CNT structure, while only the T-CNT component could be excited due to the limited penetration of the Raman laser. As shown in **Figure 1-25c**, the T-CNT component shows a D-band at 1317 cm^{-1} , a G-band at 1580 cm^{-1} , and a 2D band at 2620 cm^{-1} , also with RBMs at 188 cm^{-1} and 214 cm^{-1} . The Raman spectra were quite similar between the T-CNT component (**Figure 1-24c**) and the T-CNT/graphene/B-CNT sandwich structure (**Figure 1-25c**).

To better understand the behavior and presence of graphene in the sandwich structures, TEM images of T-CNT/graphene/B-CNT or graphene/B-CNT on a Cu grid are shown in **Figure 1-27**. **Figure 1-27a** shows the existence of a graphene sheet in close contact with CNT bundles, though covalent attachment cannot be conclusively confirmed; breakages occur in the graphene during the growth as well as during sonication processing for TEM sample preparation. **Figure 1-28a,b** show the CNTs in the T-CNT/graphene/B-CNT structure. Single-walled, double-walled, and triple-walled CNTs were identified from the TEM images, suggesting all small diameter CNTs as we saw previously.²⁸

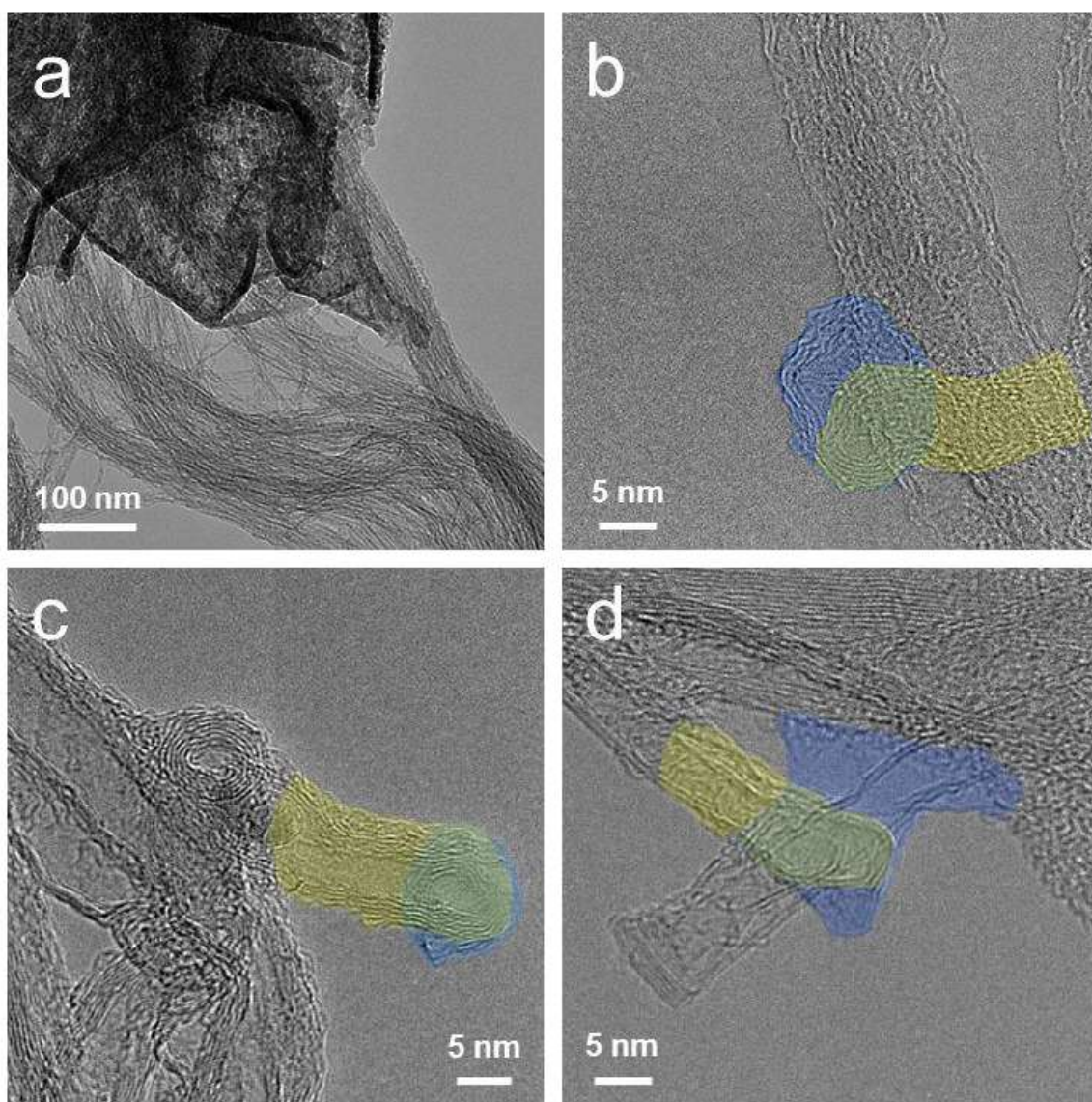


Figure 1-27. TEM images of T-CNT/graphene/B-CNT structure (a-c) and graphene/B-CNT structure (d-f).

(a) The presence of a graphene sheet within T-CNT/graphene/B-CNT structure. (b-d) Connection between graphene and B-CNT. The blue color represents graphene, and the yellow color represents CNTs growing from graphene sheets. The overlap of the blue and yellow is forming the green sections.

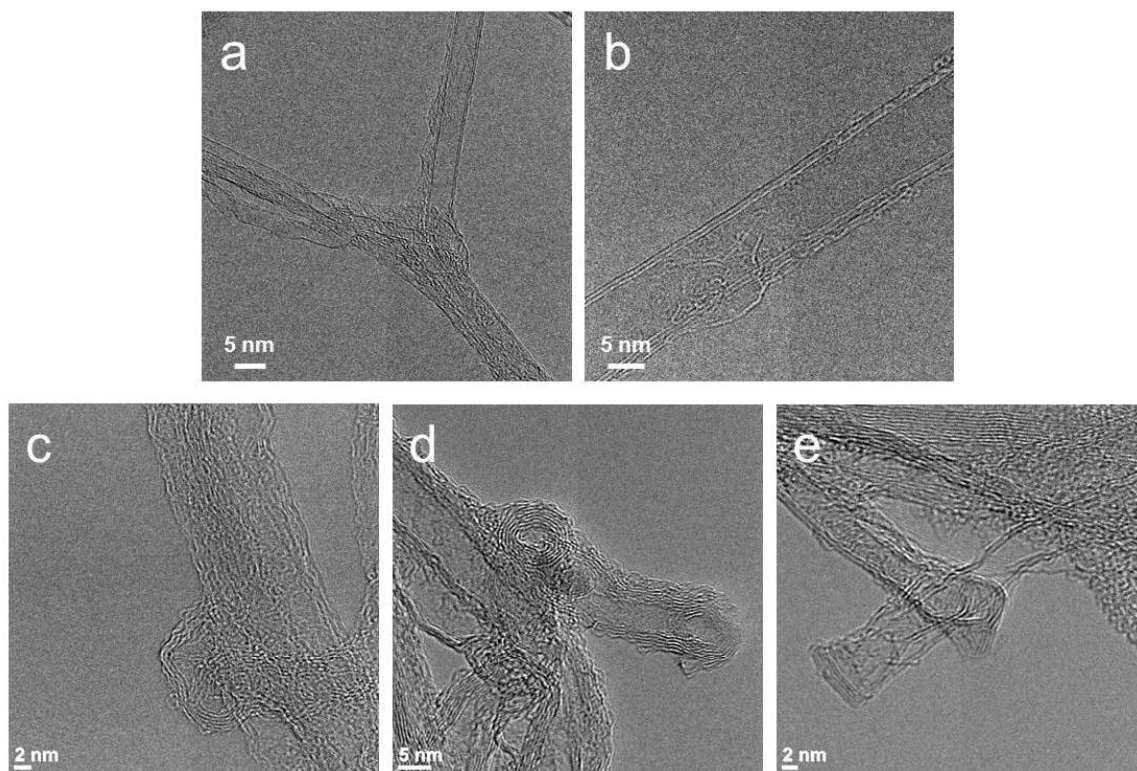


Figure 1-28. Additional TEM images.

(a,b) TEM images of the CNTs in the T-CNT/graphene/B-CNT structure. (c-e) TEM images of graphene/B-CNT structure, same images as Figure 1-27a-c, but without highlighted color.

Since a seamless (covalent) CNT/graphene connection has been observed with the previously reported T-CNT/graphene structure,²⁸ it becomes an interesting question whether covalent connection also exists between graphene and CNTs in the sandwich T-CNT/graphene/B-CNT structure. Given that the catalyst composition and the yielding structure for the upper T-CNT/graphene component are nearly identical to the seamless T-CNT/graphene structure reported,²⁸ it is likely that a covalent interaction also exists between graphene and the top T-CNT in the

sandwich structure. Thus, what remains to be proven is the interaction between graphene and the B-CNT. To simplify the sample structure for imaging, the graphene/B-CNT structure alone was used for TEM characterization as it should represent a similar behavior with the lower graphene/B-CNT component of the sandwich structure. As shown in **Figure 1-27b-d**, the root areas where CNTs might have grown from broken graphene flakes are highlighted in blue and yellow colors (unhighlighted TEM images are shown in **Figure 1-28c-e**). Although there is no direct microscopic evidence to prove the covalent bonding between graphene and B-CNT structures, the close attachment (good contact) between the graphene layer and the CNTs could be beneficial for the fabrication of such T-CNT/graphene/B-CNT into electronic devices. Furthermore, the seamless connection was indeed observed by aberration corrected TEM in our original graphene-CNT disclosure.²⁸

As an ohmic contact should be expected from the covalently bonded CNT/graphene hybrids,²⁸ the potentially seamless-connected T-CNT/graphene/B-CNT structure (with 10 min growth time) was transferred onto Au/polyethylene terephthalate (PET) substrate to test the electric contact between the top T-CNT and the bottom B-CNT. As shown in **Figure 1-29a**, due to the fact that B-CNT is upright while T-CNT is significantly curved, the entire structure is intentionally flipped over during transfer, leaving the B-CNT facing up and T-CNT directly contacting the Au electrode. In this orientation, the dense and straight (**Figure 1-29b**) B-CNT should provide a better contact between the probe tip and the CNT carpet structure, while a good contact between the Au layer and the bent T-CNT is maintained. The I-V curves

of three different contacts (Au to Au, Au to B-CNT, and B-CNT to B-CNT) are shown in **Figure 1-29c**, all of which show a “straight line” feature that corresponds to typical ohmic contact rather than nonlinear Schottky contact.⁸⁶ Although this macroscopic efficient electrical contact throughout the sandwich structure gives limited information about the microscale interaction within the hybrid structure, the good ohmic contact could make the T-CNT/graphene/B-CNT a promising candidate for electronic devices.

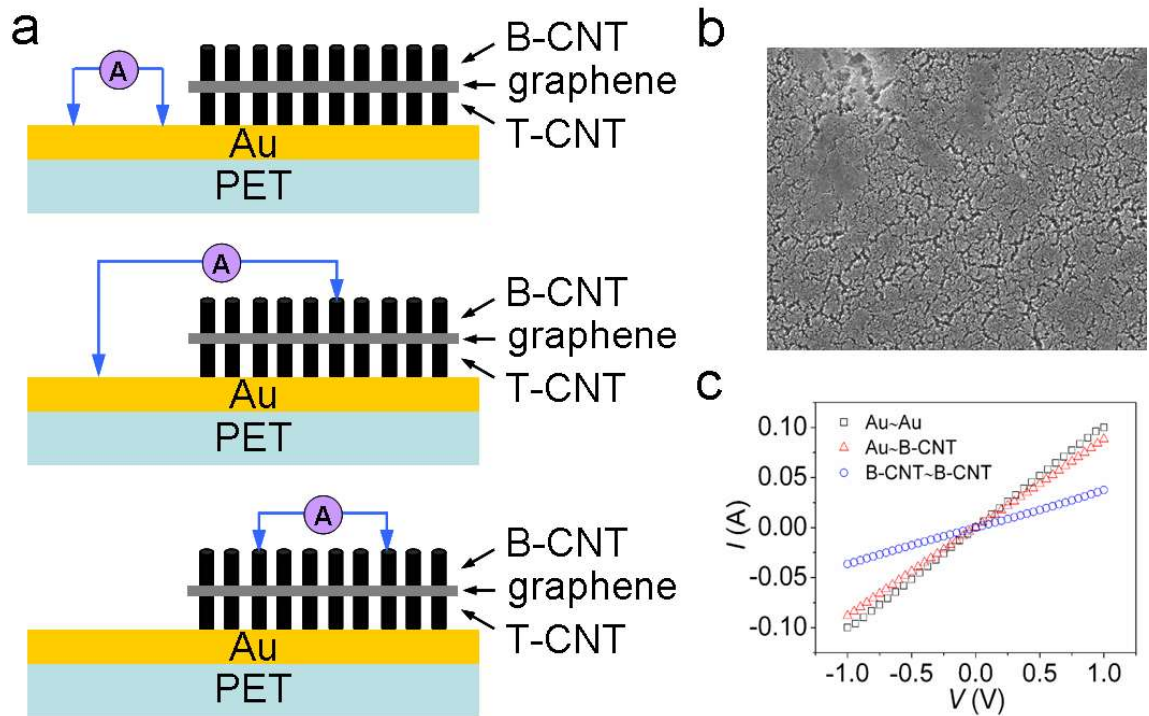


Figure 1-29. Electrical measurement between sub-structures.

(a) The scheme for three different kind of probe contacts. From top to bottom: Au to Au, Au to B-CNT, B-CNT to B-CNT. The distance between the two probe tips during the measurements is ~ 3 mm. **(b)** SEM image of the B-CNT component of the up-side-down T-CNT/graphene/B-CNT. **(c)** The I - V curves of the three contacts described in (a).

The T-CNT/graphene/B-CNT sandwich structure could have applications in various areas. Owing to the high surface area provided by the vertically aligned CNT carpets, and the good electrical contact throughout the structure, the T-CNT/graphene/B-CNT could be used as an electrode material for supercapacitors and Li-ion batteries, similar to previous reports.^{25, 28, 30, 32} In addition, the rational design of this sandwich structure could be an important tool for other nanofabrication efforts. For example, the T-CNT/graphene/B-CNT provides an interesting approach to fabricate graphene/CNTs hybrids with even more layers. By starting with more layers of catalyst and graphene sitting in-between each other, one might get an organized multilayer structure of CNT carpets/graphene/CNT carpets/graphene/CNT carpets/, etc., as previously reported in several theoretical computational studies as “pillared graphene”.^{87, 88} In this case, the vertical CNT carpets could stabilize or strengthen the horizontal graphene layer, and the horizontal graphene layer would provide extra ductility to the high-raised 3D carbon structure, while other properties such as high surface, good electrical and thermal conductivities could be maintained.^{87, 88}

1.3.3. Conclusion

We have successfully synthesized large-area 3D hybrid structures of vertically aligned CNT carpets beneath graphene (graphene/B-CNT) and CNT carpets on both sides of graphene (T-CNT/graphene/B-CNT). By comparing with typical base-growth CNT carpets and tip-growth CNT carpets, we confirmed that CNT carpets can grow from both sides of graphene through different mechanisms. A

near ohmic contact from the top T-CNT, through the graphene interface, and to the B-CNT was observed, as well as a close attachment between the graphene and CNT components. Due to the unique structure and properties of the sandwich structure, the rationally designed T-CNT/graphene/B-CNT hybrid material could provide a more complex design for 3D CNT/graphene hybrids, and have potential applications in the fields of energy storage and nanomanufacturing.

1.4. Growth and Transfer of Seamless 3D Graphene/CNT Hybrids

1.4.1. Experimental Section

Chemical Vapor Deposition (CVD) graphene growth. Few-layer graphene was grown on the copper substrate *via* chemical vapor deposition (CVD). A quartz tube (22-mm ID, 25-mm OD, Technical Glass Products) was heated in a furnace and graphene films were grown on a copper foil. The copper foil was inserted into and removed from the furnace using a magnet assisted boat-shaped quartz holder. The substrate was first annealed at 1000 °C for 10 min under H₂ flow (300 sccm) and H₂ pressure was controlled with a needle valve to 350 Torr. Then the carbon source gas, CH₄ (10 sccm), was introduced into the quartz tube. After 15 min, the CH₄ gas was turned off and the copper substrate was removed from the furnace area to cool to room temperature under H₂ flow.

Selective growth of CNT on patterned graphene. The patterned graphene was directly made by photolithography on copper substrate. The photoresist (MICROPOSIT S1813) was spin-coated on as-synthesized graphene atop the copper substrate and patterning was done using negative mask and Ar RIE process to produce the graphene pattern. Catalyst (1 nm Fe and 10 nm Al₂O₃) for vertically aligned carbon nanotube (VA-CNT) growth were deposited by e-beam evaporation. The patterned VA-CNT carpet was grown by CVD using a water-assisted hot filament furnace at reduced pressure, as described elsewhere.³⁰

Polymer-free transfer of patterned graphene carbon nanotube (GCNT) structure. After growing the patterned GCNT structure on the copper substrate, the entire structure was placed on the surface of the etching solution, 0.2 M (NH₄)₂S₂O₈. After completely etching the copper substrate, the etching solution was replaced with DI water 3× and the substrate was floated on the surface of the water to remove impurities. The entire GCNT structure was then transferred onto the desired substrate and was treated with 1 M HF solution or buffered oxide etch (J. T. Baker, 10:1) solution to remove the growth catalyst on top of the GCNT structure. After washing 3× each with water and ethanol, the structure was dried using the critical point drying instrument (Automegasamdri®-915B, Tousimis), while it was still wet in the ethanol to prevent the CNT carpet from collapsing.

Characterization. The morphology of the patterned GCNT structure was characterized by FE-SEM (JEOL 6500F). Raman spectra were collected using a Renishaw Raman microscope with a 514 nm Ar laser. The XPS spectra were

obtained using a 100 μm X-ray beam in a PHI Quantera SXM scanning X-ray microprobe system. All binding energies (BEs) are referenced to the adventitious C 1s line at 284.5 eV. The electrical property measurements were performed using a B1500 semiconductor parameter analyzer after transferring the GCNT material onto a Ti/Au (5/50 nm) patterned electrode substrate. The width of electrode was 50 μm and the distance between 2 electrode lines was 450 μm .

1.4.2. Result and Discussion

Figure 1-30 is a schematic diagram summarizing the fabrication process. In the first step, few-layer graphene was prepared on the Cu foil using a chemical vapor deposition (CVD) process.⁵⁵ Using photolithography, the graphene on the Cu foil substrate was patterned, followed by an Ar reactive ion etch (RIE) process to remove the unprotected graphene. After mask lift-off, the catalysts for VA-CNT growth (1 nm Fe and 10 nm Al_2O_3) were deposited by e-beam evaporation over the entire substrate. Even though the catalyst was deposited everywhere on the substrate, the VA-CNT carpet grew only on the graphene pattern. The selectively grown patterned GCNT structure floated on the etching solution even after the Cu substrate was completely etched. After picking the structure up with another substrate, the catalyst on top was removed by a simple etching solution treatment. Critical point drying (CPD) with CO_2 removed the absorbed solvent without collapsing the carbon structure. Without CPD, the nanotube array collapse into bundles due to solvent adhesion forces upon drying. This allows the GCNT structure to be cleanly transferred onto the desired substrate.

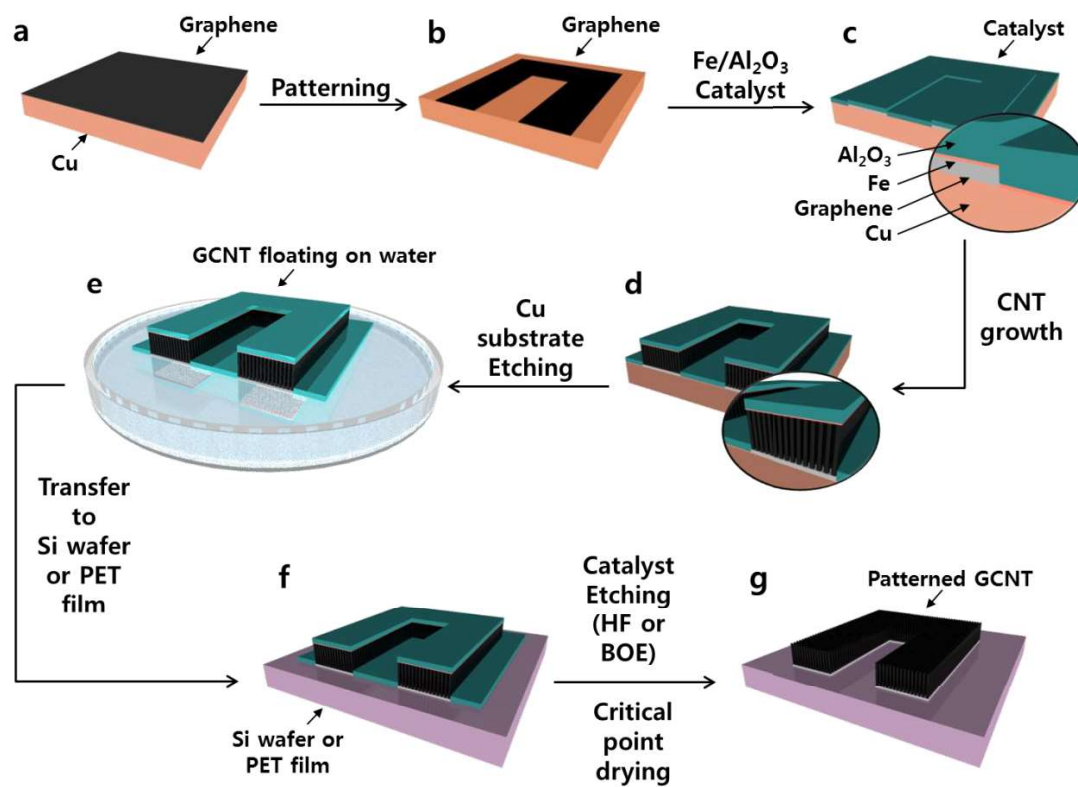


Figure 1-30. Schematic illustration for fabrication and transfer of a patterned 3D GCNT hybrid structure.

(a) Graphene growth on copper substrate *via* a CVD method; (b) making graphene pattern using photolithography followed by RIE treatment; (c) catalyst (Fe, 1 nm) and catalyst support (Al₂O₃, 10 nm) deposition using e-beam evaporation; (d) selective growth of VA-CNT only on the patterned graphene regions; (e) etching the copper substrate by floating on the etching solution; (f) picking up the floating patterned GCNT structure with another substrate; and (g) completing the transfer of the patterned GCNT structure by etching the VA-CNT growth catalyst followed by a critical point drying process.

Figure 1-31a,b show SEM images of selectively grown patterned GCNT on Cu substrate with 50 μm width and 50 μm gap between the patterned GCNTs. Little widening of the VA-CNT broader than the underlying graphene was noted. The

thickness of the Al_2O_3 layer plays a critical role in the morphology of the VA-CNT carpet. If the Al_2O_3 layer is too thin (~ 3 nm), the tip grown VA-CNTs do not maintain their vertical alignment and they start to spread out of the graphene patterned area (**Figure 1-32**). If the Al_2O_3 layer is too thick (~ 15 nm), the carbon source for VA-CNT growth cannot easily reach the catalyst and uniform growth of the VA-CNT carpet is difficult (**Figure 1-32**).²⁸ The optimal thickness of the Al_2O_3 layer is critical not only for the well-aligned GCNT structure, but also for a facile transfer process. The effect of this selective growth of the GCNT structure can be seen from low magnification SEM images (**Figure 1-31b**). The VA-CNT carpet was grown only on the exposed graphene lines. The cross sectional analysis confirmed that thickness of VA-CNT carpet is ~ 30 μm after 3 min growth (**Figure 1-31c**). This technique can also be applied to narrower graphene ribbons (GRs). **Figure 1-31d-f** shows patterned VA-CNT grown on GRs with 15, 12, and 9 μm widths and 4, 7, and 10 μm gaps, respectively. Even though the width of the patterns and the gap between the patterns is much smaller than the height of the VA-CNTs carpet (~ 30 μm), the vertically aligned morphology of the VA-CNT carpet is well-maintained. The high selectivity of the VA-CNT growth on GRs was confirmed by the Raman spectra taken of the GCNTs or of the gap between the GCNTs (**Figure 1-31g**). Strong characteristic CNT peaks are seen from the top of the GCNTs, while a negligible amount of carbon species was found between the GRs. The inset of **Figure 1-31g** shows the radial breathing modes (RBMs) of the CNTs. The CNTs in the VA-CNTs are

mainly single-walled, double-walled, or triple-walled CNTs with a diameter of 1 to 7 nm, as previously reported.^{28, 89, 90}

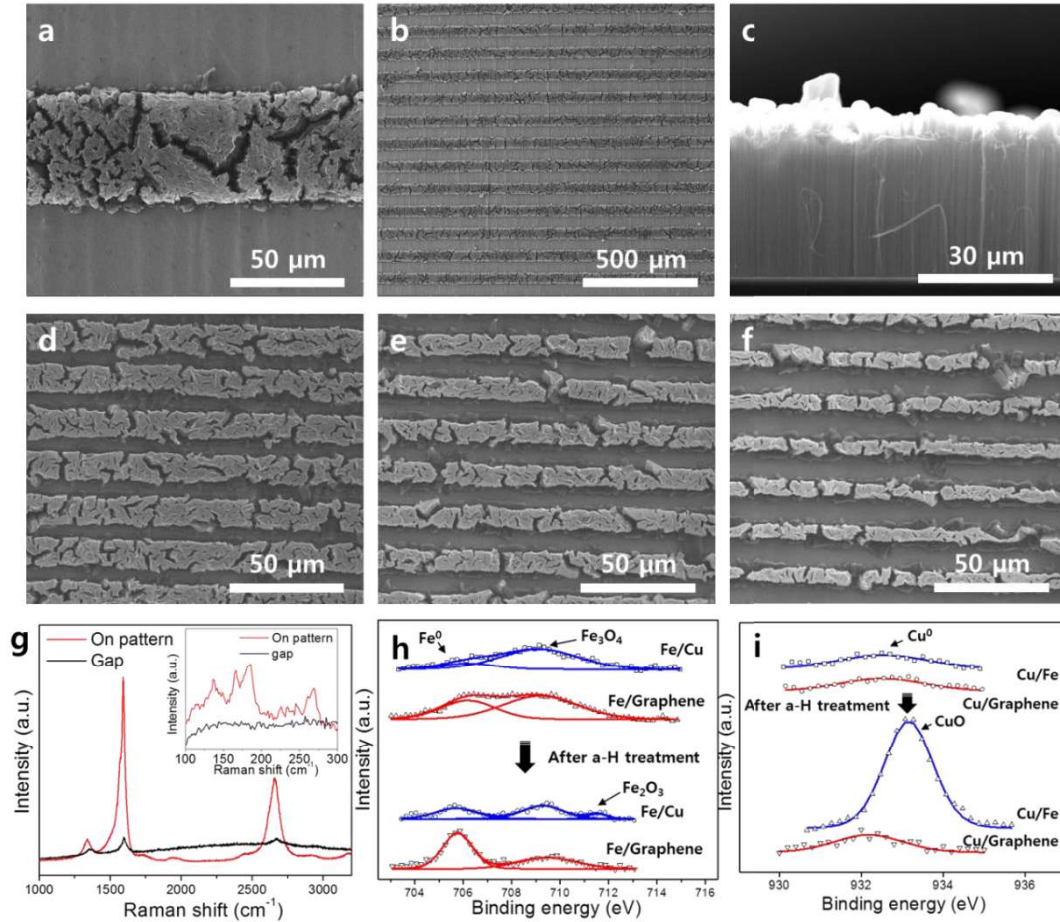


Figure 1-31. Selective growth of VA-CNTs on patterned GRs.

(a,b) SEM images of selectively grown GCNTs with 50 μm widths and 50 μm gaps. (c) Cross sectional view of GCNT grown for 3 min, showing VA-CNT carpet with ~ 30 μm thickness. The VA-CNT carpet was also grown selectively on graphene patterns with different widths and gaps: (d) 15 μm width and 4 μm gap, (e) 12 μm width and 7 μm gap, and (f) 9 μm width and 10 μm gap. (g) Raman spectroscopic analysis of CNTs on the GRs and the space between GCNTs. Comparison XPS study of (h) Fe and (i) Cu species before and after the atomic hydrogen (a-H) reduction process.

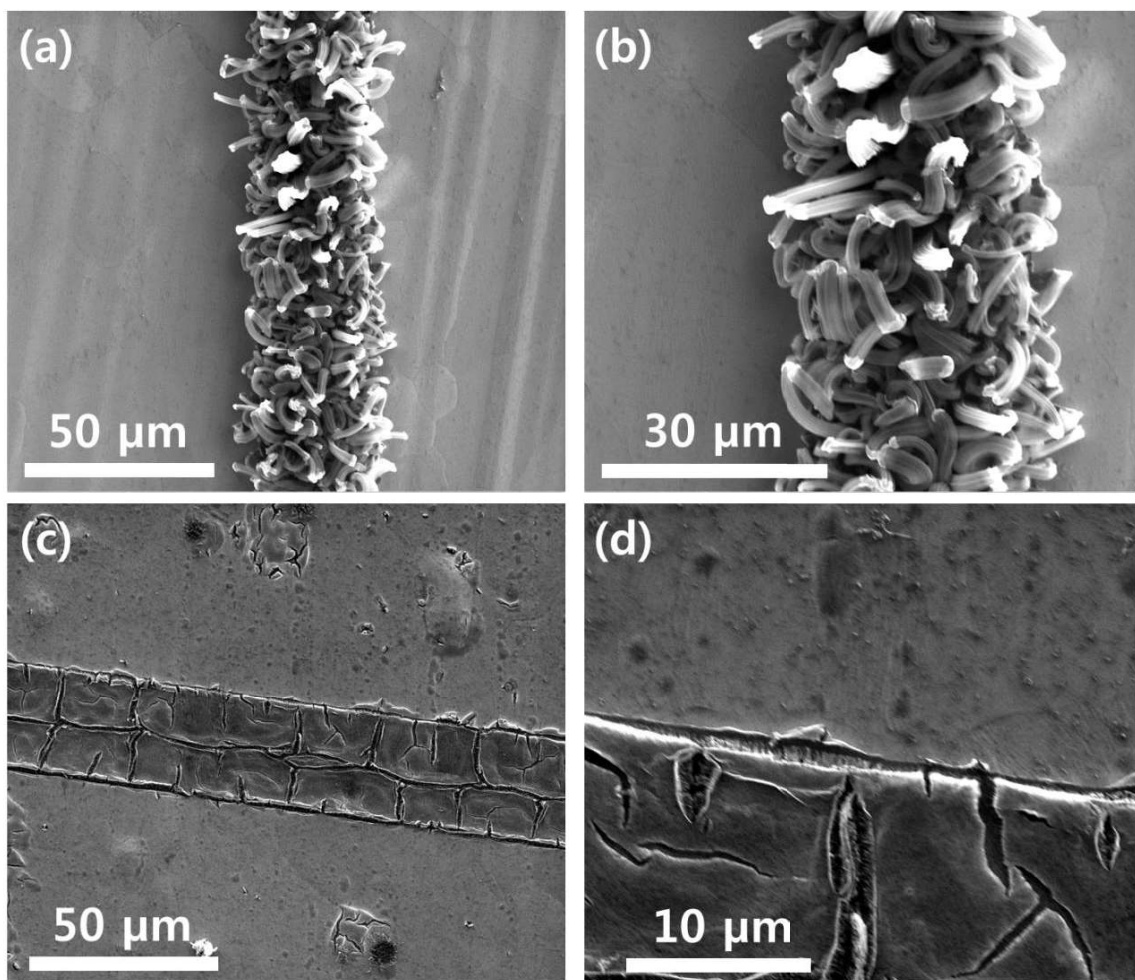


Figure 1-32. VA-CNT growth on graphene pattern of 30 μm width with different thicknesses of catalyst supports (Al_2O_3 layer). (a, b) With an Al_2O_3 layer of 3 nm, the morphology of the VA-CNT is more like bundles, not carpets. (c, d) When the Al_2O_3 layer is 15 nm, the VA-CNT does not grow well under the same growth time and conditions.

In the CNT growth system, samples were treated by atomic hydrogen (a-H) produced by a tungsten hot filament. As the current (~ 10 A) passes through the filament, it generates intense thermal energy (typically ~ 2500 $^{\circ}\text{C}$), which can dissociate H_2 into a-H.⁹¹ The major role of a-H is to achieve rapid reduction of the

catalyst from a stable Fe_2O_3 to metallic Fe.⁹² It was assumed that the origin of selective growth of the VA-CNT on the graphene arose from the deactivation of the Fe catalyst on Cu due to its alloying with the Cu substrate.²⁸ To provide evidence for the Fe catalyst deactivation, X-ray photoelectron spectroscopy (XPS) analysis was conducted of the catalyst deposited either on graphene or on a Cu substrate. In the Fe spectra (**Figure 1-31h**), the ratio between Fe^0 and Fe_3O_4 species on Cu or graphene is different after the catalyst deposition. The difference becomes greater after the atomic hydrogen treatment, with a higher amount of reduced Fe^0 species on the graphene surface, while Fe on the Cu surface was further oxidized (Fe_2O_3). Based on these results, we conclude that the graphene plays an important role in preventing Fe from alloying with Cu; the graphene may also protect the catalytic activity of the reduced Fe. The Cu alloying process produces the Fe catalyst that is inactive for CNT growth, subsequently leading to selective growth of VA-CNTs only on the graphene. In the Cu spectra in **Figure 1-31i**, there was no significant change in the Cu underneath graphene even after the atomic hydrogen treatment. However, the spectrum for Cu that had been coated with the Fe catalyst was shifted to the more oxidized region and its intensity increased after atomic hydrogen treatment. Considering the XPS penetration depth of $< 10 \text{ nm}$,⁹³ the increased intensity in the Cu spectrum indicates the Cu is closer to the surface, which is additional evidence of alloy formation.

Easy transfer to any other desirable substrate should be one of the most important criteria for a good platform structure. **Figure 1-33** shows how the

patterned GCNT structure was transferred to another substrate. The process is quite similar to the transfer of CVD-grown graphene from its Cu substrate without the assistance of supporting polymer materials. **Figure 1-33a** shows the Cu substrate containing a GCNT structure in an owl pattern floating on the etching solution. This owl pattern remains intact even after the Cu substrate is etched away (**Figure 1-33b**). A combination of the mechanical properties of the graphene, including its flexibility, and the strength of the hybrid structures are factors in the stability of the GCNT. In addition, the thin catalyst layer, ~ 10 nm Al_2O_3 , between GCNTs is key to maintaining the patterned morphology. Without the catalyst layer, the GCNT structure collapses (**Figure 1-34**).

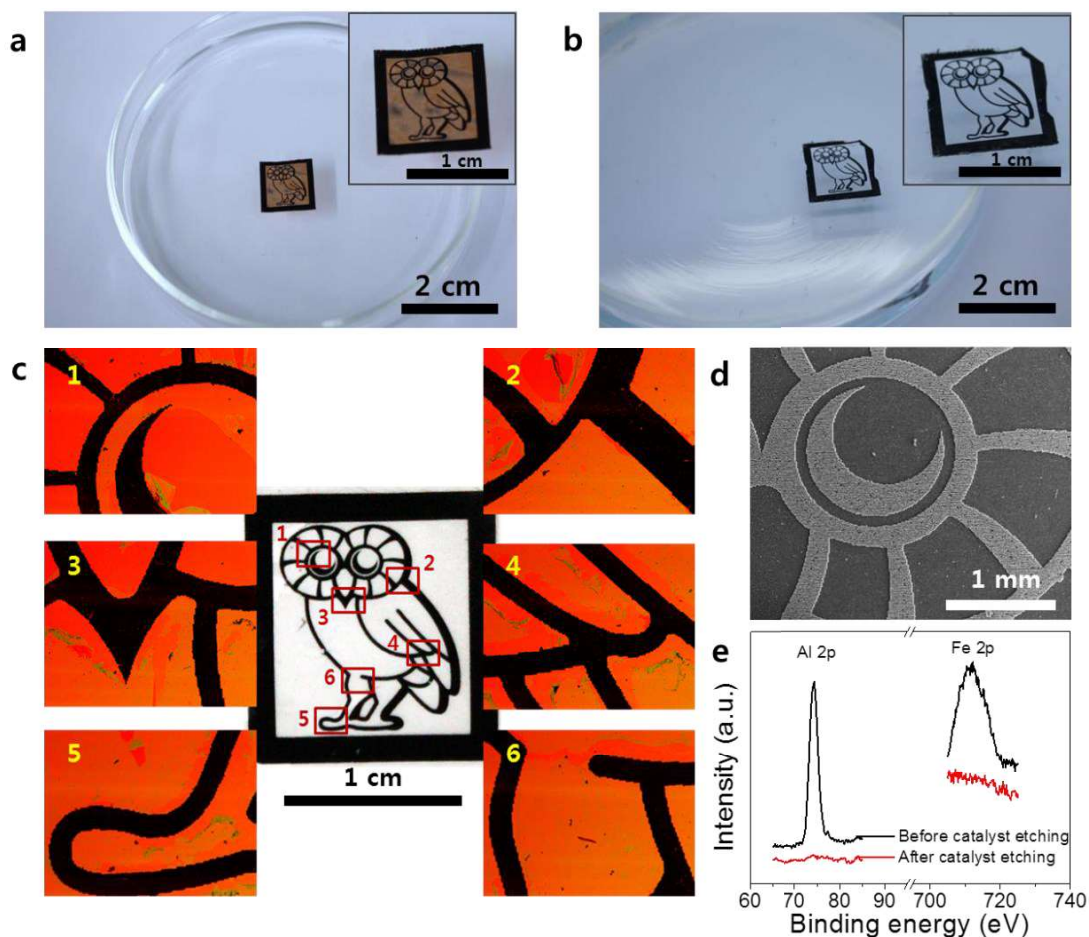


Figure 1-33. Polymer-free transfer of patterned GCNT structures.

Optical images of a floating patterned GCNT structure (a) before, and (b) after copper substrate etching. (c) Optical images of completely transferred owl pattern after catalyst etching and the CPD process. Each sub panel 1 to 6 shows an enlarged part of the transferred owl pattern. (d) SEM images of the transferred GCNT owl pattern shows that the VA-CNT carpet morphology is well-maintained after the CPD process. (e) XPS analysis for Al and Fe before and after catalyst etching process.

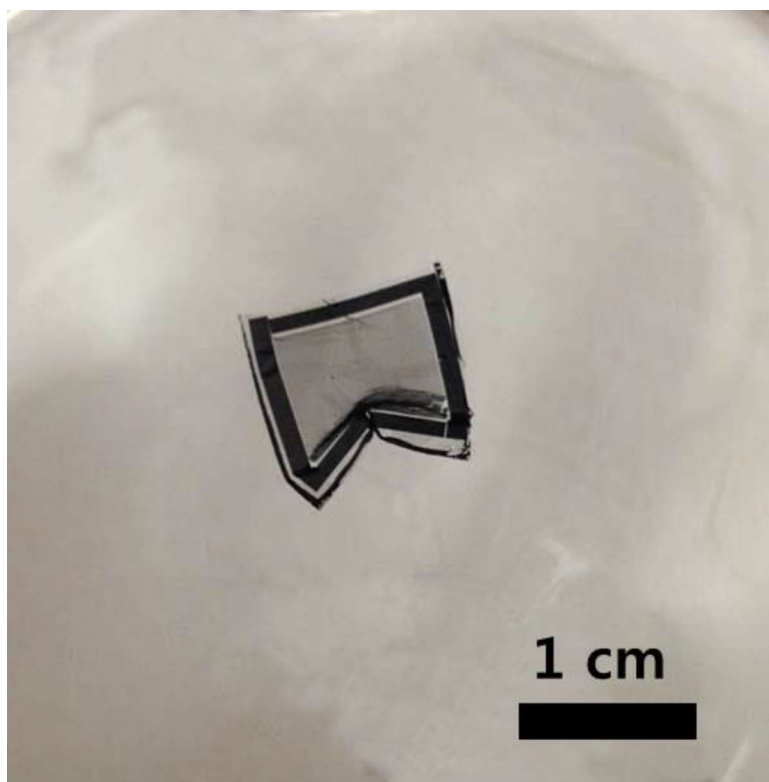


Figure 1-34. Photo of collapsed interdigitated pattern.

Line width $\sim 30\ \mu\text{m}$, on the etching solution after the Cu substrate was all etched away. The VA-CNT growth catalyst was removed before the Cu etching process.

Figure 1-33c shows optical images of the owl pattern transferred onto a poly(ethylene terephthalate) (PET) film in the middle, and magnified images of the marked regions. The entire owl pattern was successfully transferred, including the isolated crescent-shaped eyes. VA-CNT carpets usually collapse when they are dried under normal drying conditions (**Figure 1-35**). However, CPD makes it possible to preserve the full carpet morphology (**Figure 1-33d** and **Figure 1-36**). In order to obtain a pure 3D carbon platform structure, the CNT growth catalyst that remains

on top of the GCNTs should be completely removed. This was accomplished by etching with dilute HF, buffered oxide etchant (BOE), or 1 M HCl solution for 30 s. In the XPS analysis after the etching process, the presence of the CNT growth catalyst was not detected (**Figure 1-33e** and **Figure 1-37**). Note that the Fe is a tip-growth CNT catalyst and it remains associated with the Al_2O_3 ; Fe is not at the base of the CNTs.²⁸

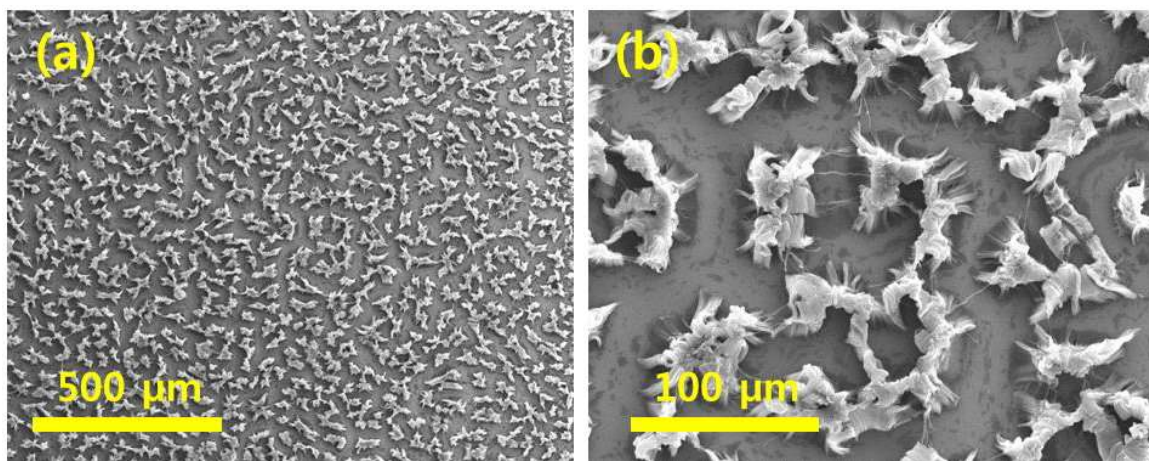


Figure 1-35. SEM images of transferred and collapsed GCNT structures after drying under atmospheric conditions.

After the Cu substrate was etched, the GCNT floating on the etching solution was picked up with a Si wafer and dried without further treatment.

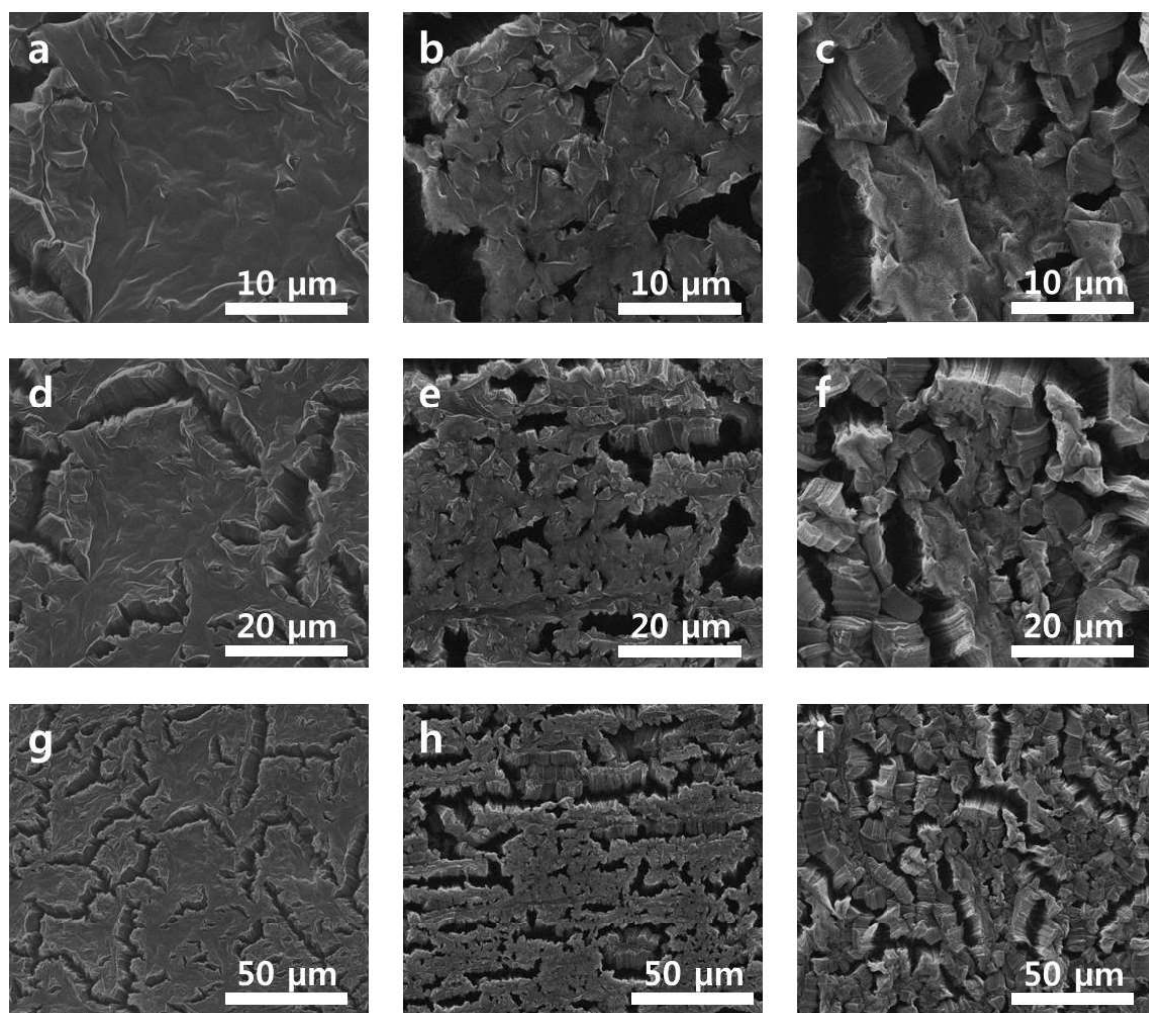


Figure 1-36. SEM images of transferred GCNT.

SEM images of (a,d,g) as-synthesized GCNT on Cu, (b,e,h) GCNT transferred onto a PET film without the catalyst etching process, and (c,f,i) GCNT transferred onto a PET film after the catalyst etching process. After transfer and the CPD process, the VA-CNT carpet structure was well-maintained, though they are slightly split into smaller bundles. This data, combined with the XPS analyses, confirms the catalyst layer is removed after the catalyst etching process.

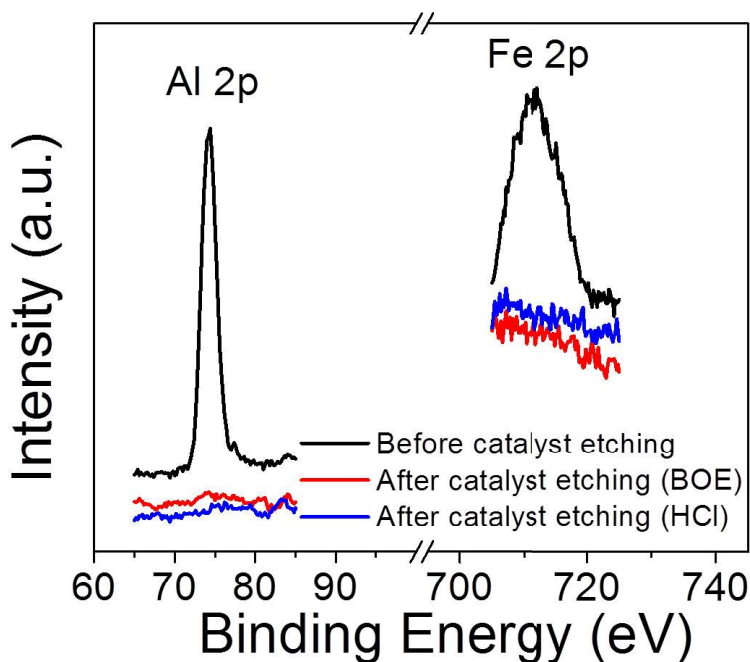


Figure 1-37. XPS analysis for Al and Fe before and after the catalyst etching process by BOE or 1 M HCl solution.

Because of the selective growth and simple and clean transfer process, it is possible to prepare GCNT structures with narrow patterns over a large area, and place them on other substrates. Transparent electrodes for energy storage devices have been reported that use interdigitated patterning with feature dimensions smaller than the resolution of the human eye.⁹⁴ A GCNT structure containing interdigitated patterns with 30 μm line widths and 70 μm gap distances was fabricated and transferred onto a transparent PET film (**Figure 1-38a,b**). Due to the high flexibility of graphene and VA-CNT carpet structure, the transparent pattern on the PET shows good flexibility (**Figure 1-38c**). Based the UV-Vis analysis, it has a

transparency of $\sim 70\%$, which corresponds to the areal portion of the non-transparent GCNT, assuming GCNTs have 0% transparency and the gaps between the GCNTs have 100% transparency (**Figure 1-38d**).

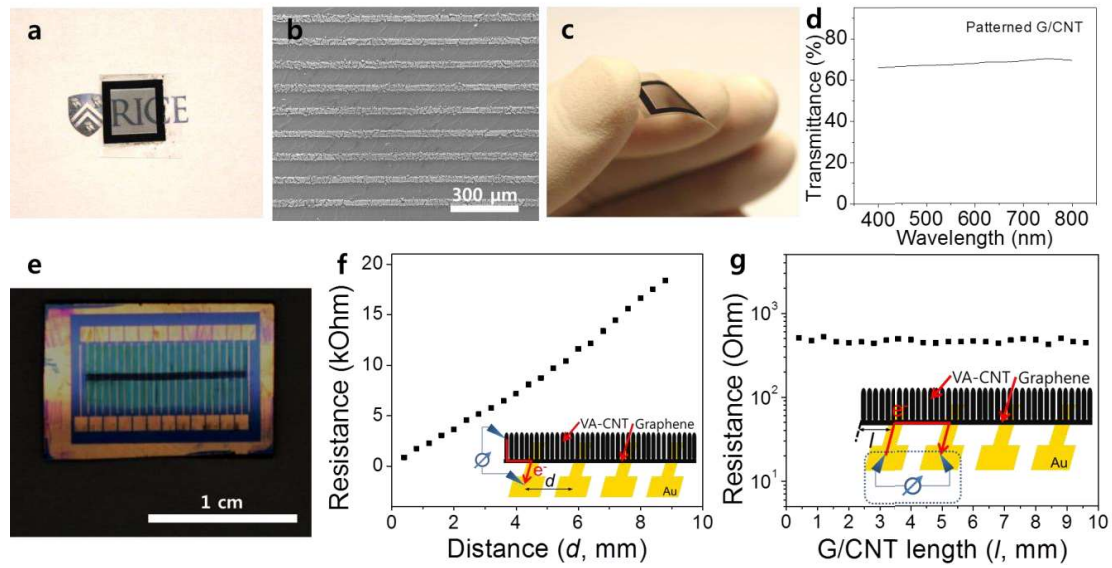


Figure 1-38. Electric property characterization of a transferred GCNT structure.

(a-c) Photographic and SEM images of a transparent and flexible interdigitated GCNT pattern, with 30 μm width and 70 μm gap distance, after being transferred onto a PET substrate; (d) its UV-VIS spectrum shows $\sim 70\%$ transparency. (e) Optical image of GCNT ribbon transferred onto the Au electrode patterned Si wafer. The length and the width of the GCNT ribbon are 1.1 cm and 300 μm , respectively. (f) The resistance of a transferred GCNT ribbon vs its distance. One tip of the analyzer was placed on the CNT and the other tip was placed on the Au electrode, varying the distance between the tips. The near linear relationship between resistance and length shows the continuity of the GCNT ribbon. (g) Resistance vs each part of the GCNT ribbon, measured by moving two tips on the adjacent two Au electrodes, showing homogeneity of transferred GCNT structure.

The electrical properties of the patterned and transferred GCNT were investigated using standard microfabrication methods. To test the conductivity and uniformity of the transferred GCNT structure, a Ti/Au (5/50 nm) electrode was prepared and the GCNT ribbon structure was transferred onto it, as shown in **Figure 1-38e**. The resistance of a GCNT ribbon was measured by placing one tip of the semiconductor analyzer on the CNT surface and the other tip on the Au electrode, with varying distance between the tips. Typical *IV* curves for this experiment shows that Ohmic contact between the VA-CNTs and the graphene has been well maintained even after the transfer process (**Figure 1-39**). The linear relationship between the resistance and length show continuity of the transferred GCNT structure (**Figure 1-38f**).⁹⁵ The uniformity of the transferred GCNT structure was confirmed by moving the 2 tips onto two adjacent Au tips, measuring the resistance of the ribbon section by section (**Figure 1-38g**). This analysis also showed uniform distribution of the resistance (~ 450 Ohm) along the GCNT ribbon, an indication of its homogeneity.⁹⁶

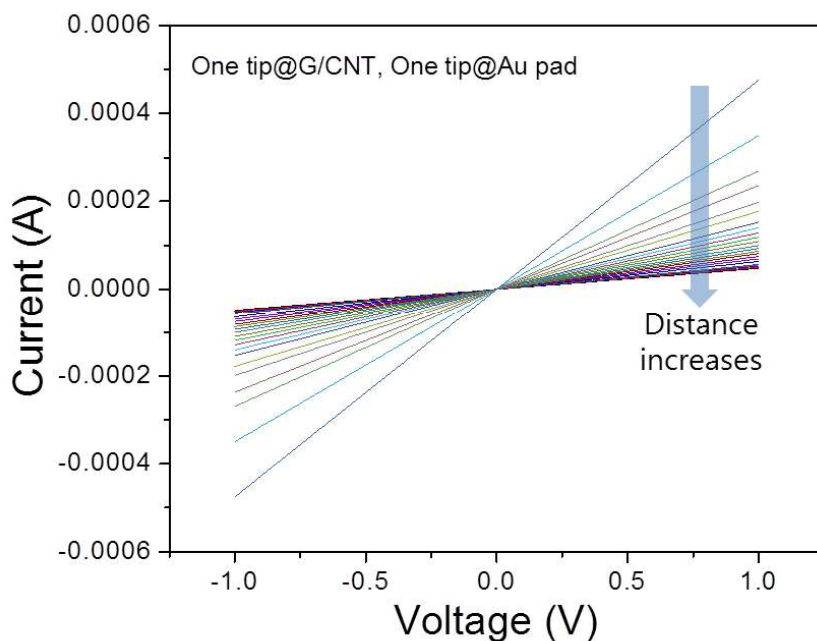


Figure 1-39. Electrical property measurements of transferred GCNT. Typical *IV* curves were obtained by placing one electrode on the CNT carpet and the other electrode on the underlying Au pad. The arrow indicates the successive curves as the distance between the electrodes is increased.

1.4.3. Conclusion

In summary, a facile approach to pattern seamlessly connected GCNT hybrid structures and transfer the patterns to other substrates has been demonstrated. Considering the relative simplicity of synthesizing large-area-patterned 3D GCNT with high surface area and highly conductive characteristics, the use of GCNTs as a platform structure in various application areas, including electronics or biological application, has enormous potential. Moreover, the mechanical compliance and chemical inertness of GCNT allows it to be fabricated onto flexible and/or nonpolar

substrates, leading to advantages in utilization of this technique when other cannot be used.^{97, 98}

1.5. Experimental Contributions

Yilun Li designed the majority of the experiments, prepared the majority of the samples, and conducted the majority of the characterizations including photographs, SEM, TEM, Raman, XPS, etc. **Zhiwei Peng** helped to design the experiments for **section 1.2**, and conducted characterizations including TEM, EELS, SAED, etc. **Jinlong Jiang** helped to design the experiments for **section 1.3**, prepared part of the samples, and conducted part of the characterizations including SEM, Raman, etc. **Nam Dong Kim** helped to design the experiments for **section 1.4**, prepared part of the samples, and conducted part of the characterizations including photographs, SEM, electrical measurements, etc.

Chapter 2

Laser-Induced Graphene Materials

This chapter was entirely copied from reference.⁹⁹

2.1. Introduction

Recently, the Tour group reported a laser-induced graphene (LIG) method as a facile and scalable approach to produce 3D porous graphene structures through a one-step laser scribing process from commercial polyimide (PI, Kapton®) films, which can be directly used as electrode materials for interdigitated microsupercapacitors, among other potential applications.^{100, 101} Various methods have then been developed to tune or improve the physical and chemical properties of the LIG by varying the laser conditions to change the thickness and morphology of LIG, or by introduction of boron or metal doping in the LIG by mixing the PI precursor with other substances.^{102, 103} Furthermore, modification can be done

through the electrochemical deposition of active materials on top of the original LIG layer for high-performance pseudo-supercapacitors.¹⁰⁴ Yet, all these LIG materials were fabricated in ambient atmosphere, and the surfaces that were produced were always hydrophilic, which allowed better contact between the graphene structures and the water-based electrolytes.

Aiming to expand the range of properties for LIG, especially to tune the hydrophobicity of the LIG surface, and eventually to further extend the field of applications for LIG based on the different properties, **Chapter 2** reports a method to fabricate LIG structures under controlled gas atmospheres, where superhydrophilic and superhydrophobic LIG are obtained by changing the gas environment. Specifically, a controlled atmosphere chamber was home-made that allows gas to controllably flow through the chamber, while a ZnSe window on top of the chamber permits the CO₂ laser beam to irradiate the PI film that resides within the chamber. The gases studied include O₂, air, Ar, H₂, and SF₆. LIG structures with different properties were obtained. This change in gas atmosphere permits an enormous change in the water contact angle on the as-prepared LIG, from 0° (superhydrophilic) when using O₂ or air, to > 150° (superhydrophobic) when using Ar or H₂. F-doping of the LIG was also demonstrated under a SF₆ gas atmosphere, where an even higher contact angle (> 160°) could be reached due to the low surface free energy of the C-F bonds. Scanning electron microscopy (SEM), X-ray photoelectron spectroscopy (XPS), and Raman spectroscopy showed that the different wetting properties are due to the LIG surface morphology and the edge and

surface chemistry of these LIG structures. While superhydrophobicity can be introduced with Ar, H₂, or SF₆ in the controlled atmosphere chamber, LIG samples fabricated under O₂ flow show an increased number of defects that produce a significantly improved specific capacitance (compared to LIG made in air) when the LIG was used as the electrode material for microsupercapacitors, showing the versatility of the controlled atmosphere chamber fabrication method.

2.2. Laser-Induced Graphene in Controlled Atmospheres

2.2.1. Experimental Section

Fabrication of LIG in different gas atmospheres. Laser induction was conducted on commercial PI (Kapton®, thickness 127 µm, McMaster-Carr, catalog #2271K6) film with a XLS10MWH (Universal Laser Systems) laser platform, equipped with a 10.6 µm CO₂ pulsed laser (75 W) and a 9.3 µm CO₂ pulsed laser (50 W). The same image density of 1000 pulses/inch in both axes and a scan rate of 15 cm/s were used for all experiments. Typically, the laser duty cycle of 2% is used for the fabrication of LIG, but different laser duty cycles have been used for specific experiments. Laser duty cycle is the percentage of time that the laser is turned on at the rated power for each laser spot; the laser is turned off for the rest of the time. 2% laser duty cycle is also referred to as 2% laser power in the control software of the laser platform, and it can be understood as the average laser power over the duration of each laser spot. For LIG made with gas assist (air or 3% H₂/Ar mixture), a nozzle provided with the instrument was used to blow the selected gas towards

the laser spot, while the general atmosphere within the laser platform was still air at ambient pressure, as shown in **Figure 2-1a**. For LIG made with the controlled atmosphere chamber (O_2 , air, Ar, H_2 , or SF_6), a controlled atmosphere chamber was used to allow different gases to flow through the chamber at 1 atm while synthesizing the LIG. A ZnSe window (thickness 6 mm) is mounted on top of the chamber to allow the CO_2 laser to irradiate the PI film, as shown in **Figure 2-1b**. The flow rates used were ~ 140 sccm for O_2 , ~ 140 sccm for air, ~ 125 sccm for Ar, ~ 175 sccm for H_2 , and ~ 70 sccm for SF_6 , all at ambient pressure. Note that Ar can be replaced by N_2 as the inert gas, and **Figure 2-4** shows the superhydrophobic LIG surface prepared with N_2 in the chamber. The LIG made with SF_6 in the chamber sample was prepared with the $9.3\text{ }\mu\text{m}$ CO_2 laser; all other samples were made with the $10.6\text{ }\mu\text{m}$ CO_2 laser.

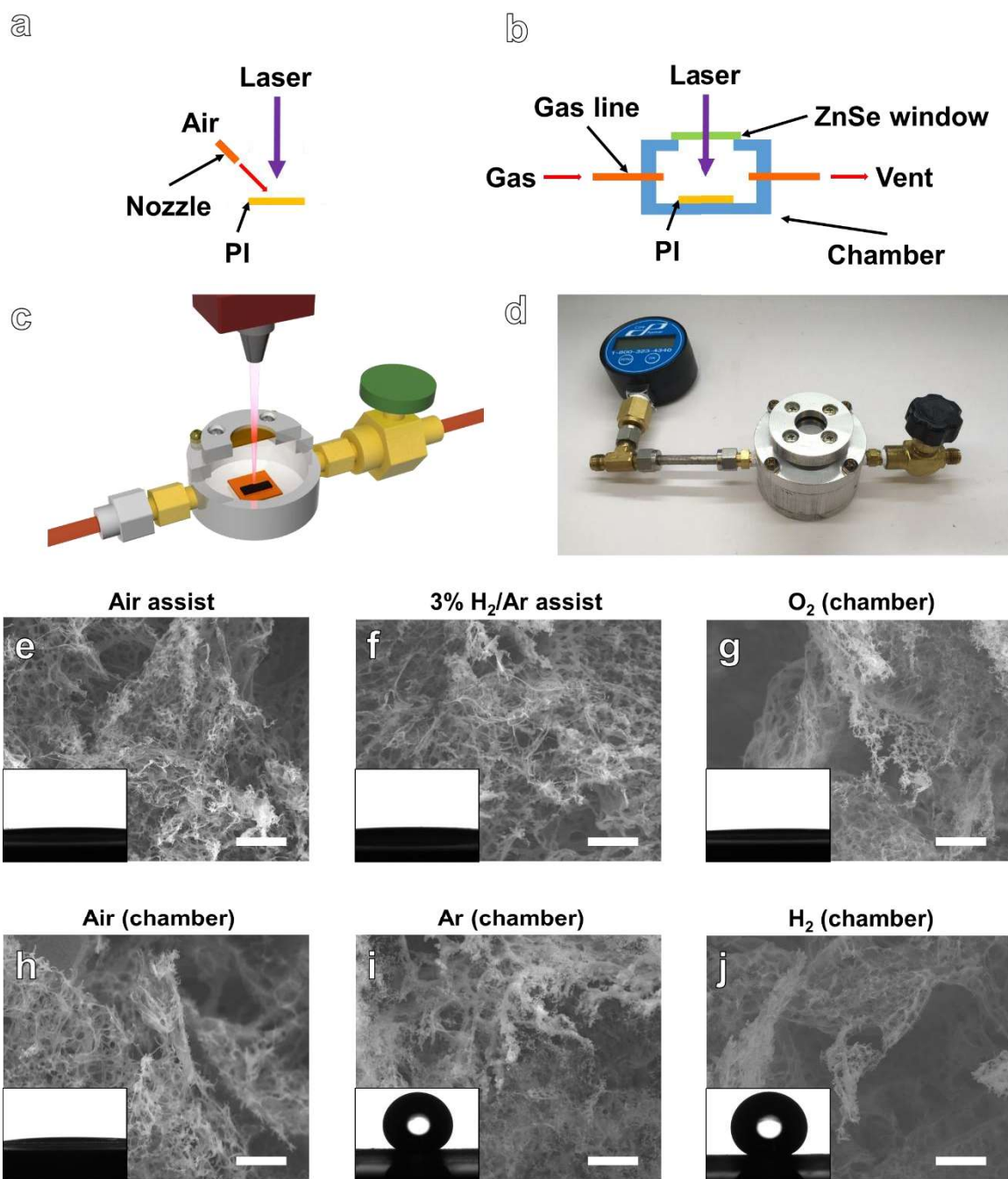


Figure 2-1. Scheme and SEM images of LIG in controlled atmospheres.
Schemes for (a) the fabrication of LIG with gas assist where a stream of air or H₂/Ar is blown across the surface of the PI without a controlled atmosphere chamber, and (b,c) the fabrication of LIG inside a controlled atmosphere chamber. (d) An actual photo of the home-built controlled atmosphere

chamber, and the schematic design drawings are shown in Figure 2-2. (e-j) Top view SEM images of LIG samples prepared under different gas atmospheres. Gas assist: (e) air, (f) 3% H_2/Ar . Controlled atmosphere chamber: (g) O_2 , (h) air, (i) Ar, (j) H_2 . Scale bars: 2 μm . Inset pictures are the water droplet appearance on the LIG surfaces. (e-h) The water droplet appears to have a contact angle of 0° , (i) 152° , (j) 157° . SEM images with lower magnification are shown in Figure 2-3 (top views and side views). 2% laser duty cycle is used for these samples.

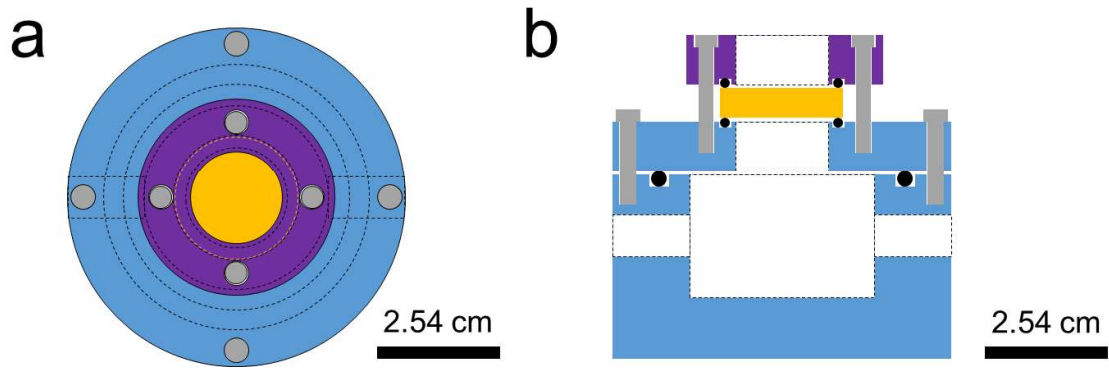


Figure 2-2. The top view and side view drawings of the home-built controlled atmosphere chamber.

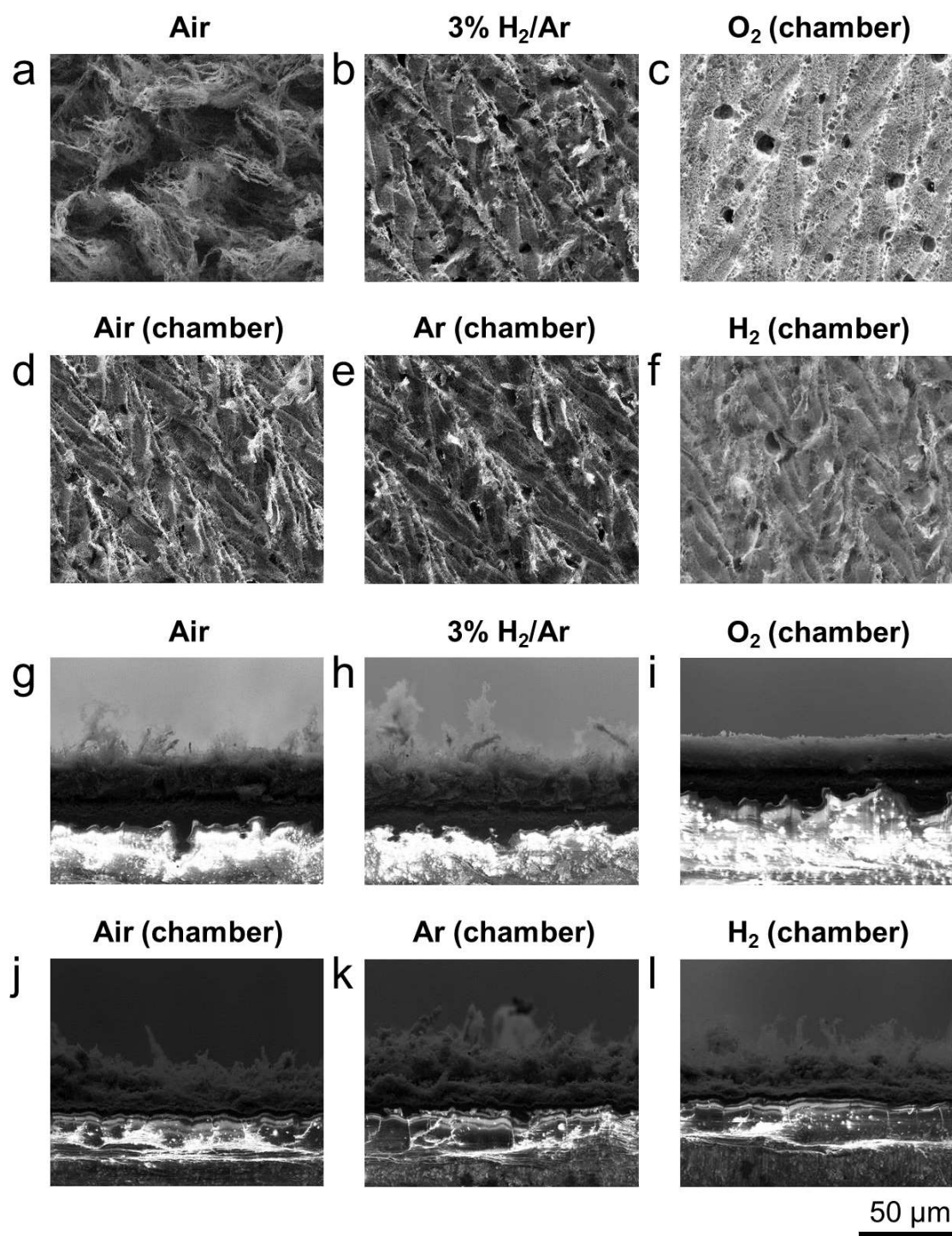


Figure 2-3. Additional SEM images of LIG in controlled atmospheres.

(a-f) Top view and (g-l) side view SEM images of LIG made under different gas atmosphere. 2% laser duty cycle is used for these samples. The scale bar is 50 μm for all images.

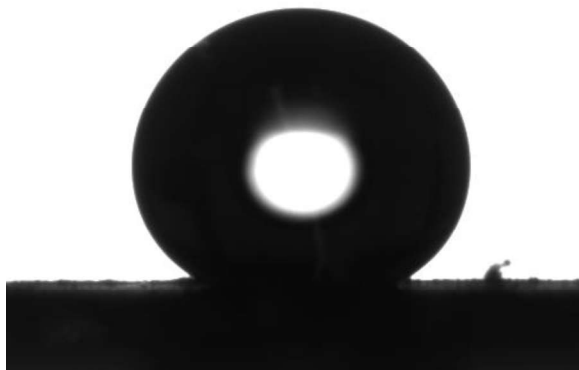


Figure 2-4. LIG made with N_2 in the chamber.

Water droplet appearance on the LIG surface prepared with N_2 in the chamber using 2% laser duty cycle. The measured contact angle is 153° .

Characterization. SEM images were taken with a FEI Quanta 400 ESEM. TEM characterizations were performed using a 200-kV JEOL 2100 Field Emission Gun TEM. Raman spectra were recorded with a Renishaw Raman RE01 scope with 514 nm laser. XPS was performed on a PHI Quantera SXM scanning X-ray microprobe with 200 μm beam size and 45° takeoff angle, and calibrated using C 1s at 284.5 eV.

Fabrication and electrochemical characterizations of LIG microsupercapacitors. LIG was patterned into interdigitated electrodes with a length of 4.1 mm, a width of 1 mm, and a spacing of $\sim 300 \mu\text{m}$ between two

neighboring microelectrodes. Colloidal silver paint was applied on the common areas of both electrodes for better electrical contact, and the electrodes were extended with conductive copper tape. A Kapton® PI tape was employed followed by an epoxy sealing to protect the common areas of the electrodes from electrolyte (H_2SO_4 /PVA polymeric gel), which was later applied on to the active area of the microsupercapacitor devices and dried in a vacuum desiccator. The electrochemical performances of the microsupercapacitors were characterized by CV and galvanostatic charge–discharge experiments using an electrochemical station, and the specific capacitance, energy density, and power density were calculated as previously reported.^{100-102, 104}

2.2.2. Result and Discussion

The schemes for the fabrication of LIG structures under controlled gas atmosphere are shown in **Figure 2-1**. Generally, a 10.6 μm CO_2 laser is used to directly convert PI into LIG structures with different gas atmosphere control methods. For the gas assist method (**Figure 2-1a**), a nozzle is used to blow the selected gas directly at the laser spot, while the sample is still surrounded by air. In this case, only non-flammable gases (or gas mixtures below their explosion limit) can be used due to safety concerns, and we selected air and 3% H_2 in Ar to explore both oxidizing and reducing or inert gas assist. For the controlled atmosphere chamber method (**Figure 2-1b-d**), different gases have been introduced through the gas line; this fabrication process mimics the traditional CVD process for graphene growth and modification,¹⁰⁵ but replaces the extended high-temperature heating

with laser irradiation. Due to the isolation from air, a larger range of gas environments were tested with the controlled atmosphere chamber method, including O₂, air, Ar, and H₂, and a significant change in LIG properties was observed in terms of hydrophilicity and hydrophobicity. Details for the fabrication of LIG samples under different gas atmospheres can be found in the Experimental Section.

Figure 2-1e-j shows the SEM images and contact angle measurements for LIG samples prepared under various atmospheres. For samples prepared with air assist, 3% H₂/Ar assist, and air in the chamber, the LIG structures share a similar porous morphology with a mixture of sheet-like and strip-like components;¹⁰⁰ this similarity could come from the fact that even though 3% H₂/Ar assist was blown at the laser spot, the overall environment still contains much air. For LIG with O₂ in the chamber, however, much rougher edges were observed, presumably resulting from the excess oxidation of the graphene structure. Rough edges were also observed from LIG with H₂ in the chamber to create a hierarchical nano-structure, as the irregular defects on graphene structures were protected from oxygen capping by the reducing environment. From the lower magnification SEM images (**Figure 2-3**), much more significant macro-porous structures can be observed for LIG samples prepared with air assist and O₂ in the chamber, presumably caused by the strong oxidizing environment. The higher-resolution SEM images show the rough edges for both samples (**Figure 2-5**). The degree of defects was analyzed by Raman spectroscopy (*vide infra*). For LIG prepared with Ar in the chamber, aggregated carbon nanoparticles were also observed on the surface of the LIG flakes, especially

from the additional TEM images shown in **Figure 2-6**. These aggregated carbon nanoparticles are probably the product of the carbonization of the PI under the inert atmosphere, forming an enhanced hierarchical microstructure for the LIG sample made with Ar in the chamber. Although certain morphology differences have been observed under SEM for LIG samples prepared under the different atmospheres, there are common features such as the similar LIG thickness of $\sim 40\ \mu\text{m}$ (**Figure 2-3**) and the randomly distributed graphene edges which were observed under TEM (**Figure 2-7**).¹⁰⁰

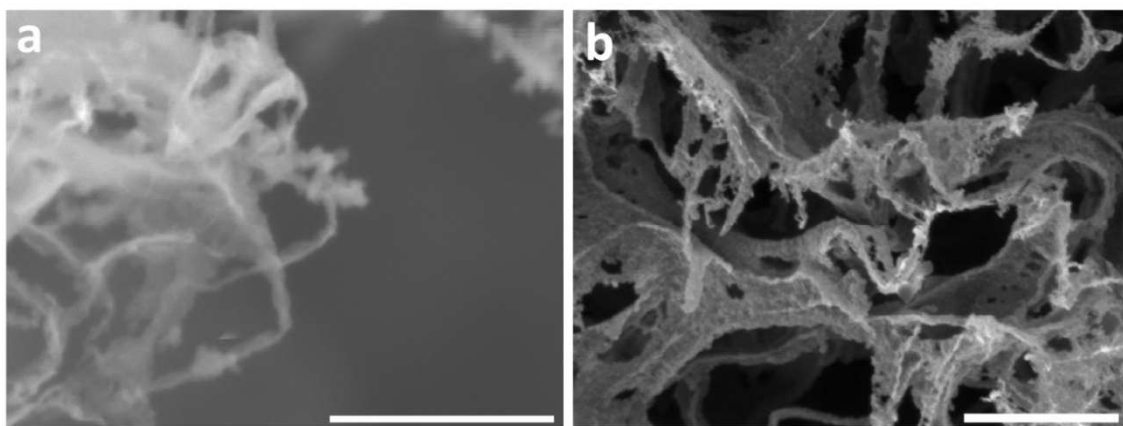
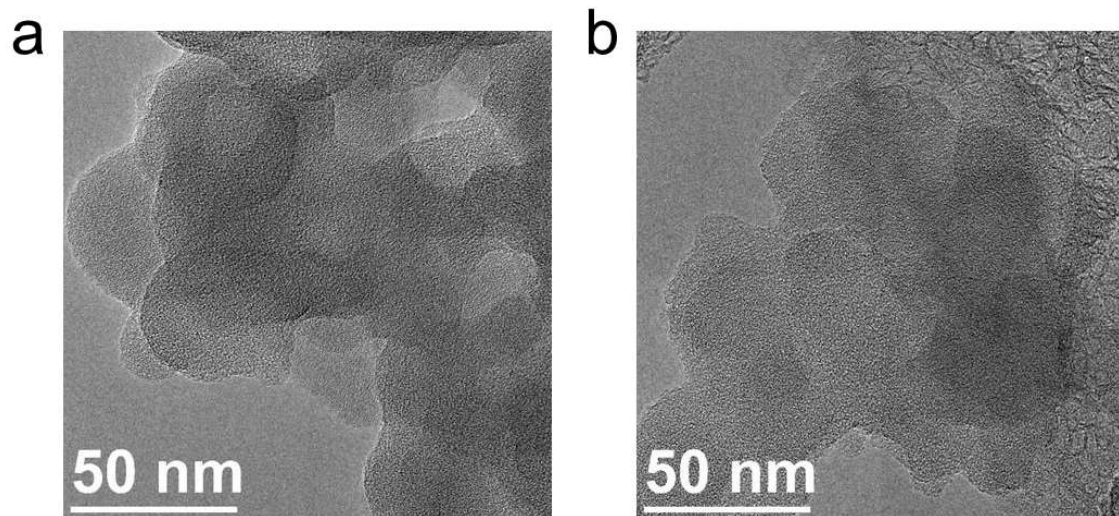


Figure 2-5. Additional SEM images of LIG in H₂ and O₂.
High resolution SEM images of (a) LIG with H₂ (chamber), (b) LIG with O₂ (chamber). Scale bars: 500 nm.



**Figure 2-6. TEM of carbon nanoparticles on the surface of LIG.
(a) aggregated carbon nanoparticles and (b) aggregated carbon nanoparticles
on the surface of LIG.**

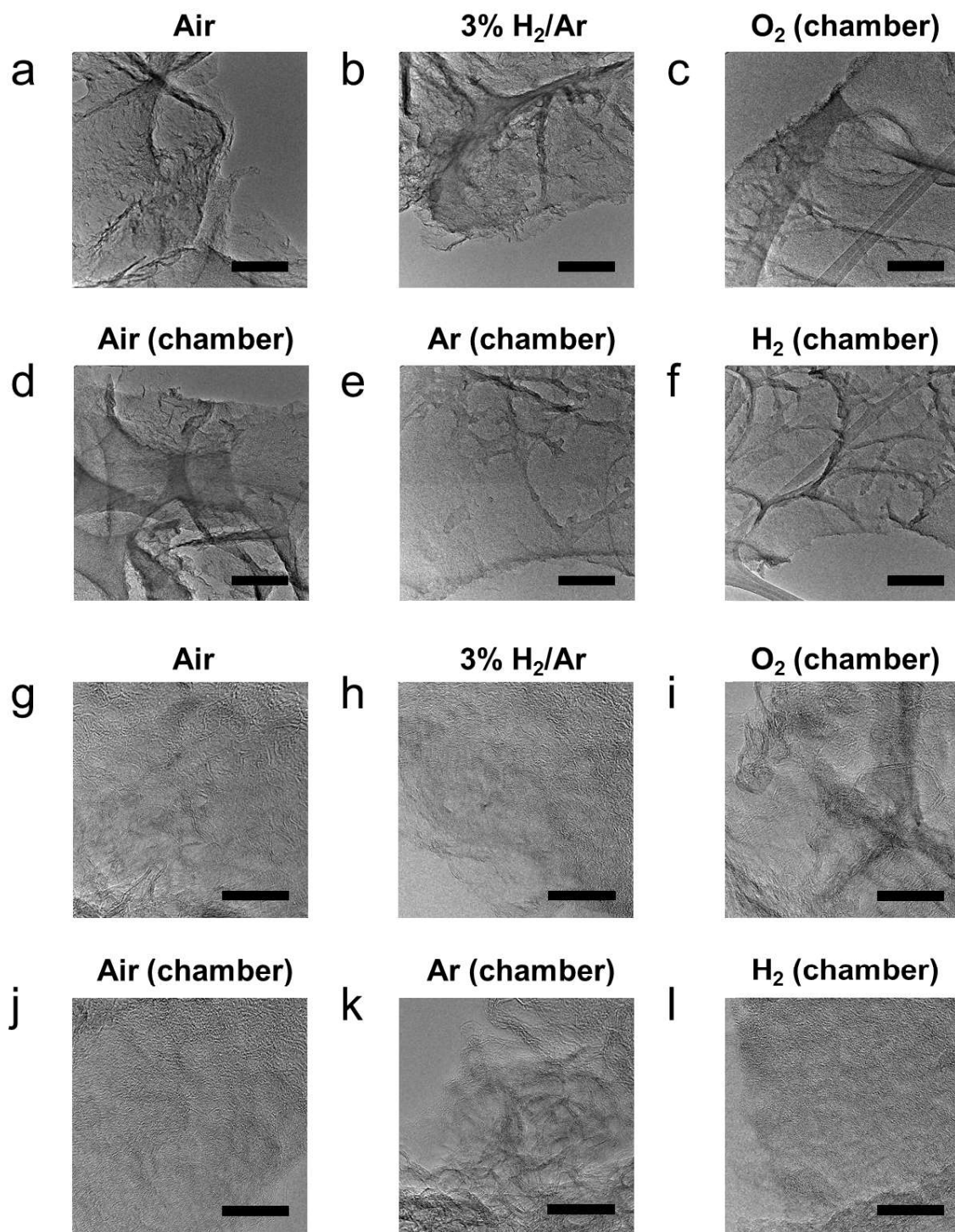


Figure 2-7. TEM images of LIG made under different gas atmosphere. 2% laser duty cycle is used for these samples. (a-f) Scale bars: 200 nm. (g-l) Scale bars: 20 nm.

The inset images in **Figure 2-1e-j** show the water contact angles for LIG samples prepared under different gas atmospheres. Superhydrophobic (contact angle $> 150^\circ$) surfaces were obtained from reducing or inert environments, namely Ar in the chamber (152°) or H_2 in the chamber (157°), while all other samples prepared with the presence of O_2 show superhydrophilicity ($\sim 0^\circ$). Interestingly, while the as-prepared LIG surface made with air assist is superhydrophilic, if we scratch off the LIG from the PI into a powder and make an LIG film by filtration, we obtain a hydrophobic surface with a contact angle of $\sim 120^\circ$, as shown in **Figure 2-8**. This might underscore the significance of the morphology, or surface orientation, of the as-prepared LIG surfaces. For the as-prepared LIG sample on PI, the hydrophilic oxidized edges might be facing upward, making direct contact with water, while the porous surface permits the water droplet to penetrate into the LIG structure. In the case of the LIG film prepared by removal and filtration, the more hydrophobic graphene basal planes are exposed to the water droplet,¹⁰⁶ retarding penetration of the water droplet. Conversely, it could be that only the upper surface of the as-prepared film is superhydrophilic, and the removed LIG exposes the hydrophobic lower portions.

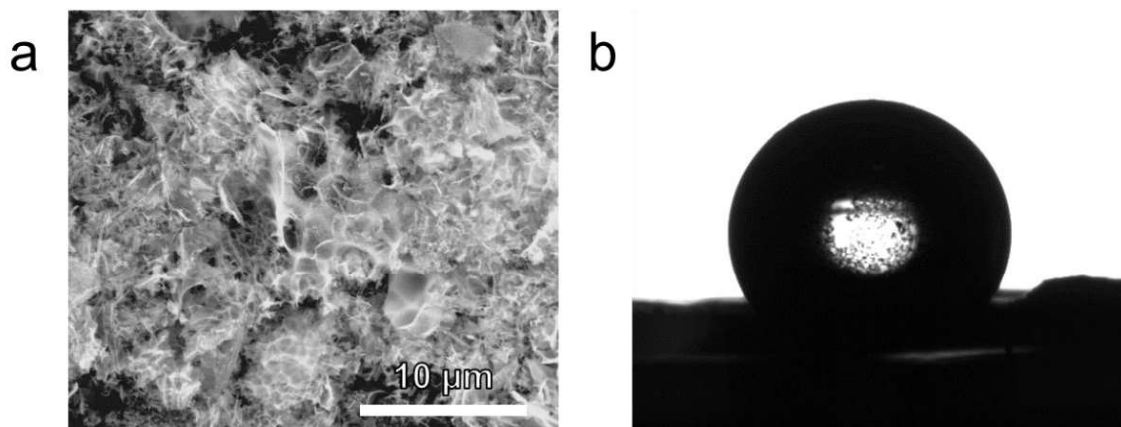


Figure 2-8. Film of LIG that was scraped from the PI surface and prepared through vacuum filtration.

This LIG was made with air assist. (a) Top view SEM image of the filtered LIG film. (b) Image of water droplet on the filtered LIG film; the measured contact angle is $\sim 120^\circ$.

In another interesting and controllable protocol, if we change the laser rastering direction relative to the gas assist direction during LIG fabrication, carbon nanoparticles generated under laser irradiation are blown back onto the previously formed LIG surface instead of being blown away (the normal setup), as shown in **Figure 2-9**. In this case, hydrophobic surfaces are obtained affording a contact angle of 143° . Here, the hydrophobic surface properties apparently come from the enhanced hierarchical structure created by the carbon nanoparticles, a frequently reported phenomenon that can even generate superhydrophobic surfaces.¹⁰⁷⁻¹⁰⁹ Taken together, surface morphology significantly impacts the hydrophobicity of the LIG samples, more specifically, the superhydrophilic as-prepared LIG (air assist) surface with exposed graphene edges, the hydrophobic film (filtered LIG powders,

Figure 2-8) with the exposed graphene basal planes, and the hydrophobic as-prepared LIG (reversed air assist) with hierarchical structure covered by the carbon nanoparticles all present different surfaces to the applied water.

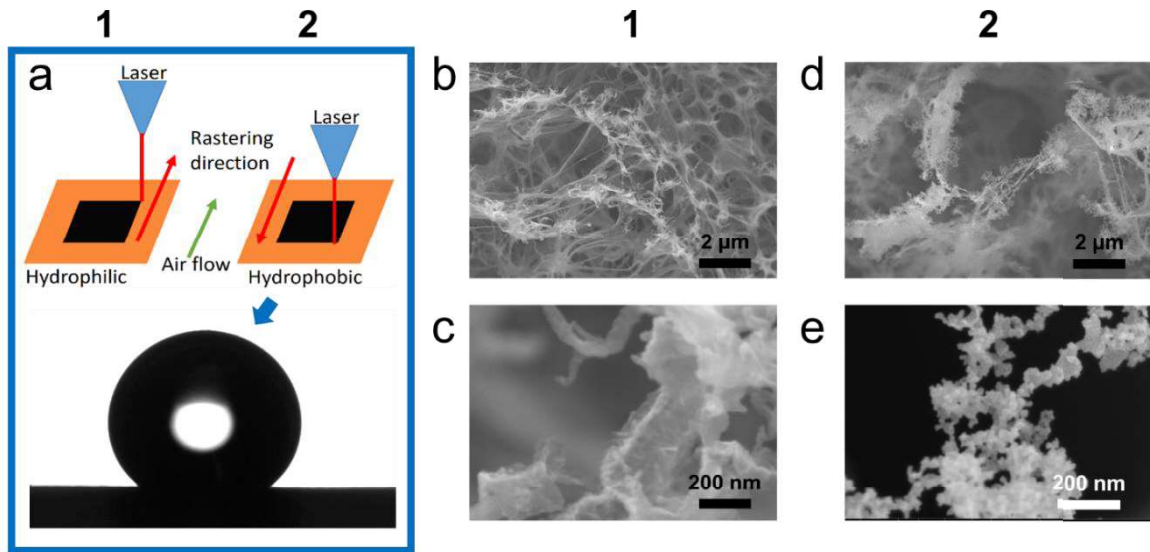


Figure 2-9. Rastering directions and hydrophobicity.

(a) Scheme of different laser rastering directions (method 1 and 2) provide different wetting properties. The picture shows a water droplet sitting on the hydrophobic LIG surface from method 2, the measured contact angle is 143°. (b,c) SEM images of hydrophilic LIG which has few carbon nanoparticles (method 1); (d,e) SEM images of hydrophobic LIG which are coated with carbon nanoparticles (method 2). All fabrications of LIG with gas assist for this manuscript used method 1.

Figure 2-10 shows a statistical summary of the water contact angles of LIG samples prepared under different gas atmospheres. Even with different laser duty cycles, except for LIG prepared with Ar or H₂ in the chamber, almost all other samples show superhydrophilicity with ~ 0° contact angle (except for 0.5% duty cycle with 3% H₂/Ar assist). For LIG made with Ar in the chamber,

superhydrophobicity is produced and the contact angles remain relative constant ($\sim 152^\circ$) with different laser duty cycles. For LIG made with H_2 in the chamber, superhydrophobicity with a larger variance is observed, and 2% laser duty cycle gives the highest contact angle of 157° . We conclude that as H_2 is much more reactive (reducing) than Ar (inert), when the laser irradiation condition changes, there will also be a larger response or change regarding the properties of LIG structures; this topic will be further discussed in the following paragraphs especially in terms of the changes in O content. To further demonstrate the different wetting properties of various LIG samples, **Video 2-1** shows a superhydrophilic LIG surface patterned inside a superhydrophobic LIG frame, and water rolls off the superhydrophobic LIG surface but is trapped at the superhydrophilic LIG surface domains.

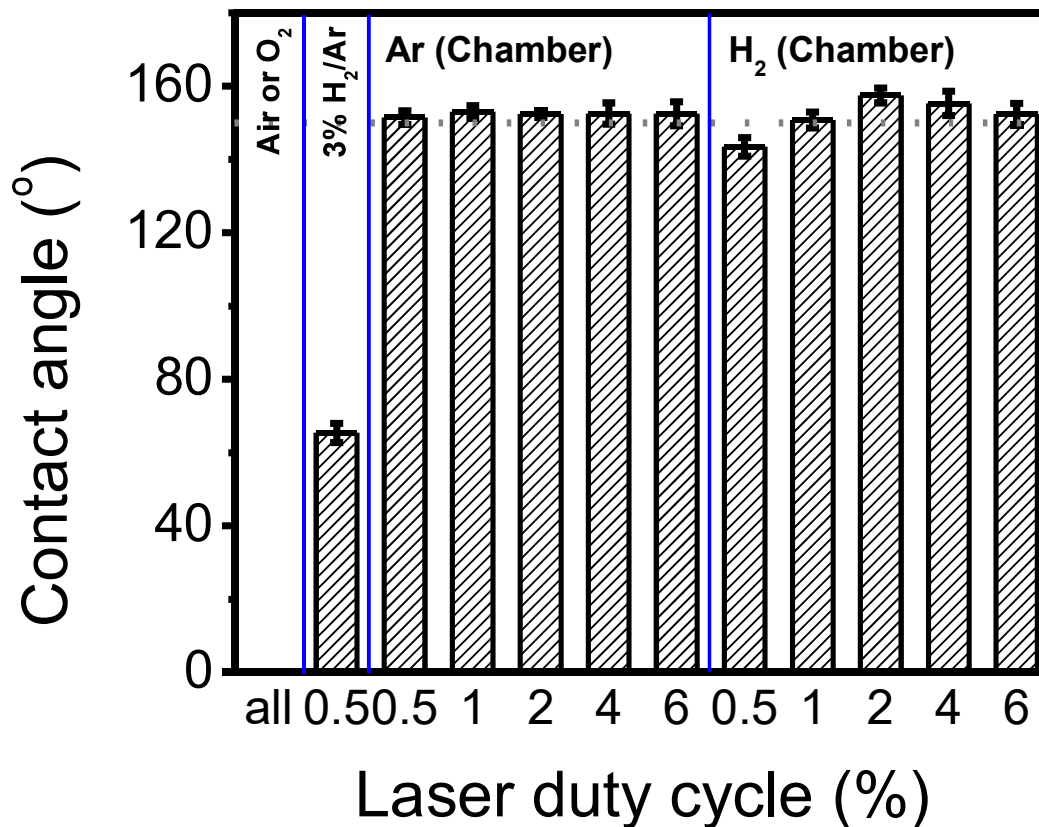


Figure 2-10. Contact angles of LIG samples prepared under different gas atmospheres with different laser duty cycles.

The dashed line at 150° is the minimum contact angle required for superhydrophobicity. The first column is done with air assist or with O₂ in the chamber, and the second column is done with 3% H₂/Ar assist. The rest of the columns are done with Ar or H₂ in the chamber. The error bars reflect the difference between various spots of the same sample.

<https://www.youtube.com/watch?v=xFBDkQH7GA>

Video 2-1. A superhydrophilic LIG surface patterned inside a superhydrophobic LIG frame, and water rolls off the superhydrophobic LIG surface but is trapped at superhydrophilic LIG surface domains.

Figure 2-11 shows the XPS spectra for LIG samples made under different gas atmospheres. From the C 1s spectra shown in **Figure 2-11a**, the graphitic C peak (284.5 eV) is observed as the major component for all LIG samples and is used to calibrate the XPS peak position.¹⁰⁰ LIG made with air assist or 3% H₂/Ar assist shows obvious shoulder peaks at 286 to 290 eV, corresponding to C-O/C=O bonds.^{110, 111} For the O 1s spectra, different peak heights (normalized with C 1s peak) are observed for different LIG samples in **Figure 2-11b**, and the O content as well as C-O content (relative to total O content, i.e. total of C-O and C=O content) are quantified in **Figure 2-11c** after deconvolution. Generally, LIG samples made with gas assist (not isolated from air) shows significantly higher O content relative to LIG samples made in the controlled atmosphere chamber. Samples with superhydrophobicity, specifically LIG made with Ar or H₂ in the chamber, show significantly lower O and C-O content compared to the hydrophilic samples. In the controlled atmosphere chamber, more oxidizing atmospheres yield higher O and C-O content.

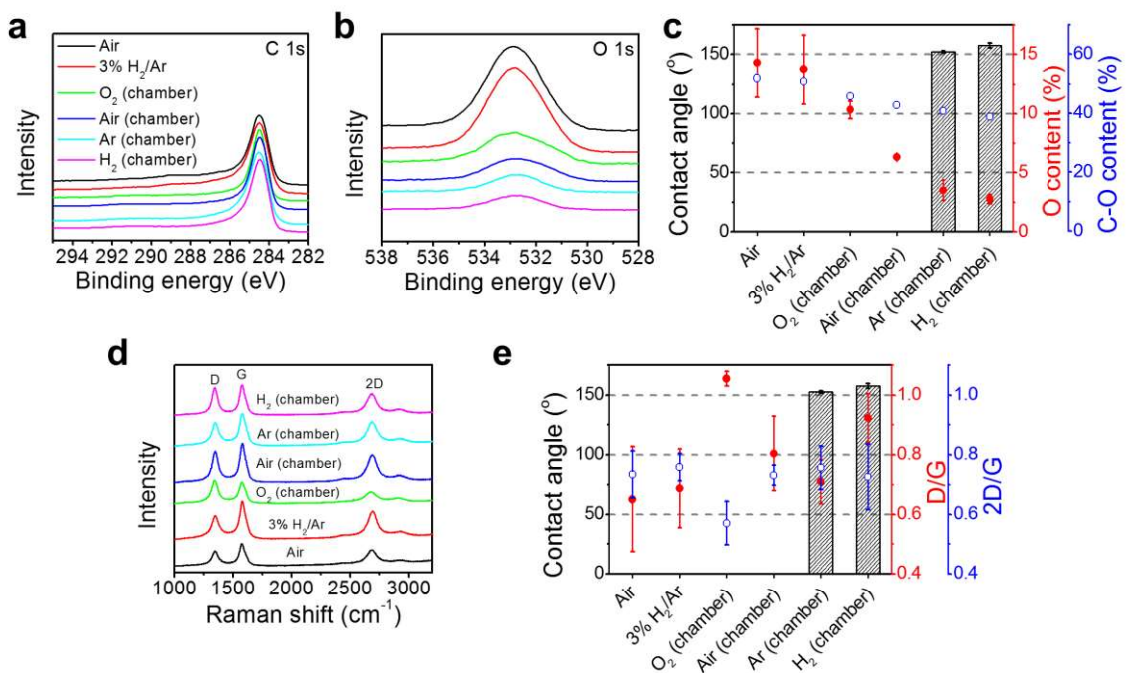


Figure 2-11. XPS and Raman spectra of LIG in controlled atmospheres. (a,b) XPS spectra for LIG samples made under different gas atmospheres. (a) Normalized C 1s spectra, (b) O 1s spectra. (c) The relationship between water contact angle (bars), O content (red dots), and C-O bond content (of total O content, blue circles) for LIG samples made under different gas atmospheres. 2% laser duty cycle is used for these samples. For the calculation of C-O content (relative to total O content, i.e. total of C-O and C=O content), the C-O peak was assigned at 533.4 eV and the C=O peak was assigned at 532.3 eV for the deconvolution.^{110, 112} (d) Raman spectra for LIG samples made under different gas atmospheres. (e) The relationship between contact angle (bars), D/G ratio (red dots), and 2D/G ratio (blue circles) for LIG samples made under different gas atmospheres. 2% laser duty cycle is used for these samples. The error bars reflect the difference between various spots of the same sample.

To further investigate the relationship between O content and water contact angle, for LIG made with Ar or H₂ in the chamber, the data for different laser duty cycles is also plotted in **Figure 2-12**. Clearly, the difference in surface chemistry

does correlate to the difference in contact angle. LIG samples with lower O content and lower C-O content almost always have a higher water contact angle. This trend holds despite the fact that the changes in O content and contact angle are smaller for LIG made with Ar (less reactive than H₂) in the chamber. This correlation is rationalized by the fact that C-O and C=O bonds are more polar than C-C or C-H bonds, so that more O content means the edges are more favorable to interact with water, and thus more hydrophilic. In addition, C-O bonds can terminate in H making it C-OH, therefore more hydrophilic than C=O bonds. This trend is also confirmed by using the captive bubble method to evaluate the contact angle for air (instead of water) and thus the difference in surface properties for the superhydrophilic LIG samples.¹¹³ Using this method, **Figure 2-13** shows that with the controlled atmosphere chamber, LIG samples with a less oxidizing atmosphere (air), compared to O₂, gives lower O and C-O content, and thus a lower air contact angle of ~ 146°. The air bubble cannot even stay on the LIG made with O₂ in the chamber, indicating a much higher air contact angle, thus greater hydrophilicity. As with the water contact angle measurements, the captive bubble contact angles (~ 0°) for LIG samples prepared with Ar and H₂ in the chamber both afford superhydrophobic structures.

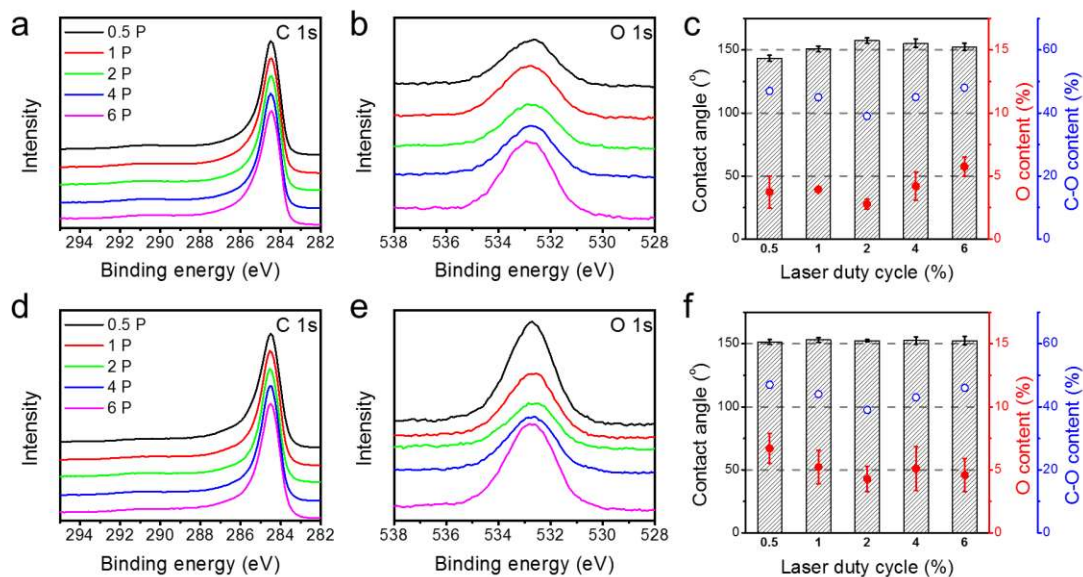


Figure 2-12. Additional XPS spectra for LIG in H₂ and Ar.

(a) C 1s and (b) O 1s peaks of LIG made with H₂ in the chamber with different laser powers. (c) The relationship between contact angle (bars), O content (red dots), and C-O bond content (of total O content, blue circles) for LIG samples made with H₂ in the chamber with different laser duty cycles. (d) C 1s and (e) O 1s peaks of LIG made with Ar in the chamber with different laser duty cycles. (f) The relationship between contact angle, O content, and C-O bond content (of total O content) for LIG samples made with Ar in the chamber with different laser duty cycles. The error bars reflect the difference between various spots of the same sample.

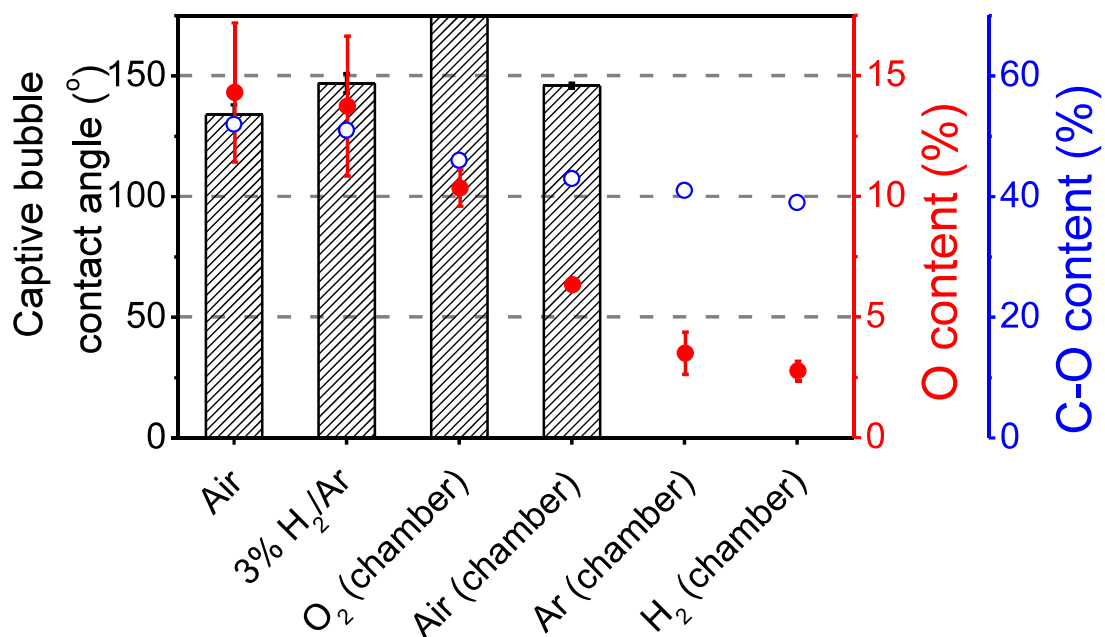


Figure 2-13. Captive bubble contact angels for LIG.

The relationship between captive bubble contact angle (bars), O content (red dots), and C-O bond content (of total O content, blue circles) for LIG samples made under different gas atmospheres. 2% laser duty cycle is used for these samples. C-O peak assigned at 533.4 eV, C=O peak assigned at 532.3 eV for the calculation of C-O content. The error bars reflect the difference between various spots of the same sample.

In summary, based on the experimental results discussed above, both surface morphology and surface chemistry could contribute to the hydrophilicity or hydrophobicity of the LIG surfaces. Specifically, superhydrophilic or hydrophobic LIG surfaces can be obtained by varying the morphology of LIG samples prepared with air assist, and superhydrophilic or superhydrophobic LIG surfaces can be obtained by tuning the O content with different gas atmospheres. However, both

factors should be taken into consideration when synthesizing superhydrophobic or superhydrophilic LIG samples, since the changes in surface chemistry are often accompanied by changes in surface morphology. As shown in **Figure 2-1** and **Figure 2-3**, superhydrophobic surfaces with their lower O content LIG contains a hierarchical structure with rough edges (H_2 in chamber) or carbon nanoparticles (Ar in chamber), and superhydrophilic surfaces with their higher O content LIG contains more macro-pores (air assist and O_2 in chamber).

Raman spectroscopy is also used to study the degree of graphitization and defect formation for various LIG samples under different atmospheres.^{56, 62} As shown in **Figure 2-11d**, D, G, and 2D peaks are observed for the LIG samples, similar to the previously reported LIG.¹⁰⁰ **Figure 2-11e** shows the quantified results of D/G and 2D/G ratios as they are commonly used to analyze the quality of graphitic structures. Among the samples analyzed, a similar 2D/G ratio of 0.6 to 0.7 is observed that indicates good graphitization. The exception is for LIG made with O_2 in the chamber, which shows a significantly lower 2D/G ratio of ~ 0.55 as well as a much higher degree of defects (higher D/G ratio). This could be due to the higher oxidation induced by the O_2 environment, which can be related to the rough edges and large pores observed in the SEM images. LIG made with H_2 in the chamber also shows a slightly increased D/G ratio, most likely because of the reducing environment, which prevents the decomposition or rearrangement of the defects within the graphitic structures. Yet no significant correlation could be found between the Raman spectra and the superhydrophobicity.

The low surface energy of C-F bonds can yield superhydrophobic surfaces.¹¹⁴⁻

¹¹⁸ Here we also tried to introduce C-F bonding into the LIG structures using SF₆ gas in the chamber. SF₆ is a non-flammable gas commonly used as the dielectric medium in electronics manufacturing, yet it is able to decompose to form reactive F species under extreme conditions.^{119, 120} Since SF₆ gas has a high absorbance at 10.6 μm , a 9.3 μm CO₂ laser is used to prepare LIG samples when using SF₆ in the chamber, and **Figure 2-14** shows the characterization of the samples. The typical LIG characteristics of a porous structure and D/G/2D peaks could be observed from the SEM images and the Raman spectrum (**Figure 2-14a,b**). A significantly higher water contact angle of 162° was achieved. **Video 2-2** also shows the water droplet bouncing on the surface of this LIG sample with SF₆ in the chamber until it settles on the neighboring PI film. High F-content (~ 10%) of the LIG surface was confirmed by XPS as shown in **Figure 2-14c-f**. Both CF₂ (689 eV) and CF (687 eV) bonds are detected in the F 1s spectrum and the tailing part for C 1s spectrum.^{121, 122} Interestingly, elemental S was also identified by the peak position of the S 2p peak (164.5 eV). The SF₆ molecules decomposed under laser irradiation into elemental S that is deposited on LIG surface while active F species functionalized the graphene structures. To further analyze the degree of F-functionalization throughout the entire LIG layer (~ 40 μm), an XPS depth profile was obtained for the LIG sample, and is shown in **Figure 2-16**. It is clearly observed that the F functional groups are mainly distributed on the surface of LIG, possibly due to the limited diffusion of the highly active F species into the porous structures of LIG. The abundance of CF₂ (689

eV) decreases much faster than the CF (687 eV) component, as shown in **Figure 2-16c**. Different laser duty cycles were also applied to the LIG made with SF₆ in the chamber, and the acquired contact angles and F content are plotted in **Figure 2-17**. Generally, higher laser duty cycles induce higher F content since more active F species are generated. A laser duty cycle of 4% is chosen as the optimal condition since it reaches a high contact angle (162°) but still maintains a relatively high C content of 86%.

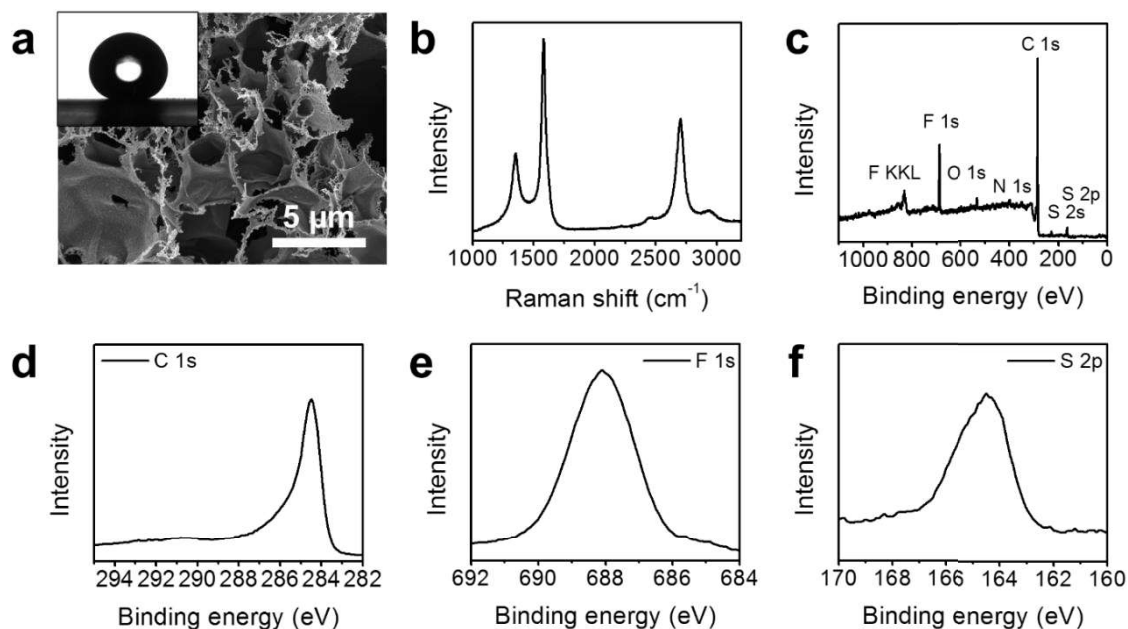


Figure 2-14. Characterization of LIG made with an atmosphere of SF₆ in the chamber.

(a) Top-view SEM image; the inset is the water droplet on the LIG surface with a contact angle of 162°. (b) Raman spectrum. (c) XPS survey spectrum, (d) C 1s spectrum, (e) F 1s spectrum, (f) S 2p spectrum. Additional SEM and TEM images are shown in Figure 2-15. A 9.3 μm CO₂ laser was used when SF₆ was present. A 4% laser duty cycle is used for this sample.

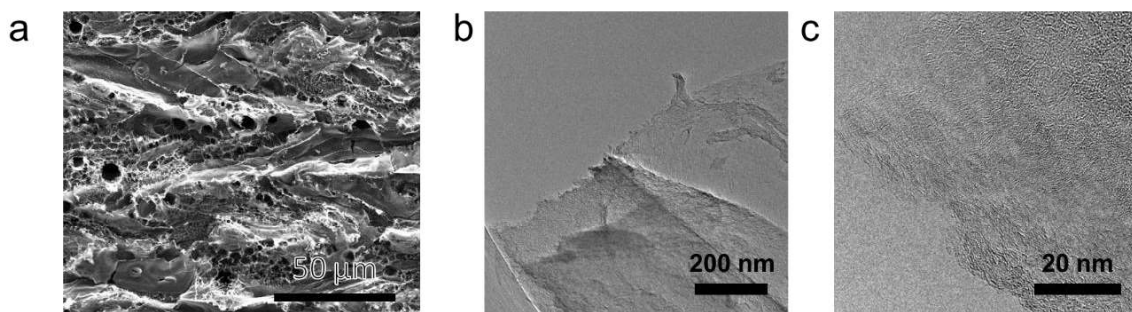


Figure 2-15. SEM and TEM images of LIG prepared with SF₆ (chamber). A 9.3 μm CO₂ laser was used when SF₆ was present. 4% laser duty cycle is used for this sample.

<https://www.youtube.com/watch?v=qAuyVgYI9m8>

Video 2-2. Water droplet bouncing on the surface of LIG with SF₆ in the chamber.

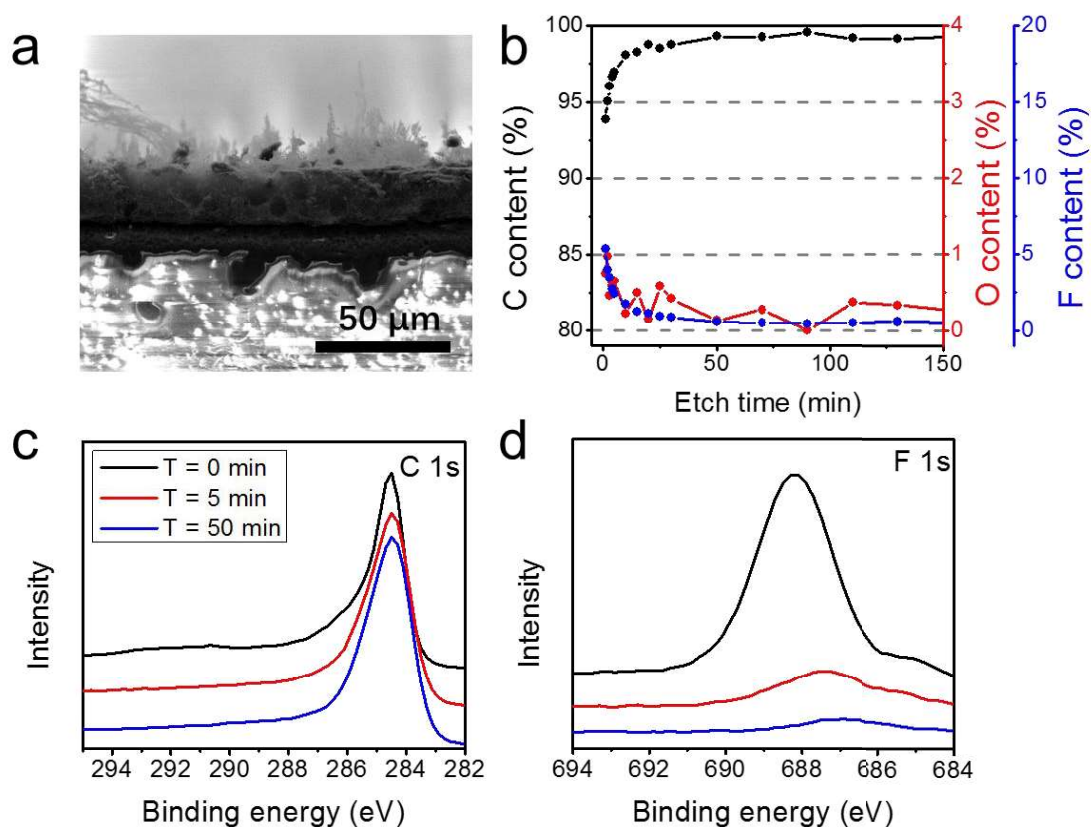


Figure 2-16. XPS depth profile for LIG in SF₆.

(a) Side view SEM image of LIG made with SF₆ in the chamber. **(b)** Depth profile of C/O/F content (black, red and blue dots, respectively) of LIG made with SF₆. An Argon ion beam is used to etch the LIG surface, the estimated etch rate is ~ 20 nm/min. **(c)** C 1s and **(d)** F 1s spectra of LIG made with SF₆ with different etch times. A 9.3 μm CO₂ laser was used when SF₆ was present. 4% laser duty cycle is used for this sample.

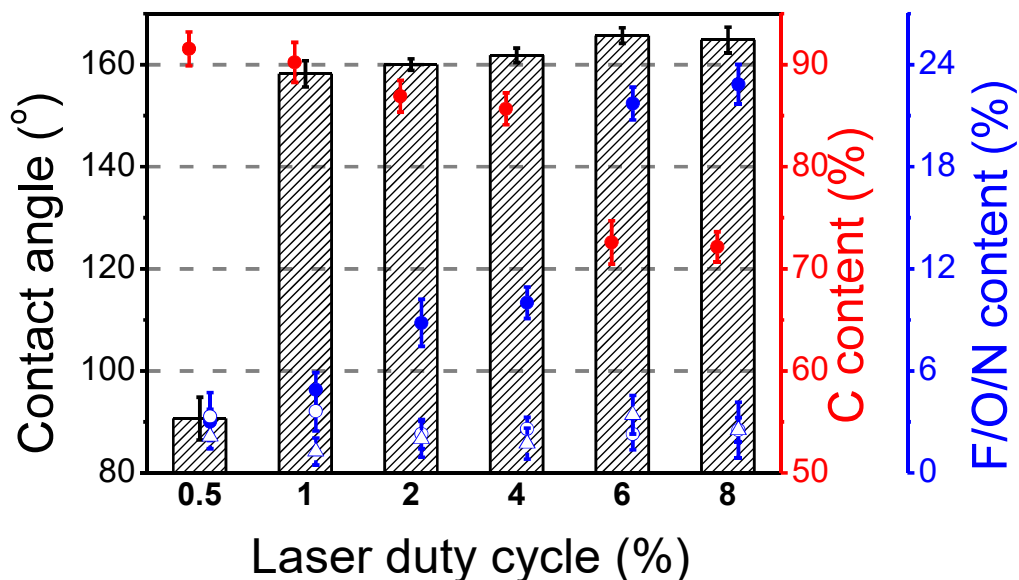


Figure 2-17. Additional XPS data for LIG in SF₆.

The relationship between contact angle (bars) and C/F/O/N content (red dots, blue dots, blue cycles, blue triangles, respectively) for LIG samples made with SF₆ in the chamber with different laser duty cycles. A 9.3 μm CO₂ laser was used when SF₆ was present. The error bars reflect the difference between various spots of the same sample.

To evaluate the stability of various superhydrophilic or superhydrophobic LIG surfaces obtained under different fabrication conditions, we re-tested the contact angles of the LIG samples after being under ambient conditions for one week and one year, and the results are shown in **Figure 2-18**. As shown, the superhydrophilicity was maintained after one year, while the superhydrophobicity remained unchanged after one week, with decreases in contact angles observed if kept in the air for extended periods of time. Also, to evaluate the robustness of the superhydrophobic LIG, we performed different surface treatments for the LIG made

with Ar in the chamber; the superhydrophobicity was maintained with: 1) blowing air at the surface for 1 min; 2) bending 100 times; 3) soaking in ethanol for 1 min; or 4) soaking in acetone for 1 min. However, the LIG tends to come off from the PI surface if sonicated in water for 1 min, and becomes superhydrophilic if treated with O₂ plasma for 10 s. In general, the superhydrophobic LIG samples has shown good stability and robustness, while the superhydrophobicity was lost with intense treatments such as sonication or surface oxidation, both of which are expected to affect the morphology or graphene-like nature of the LIG materials.

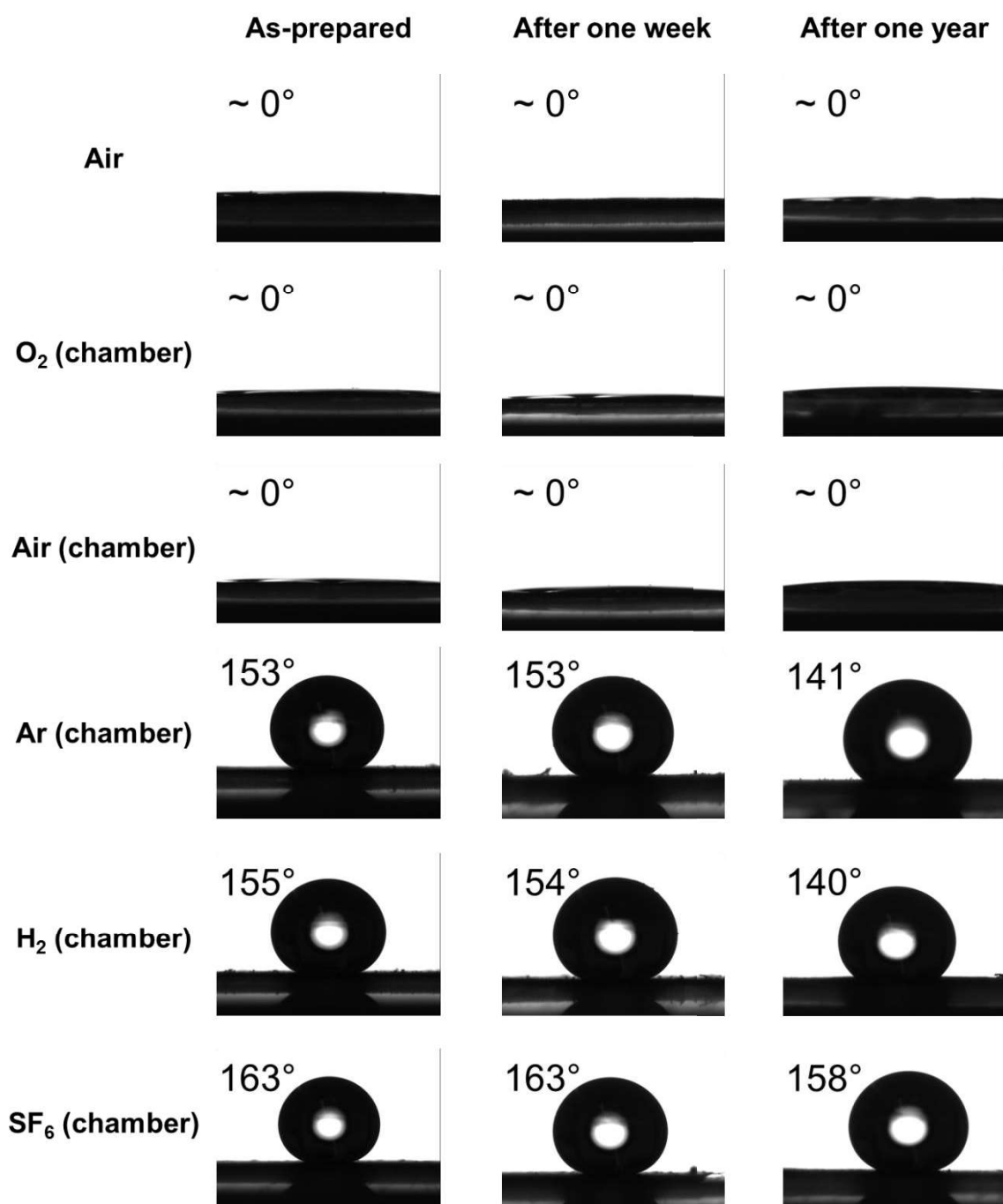


Figure 2-18. Stability of the superhydrophilic/superhydrophobic LIG samples. Contact angles are measured as prepared, after one week in ambient air, and after one year in ambient air.

Another important parameter to evaluate towards hydrophobicity is the hysteresis between the advancing contact angle and receding contact angle.¹²³ **Figure 2-19** shows the advancing and receding contact angles for three kind of superhydrophobic samples demonstrated: LIG made with Ar in the chamber shows the highest hysteresis of 12° in contrast to 4° and 5° for LIG made with H₂ and SF₆, respectively. This difference results from the lower O content for LIG made with H₂, and the F-functionalization for LIG made with SF₆.

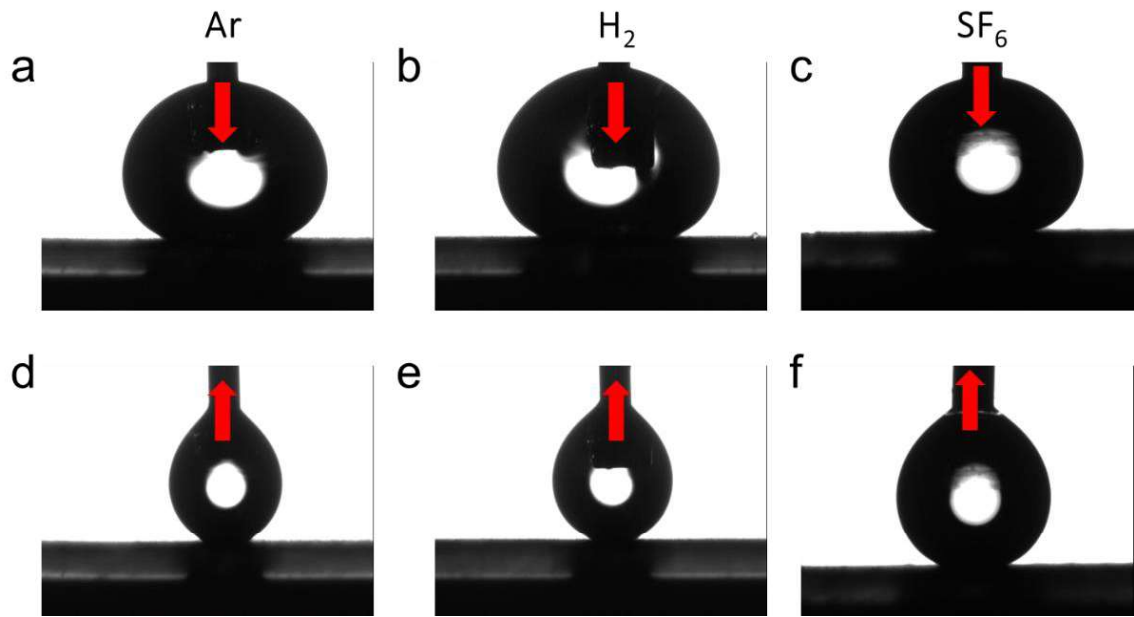


Figure 2-19. Hysteresis in water contact angle for LIG.

(a-c) Advancing and (d-f) receding contact angles of LIG with Ar, H₂, and SF₆. The values are 159°/147°, 160°/156°, and 164°/159°, respectively. 2% laser duty cycle is used for LIG samples prepared with Ar and H₂ (chamber). A 9.3 μm CO₂ laser was used when SF₆ was present, and 4% laser duty cycle is used for LIG samples prepared with SF₆ (chamber).

While superhydrophobic structures and surfaces could have varied applications,¹²⁴ two examples, water/oil separation and anti-icing, are demonstrated in **Figure 2-20** and **Figure 2-21**. For water/oil separation (**Figure 2-20**), a LIG filter is produced by first using a high laser power (a laser duty cycle of 10% at a rastering speed of 3 cm/s) to create $\sim 100\ \mu\text{m}$ holes in the PI sheets, and then using Ar in the chamber to afford a superhydrophobic surface on the porous substrate. Interestingly, despite the existence of the $\sim 100\ \mu\text{m}$ holes, the LIG filter still maintains a high contact angle of 155° , which allows CHCl_3 to pass through the filter while water is repelled. The video of the separation process is shown in **Video 2-3**. For the anti-icing application (**Figure 2-21**), the comparison is made between superhydrophilic LIG made with air assist and superhydrophobic LIG made with Ar in the chamber. At -15 to $-20\ ^\circ\text{C}$, the water droplet ($\sim 0\ ^\circ\text{C}$) sticks on the surface of LIG made in air even though tilted at 45° , and ice consequentially forms. Conversely, LIG made with Ar in the chamber, being superhydrophobic, does not permit freezing to ensue. Ice forms only on the PI substrate, similar to the case of F-functionalized GNRs.¹¹⁴

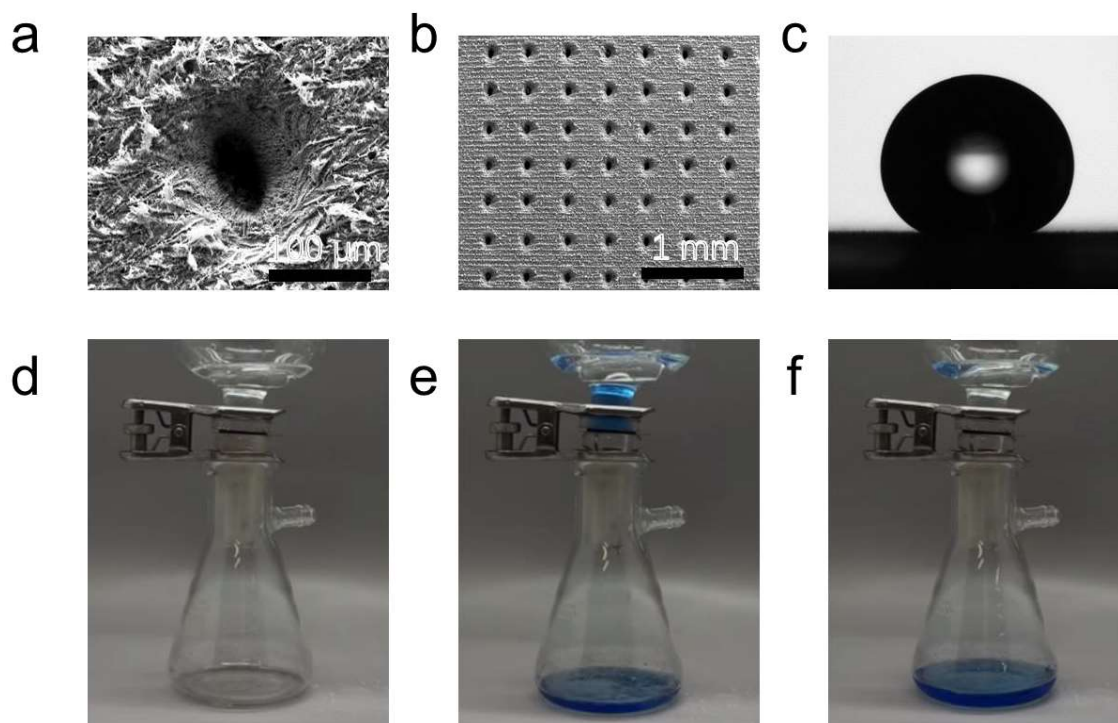


Figure 2-20. Oil/water separation of LIG.

(a,b) Top-view SEM image of LIG filter. (c) A water droplet on the surface of the LIG filter, the measured contact angle is 155°. (d-f) Filtration of $\text{CHCl}_3/\text{H}_2\text{O}$ mixture with the LIG filter. A CHCl_3 -soluble blue dye is used for oil phase visualization. (d) Water does not go through the filter; (e) CHCl_3 goes through the filter; (f) water stays on top of the filter even after all of the CHCl_3 went through.

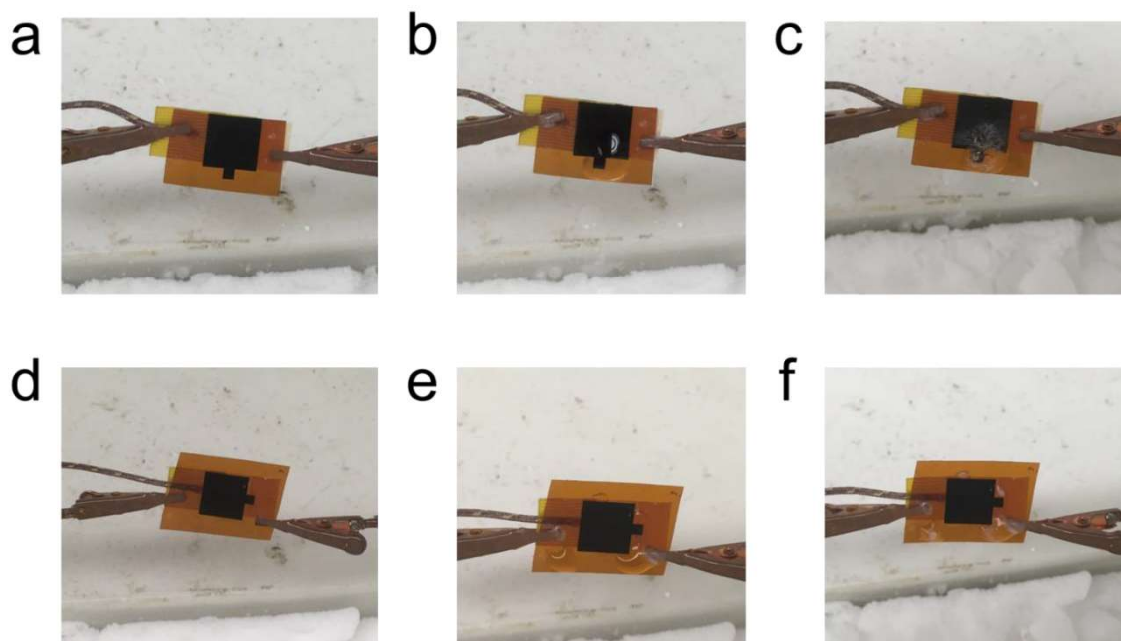


Figure 2-21. Anti-icing properties of LIG.

(a) LIG sample (made in air) tilted 45° at a temperature of -15 to -20 °C. (b) Water (~ 0 °C) dripped onto the LIG sample in (a). (c) Ice formed on LIG sample in (b) after 1 min. (d-f) The same process as with (a-c) but using a LIG sample made in Ar (chamber); ice only formed on PI but not on LIG. 2% laser duty cycle is used for these samples.

<https://www.youtube.com/watch?v=D1vexX-ZjVA>

Video 2-3. Oil filter in performance.

Figure 2-22 shows the performance of LIG microsupercapacitors fabricated with LIG made with air in the chamber compared to O₂ in the chamber.¹⁰⁰⁻¹⁰² LIG microsupercapacitors made with O₂ in the chamber has a significantly improved specific capacitance (3×), energy density, and power density when compared with

the LIG sample made with air in chamber under the same laser duty cycle of 2%. This performance can be further improved by increasing the laser duty cycle to 5% with O₂ in the chamber where a specific capacitance of 37 mF/cm² was achieved (**Figure 2-23**). The increased performance should partially results from the enhanced hydrophilicity that provides better contact with the H₂SO₄/PVA electrolyte.¹²⁵ Another important factor is the increased degree of defects and active sites when using O₂ in chamber, as observed in the Raman spectra in **Figure 2-11**. This is expected to improve the charge storage performance of graphene materials, as is described theoretically and experimentally.¹⁰⁰ In general, the enhancement in supercapacitor performance underscores the utility of the controlled atmosphere chamber for LIG preparation.

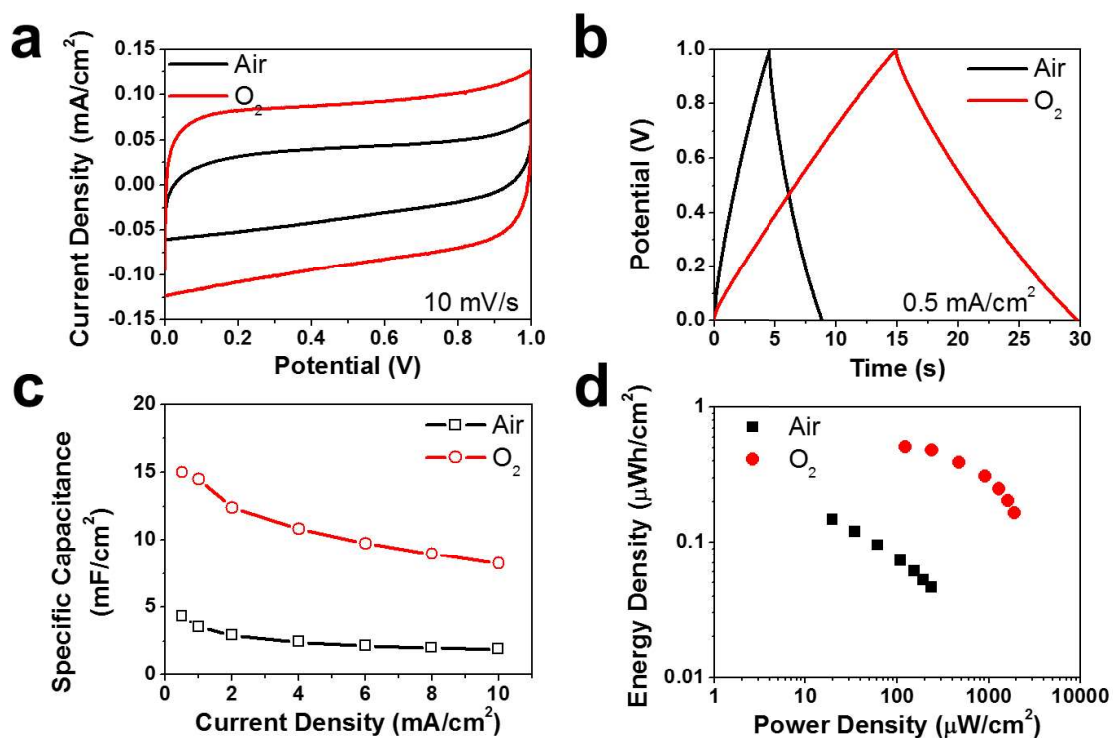


Figure 2-22. Performance of microsupercapacitors prepared from LIG with O_2 in the chamber vs air in the chamber.

(a) CV curves with a scan rate of 10 mV/s. (b) Charge/discharge curves with a current density of 0.5 mA/cm^2 . (c) Specific capacitance plotted against current density. (d) Ragone plot showing the energy and power densities of the devices.

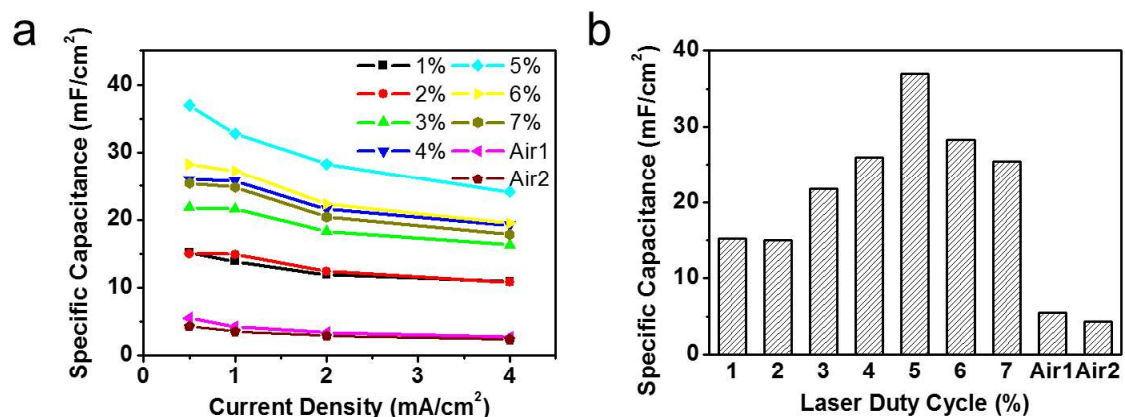


Figure 2-23. Additional data for LIG supercapacitors.

The specific capacitances of supercapacitors made from LIG samples made with O₂ in the chamber (different laser duty cycles) and with air (2% laser duty cycle). The X% in the label in (a) stands for the laser duty cycle of LIG samples made with O₂ in the chamber. “Air1” stands for air assist, “Air2” stands for air in the chamber.

2.2.3. Conclusion

In conclusion, we have successfully demonstrated the fabrication of LIG under various gas atmospheres with a home-made controlled atmosphere chamber device. LIG samples with different surface morphologies and surface chemistries have been obtained, thus generating superhydrophilic or superhydrophobic LIG surfaces depending on the gas environment introduced. The as-produced LIG structures can be directly used for improved microsupercapacitors, oil/water separation, and anti-icing films, all afforded by the varied surface properties in the LIG. This laser fabrication method in controlled gas atmospheres will allow for further broad-based LIG materials development.

2.3. Experimental Contributions

Yilun Li designed the majority of the experiments, manufactured the controlled atmosphere chamber, prepared the majority of the samples, and conducted the majority of the characterizations including photographs, SEM, TEM, Raman, XPS, contact angle measurements, etc. **Luong Xuan Duy** helped to design the experiments, helped to manufacture the controlled atmosphere chamber, prepared part of the samples, and conducted part of the characterizations including SEM, etc.

Chapter 3

Three-Dimensional Graphene Foams

This chapter was entirely copied from reference.¹²⁶

3.1. Introduction

As most of applications for graphene require a large mass or volume of graphene materials, two-dimensional (2D) graphene films or individual graphene nanosheets need to be extended into the third dimension to build a three-dimensional (3D) macroscopic structure.⁶

Several methods have been developed to prepare 3D graphene foams (GFs), such as chemical vapor deposition (CVD) using commercial Ni or Cu foams,¹²⁷ pyrolysis using templates such as NaCl,¹²⁸ polystyrene colloidal particles,¹²⁹ or porous silica opal crystals,¹³⁰ and self-assembly of graphene oxide (GO) by hydrothermal reactions.¹³¹ However, these methods still have limitations such as an

inability to control pore structures, incapability to be free-standing, low mechanical strength, and they often require complicated preparation processes. The GO-derived 3D GF is framed on discrete defective GO sheets rather than a single and uniform graphene structure. In our previous work, a powder metallurgy template method was developed to prepare 3D GFs.^{132, 133} Yet, this process required the fabrication of a mold to contain the monolith that was formed. A 1000 °C CVD process as well as a ~ 2.8 h heating and cooling process was required. Thus, a simple and efficient method to directly prepare 3D carbon materials was sought.

3D printing is a simple and efficient technique enabling the direct production of 3D bulk objects. In 3D printing, polymers, ceramics, or metals can be heated and deposited layer by layer under computer control to build 3D monoliths that are designed using software associated with the printer.¹³⁴ But when this 3D printing technique has been used for carbon or carbon-containing objects, the as-prepared material has been limited to micro-sized scales, with the precursors contained in inkjet-printable or UV-curable inks.^{134, 135} Thus, for the fabrication of graphene or graphene-related materials by 3D printing, GO or chemically modified graphene have been used as the precursor or the ink additive. Yet, the direct 3D printing of all-carbon objects with a binder-free system remains a challenge, especially when inkjet printing is not possible due to solubility or contamination concerns.

In **Chapter 3**, 3D GFs were fabricated *in situ* by manually feeding multiple layers of a mixture of Ni and sucrose onto a stage. After each layer was deposited, the Ni/sucrose scaffold was sintered by a CO₂ laser, with the Ni acting as the

template and catalyst, and sucrose acting as the solid carbon source for graphene growth. This manual process modelled the automated 3D laser metal additive printing process. The 3D printed GF had high graphitization quality, high porosity, and good mechanical properties. This method is simple and efficient, not limited to inkjet-printable and UV-curable ink materials, and can be used to form macroscopic monoliths of various shapes, thus demonstrating a promising approach to the fabrication of 3D graphene materials.

3.2. Three-Dimensional Printed Graphene Foams

3.2.1. Experimental Section

Synthesis. All chemicals were used as received without further purification. The procedures for preparing the Ni/sucrose mixture powders have been described.¹³² Briefly, 3 g of Ni powder (particle size: 2.2 to 3.0 μm) and 0.5 g of sucrose were mixed in 200 mL DI water. Under mechanical stirring (300 RPM), the mixture was heated at $\sim 80\text{ }^{\circ}\text{C}$ until the water was completely evaporated. The Ni/sucrose powders were dried at $75\text{ }^{\circ}\text{C}$ in a vacuum oven ($\sim 2\text{ Torr}$) overnight, and then ground using a mortar and pestle. A 2032-coin cell lithium ion battery steel case was employed as the powder-bed for 3D printing. The steel case was filled to $\sim 1\text{ mm}$ thick with the Ni/sucrose mixture, and then transferred into a controlled atmosphere chamber which allowed pure H_2 gas ($\sim 175\text{ sccm}$) to flow through under ambient pressure.⁹⁹ A ZnSe window (thickness 6 mm) was mounted on top of the chamber, which allowed an external CO_2 laser to irradiate the Ni/sucrose

powder inside the chamber. The Ni/sucrose powder was irradiated with a 10.6 μm CO₂ pulsed laser (75 W) on a XLS10MWH (Universal Laser Systems) laser platform with a maximum laser writing speed of 304.8 cm/s (120 inch/s). The image density was 1000 pulses/2.54 cm (1000 pulses/inch) in both axes. The laser duty cycles used in this experiment are 10, 20, 50, and 100%, which are referred to as 10P, 20P, 50P, and 100P, respectively. Similarly, the rastering speeds are 1, 2, 3, and 5%, which are referred to as 1S, 2S, 3S, and 5S, respectively. After the first laser rastering, another thin layer of powder (~ 50 to $100 \mu\text{m}$) was manually added onto the top of the sample. Then the sample was irradiated by laser again in H₂ atmosphere. After repeating 20 \times , the 3D printed GF/Ni was obtained. The 3D printed GF/Ni products were etched in 1 M of FeCl₃ aqueous solution (~ 200 mL) for 2 days to remove the Ni, and then transferred into DI water. The foams were purified in DI water for 4 days (200 mL, refreshed with DI water 1 \times /day), and dried using CPD (Supercritical Automegasamdri-915B) to obtain free-standing 3D printed GFs. During the entire process, no further heat-treatment in a furnace was needed and no binder additive was applied.

Characterization. The morphology and microscopic structures of 3D printed GFs were studied using SEM (FEI Quanta 400 ESEM) operated at 5 kV and a high-resolution JEOL JEM-2100F TEM operated at 200 kV. Raman spectra were collected using a Renishaw *inVia* Raman Microscope RE04 with a 633 nm laser. The XRD patterns were taken using a powder X-ray diffraction system (Rigaku D/Max Ultima II, Cu K α radiation). TGA (Q-600 Simultaneous TGA/DSC from TA Instruments) were

carried out from room temperature to 900 °C in air. XPS (PHI Quantera SXM scanning X-ray microprobe) was tested with a 100 μm beam size and a 45° take off angle. ATR-IR spectra were tested using a Nicolet Nexus 670 Fourier transform infrared spectrometer that is equipped with an attenuated total reflectance system (Nicolet, Smart Golden Gate) and a MCT-A detector. Under ambient atmosphere and room temperature, electrical conductivity was analyzed with an Agilent B1500A semiconductor parameter analyzer using a customized DC probe station by a two-probe configuration measurement method. Pt contact pads (250 μm \times 250 μm) were deposited onto 3D printed GFs using shadow mask evaporation; the distance between the contacts was 120 μm . The size of the GFs is \sim 1 cm \times 1 cm, the thickness of the original GFs is \sim 2 mm, and it is pressed by hand to a film thickness of \sim 70 μm before depositing the Pt contact pads. The mechanical properties of 3D printed GFs were tested by using a DMA Q800 system (TA Instruments) under 1 Hz of constant frequency at room temperature. Tests were performed with 20 μm of amplitude (fixed displacement) by up to 70000 cycles.

3.2.2. Result and Discussion

As shown in **Figure 3-1a**, hybrid powders of Ni coated with sucrose were prepared and then used in a simulated powder-bed system for 3D printing. The specific 3D printing process is similar to the previously reported laser sintering process.¹³⁶ Specifically, during the laser irradiation process under H₂ atmosphere, both Ni powder and sucrose can absorb the laser light and be locally heated to a high temperature (**Figure 3-2**), enabling the sintering of Ni powders to Ni scaffolds

at the laser spot. Simultaneously, the sintered Ni scaffolds act as the template and catalyst for graphene growth through the dissolution-precipitation process,¹³⁷ while the sucrose acts as the solid carbon source.⁵⁹ As the laser is rastering across the entire printing area, each laser spot ($\sim 100\ \mu\text{m}$) exposure time is $< 1\ \text{ms}$ before the laser moves to another spot. For each spot, the local heating will first allow the carbon from sucrose to dissolve in the Ni, and as the laser moves away the carbon will then precipitate during the fast cooling process to form graphene on the surface of the sintered Ni scaffolds. The laser rasters over the entire area. After the first rastering, another thin layer of powder was manually added onto the top of the sample, followed by another laser irradiating process. After repeating 20 \times , the 3D printed GF/Ni was obtained. After etching of Ni in FeCl_3 aqueous solution (1 M), purifying in DI water, and drying by a critical point dryer (CPD), a free-standing 3D printed GF with the designed shape was obtained. The method is simple and efficient, with no high-temperature CVD furnace employed and no extended growth process applied. The starting materials are only Ni powder and sucrose which are inexpensive and abundant, without any binder additives added, and not limited to inkjet-printable and UV-curable ink materials. Moreover, the shapes of the samples are designable by the laser cutter, as shown in **Figure 3-1b**. The free-standing 3D printed GFs can be designed into various structures, which can be well-maintained after the etching and drying process. Compared to freeze-drying and heat-drying, CPD can dry the GF samples with minimum changes in volume, ensuring the structural integrity of the 3D printed GFs.^{12, 138, 139} Compared to the desired size of 1

cm in width, the 3D printed GF showed $\sim 20\%$ shrinkage in width, which could be avoided by introducing carbon nanotubes (CNTs), as demonstrated in our previous work.¹³³ In addition, this shrinkage might also be solved by reducing the size of the Ni particles, further changing to other carbon precursors or quantities of carbon precursors.

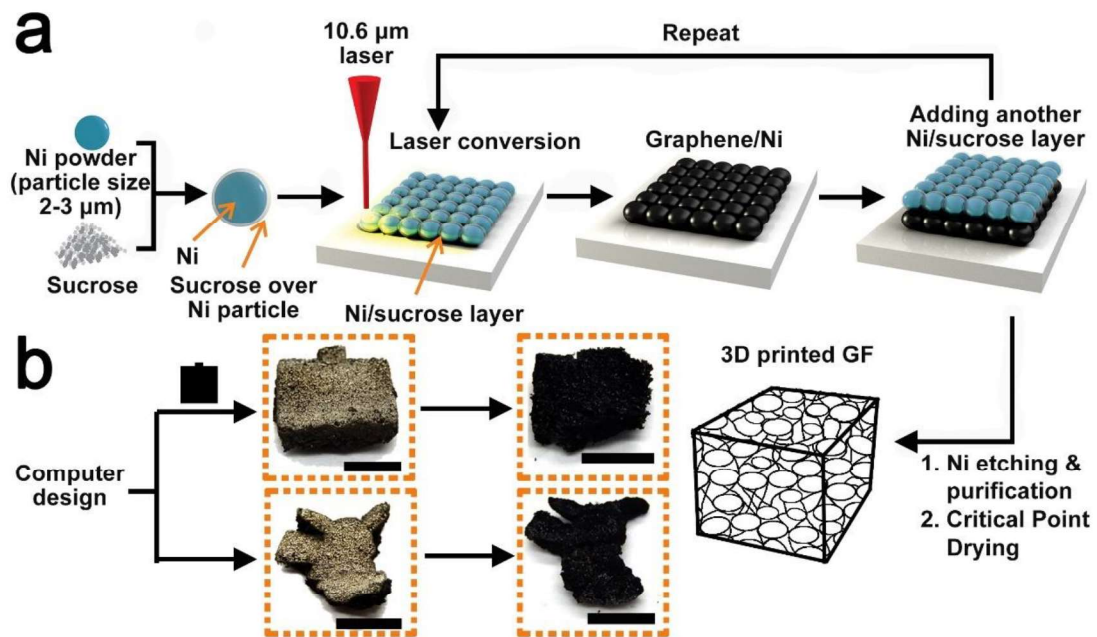


Figure 3-1. The synthesis of 3D GF.

(a) Schematic of *in situ* synthesis of 3D GF using a simulated 3D printing process. (b) Photographs of 3D printed GF before and after dissolving the Ni. The scale bars are 5 mm.

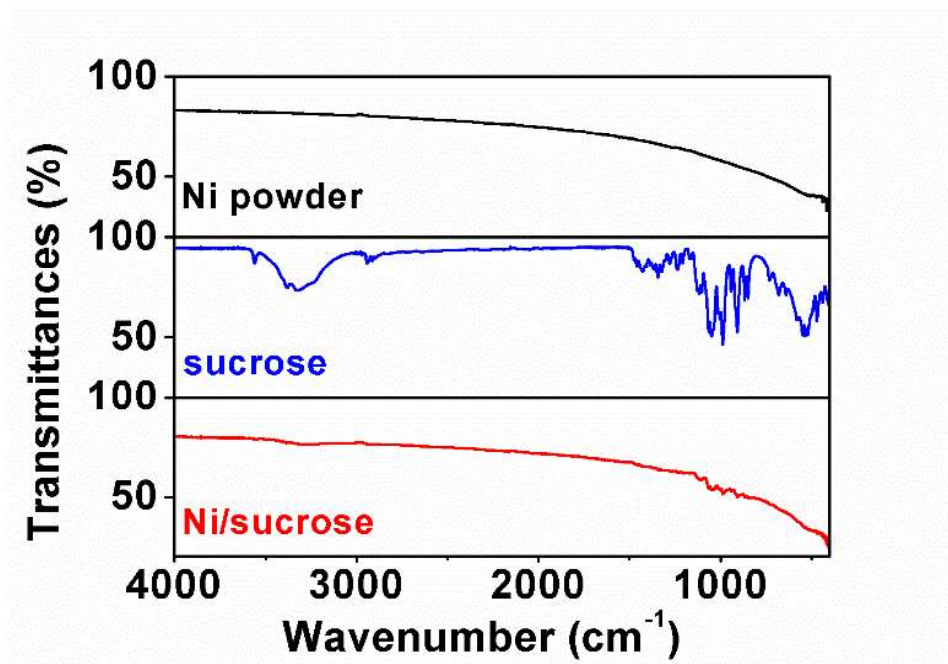


Figure 3-2. ATR-IR spectra of Ni powder, sucrose, and Ni/sucrose hybrid powder.

As shown in **Figure 3-2**, sucrose absorbs light $\sim 1000 \text{ cm}^{-1}$ ($\sim 10 \text{ }\mu\text{m}$). Ni absorbs at low wavenumbers. Thus, a $10.6 \text{ }\mu\text{m}$ CO_2 laser, which should heat both Ni and sucrose, was employed in this work to grow graphene.^{100,102} Based on known graphene growth mechanisms, the Ni particles will be sintered and sucrose will decompose to generate atomic C. The C will dissolve in the hot Ni and precipitate during the fast cooling process to form multi-layered graphene on the Ni surface.

Two of the critical variables for control of the laser irradiation process are the laser duty cycle and the rastering speed. In general, higher laser duty cycle and lower rastering speed will result in higher energy input per unit area. Here, samples fabricated using different rastering speeds and duty cycles were systematically

analyzed. The rastering speeds are 1, 2, 3, and 5%, which are referred to as 1S, 2S, 3S, and 5S, respectively. Similarly, the laser duty cycles used in this experiment are 10, 20, 50, and 100%, which are referred to as 10P, 20P, 50P, and 100P, respectively. As shown in the scanning electron microscope (SEM) images in **Figure 3-3** and **Figure 3-4**, although graphene sheets can be grown on the surface of sintered Ni scaffolds with 100P and 1S, 2S, 3S, and 5S, large amounts of unreacted sucrose were observed in **Figure 3-3a-b** at the highest 5S speed, indicating that the sucrose was not completely converted. When the rastering speed was decreased, the amount of unreacted sucrose decreased, and the sintered Ni scaffolds were larger and had smoother surfaces. With the slower rastering speed, the laser remained at each spot for more time, delivering more energy and heat to each particular spot. This increased energy and heat converted more sucrose to graphene and allowed the Ni crystalline grain to grow larger. While graphene wrinkles can be observed on the surface of Ni scaffolds for 2S, 3S, and 5S, as shown in **Figure 3-3a,c,e**, when the rastering speed was decreased to 1S, no graphene wrinkles were observed (**Figure 3-3g**), an indication that the graphene is much thinner with 1S. With a fixed speed at 5S, higher duty cycles also reduced the amount of unreacted sucrose, and resulted in higher graphene quality because of the higher heat and energy input, as illustrated in **Figure 3-5**. Considering the experimental time for rastering, the amount of residual sucrose, and the fact that thicker graphene will possess better mechanical performance, the combination of a rastering speed of 2S and a laser duty cycle of

100P were chosen as the optimal conditions for further experiments and characterization.

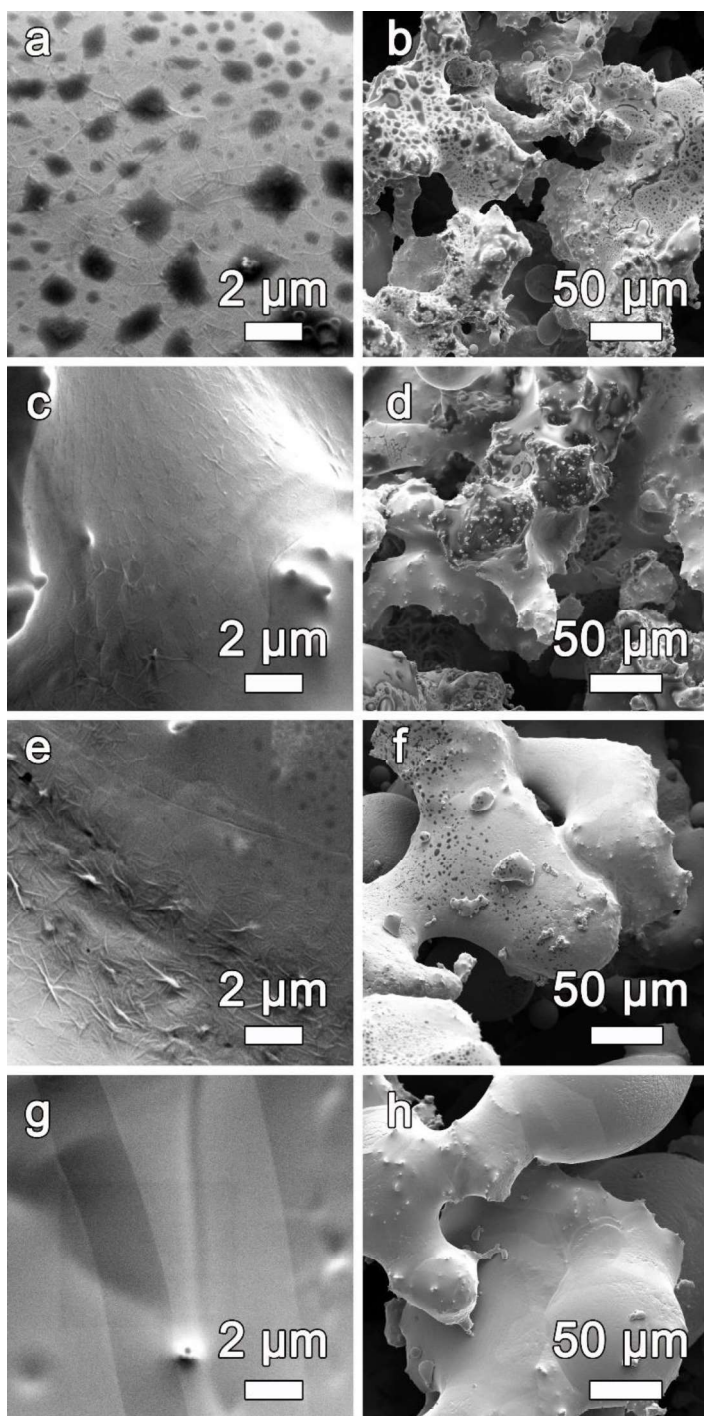


Figure 3-3. SEM images of 3D printed GFs with Ni scaffold prepared using 100P. (a-b) 5S, (c-d) 3S, (e-f) 2S, and (g-h) 1S in a H₂ atmosphere.

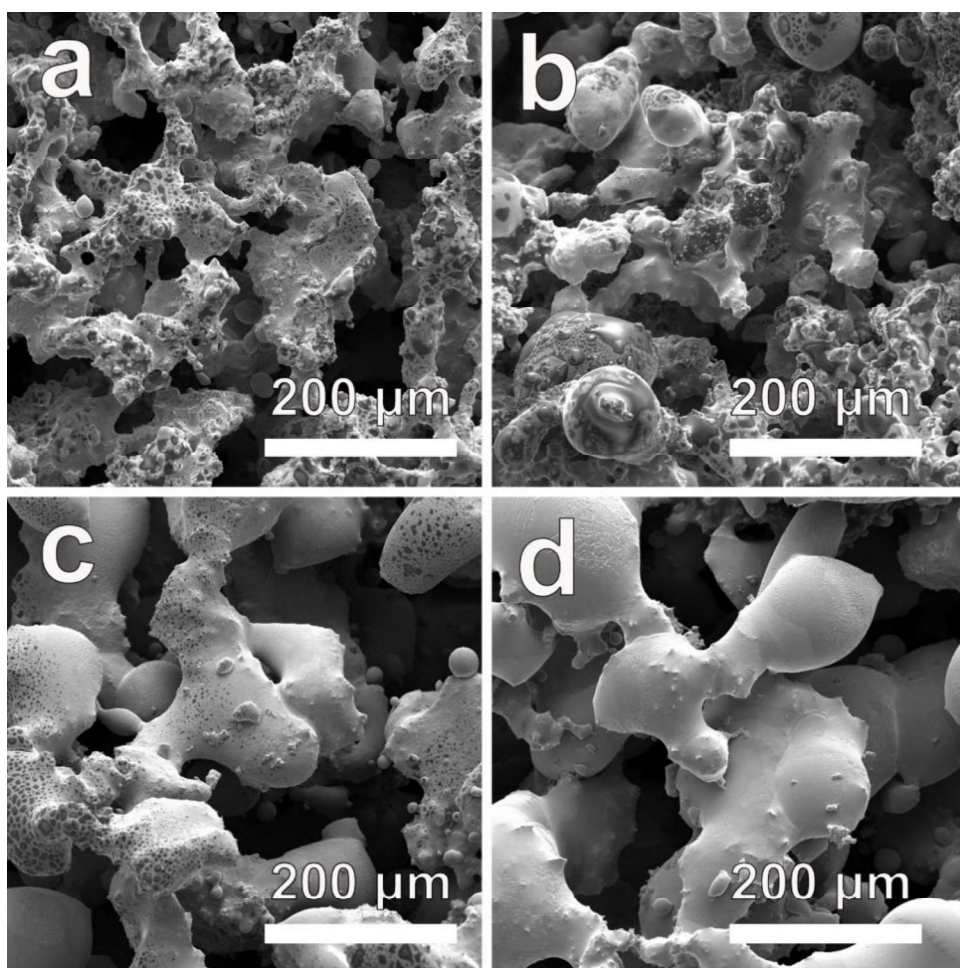


Figure 3-4. Low magnification SEM images of 3D printed GFs with Ni scaffold prepared using 100P.

(a) 5S, (b) 3S, (c) 2S, and (d) 1S in a H₂ atmosphere.

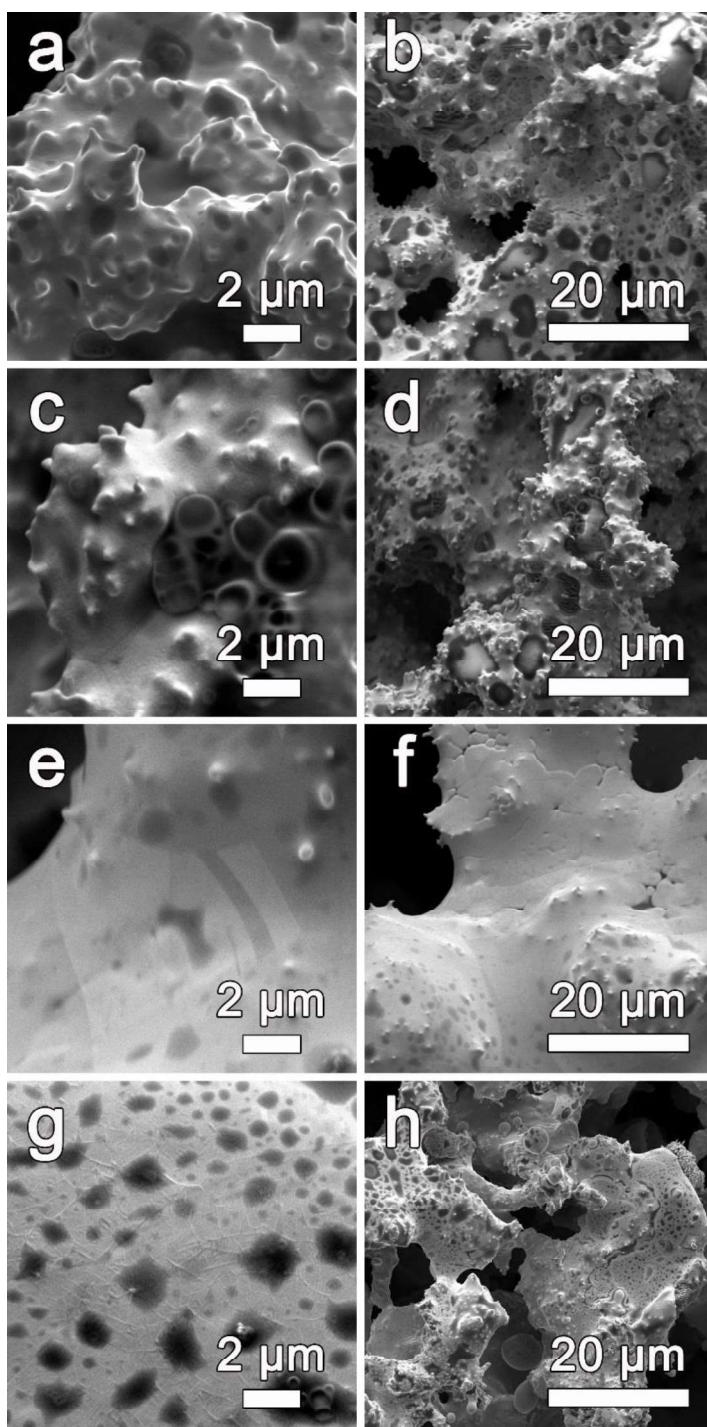


Figure 3-5. SEM images of 3D printed GFs with Ni scaffold prepared using 5S. (a-b) 10P, (c-d) 20P, (e-f) 50P, and (g-h) 100P in a H₂ atmosphere.

The effect of changing laser duty cycles was systematically investigated at a constant rastering speed of 5S. With lower laser duty cycles of 10P and 20P, graphene was not detected on the surface of the Ni scaffolds, as shown in **Figure 3-5a-d**. When increasing the laser duty cycle, graphene with wrinkled features was observed on the surface of the Ni scaffolds. Even at a duty cycle of 100P, large amounts of unreacted sucrose were still observed, indicating that the 5S rastering speed of was too fast. The laser duty cycle of 100P was chosen in the next experiments.

To further investigate the quality of the graphene printed by varying the laser duty cycle and rastering speed, Raman spectroscopy was employed, as shown in **Figure 3-6**. For all duty cycles and rastering speeds, the Raman spectra have the typical sp^2 carbon modes, showing the D bands ($\sim 1350\text{ cm}^{-1}$), G bands ($\sim 1580\text{ cm}^{-1}$), and 2D bands ($\sim 2670\text{ cm}^{-1}$), indicating the existence of graphene.^{1, 31, 140-142} The calculated I_D/I_G ratios of samples printed with different rastering speeds and laser duty cycles are in the range of 0.2-0.4, demonstrating the high structural quality of the as-printed graphene. The comparable I_G/I_{2D} ratios (0.6 to 1.8) indicate the as-printed samples are multi-layered graphene, which would contribute to the good mechanical performance of the 3D printed GFs. Moreover, the position of the 2D bands as well as the I_G/I_{2D} ratios indicate that the number of layers in the as-printed GFs should be 1 to 10 layers, since when the layer number is > 10 , the 2D band shifts to $\sim 2700\text{ cm}^{-1}$.⁵⁶

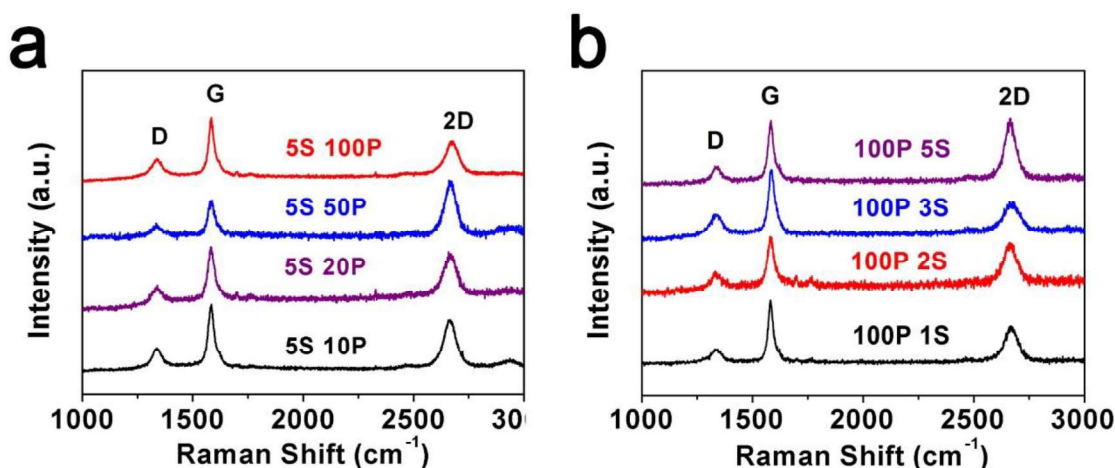


Figure 3-6. Raman spectra of 3D printed GFs with Ni scaffold. Prepared using (a) 10 to 100P with 5S, and (b) 1 to 5S and 100P in a H₂ atmosphere.

With 100P laser duty cycle and 2S rastering speed, the morphology and structure of 3D printed GFs after removing the Ni scaffolds were investigated by SEM and transmission electron microscope (TEM), as shown in **Figure 3-7**. Even after the three-step removal of the Ni scaffolds, the 3D printed GFs retained the structure of the sintered Ni scaffold, as shown in **Figure 3-7a-c**. The 3D printed GFs consist of graphene sheets and graphene shells that show structures similar to the Ni scaffolds and Ni particles since Ni acted as templates during growth, thereby permitting pore size commensurate with the metal particle sizes used. The porous structure of the 3D printed GFs could benefit applications in vibration damping and energy storage related fields.^{132, 133, 141} The density of 3D printed GFs was 0.015 ± 0.003 g cm⁻³ calculated by measuring the mass and volume of the CPD dried

monoliths. The porosity of 3D printed GFs was $99.3 \pm 0.2\%$ calculated by **Equation 3-1**:

$$\theta = \left(1 - \frac{m}{Vd}\right) \times 100\%$$

Equation 3-1. Calculation of the porosity of 3D printed GFs.

where θ , m , V , and d are the porosity, mass, volume, and density of graphite (which is 2.09 to 2.23 g cm⁻³), respectively.¹⁴² Both the density and porosity values of the 3D printed GFs are comparable to other carbon foam materials.¹⁴³ The TEM image in **Figure 3-7d** shows a large graphene sheet; the inset is the selected area electron diffraction (SAED) pattern showing the hexagonal single crystal signal of the graphene. The carbon shells in **Figure 3-7e** are similar to those shown in the SEM images (**Figure 3-7a-c**). The high magnification image in **Figure 3-7f** shows the few-layered structure of 3D printed GFs, which can be observed from the edge of graphene sheet, and is in good accordance with the results from the Raman spectra in **Figure 3-6**.

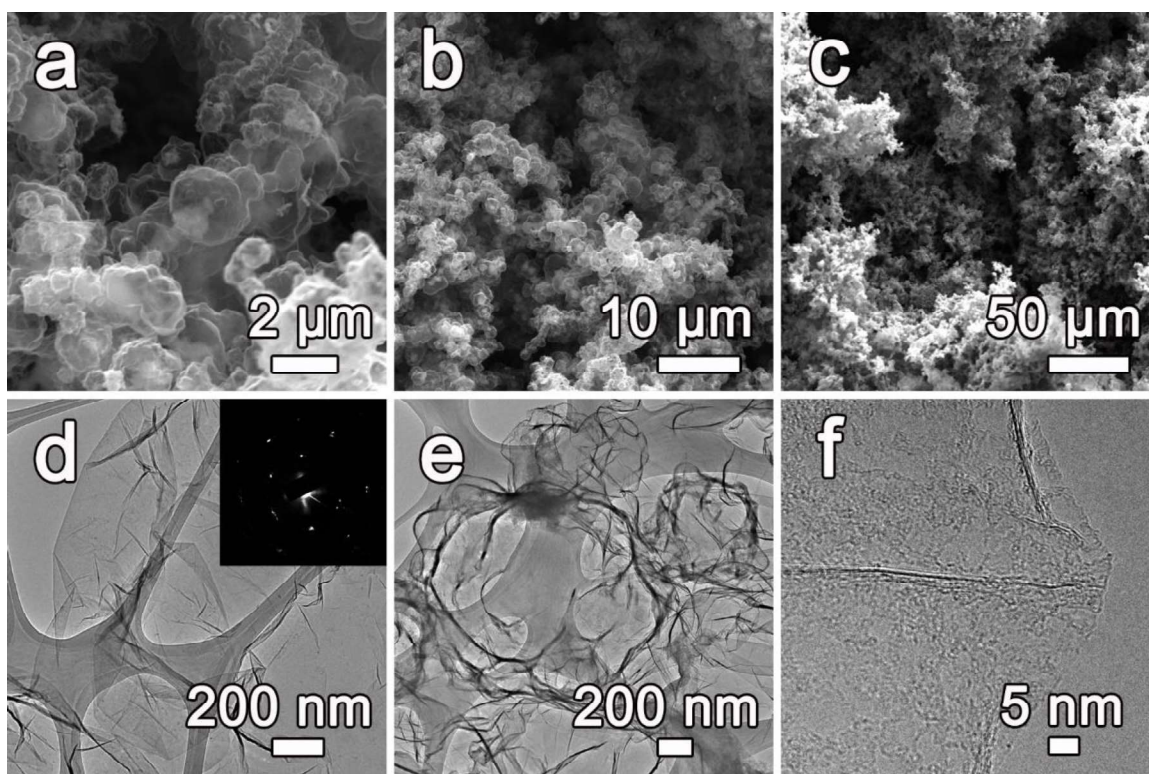


Figure 3-7. SEM and TEM images of 3D printed GFs after removing Ni. (a-c) SEM images and (d-f) TEM images of 3D printed GFs after removing Ni scaffolds prepared using 100P and 2S in a H₂ atmosphere. The inset in (d) is the SAED pattern.

The crystalline quality, elemental composition, phases, and purity of the 3D printed GFs were further investigated by Raman, X-ray photoelectron spectroscopy (XPS), X-ray diffraction (XRD), and thermogravimetric analyses (TGA), as shown in **Figure 3-8**. Similar to the spectra in **Figure 3-6**, typical D ($\sim 1350\text{ cm}^{-1}$), G ($\sim 1580\text{ cm}^{-1}$) and 2D ($\sim 2670\text{ cm}^{-1}$) bands can be detected by Raman with a 633 nm laser, shown in **Figure 3-8a**. The I_D/I_G ratio of the purified GFs was 0.44, indicating a high quality of the 3D printed GFs. The I_G/I_{2D} ratio of 2.28 is indicative of multi-layered graphene,^{1, 31, 140, 141} which should contribute to the good mechanical properties of

the 3D printed GFs. The 2D bands at $\sim 2670\text{ cm}^{-1}$ demonstrate that the content of the 3D printed GFs is indeed graphene, rather than graphite.⁵⁶ The C 1s peak (284.5 eV) in the XPS elemental spectra, as shown in **Figure 3-8b**, indicates the material is graphene or graphite.^{1, 31, 70} Small amounts of Fe impurities (C 1s: 76.7 at%; O 1s: 23.0 at%; Fe 2p3: 0.3 at%.) are also detected by XPS, which came from the FeCl₃ etching solution and can be further removed with additional treatment if necessary.¹³² The XRD patterns in **Figure 3-8c** also indicate the low content of impurities in the 3D printed GFs. No obvious Ni peaks are detected, and most of the peaks match well with the expected peaks of a multi-layered graphene phase.^{132, 133, 144} An additional small peak at $\sim 35^\circ$ is also detected (as shown in **Figure 3-8c**). The small peak could be attributed to Fe₂O₃,¹⁴⁵ arising from the FeCl₃ etching solution. The Fe contamination could be eliminated by using HCl as the etching reagent instead. TGA testing was performed in air from room temperature to 900°C, as shown in **Figure 3-8d**. Only $\sim 1.9\text{ wt\%}$ remained after testing, demonstrating that the Ni scaffolds and Fe etching residues were almost completely removed by the etching process. However, the rapid weight drop before $\sim 480^\circ\text{C}$ indicates the existence of amorphous carbon and unreacted sucrose, since the laser rastering process could still be too fast to completely convert the carbon from sucrose into graphene.

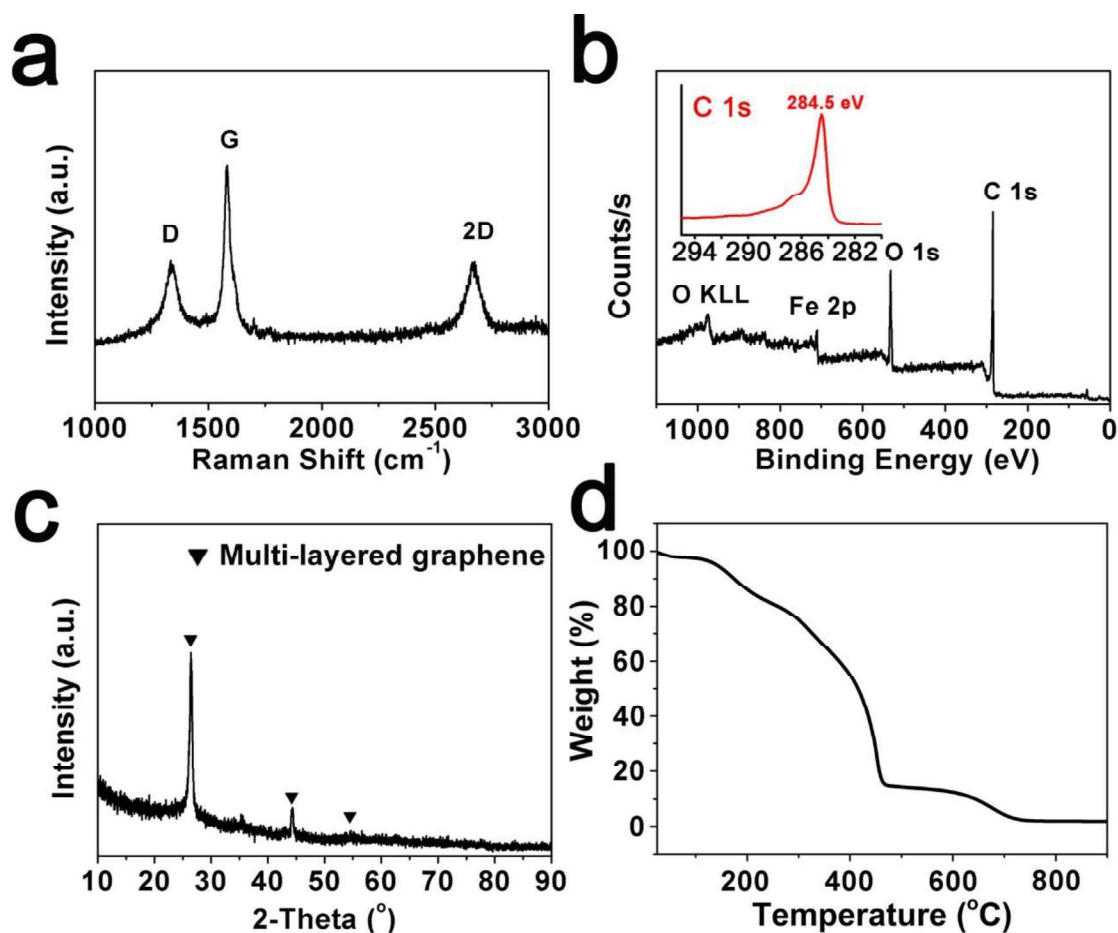


Figure 3-8. Additional characterizations for the 3D GF.

(a) Raman spectrum, (b) XPS curves with inset elemental scanning result of C 1s peak, (c) XRD pattern, and (d) TGA curve of 3D printed GFs after removing Ni prepared using 100P and 2S in a H_2 atmosphere.

The conductivity of 3D printed GFs was tested, as shown in **Figure 3-9a**. Pt contact pads ($250\ \mu\text{m} \times 250\ \mu\text{m}$) were deposited directly onto the surface of 3D printed GFs using a shadow mask evaporation method. The distance between the contact pads is $120\ \mu\text{m}$. **Figure 3-9b** shows the room temperature conductivity of

3D printed GFs. **Figure 3-9c** indicates the ohmic contact between the Pt pads and the 3D printed GFs. The average electrical conductivity of the 3D printed GFs is $\sigma = I \cdot \ell / V \cdot A = 8.7 \pm 1.8 \text{ S cm}^{-1}$, where I , ℓ , V , and A is the measured current, channel length, applied voltage, and cross-sectional area of 3D printed GFs, respectively. This value was comparable but lower than that of 3D GFs (13.8 S cm^{-1}) prepared using powder metallurgy templates and other methods.^{127, 129, 146-151} Although the high quality and multi-layered graphene features as demonstrated in **Figure 3-8** indicate that the 3D printed GFs should possess high electrical conductivity, since the 3D printed GFs were prepared from loose powder rather than a hydraulic cold-pressing process, the resulting GFs have a relatively lower density, high porosity structure with low conductivity. The 3D printed GFs were quite soft, so it was difficult to avoid damaging the Pt contact pads when touched by the probe tips during testing, which would also lead to a lower conductivity value. However, the conductivity of the foamed GFs structure might be further improved by introducing CNTs to prepare 3D printed rebar GFs, which can also make the GFs mechanically stronger, as demonstrated in our previous work.^{31, 133}

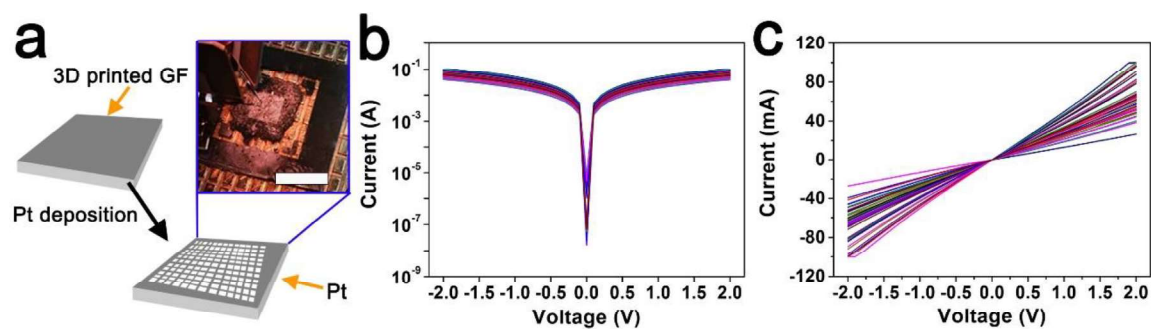


Figure 3-9. Electrical testing for 3D GF.

(a) Schematic diagram of electrical conductivity testing. The scale bar is 1 cm. (b) Current–voltage curves (I vs V) in semilogarithmic scale and (c) linear scale of 3D printed GFs after removing Ni, prepared using 100P and 2S in a H₂ atmosphere.

To further investigate the mechanical properties of the 3D printed GFs, dynamic mechanical analysis (DMA) testing was carried out under a constant frequency of 1 Hz with an amplitude of 20 μm (fixed displacement) up to 70000 cycles at room temperature. As shown in **Figure 3-10a**, the storage modulus of 3D printed GFs is ~ 11 kPa, which is comparable with 3D GFs prepared by powder metallurgy templates and other methods.^{133, 141, 142} After testing for 70000 cycles, no collapse was detected, indicating a good structural stability of the 3D printed GFs. The room temperature damping capacity of 3D printed GFs was calculated using **Equation 3-2**:

$$\text{Tan}\delta = \text{loss modulus}/\text{storage modulus}$$

Equation 3-2. Calculation for damping capacity.

where Tanδ is the damping capacity of the sample. As shown in **Figure 3-10b**, the damping capacity of the 3D printed GFs is 0.13 to 0.06, which is comparable with values reported previously, as listed in **Table 3-1**. The damping capacity of 3D printed GFs is also comparable to that of some foamed metal materials. Moreover, this 3D printing method reported here is much easier and faster than other reported

3D GF preparation methods,^{127-133, 142} and there is no requirement for a high-temperature furnace or long growth process.

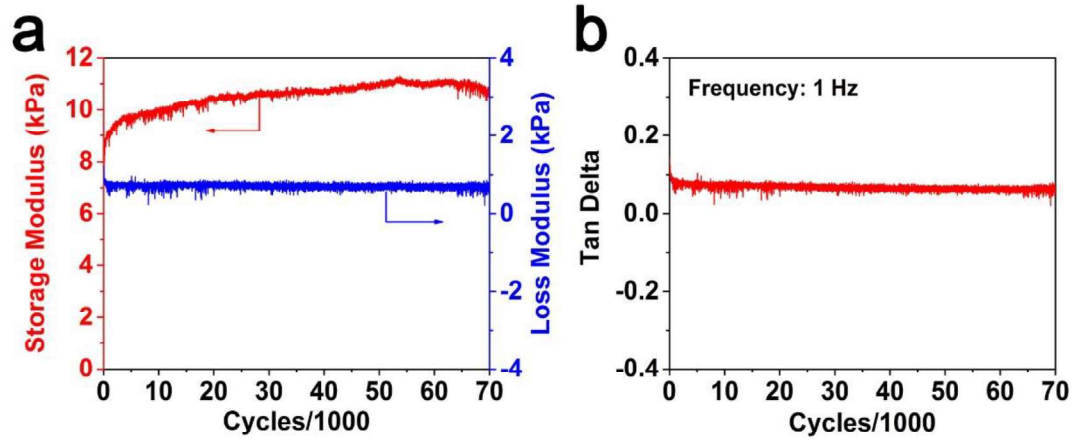


Figure 3-10. Mechanical properties of 3D GF.

DMA results of as-prepared 3D printed GF after removing Ni prepared using 100P and 2S in a H₂ atmosphere: (a) storage modulus and loss modulus, and (b) damping capacity at room temperature. The frequency of testing is 1 Hz.

Materials	Damping capacity	Reference
3D printed GF	0.13 - 0.06	126
3D GF	0.19	133
3D rebar GF with 10 wt% of CNTs	0.13	133
3D rebar GF with 18 wt% of CNTs	0.07	133
Graphene sponge	~ 0.04	142
CNTs/GO aerogels	~ 0.05-0.1	141
20 vol% SiC reinforced A365 Al alloy	0.034-0.04	151
Pure Al foam	0.022	152
CNTs reinforced 2024Al alloy	~ 0.005	153

Table 3-1. Room temperature damping capacities reported in the literature.

The untreated sucrose coated Ni particles were analyzed by SEM, as shown in **Figure 3-11a-b**. The Ni particles were aggregated, with sucrose apparently acting as

a binder. The charging effect was observed during SEM operation, indicating the low conductivity of the Ni/sucrose mixture. The sucrose on the surface was detected by Raman spectroscopy, as shown in **Figure 3-11c**.

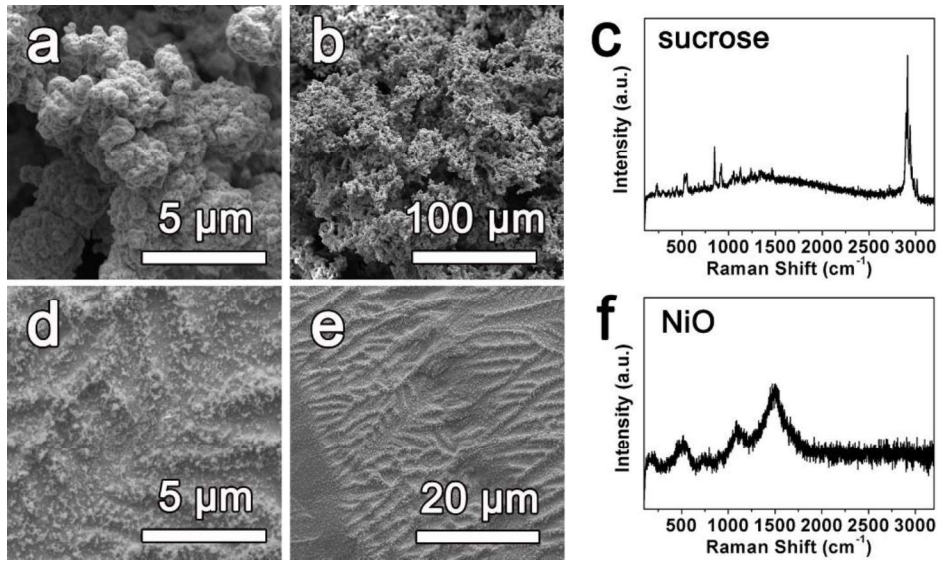


Figure 3-11. Additional control experiments.

(a-b) SEM images and (c) Raman spectrum of Ni/sucrose mixture without laser treatment, and (d-e) SEM images and (f) Raman spectrum of the sample prepared using 100P and 2S in air.

The 3D printing process was performed in air using a laser duty cycle of 100P and rastering speed of 2S. As shown in **Figure 3-11d-e**, a large number of particles are observed on the surface of the sintered Ni scaffolds, and little or no graphene was present. The Raman spectrum in **Figure 3-11f** displays NiO_x signals, and no graphene-based D, G, or 2D bands. It is presumed that the sucrose was burned away by the laser in air; the Raman analysis shows the Ni was oxidized.

Based on this result, the laser reaction should be done in an inert or reducing (H_2) atmosphere.

We tried synthesizing 3D GFs using a commercial automated 3D metal printer (Concept Laser, Mlab) at Qualified Rapid Products Company. The 3D metal printer was equipped with a $1.06\ \mu\text{m}$ fiber laser system. The samples were printed under a N_2 -flushed atmosphere. As shown in **Figure 3-12a**, a $1\ \text{cm} \times 1\ \text{cm} \times 1\ \text{cm}$ product was obtained. However, the SEM images (**Figure 3-12b,c**) indicate the lack of graphitic structures and the presence of what is assumed to be unconverted sucrose. Ni particles, rather than sintered Ni scaffolds, were observed. We presume the sucrose melted under the high heat conditions and acted as a binder in the cubic sample, instead of decomposing. The Raman spectrum in **Figure 3-12d** shows no graphene. This result indicates that the use of a $10.6\ \mu\text{m}$ CO_2 laser is necessary to make 3D GFs, while the $1.06\ \mu\text{m}$ fiber laser is not absorbed by the Ni and sucrose mixture in accordance with the absorption data in **Figure 3-2**.

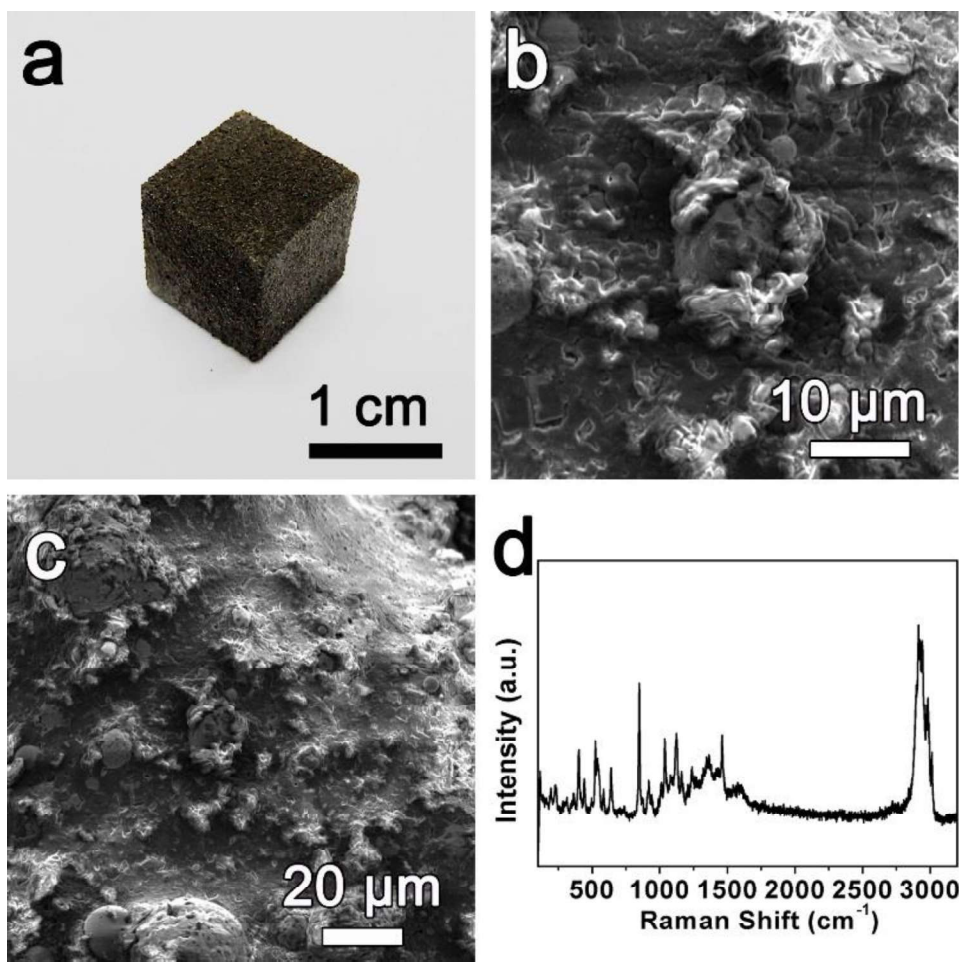


Figure 3-12. 3D printed sample with fiber laser.

(a) Photograph, (b-c) SEM images, and (d) Raman spectrum of a 3D printed sample prepared using the same mixture of Ni and sucrose but with a commercial fiber laser 3D metal printer at 20 W of power and 100 cm/s rastering speed in a N₂-flushed atmosphere.

3.2.3. Conclusion

An automated powder-bed 3D printing method for *in situ* synthesis of free-standing 3D GFs has been successfully modelled by manually feeding layer-by-layer a mixture of Ni and sucrose powder, with each layer treated by CO₂ laser. The 3D

printed GFs have a large porosity of $\sim 99.3\%$ and very low density of $\sim 0.015 \text{ g cm}^{-3}$, and contain high quality multi-layered graphene. The 3D printed GFs also have a remarkable storage modulus of $\sim 11 \text{ kPa}$, as well as high room temperature damping capacity of ~ 0.06 , comparable to GFs made using other processes. This simple and efficient method for 3D printing of GFs negates the need for cold-press molds or high temperature CVD treatment. In addition, by using carbon precursors other than sucrose, various 3D carbon composite materials including 3D printed rebar graphene and N-/S- doped graphene foam could be produced. The 3D GFs prepared by this method show promising applications in fields requiring rapid prototyping and manufacturing of 3D carbon materials, energy storage devices, damping materials, and sound absorption.

3.3. Experimental Contributions

Yilun Li designed part of the experiments, prepared the majority of the samples, and conducted part of the characterizations including SEM, Raman, BET, etc. **Junwei Sha** designed part of the experiments, prepared the part of the samples, and conducted part of the characterizations including TEM, TGA, XPS, XRD, etc.

Chapter 4

Porous Carbon for CO₂ Capture

This chapter was entirely copied from reference.¹⁵⁴

4.1. Introduction

Natural gas is a major source of fuel that serves to meet the world's rapidly growing demand for electrical power. However, natural gas wells contain significant amounts of carbon dioxide (CO₂), a component generally vented to the atmosphere after gas purification, which contributes to global climate change.^{155, 156} Thus, it is important to efficiently separate CO₂ from high pressure natural gas in order to reduce the concentration of atmospheric CO₂, and to pursue the "green carbon" approach.¹⁵⁷⁻¹⁵⁹ Various technologies and materials have been developed to separate CO₂ from natural gas in a sorption process.¹⁶⁰⁻¹⁶⁴ Although aqueous amine-based solutions are commonly used for CO₂ capture, they are corrosive, there is the

loss of sorbent with amine degradation, high energy is required for sorbent regeneration, and there is a large space requirement that cannot be used offshore.^{162, 164} The less developed solid-state sorbents such as porous carbons,¹⁶⁵⁻¹⁷² zeolites,¹⁷³ metal organic frameworks (MOFs),¹⁷⁴⁻¹⁷⁶ and functionalized porous silica¹⁷⁷⁻¹⁸⁰ have also shown potential as alternative materials for CO₂ sorption, having advantages such as low energy regeneration requirements, high capacity and selectivity, non-corrosive nature, and easier handling. The use of solid state sorbents in pressure swing processes could make them more efficient in CO₂ capture due to their high thermal and chemical stability, low heat capacities and fast sorption-desorption kinetics.^{181, 182}

Among the family of solid state CO₂ sorbents, meso- and microporous carbon materials have superior features such as high surface area, a metal-free framework, efficient CO₂ uptake at high pressure, and the wide variety of carbon sources available.^{160, 161, 163} Compared to porous carbon sorbents made from synthetic polymer precursors,^{165, 167, 169} directly using natural products as the feedstock for activation could significantly simplify the manufacturing process, and thus make it cost-efficient at the industrial production level.^{166, 168, 170-172} Recently, we reported that porous carbon materials synthesized from natural asphalt, designated A-rNPC, showed an absolute CO₂ uptake of 26 mmol g⁻¹ (1.14 g g⁻¹) at 30 bar and 23 °C; 30 bar is the estimated CO₂ partial pressure at natural gas well heads.¹⁶⁸ Unfortunately, specialty asphalt Versatrol-HT was the only feedstock that yielded porous carbons with such good CO₂ uptake performance after KOH activation. Thus, the use of an

alternative raw material that gives high surface area porous carbon sorbent with similar performance, especially at high pressure, would be advantageous, especially if it were a renewable natural source.

Biochar, an alternative natural carbon source, can be easily prepared from low-cost or negative-cost biomass through a pyrolysis process at 200 to 900 °C with limited oxygen exposure.¹⁸³⁻¹⁸⁵ Biomass includes agricultural crops, crop residues, grass, wood, animal litter, dairy manure, and other solid biologic wastes. The biomass is abundant and the producers are sometimes forced to pay for their disposal, rendering it a negative-cost material. Thus, the use of biochar as the raw material for the synthesis of porous carbon as CO₂ sorbents would be both economically efficient and environmentally helpful. Although biosources have been used to prepare porous carbons for CO₂ capture,^{166, 170-172} the CO₂ uptake performances were usually evaluated only at the low pressure of 1 bar. Moreover, the biosources were usually directly activated without pyrolysis into biochar, and studies on how different types of biochar could yield porous carbon sorbents with different properties are limited.

In **Chapter 4**, we demonstrate a one-step synthesis of biochar-derived porous carbon (B-PC) for high pressure CO₂ capture. A variety of activation conditions have been studied regarding physical properties and CO₂ uptake performances of B-PC. An absolute CO₂ uptake of 26.0 mmol g⁻¹ (1.15 g g⁻¹) at 30 bar and 25 °C was achieved from mesquite biochar (pyrolyzed at 450 °C) using the optimized KOH amount and activation temperature, with a BET surface area as high

as 3167 m² g⁻¹. In addition, biochar made from various biosources activated at different pyrolysis temperatures was evaluated based on the CO₂ uptake values of the synthesized B-PCs. Wood wastes pyrolyzed at 450 °C are the most promising type of biochar for the synthesis of high performance B-PC sorbents for CO₂ capture at high pressure.

4.2. Biochar as a Renewable Source for High-Performance CO₂ Sorbent

4.2.1. Experimental Section

Synthesis of biochar. Novus pallet scrap biochar was synthesized by Novus Wood Group using an industrial gasifier at 450 to 550 °C for ~ 8 min. Other biochar was synthesized using a published procedure.¹⁸⁵ Typically, the biosources were pyrolyzed at 450 °C for 4 h with restricted O₂ exposure.

Synthesis of B-PC. 0.50 g of mesquite biochar (pyrolyzed at 450 °C) and 2.50 g of KOH were well-mixed using a mortar and pestle, and the solid was heated from room temperature to 800 °C at a rate of 25 °C min⁻¹ in a tube furnace under an Ar flow rate of 500 sccm at 1 atm; the intermediate was then activated by holding at 800 °C at 1 atm under 500 sccm Ar for 45 min before being allowed to cool to room temperature. The solid product was then washed with 200 mL of DI water (3×) and dried at 120 °C for 12 h to yield 0.20 g of B-PC. Biochar pyrolyzed from other sources at different temperatures were also used to synthesize B-PC.

Volumetric sorption. Volumetric sorption measurements of CO₂ or CH₄ were carried out in an automated Sievert instrument (Setaram PCTPro).^{167, 168} Typically, ~ 120 mg of sorbent was placed in a stainless steel sample cell and pretreated at 150 °C for 2 h under vacuum (~ 20 mTorr). The sample volume was calibrated by He (absorption at ~ 3 bar, desorption at ~ 1 bar, 23 °C) before the sorption measurement. Excess gas uptake data was acquired from the sorption measurements.

Gravimetric sorption. Gravimetric sorption measurements of CO₂ were carried out in a Rubotherm magnetic suspension balance (Rubotherm, Germany).¹⁶⁸ A blank test without sample was used to measure the weight and volume of the sample holder. For a typical CO₂ uptake measurement, ~ 120 mg of sorbent was placed in the sample holder and pretreated at 120 °C for 4 h under vacuum (~ 20 mTorr). A buoyancy test with He (absorption from 0 to 50 bar, 25 °C) was used to measure the sample weight and volume before the sorption measurement, and the density of the sample is calculated from the measured weight and volume from the buoyancy test. Excess gas uptake data was acquired from the sorption measurements.

Calculation of absolute gas uptake. Absolute gas uptakes were calculated as:

$$\text{absolute gas uptake} = \text{excess gas uptake} + \text{total pore volume} \times \text{gas density}$$

Equation 4-1. Calculation of absolute gas uptake.^{167, 168, 186}

Detailed explanations are shown in **Figure 4-1**.

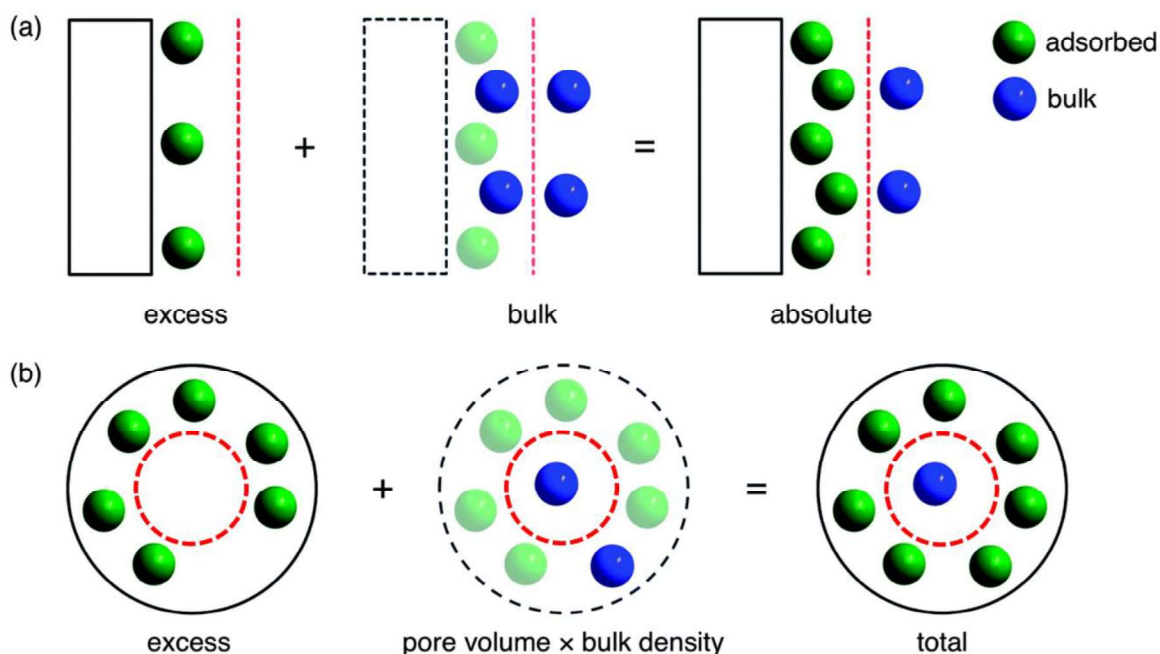


Figure 4-1. Calculation of absolute gas uptake.

(a) Pictorial description of excess and absolute gas uptake on a two-dimensional surface. The red dashed line indicates the Gibbs dividing surface that separates the free volume into two regions in which gas molecules are either in an adsorbed (green) or bulk state (blue). Absolute adsorption includes all gas in the adsorbed state, equals the experimentally measured excess uptake plus the bulk gas molecules that would have been present in the adsorbed region in the absence of a surface; the absolute uptake is colored in green in the third part on the far right. **(b) For porous materials, total gas uptake includes all gas molecules in the adsorbed state, which is the sum of the experimentally measured excess uptake and the bulk gas molecules within the pore volume.** For microporous materials with negligible external surface area, total gas uptake is often used as an approximation for absolute uptake: $\text{absolute uptake} \approx \text{total uptake} = \text{excess uptake} + \text{total pore volume} \times \text{gas density}$, as it is hard to experimentally determine the position of the Gibbs dividing surface (red dashed circle); the absolute uptake is the green gas molecules and the total uptake is the sum of the green and blue gas molecules in the third part on the far right. This figure is adapted from reference,¹⁸⁷ published by The Royal Society of Chemistry.

Characterization. The XPS spectra were obtained on a PHI Quantera SXM scanning X-ray microprobe system using a 100 μm X-ray beam of which the take-off angle was 45° and the pass energy was 140 eV for the survey and 26 eV for the high resolution elemental analysis. The N_2 adsorption-desorption isotherms (at 77 K) were obtained using an automated BET surface analyzer (Quantachrome Autosorb-3b), and the samples were heated at 150 $^\circ\text{C}$ for 15 h under vacuum (~ 20 mTorr) before each measurement. SEM images were taken in a FEI Quanta 400 high resolution field emission scanning electron microscope. TEM images were obtained in a 2100F field emission gun transmission electron microscope.

4.2.2. Result and Discussion

The synthesis of B-PC is shown in Figure 4-2a. Biochar was synthesized by the pyrolysis of biomass using a published procedure.¹⁸⁵ The biochar was then activated with KOH in a tube furnace at elevated temperature under an inert atmosphere.^{167, 168} This activation process was performed with different biochar/KOH weight ratios and at various temperatures, where the B-PC prepared with 0.5 g mesquite biochar (pyrolyzed at 450 $^\circ\text{C}$) and 2.5 g KOH by activating at 800 $^\circ\text{C}$ was used as the optimized sample for detailed characterizations. Figure 4-2b,c shows the scanning electron microscope (SEM) images of B-PC at different scales. A wood-like macro-structure could be identified, and the combination of larger channels ($> 10 \mu\text{m}$) and smaller pores ($< 100 \text{ nm}$) could be beneficial for fast CO_2 adsorption-desorption kinetics. The amorphous nature of B-PC is shown by the transmission electron micrograph (TEM) in Figure 4-2d, where no ordered domains

could be observed, similar to other porous carbon materials with high surface areas.¹⁶⁷⁻¹⁶⁹

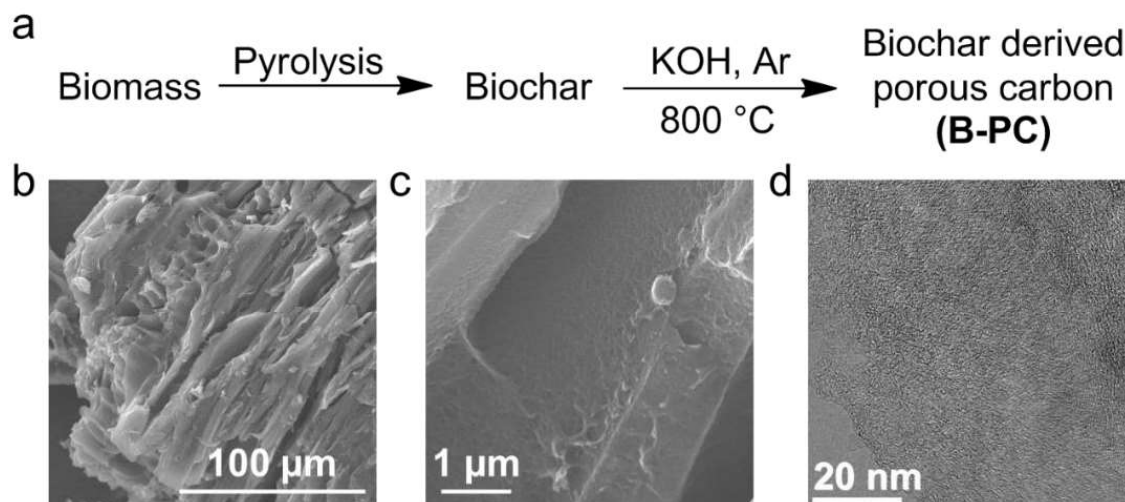


Figure 4-2. The scheme of synthesis and SEM/TEM images of B-PC.

(a) The scheme for the synthesis of B-PC. **(b,c)** SEM images of B-PC at different scales. **(d)** TEM image of B-PC. The shown B-PC sample was prepared with 0.5 g of mesquite biochar (pyrolyzed at 450 °C) and 2.5 g KOH by activation at 800 °C.

To analyze the physical properties of the B-PC prepared with different activation conditions, Brunauer–Emmett–Teller (BET) measurements have been conducted with the N₂ adsorption-desorption isotherms at 77 K shown in **Figure 4-3a**. With mesquite biochar (450 °C) as the starting material, all B-PC samples exhibit a typical type I isotherm, with a narrow knee indicated rapid N₂ uptake at low pressure range ($P/P_0 < 0.3$), a plateau that indicates limited adsorption at higher pressure range, and an absence of hysteresis between the adsorption and desorption cycles. These characteristics show that the B-PC samples prepared are

mainly microporous (< 2 nm) with limited mesopore (2 to 50 nm) generation. To further evaluate the pore size distributions of the microporous B-PC, the non-local density functional theory (NLDFT) model was applied to the N₂ isotherms in **Figure 4-3a**, and the pore size distribution curves are shown in **Figure 4-3b**. With lower activation temperature and less KOH, the pore sizes of the prepared B-PC are mostly < 2 nm with a shoulder peak at ~ 1.8 nm, resulting from the reaction between the carbon framework and the KOH reagent ($C + 6KOH \rightarrow K_2CO_3 + 3H_2O + 4K$).^{165, 169, 188} Under stronger activation conditions, however, the calculated pore size distribution curves gradually shift to larger pore sizes with an increased degree of reaction, yet the pore sizes mostly remain < 3 nm. **Figure 4-3c** shows the BET surface areas of B-PC samples calculated with the multi-point BET method at low pressure range of the N₂ isotherms; the total pore volumes (at $P/P_0 = 0.99$) and micropore volumes (cumulative pore volume by NLDFT) of the B-PC samples are plotted in **Figure 4-3d**. The highest surface area of 3167 m² g⁻¹ and near-highest micropore volume of 1.02 cm³ g⁻¹ is reached with 2.5 g KOH (per 0.5 g biochar) and an activation temperature of 800 °C. With weaker activation conditions, fewer pores are formed due to the limited activation, so that both surface area and total/micro- pore volumes are lower. With stronger activation conditions however, the overreaction between KOH and the carbon framework would expand or destroy the previously formed microporous structures, such that the total pore volume would increase but both surface area and micropore volume would decrease, as would the percentage of micropore volume relative to total pore volume.^{165, 169, 188} **Table 4-1** summaries the

physical properties and yields of the B-PC samples prepared from mesquite biochar (pyrolyzed at 450 °C) under different activation conditions, the raw mesquite biochar (pyrolyzed at 450 °C) is also listed as a reference. While the yields of B-PC also decrease with increased activation parameters, a moderate yield of 40% is recorded for the optimal B-PC sample with the highest surface area.

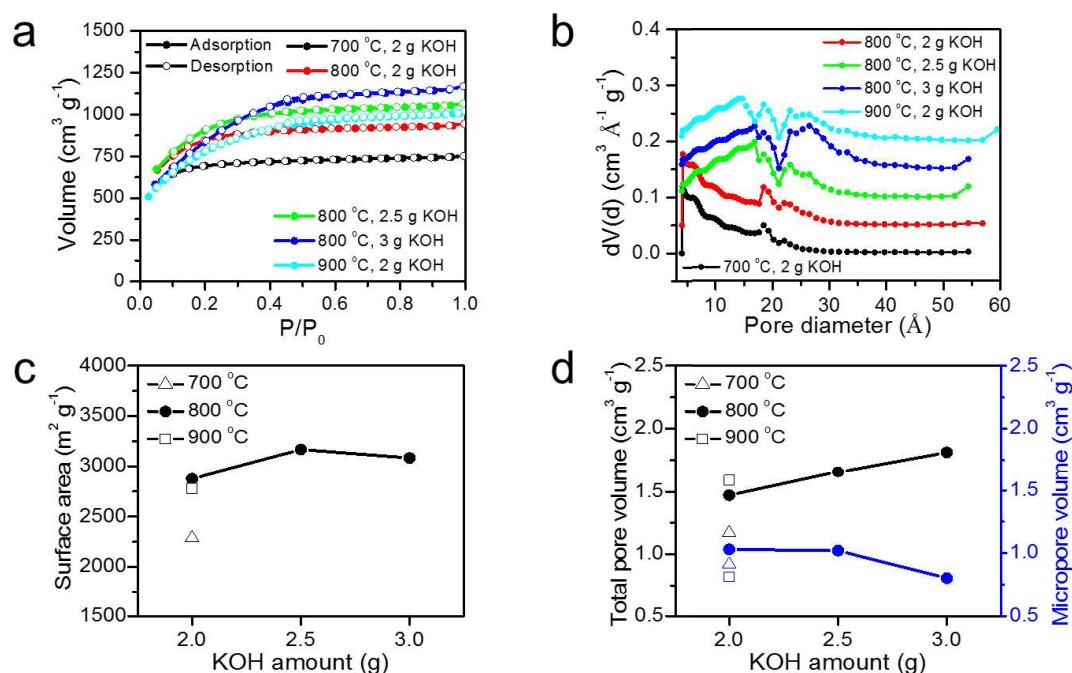


Figure 4-3. Textural properties of B-PC characterized by BET measurements. (a) N₂ adsorption-desorption isotherms (at 77 K), (b) NLDFT pore size distribution curves, offset vertically in steps of 0.05 cm³ Å⁻¹ g⁻¹ for purposes of clarity, (c) BET surface areas, and (d) total pore volumes and NLDFT micropore volumes of B-PC prepared with different activation temperatures and different KOH amounts. (b), (c), and (d) are calculated based on the N₂ isotherms in (a). All B-PC samples were prepared with mesquite biochar pyrolyzed at 450 °C.

Activation temperature	KOH ^b	Elemental content			S _{BET} ^c	V _{tot} ^d	V _{MicDFT} ^e
(°C)	(g)	C%	O%	N%	(m ² g ⁻¹)	(cm ³ g ⁻¹)	(cm ³ g ⁻¹)
700	2.0	85.0	14.5	0.5	2287	1.16	0.91 (79%)
800	2.0	86.7	12.5	0.8	2878	1.46	1.03 (70%)
800	2.5	93.2	6.8	< 0.1	3167	1.65	1.02 (62%)
800	3.0	88.7	11.1	0.2	3083	1.81	0.80 (44%)
900	2.0	85.0	15.0	< 0.1	2781	1.58	0.81 (51%)
Mesquite 450 °C ⁱ	N/A	83.6	14.8	1.6	10	0.02	0.00 (0%)
Activation temperature	KOH ^b	Density ^f	Absolute CO ₂ uptake at 3 bar ^g	Excess CO ₂ uptake at 30 bar ^g	Absolute CO ₂ uptake at 30 bar ^g		Yield ^h
(°C)	(g)	(g cm ⁻³)	(mmol g ⁻¹)	(mmol g ⁻¹)	(mmol g ⁻¹)	(g g ⁻¹)	(wt%)
700	2.0	2.12	6.9	19.3	21.0	0.92	52
800	2.0	2.50	6.7	21.8	23.9	1.05	46
800	2.5	2.44	6.5	23.6	26.0	1.15	40
800	3.0	2.62	5.7	24.1	26.7	1.18	28
900	2.0	2.55	4.5	18.2	20.5	0.90	12
Mesquite 450 °C ⁱ	N/A	N/A	N/A	3.2	3.2	0.14	N/A

Table 4-1. Summary of B-PC synthesized under different activation conditions^a.

^aAll samples were made with mesquite biochar (pyrolyzed at 450 °C).

^bAmount of KOH per 0.5 g biochar. ^cCalculated in the low pressure range of the N₂ isotherms with the multi-point BET method. ^dTotal pore volume at P/P₀ = 0.99. ^eMicropore volume (< 2 nm) calculated by cumulative pore volume with NLDFT model. The values in parentheses are the percentages of micropore volume relative to total pore volume. ^fDensity calculated from the buoyancy tests before the CO₂ sorption measurements. ^gGravimetric uptake at 25 °C. ^hThe yield of B-PC from biochar. ⁱMesquite biochar (pyrolyzed at 450 °C) without activation.

To evaluate the elemental components of the B-PC samples, X-ray photoelectron spectroscopy (XPS) measurements were conducted and the results are shown in **Table 4-1**. For the optimal sample, the C/O/N contents are recorded

as 93.2%, 6.8%, < 0.1%, respectively, while the limited amounts of N for all B-PC samples should result from the fact that only 1.6% N is present in the original mesquite biochar (pyrolyzed at 450 °C) sample.

The CO₂ adsorption isotherms over the pressure range of 0 to 30 bar at 25 °C and the CO₂ uptake values at 30 bar and 25 °C of B-PC samples with different activation conditions are shown in **Figure 4-4**, and are listed in **Table 4-1**. The value of 30 bar was chosen as the upper pressure limit based on the approximation that a natural gas well-head with total pressure of 300 bar contains ~ 10% CO₂, yielding a partial pressure of CO₂ at 30 bar. From the data, it is observed that B-PC samples with weaker activation conditions and higher micropore volumes showed slightly higher CO₂ uptake at lower pressure (3 bar), similar to previous reports;^{189, 190} at higher pressure (30 bar), B-PC samples with higher surface areas/total pore volumes showed much higher absolute CO₂ uptake. This observed relationship, however, could be misleading towards the prediction of CO₂ uptake performance based on textural properties, since the calculation of absolute uptake includes the bulk phase gas molecules within the free space inside the larger pores (as part of the total pore volume, illustrated in **Figure 4-1**), while the free gas is not actually beneficial towards pressure-swing operations.

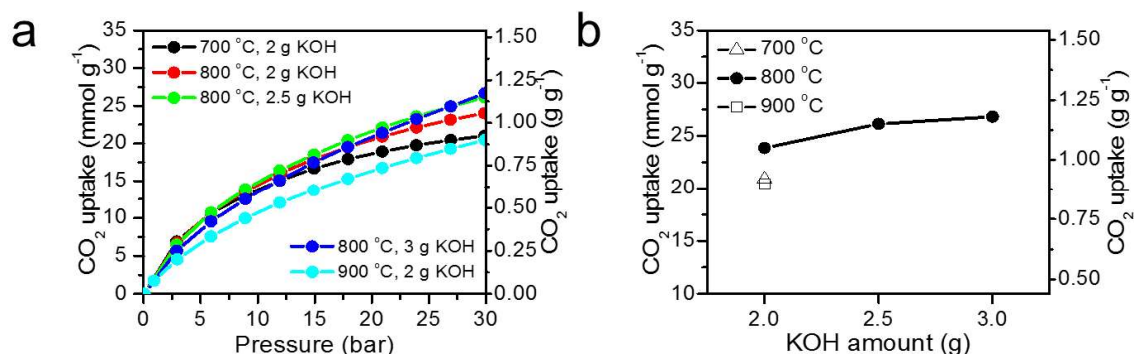


Figure 4-4. CO₂ uptake properties of B-PC.

(a) Absolute gravimetric CO₂ uptake isotherms at 25 °C and (b) absolute gravimetric CO₂ uptake values at 30 bar, 25 °C, of B-PC prepared under different activation temperatures and different KOH amounts. All B-PC samples were prepared with mesquite biochar that was pyrolyzed at 450 °C.

To better assess the contribution of surface area and pore volume towards high pressure operations, **Table 4-2** summarizes the detailed pore volumes of different pore sizes together with excess CO₂ uptake at 30 bar, as the excess uptake excludes the free-gases from the calculation; the relationship between excess CO₂ uptake and various parameters are plotted in **Figure 4-5**. Among the five parameters plotted, the better correlations are found with surface area and pore volume for pores between 1 and 3 nm, although a small variance is observed for the B-PC sample activated at 900 °C. The increase of volume in small pores (< 1 nm) or larger pores (> 3 nm) has little or no influence on the excess uptake values. These findings are in good agreement with literature reports where larger micropores/small mesopores together with apparent surface area are more crucial when designing porous carbon materials for high pressure operations.^{169, 191}

Activation temperature	KOH	S_{BET}	V_{tol}	$V_{<1\text{nm}}^{\text{b}}$	$V_{1-3\text{nm}}^{\text{c}}$	$V_{>3\text{nm}}^{\text{d}}$	Excess CO_2 uptake at 30 bar
(°C)	(g)	($\text{m}^2 \text{g}^{-1}$)	($\text{cm}^3 \text{g}^{-1}$)	($\text{cm}^3 \text{g}^{-1}$)	($\text{cm}^3 \text{g}^{-1}$)	($\text{cm}^3 \text{g}^{-1}$)	(mmol g^{-1})
700	2.0	2287	1.16	0.51	0.51	0.14	19.3
800	2.0	2878	1.46	0.56	0.71	0.19	21.8
800	2.5	3167	1.65	0.26	1.12	0.27	23.6
800	3.0	3083	1.81	0.20	1.13	0.49	24.1
900	2.0	2781	1.58	0.23	0.58	0.77	18.2

Table 4-2. Detailed pore volumes of B-PC synthesized under different activation conditions^a.

^aAll samples were made with mesquite biochar (pyrolyzed at 450 °C).

^{b,c,d}Calculated by cumulative pore volume with the NLDFT model.

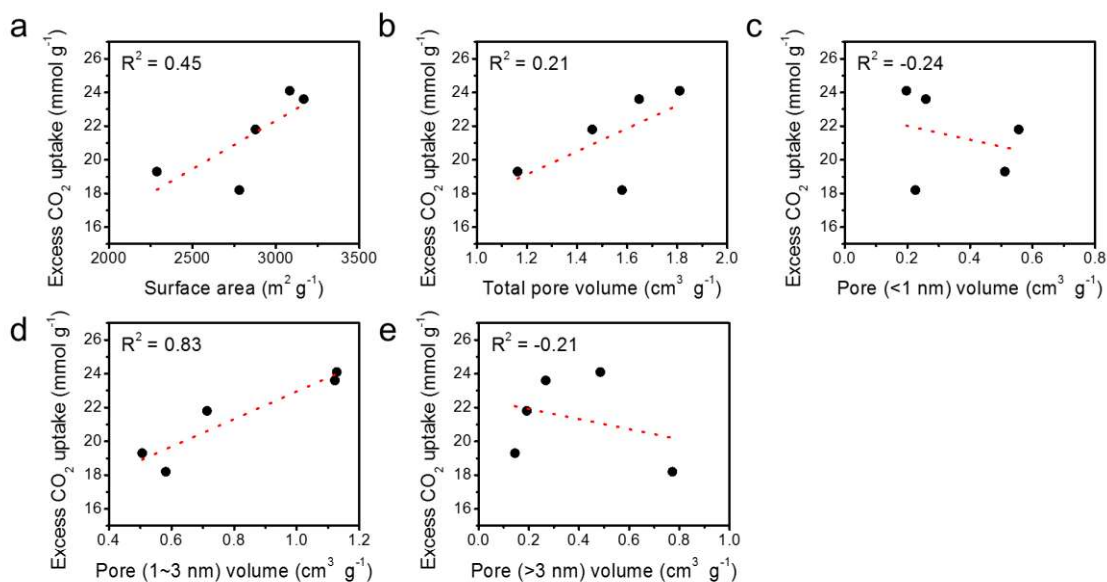


Figure 4-5. Relationship between excess CO_2 uptake and different textural properties.

(a) surface area, (b) total pore volume, (c) pore volume for pores < 1 nm, (d) pore volume for pores between 1 and 3 nm, and (e) pore volume for pores > 3 nm. The dashed red lines and R^2 show the results from linear fitting. The data points shown here are from Table 4-2.

Among the different activation conditions discussed above, the optimized B-PC sample (2.5 g KOH per 0.5 g mesquite biochar 450 °C, 800 °C activation) shows an absolute gravimetric CO₂ uptake of 26.0 mmol g⁻¹ (1.15 g g⁻¹) at 30 bar/25 °C, with a yield of 40% from biochar to B-PC. This uptake performance exceeds the CO₂ adsorption capacity of commercial activated carbon (Darco KB-G) and the previously reported polymer-derived SPC¹⁶⁷ and A-PC¹⁶⁸, and is similar to the values for A-rNPC,¹⁶⁸ polymer-derived CPC,¹⁶⁹ and MOF NU-1000.¹⁷⁵ A detailed comparison between B-PC and other porous carbons is shown in **Table 4-3**, where B-PC is the only material that could be directly prepared from a renewable biosource using one-step activation with absolute CO₂ uptake values higher than 25 mmol g⁻¹ at 30 bar and 25 °C.

Samples	S _{BET} (m ² g ⁻¹)	V _{tol} (cm ³ g ⁻¹)	Density ^c (g cm ⁻³)	Yield (%)	Absolute CO ₂ uptake at 30 bar	
					(mmol g ⁻¹)	(g g ⁻¹)
B-PC	3167 ^a	1.65 ^b	2.44	40 ^d	26.0 ^e	1.15 ^e
Activated carbon (Darco KB-G)	1526 ^a	1.55 ^b	2.09	N/A	13.6 ^e	0.60 ^e
A-PC ¹⁶⁸	2780	1.17	1.78	44	21.1 ^f	0.93 ^f
A-rNPC ¹⁶⁸	2580	1.09	2.10	34	26.0 ^f	1.14 ^f
SPC ¹⁶⁷	2500	1.01	2.21	48	18.4 ^f	0.81 ^f
CPC ¹⁶⁹	3242	1.51	N/A	36	25.7 ^g	1.13 ^g
NU-1000 ¹⁷⁵	4020	1.53	N/A	N/A	26.2 ^e	1.15 ^e

Table 4-3. Summary of CO₂ uptakes from B-PC and other porous carbons.

^aCalculated in the low pressure range of the N₂ isotherms with the multi-point BET method. ^bTotal pore volume at P/P₀ = 0.99. ^cDensity calculated from the buoyancy test before the sorption measurements. ^dThe yield of B-PC from biochar. The B-PC sample was prepared with 0.5 g of mesquite biochar (pyrolyzed at 450 °C) and 2.5 g KOH by activation at 800 °C. ^eGravimetric uptake at 25 °C. ^fVolumetric uptake at 23 °C. ^gVolumetric uptake at 25 °C.

To further characterize the CO₂ uptake performance of the optimized B-PC sample (2.5 g KOH per 0.5 g mesquite biochar 450 °C, 800 °C activation), 10 cycles of CO₂ adsorption-desorption at 23 °C were recorded in **Figure 4-6a** with the volumetric uptake instrument; the overlapping of the cycling curves shows the reversible CO₂ uptake by B-PC. **Figure 4-6b** shows the excess CO₂ uptake values at 30 bar for each cycle; the absence of performance degradation suggests the excellent stability of B-PC as a solid state CO₂ sorbent. The correlation between excess volumetric uptake and excess gravimetric uptake is shown in **Figure 4-7**; the difference between the two measuring methods is negligible considering the difference in uptake temperatures.¹⁶⁸ In general, the observed good stability and high CO₂ uptake values for B-PC should allow the pressure-swing adsorption/desorption operation for CO₂ capture from high pressure natural gas wells.

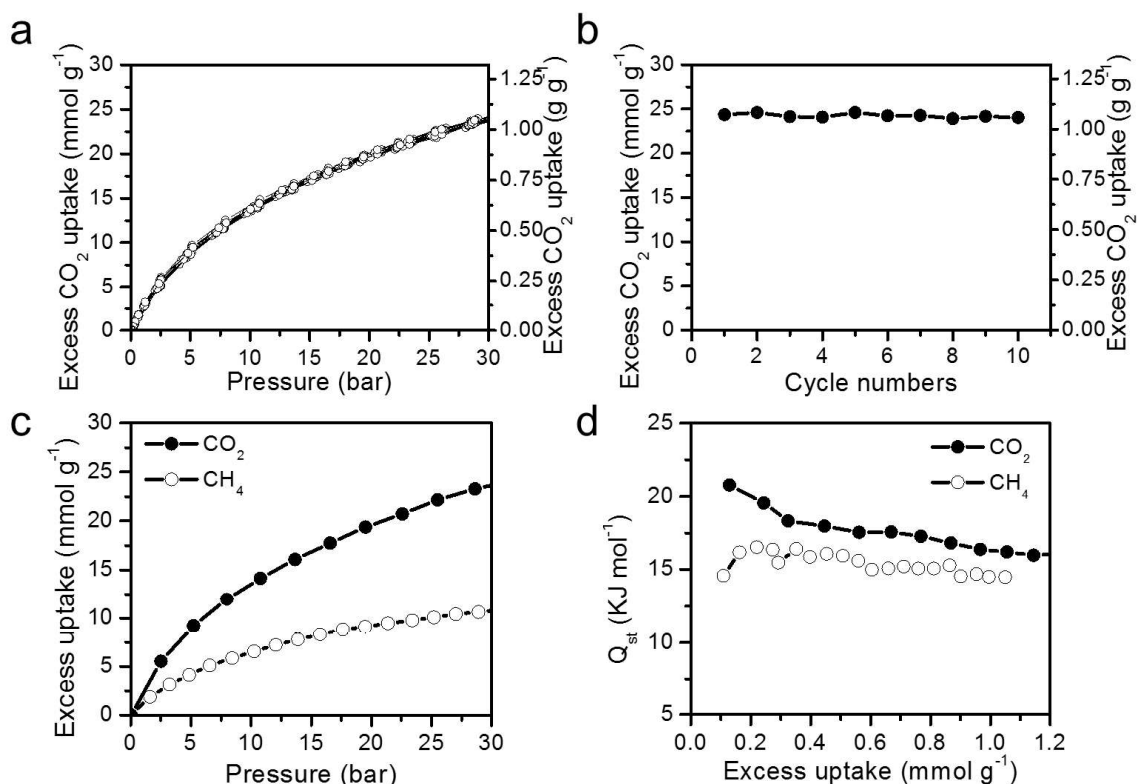


Figure 4-6. Additional CO_2 uptake properties of B-PC.

(a) Excess volumetric CO_2 uptake isotherm (at 23 °C) for B-PC with 10 adsorption-desorption cycles. **(b)** Excess volumetric CO_2 uptake values (at 30 bar, 23 °C) of B-PC for 10 cycles shown in (a). **(c)** Excess volumetric uptake isotherms of CO_2 and CH_4 for B-PC at 23 °C. **(d)** Heat of sorption of CO_2 and CH_4 for B-PC calculated at 23 °C and 40 °C. The tested B-PC sample was prepared with 0.5 g of mesquite biochar (pyrolyzed at 450 °C) and 2.5 g KOH by activation at 800 °C.

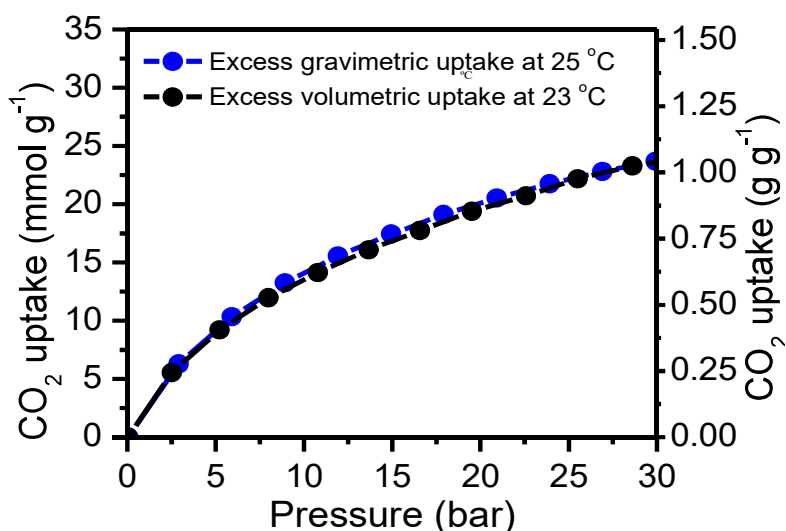


Figure 4-7. Comparison of excess gravimetric (25 °C) and volumetric (23 °C) CO₂ uptake for B-PC.

The tested B-PC sample was made with 0.5 g of mesquite biochar (pyrolyzed 450 °C) and 2.5 g KOH by activation at 800 °C.

An important factor when judging the performance of solid CO₂ sorbent is the selectivity of CO₂ over CH₄. In accordance with our previous reports, CO₂:CH₄ selectivity here is defined as the molar ratios of adsorbed CO₂ and CH₄ at the pressure of 30 bar.^{167, 168} **Figure 4-6c** shows the excess volumetric uptake of CO₂ and CH₄ for the optimized B-PC sample (2.5 g KOH per 0.5 g mesquites biochar 450 °C, 800 °C activation) at the pressure range of 0 to 30 bar, where a selectivity of ~ 2.2:1 is observed at 30 bar, slightly lower than that of SPC (2.6:1)¹⁶⁷ and A-rNPC (3:1).¹⁶⁸ To further quantify the selectivity between CO₂ and CH₄ for B-PC during pressure-swing operations, we calculated the work capacities (Δ CO₂ and Δ CH₄) of B-PC between 3 bar and 30 bar in **Table 4-4**, together with the comparison with other

porous carbon materials. As is shown in **Table 4-4**, the B-PC shows a comparable CO₂ work capacity of 19.5 mmol g⁻¹ due to the high surface area and the high total pore volume; yet the ratio of ΔCO₂/ΔCH₄ (2.0) is slightly lower than that of A-rNPC,¹⁶⁸ CPC,¹⁶⁹ and NU-1000.¹⁷⁵ As N-doping or S-doping of the porous carbon framework is believed to be beneficial for CO₂/CH₄ selectivity due to the preferred Lewis acid-base interactions between CO₂ and heteroatoms,^{165, 167-169, 172} the limited selectivity here is possibly due to the absence of heteroatoms in the B-PC framework. However, the high work capacity as well as the renewable nature¹⁹² of biochar as the feedstock for porous carbon fabrication should make it a promising candidate for industrial applications.

Sample	S _{BET} (m ² g ⁻¹)	V _{tol} (cm ³ g ⁻¹)	Absolute CO ₂ uptake			Absolute CH ₄ uptake			Ratio ΔCO ₂ /ΔCH ₄
			3 bar (mmol g ⁻¹)	30 bar (mmol g ⁻¹)	ΔCO ₂ ^b (mmol g ⁻¹)	3 bar (mmol g ⁻¹)	30 bar (mmol g ⁻¹)	ΔCH ₄ ^b (mmol g ⁻¹)	
B-PC ^a	3167	1.65	6.5	26.0	19.5	3.2	12.9	9.7	2.0
Activated carbon (Darco KB-G)	1526	1.55	3.5	13.6	10.1	1.4	6.4	5.1	2.0
A-rNPC ¹⁶⁸	2580	1.09	7.7	26.0	18.3	2.7	8.6	5.9	3.1
CPC ¹⁶⁹	3242	1.51	6.1	25.7	19.6	3.1	11.9	8.8	2.2
NU-1000 ¹⁷⁵	4020	1.53	2.7	26.2	23.5	1.7	10.3	8.6	2.7

Table 4-4. Comparison of working capacity of B-PC and various porous carbons.

^aThe B-PC sample was prepared with 0.5 g of mesquite biochar (pyrolyzed at 450 °C) and 2.5 g KOH by activation at 800 °C. ^bWorking capacity of CO₂ or CH₄ (ΔCO₂ or ΔCH₄) is calculated between 3 bar and 30 bar.

Figure 4-8 shows the excess volumetric CO₂ and CH₄ uptakes of the optimized B-PC sample (2.5 g KOH per 0.5 g mesquite biochar 450 °C, 800 °C

activation) at different temperatures; similar to other reported porous carbons,¹⁶⁷⁻¹⁶⁹ the CO₂/CH₄ adsorption capacity decreases with increasing temperature. To better understand the sorbate-sorbent interactions on the surface of B-PC, the low pressure (0 to 1 bar) adsorption isotherms in **Figure 4-8c,d** were input into the Clausius-Clapeyron equation to calculate the isosteric heat of absorption (Q_{st}) of CO₂ and CH₄ at 23 °C and 40 °C.^{167, 168, 172} As shown in **Figure 4-6d**, at the lowest surface coverage or uptake, the Q_{st} of CO₂ for B-PC is calculated to be 21 kJ mol⁻¹, similar to A-PC (20 kJ mol⁻¹),¹⁶⁸ but considerably lower than N-doped A-rNPC (29 kJ mol⁻¹)¹⁶⁸ and CPC (24 kJ mol⁻¹).¹⁶⁹ Apparently, because the surface of B-PC lacks a strong Lewis acid-base interaction between CO₂ and the N nucleophilic sites, the Q_{st} of CH₄ for B-PC is calculated to be 15 kJ mol⁻¹, in a range similar to A-PC, A-rNPC, and CPC,^{168, 169} due to the lack of strong interaction between the porous carbon surface and the nonpolar CH₄. When the CO₂/CH₄ continues to fill the pores at higher uptake, the Q_{st} of CH₄ for B-PC remains almost constant, while the Q_{st} of CO₂ gradually decreases to reach the liquefaction enthalpy of CO₂ (17 kJ mol⁻¹), indicating that the CO₂ uptake mechanism is eventually shifted from sorbate-sorbent interaction towards sorbate-sorbate interaction after the complete coverage of the porous sorbent surfaces.^{168, 169, 175} The relatively weak enthalpy, a small Q_{st} , for CO₂ adsorption on B-PC when compared to other porous materials, suggests better reversible CO₂ uptake performance as well as lower energy consumption for sorbent regeneration, especially when the adsorption-desorption operations are conducted at a higher pressure range.

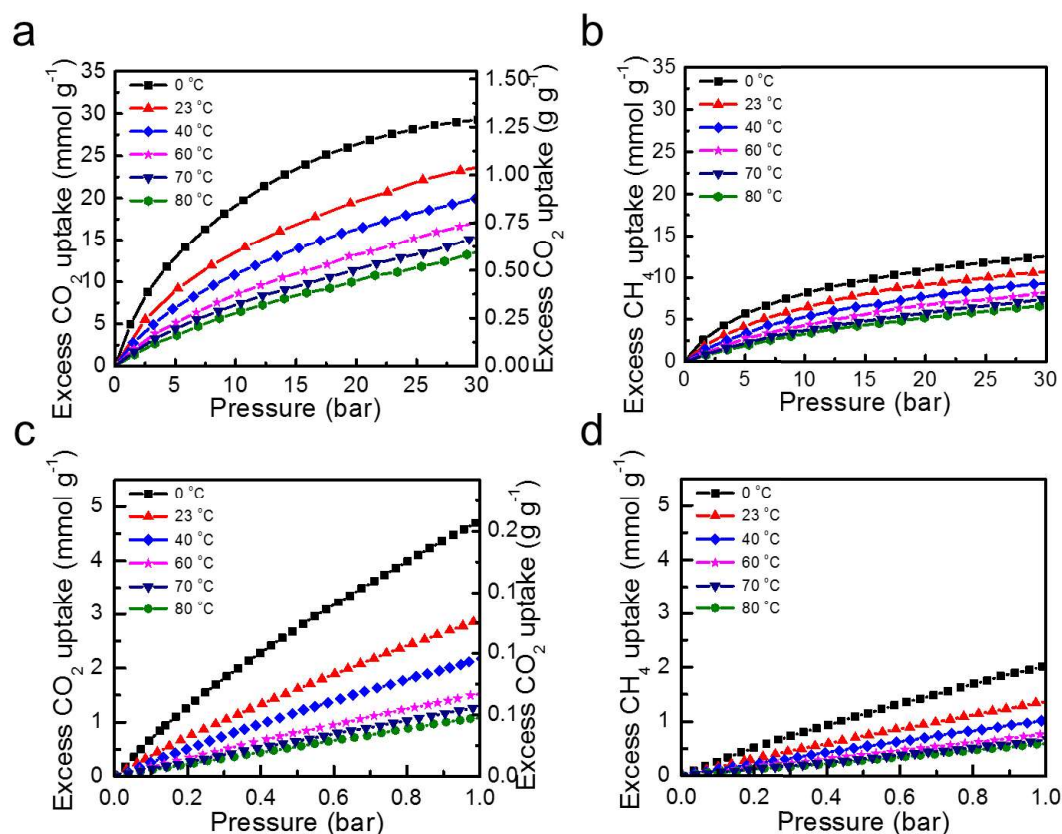


Figure 4-8. Excess CO₂ and CH₄ uptake of B-PC at different temperatures.
(a) Excess volumetric CO₂ uptake for B-PC at various temperatures (0-30 bar).
(b) Excess volumetric CH₄ uptake for B-PC at various temperatures (0-30 bar).
(c) Excess volumetric CO₂ uptake for B-PC at various temperatures (0-1 bar).
(d) Excess volumetric CH₄ uptake for B-PC at various temperatures (0-1 bar).
 The tested B-PC sample was made with 0.5 g of mesquite biochar (pyrolyzed at 450 °C) and 2.5 g KOH by activation at 800 °C.

With the optimized activation condition, B-PC synthesized from mesquite biochar, pyrolyzed at 450 °C, had a surface area of 3167 m² g⁻¹ with an absolute CO₂ uptake of 26.0 mmol g⁻¹ (1.15 g g⁻¹) at 30 bar and 25 °C. Nevertheless, as biochar may come from different sources of biomass, screenings were conducted to find an

optimal biosource to serve as the starting material for the production of CO₂ sorbents. **Figure 4-9** shows the physical properties and CO₂ uptake performances of B-PC synthesized with different types of biochar under the same activation condition (2.5 g KOH per 0.5 g biochar, 800 °C); the values are listed in **Table 4-5**. Two key parameters are considered in the comparisons: the type of biosource and the temperature of pyrolysis. When the biosource is mesquite wood, three biochar samples with different pyrolysis conditions (no pyrolysis, 450 °C, or 750 °C) were used to prepare B-PC. As shown in **Figure 4-9**, among the three pyrolysis conditions, the B-PC sample made from biochar pyrolyzed at 450 °C shows a moderate yield (40 wt%), the highest surface area (3167 m² g⁻¹), the highest pore volume (1.02 cm³ g⁻¹) and the highest CO₂ uptake (26 mmol g⁻¹) at 30 bar and 25 °C. When the pyrolysis was done at 700 °C, although the yield of the activation reaction (63 wt%) was considerably higher, the CO₂ uptake performance (13.9 mmol g⁻¹) was much lower; when the wood source was directly reacted with KOH without pyrolysis, both the yield (6 wt%) and the CO₂ uptake (6.3 mmol g⁻¹) of B-PC were significantly lower. This correlation between pyrolysis temperatures and B-PC performance could be explained by the phase transition that biochar undergoes during the pyrolysis process. According to previous studies, as the pyrolysis temperature and thus charring intensity increases, the natural plant bio-polymers lignin and cellulose gradually dehydrate and depolymerize to form an amorphous mixture of short-range ordered aliphatic and aromatic oligomers (amorphous char), while the amorphous oligomers would further fuse/condense under higher

temperatures to form long-range ordered graphene-like turbostratic crystallites or char.^{193, 194} While the amorphous char, mesquite pyrolyzed at 450 °C, tends to have the most active sites for KOH activation, the raw mesquite wood has too much volatile components to retain a porous carbon framework after reacting with KOH, thus the yield to prepare B-PC is extremely low (6 wt%). And the turbostratic char (mesquite pyrolyzed at 750 °C) has already lost the active sites as well as the smaller pores so that the yield to prepare B-PC is higher (63 wt%), but both surface area (1539 m² g⁻¹) and total pore volume (0.78 cm³ g⁻¹) are significantly lower than those of B-PC prepared from mesquite wood charred at the mid-range temperature of 450 °C.

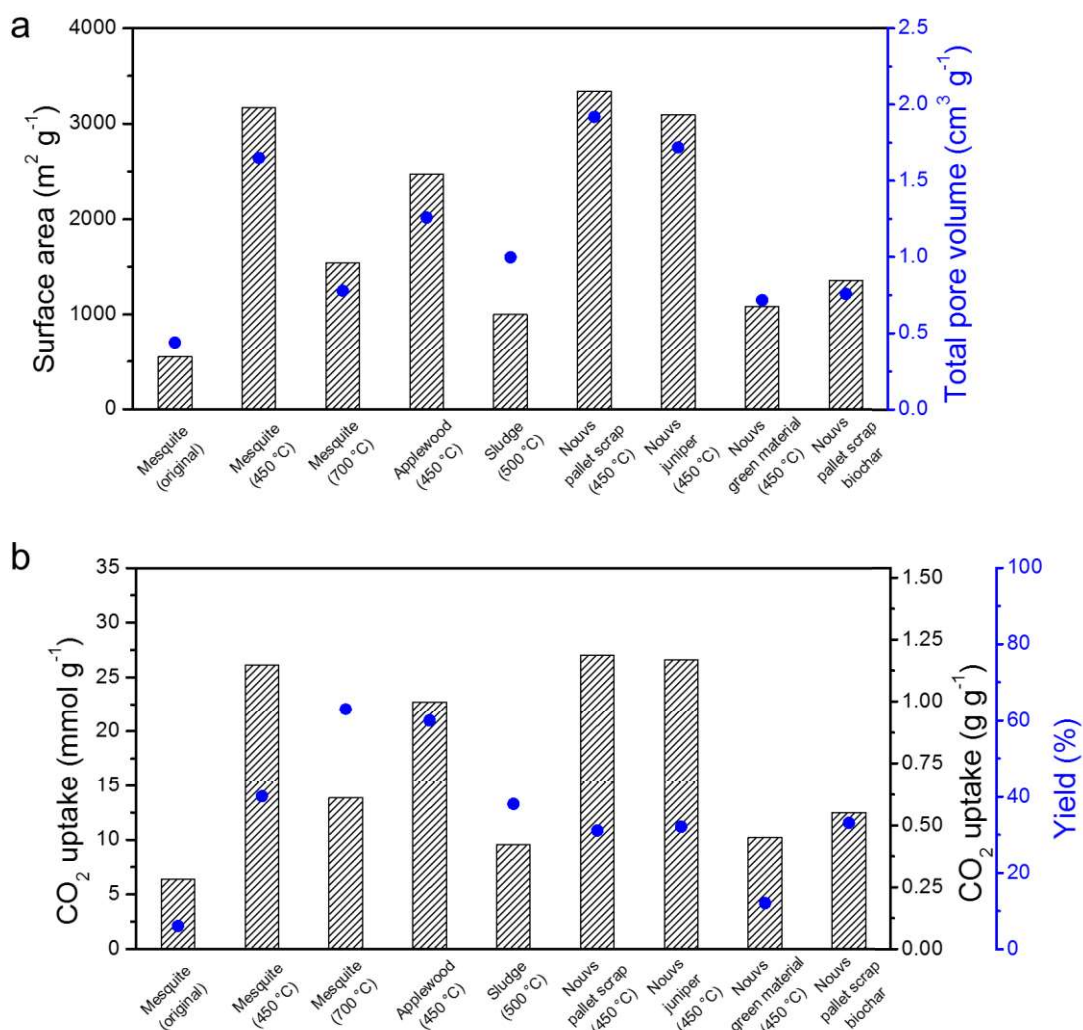


Figure 4-9. Properties of B-PC synthesized from biochar made from different biosources.

(a) BET surface areas, total pore volumes, (b) absolute gravimetric CO₂ uptake values (at 30 bar, 25 °C), and yields for B-PC synthesized with biochar made from different biosources. All B-PC samples are prepared with 0.5 g biochar and 2.5 g KOH by activation at 800 °C. The Novus pallet scrap biochar was prepared with an industrial gasifier at 450 to 550 °C for ~ 8 min, all other biochar was prepared in-house in a gasifier at the temperatures listed in the parentheses. Mesquite (original) means that the raw mesquite wood was directly activated by KOH without pyrolysis.

Biosources and pyrolysis temperature	Yield of biochar ^b	Elemental content			S _{BET}	V _{tol}
	(wt%)	C%	O%	N%	(m ² g ⁻¹)	(cm ³ g ⁻¹)
Mesquite 450 °C	40	93.2	6.8	< 0.1	3167	1.65
Mesquite	N/A	64.1	35.6	0.1	550	0.44
Mesquite 700 °C	30	85.9	13.4	0.7	1539	0.78
Applewood 450 °C	34	93.5	6.2	0.3	2475	1.26
Sludge 500 °C	46	53.7	45.0	1.3	1000	1.00
Novus pallet scrap 450 °C	24	89.8	10.1	0.1	3341	1.92
Novus juniper 450 °C	34	90.0	9.8	0.2	3093	1.72
Novus green material 450 °C	32	54.8	45	0.2	1081	0.72
Novus pallet scrap biochar	N/A	84.5	14.6	0.9	1360	0.76
Biosources and pyrolysis temperature	V _{MicDFT}	Density	Excess CO ₂ uptake at 30 bar ^c	Absolute CO ₂ uptake at 30 bar ^c		Yield
	(cm ³ g ⁻¹)	(g cm ⁻³)	(mmol g ⁻¹)	(mmol g ⁻¹)	(g g ⁻¹)	(wt%)
Mesquite 450 °C	1.02 (62%)	2.44	23.6	26.0	1.15	40
Mesquite	0.20 (46%)	1.93	5.7	6.3	0.28	6
Mesquite 700 °C	0.64 (82%)	2.17	12.7	13.9	0.61	63
Applewood 450 °C	0.98 (78%)	2.53	20.9	22.7	1.00	60
Sludge 500 °C	0.31 (31%)	2.60	8.2	9.6	0.42	38
Novus pallet scrap 450 °C	0.87 (45%)	2.50	24.3	27.1	1.19	31
Novus juniper 450 °C	0.87 (50%)	2.10	24.1	26.6	1.17	32
Novus green material 450 °C	0.31 (43%)	2.20	9.1	10.1	0.45	12
Novus pallet scrap biochar	0.55 (73%)	2.31	11.4	12.5	0.55	33

Table 4-5. Properties of B-PC synthesized from different biosources^a.

^aAll samples were made with 2.5 g KOH (per 0.5 g biochar) at 800 °C. ^bYield of biochar from biosources. ^cGravimetric uptake at 25 °C.

The other key factor when choosing the optimal biochar for CO₂ capture is the biosource. According to **Figure 4-9**, when the pyrolysis temperature is fixed at 450 °C, B-PC made from most wood wastes, including mesquite, Novus pallet scrap, and Novus juniper, all show high surface area > 3000 m² g⁻¹ and good CO₂ uptake performances > 26 mmol g⁻¹ at 30 bar and 25 °C. B-PC made from applewood biochar, pyrolyzed at 450 °C, shows slightly lower surface area and CO₂ uptake of 2475 m² g⁻¹, 22.7 mmol g⁻¹ at 30 bar and 25 °C, yet a significantly higher 60 wt% yield is achieved. Other wastes such as sludge and Novus green material, however, yield B-PC samples with poor surface area and CO₂ uptake performance, possibly due to the limited amounts of cellulose/lignin or other biopolymers compared to the wood wastes, as those are believed to be the source of active sites during KOH activation as previously discussed. Interestingly, for the B-PC sample made from industrial Novus pallet scrap biochar, although it also originates from wood waste, the measured CO₂ uptake performance is significantly lower, < 13 mmol g⁻¹ at 30 bar 25 °C, relative to the B-PC from lab-made biochar samples. This observation is most likely due to the limited charring progress provided by the industrial gasifier, where the raw material was only pyrolyzed for ~ 8 min at 450 to 550 °C; a much shorter time comparing to the 4 h pyrolysis process for the other lab-made biochar samples. Note that for the different B-PC samples tested in **Figure 4-9**, the differences in CO₂ uptake performances at 30 bar almost overlaps with the differences in BET surface area and total pore volume, which further confirms the previous reports on the

relation between the physical properties and CO₂ adsorption values at high pressure.^{169, 191}

4.2.3. Conclusions

To capture CO₂ from high-pressure natural gas wells, low-cost and renewable biochar materials were used as the feedstock to synthesize porous carbon sorbents with a one-step KOH activation. The physical properties of B-PC samples made using different activation conditions were analyzed against CO₂ uptake performances. Under the optimized activation condition, B-PC made from mesquite biochar that was pyrolyzed at 450 °C shows CO₂ uptake performance of 26.0 mmol g⁻¹ (1.15 g g⁻¹) at 30 bar and 25 °C, with a surface area of 3167 m² g⁻¹. The stability of the B-PC has been tested through adsorption-desorption cycling, and the uptake selectivity between CO₂ and CH₄ has been evaluated as well as the heat of adsorption values for both gases. Activity screenings of B-PC made from different types of biochar show that wood wastes pyrolyzed at a mid-range temperature yield B-PC sorbents with preferred CO₂ uptake performances towards industrial applications.

4.3. Experimental Contributions

Yilun Li designed the majority of the experiments, prepared the majority of the samples, and conducted the majority of the characterizations including SEM, TEM, Raman, BET, TEM, CO₂ uptake measurements, etc. **Gedeng Ruan** helped to

designed the experiments, prepared the part of the samples, and conducted part of the characterizations including BET, CO₂ uptake measurements, etc.

References

1. Li, Y.; Peng, Z.; Larios, E.; Wang, G.; Lin, J.; Yan, Z.; Ruiz-Zepeda, F.; José-Yacamán, M.; Tour, J. M. Rebar Graphene from Functionalized Boron Nitride Nanotubes. *ACS Nano* **2015**, *9*, 532-538.
2. Jiang, J.; Li, Y.; Gao, C.; Kim, N. D.; Fan, X.; Wang, G.; Peng, Z.; Hauge, R. H.; Tour, J. M. Growing Carbon Nanotubes from Both Sides of Graphene. *ACS Appl. Mater. Interfaces* **2016**, *8*, 7356-7362.
3. Kim, N. D.; Li, Y.; Wang, G.; Fan, X.; Jiang, J.; Li, L.; Ji, Y.; Ruan, G.; Hauge, R. H.; Tour, J. M. Growth and Transfer of Seamless 3d Graphene-Nanotube Hybrids. *Nano Lett.* **2016**, *16*, 1287-1292.
4. Iijima, S. Helical Microtubules of Graphitic Carbon. *Nature* **1991**, *354*, 56-58.
5. Baughman, R. H.; Zakhidov, A. A.; de Heer, W. A. Carbon Nanotubes-the Route toward Applications. *Science* **2002**, *297*, 787-792.
6. Geim, A. K.; Novoselov, K. S. The Rise of Graphene. *Nat. Mater.* **2007**, *6*, 183-191.
7. Geim, A. K. Graphene: Status and Prospects. *Science* **2009**, *324*, 1530-1534.
8. Treacy, M.; Ebbesen, T.; Gibson, J. Exceptionally High Young's Modulus Observed for Individual Carbon Nanotubes. *Nature* **1996**, *381*, 678-680.
9. Lee, C.; Wei, X.; Kysar, J. W.; Hone, J. Measurement of the Elastic Properties and Intrinsic Strength of Monolayer Graphene. *Science* **2008**, *321*, 385-388.
10. Martel, R.; Schmidt, T.; Shea, H.; Hertel, T.; Avouris, P. Single- and Multi-Wall Carbon Nanotube Field-Effect Transistors. *Appl. Phys. Lett.* **1998**, *73*, 2447-2449.

11. Novoselov, K. S.; Geim, A. K.; Morozov, S. V.; Jiang, D.; Zhang, Y.; Dubonos, S. V.; Grigorieva, I. V.; Firsov, A. A. Electric Field Effect in Atomically Thin Carbon Films. *Science* **2004**, *306*, 666-669.
12. Bolotin, K. I.; Sikes, K.; Jiang, Z.; Klima, M.; Fudenberg, G.; Hone, J.; Kim, P.; Stormer, H. Ultrahigh Electron Mobility in Suspended Graphene. *Solid State Commun.* **2008**, *146*, 351-355.
13. Berber, S.; Kwon, Y.-K.; Tomanek, D. Unusually High Thermal Conductivity of Carbon Nanotubes. *Phys. Rev. Lett.* **2000**, *84*, 4613-4616.
14. Balandin, A. A.; Ghosh, S.; Bao, W.; Calizo, I.; Teweldebrhan, D.; Miao, F.; Lau, C. N. Superior Thermal Conductivity of Single-Layer Graphene. *Nano Lett.* **2008**, *8*, 902-907.
15. Peigney, A.; Laurent, C.; Flahaut, E.; Bacsá, R.; Rousset, A. Specific Surface Area of Carbon Nanotubes and Bundles of Carbon Nanotubes. *Carbon* **2001**, *39*, 507-514.
16. Chae, H. K.; Siberio-Perez, D. Y.; Kim, J.; Go, Y.; Eddaoudi, M.; Matzger, A. J.; O'Keeffe, M.; Yaghi, O. M. A Route to High Surface Area, Porosity and Inclusion of Large Molecules in Crystals. *Nature* **2004**, *427*, 523-527.
17. Che, G.; Lakshmi, B. B.; Fisher, E. R.; Martin, C. R. Carbon Nanotubule Membranes for Electrochemical Energy Storage and Production. *Nature* **1998**, *393*, 346-349.
18. Stoller, M. D.; Park, S.; Zhu, Y.; An, J.; Ruoff, R. S. Graphene-Based Ultracapacitors. *Nano Lett.* **2008**, *8*, 3498-3502.

19. Dai, L.; Chang, D. W.; Baek, J. B.; Lu, W. Carbon Nanomaterials for Advanced Energy Conversion and Storage. *Small* **2012**, *8*, 1130-1166.
20. Tans, S. J.; Verschueren, A. R.; Dekker, C. Room-Temperature Transistor Based on a Single Carbon Nanotube. *Nature* **1998**, *393*, 49-52.
21. Lin, Y.-M.; Dimitrakopoulos, C.; Jenkins, K. A.; Farmer, D. B.; Chiu, H.-Y.; Grill, A.; Avouris, P. 100-Ghz Transistors from Wafer-Scale Epitaxial Graphene. *Science* **2010**, *327*, 662-662.
22. Wang, J. Carbon-Nanotube Based Electrochemical Biosensors: A Review. *Electroanalysis* **2005**, *17*, 7-14.
23. Shao, Y.; Wang, J.; Wu, H.; Liu, J.; Aksay, I. A.; Lin, Y. Graphene Based Electrochemical Sensors and Biosensors: A Review. *Electroanalysis* **2010**, *22*, 1027-1036.
24. Tung, V. C.; Chen, L.-M.; Allen, M. J.; Wassei, J. K.; Nelson, K.; Kaner, R. B.; Yang, Y. Low-Temperature Solution Processing of Graphene–Carbon Nanotube Hybrid Materials for High-Performance Transparent Conductors. *Nano Lett.* **2009**, *9*, 1949-1955.
25. Fan, Z.; Yan, J.; Zhi, L.; Zhang, Q.; Wei, T.; Feng, J.; Zhang, M.; Qian, W.; Wei, F. A Three-Dimensional Carbon Nanotube/Graphene Sandwich and Its Application as Electrode in Supercapacitors. *Adv. Mater.* **2010**, *22*, 3723-3728.
26. Tung, V. C.; Huang, J.-H.; Tevis, I.; Kim, F.; Kim, J.; Chu, C.-W.; Stupp, S. I.; Huang, J. Surfactant-Free Water-Processable Photoconductive All-Carbon Composite. *J. Am. Chem. Soc.* **2011**, *133*, 4940-4947.

27. Sui, Z.; Meng, Q.; Zhang, X.; Ma, R.; Cao, B. Green Synthesis of Carbon Nanotube–Graphene Hybrid Aerogels and Their Use as Versatile Agents for Water Purification. *J. Mater. Chem.* **2012**, *22*, 8767-8771.
28. Zhu, Y.; Li, L.; Zhang, C. G.; Casillas, G.; Sun, Z. Z.; Yan, Z.; Ruan, G. D.; Peng, Z. W.; Raji, A. R. O.; Kittrell, C.; Hauge, R. H.; Tour, J. M. A Seamless Three-Dimensional Carbon Nanotube Graphene Hybrid Material. *Nat. Commun.* **2012**, *3*, 1225.
29. Li, Y.; Yang, J.; Zhao, Q.; Li, Y. Dispersing Carbon-Based Nanomaterials in Aqueous Phase by Graphene Oxides. *Langmuir* **2013**, *29*, 13527-13534.
30. Lin, J.; Zhang, C.; Yan, Z.; Zhu, Y.; Peng, Z.; Hauge, R. H.; Natelson, D.; Tour, J. M. 3-Dimensional Graphene Carbon Nanotube Carpet-Based Microsupercapacitors with High Electrochemical Performance. *Nano Lett.* **2013**, *13*, 72-78.
31. Yan, Z.; Peng, Z.; Casillas, G.; Lin, J.; Xiang, C.; Zhou, H.; Yang, Y.; Ruan, G.; Raji, A.-R. O.; Samuel, E. L. G.; Hauge, R. H.; Yacaman, M. J.; Tour, J. M. Rebar Graphene. *ACS Nano* **2014**, *8*, 5061-5068.
32. Tang, C.; Zhang, Q.; Zhao, M. Q.; Huang, J. Q.; Cheng, X. B.; Tian, G. L.; Peng, H. J.; Wei, F. Nitrogen-Doped Aligned Carbon Nanotube/Graphene Sandwiches: Facile Catalytic Growth on Bifunctional Natural Catalysts and Their Applications as Scaffolds for High-Rate Lithium-Sulfur Batteries. *Adv. Mater.* **2014**, *26*, 6100-6105.
33. Golberg, D.; Bando, Y.; Tang, C.; Zhi, C. Boron Nitride Nanotubes. *Adv. Mater.* **2007**, *19*, 2413-2432.
34. Golberg, D.; Bando, Y.; Huang, Y.; Terao, T.; Mitome, M.; Tang, C.; Zhi, C. Boron Nitride Nanotubes and Nanosheets. *ACS Nano* **2010**, *4*, 2979-2993.

35. Watanabe, K.; Taniguchi, T.; Kanda, H. Direct-Bandgap Properties and Evidence for Ultraviolet Lasing of Hexagonal Boron Nitride Single Crystal. *Nat. Mater.* **2004**, *3*, 404-409.
36. Kawaguchi, M.; Kawashima, T.; Nakajima, T. Syntheses and Structures of New Graphite-Like Materials of Composition Bcn(H) and Bc₃n(H). *Chem. Mater.* **1996**, *8*, 1197-1201.
37. Stephan, O.; Ajayan, P.; Colliex, C.; Redlich, P.; Lambert, J.; Bernier, P.; Lefin, P. Doping Graphitic and Carbon Nanotube Structures with Boron and Nitrogen. *Science* **1994**, *266*, 1683-1685.
38. Golberg, D.; Bando, Y.; Han, W.; Kurashima, K.; Sato, T. Single-Walled B-Doped Carbon, B/N-Doped Carbon and Bn Nanotubes Synthesized from Single-Walled Carbon Nanotubes through a Substitution Reaction. *Chem. Phys. Lett.* **1999**, *308*, 337-342.
39. Ci, L.; Song, L.; Jin, C.; Jariwala, D.; Wu, D.; Li, Y.; Srivastava, A.; Wang, Z.; Storr, K.; Balicas, L. Atomic Layers of Hybridized Boron Nitride and Graphene Domains. *Nat. Mater.* **2010**, *9*, 430-435.
40. Wang, S.; Zhang, L.; Xia, Z.; Roy, A.; Chang, D. W.; Baek, J. B.; Dai, L. Bcn Graphene as Efficient Metal-Free Electrocatalyst for the Oxygen Reduction Reaction. *Angew. Chem., Int. Ed.* **2012**, *51*, 4209-4212.
41. Gong, Y.; Shi, G.; Zhang, Z.; Zhou, W.; Jung, J.; Gao, W.; Ma, L.; Yang, Y.; Yang, S.; You, G. Direct Chemical Conversion of Graphene to Boron- and Nitrogen- and Carbon-Containing Atomic Layers. *Nat. Commun.* **2014**, *5*.

42. Shinde, P. P.; Kumar, V. Direct Band Gap Opening in Graphene by Bn Doping: *Ab Initio* Calculations. *Phys. Rev. B* **2011**, *84*, 125401.
43. Pastine, S. J.; Okawa, D.; Kessler, B.; Rolandi, M.; Llorente, M.; Zettl, A.; Fréchet, J. M. A Facile and Patternable Method for the Surface Modification of Carbon Nanotube Forests Using Perfluoroarylazides. *J. Am. Chem. Soc.* **2008**, *130*, 4238-4239.
44. Fan, S.; Chapline, M. G.; Franklin, N. R.; Tomblor, T. W.; Cassell, A. M.; Dai, H. Self-Oriented Regular Arrays of Carbon Nanotubes and Their Field Emission Properties. *Science* **1999**, *283*, 512-514.
45. Lee, D. H.; Kim, J. E.; Han, T. H.; Hwang, J. W.; Jeon, S.; Choi, S. Y.; Hong, S. H.; Lee, W. J.; Ruoff, R. S.; Kim, S. O. Versatile Carbon Hybrid Films Composed of Vertical Carbon Nanotubes Grown on Mechanically Compliant Graphene Films. *Adv. Mater.* **2010**, *22*, 1247-1252.
46. Hayamizu, Y.; Yamada, T.; Mizuno, K.; Davis, R. C.; Futaba, D. N.; Yumura, M.; Hata, K. Integrated Three-Dimensional Microelectromechanical Devices from Processable Carbon Nanotube Wafers. *Nat. Nanotechnol.* **2008**, *3*, 289-294.
47. Cheong, F. C.; Lim, K. Y.; Sow, C. H.; Lin, J.; Ong, C. K. Large Area Patterned Arrays of Aligned Carbon Nanotubes Via Laser Trimming. *Nanotechnology* **2003**, *14*, 433.
48. Elmer, J.; Yaglioglu, O.; Schaeffer, R.; Kardos, G.; Derkach, O. Direct Patterning of Vertically Aligned Carbon Nanotube Arrays to 20 μ m Pitch Using Focused Laser Beam Micromachining. *Carbon* **2012**, *50*, 4114-4122.

49. Yan, Z.; Ma, L.; Zhu, Y.; Lahiri, I.; Hahm, M. G.; Liu, Z.; Yang, S.; Xiang, C.; Lu, W.; Peng, Z.; Sun, Z.; Kittrell, C.; Lou, J.; Choi, W.; Ajayan, P. M.; Tour, J. M. Three-Dimensional Metal–Graphene–Nanotube Multifunctional Hybrid Materials. *ACS Nano* **2012**, *7*, 58-64.
50. Yan, Z.; Lin, J.; Peng, Z.; Sun, Z.; Zhu, Y.; Li, L.; Xiang, C.; Samuel, E. L. c.; Kittrell, C.; Tour, J. M. Toward the Synthesis of Wafer-Scale Single-Crystal Graphene on Copper Foils. *ACS Nano* **2012**, *6*, 9110-9117.
51. Smith, M. W.; Jordan, K. C.; Park, C.; Kim, J.-W.; Lillehei, P. T.; Crooks, R.; Harrison, J. S. Very Long Single- and Few-Walled Boron Nitride Nanotubes Via the Pressurized Vapor/Condenser Method. *Nanotechnology* **2009**, *20*, 505604.
52. Ciofani, G.; Genchi, G. G.; Liakos, I.; Athanassiou, A.; Dinucci, D.; Chiellini, F.; Mattoli, V. A Simple Approach to Covalent Functionalization of Boron Nitride Nanotubes. *J. Colloid Interface Sci.* **2012**, *374*, 308-314.
53. Zhi, C.; Bando, Y.; Tang, C.; Honda, S.; Sato, K.; Kuwahara, H.; Golberg, D. Covalent Functionalization: Towards Soluble Multiwalled Boron Nitride Nanotubes. *Angew. Chem., Int. Ed.* **2005**, *44*, 7932-7935.
54. Emtsev, K. V.; Bostwick, A.; Horn, K.; Jobst, J.; Kellogg, G. L.; Ley, L.; McChesney, J. L.; Ohta, T.; Reshanov, S. A.; Röhrl, J. Towards Wafer-Size Graphene Layers by Atmospheric Pressure Graphitization of Silicon Carbide. *Nat. Mater.* **2009**, *8*, 203-207.

55. Sun, Z.; Raji, A.-R. O.; Zhu, Y.; Xiang, C.; Yan, Z.; Kittrell, C.; Samuel, E. L. G.; Tour, J. M. Large-Area Bernal-Stacked Bi-, Tri-, and Tetralayer Graphene. *ACS Nano* **2012**, *6*, 9790-9796.
56. Ferrari, A. C.; Meyer, J. C.; Scardaci, V.; Casiraghi, C.; Lazzeri, M.; Mauri, F.; Piscanec, S.; Jiang, D.; Novoselov, K. S.; Roth, S.; Geim, A. K. Raman Spectrum of Graphene and Graphene Layers. *Phys. Rev. Lett.* **2006**, *97*, 187401-187404.
57. Edwards, R. S.; Coleman, K. S. Graphene Film Growth on Polycrystalline Metals. *Acc. Chem. Res.* **2012**, *46*, 23-30.
58. Ruan, G.; Sun, Z.; Peng, Z.; Tour, J. M. Growth of Graphene from Food, Insects, and Waste. *ACS Nano* **2011**, *5*, 7601-7607.
59. Sun, Z.; Yan, Z.; Yao, J.; Beitler, E.; Zhu, Y.; Tour, J. M. Growth of Graphene from Solid Carbon Sources. *Nature* **2010**, *468*, 549-552.
60. Yan, Z.; Peng, Z.; Sun, Z.; Yao, J.; Zhu, Y.; Liu, Z.; Ajayan, P. M.; Tour, J. M. Growth of Bilayer Graphene on Insulating Substrates. *ACS Nano* **2011**, *5*, 8187-8192.
61. Peng, Z.; Yan, Z.; Sun, Z.; Tour, J. M. Direct Growth of Bilayer Graphene on SiO₂ Substrates by Carbon Diffusion through Nickel. *ACS Nano* **2011**, *5*, 8241-8247.
62. Pimenta, M.; Dresselhaus, G.; Dresselhaus, M. S.; Cancado, L.; Jorio, A.; Saito, R. Studying Disorder in Graphite-Based Systems by Raman Spectroscopy. *Phys. Chem. Chem. Phys.* **2007**, *9*, 1276-1290.
63. Geick, R.; Perry, C.; Rupprecht, G. Normal Modes in Hexagonal Boron Nitride. *Phys. Rev.* **1966**, *146*, 543.

64. Arenal, R.; Ferrari, A.; Reich, S.; Wirtz, L.; Mevellec, J.-Y.; Lefrant, S.; Rubio, A.; Loiseau, A. Raman Spectroscopy of Single-Wall Boron Nitride Nanotubes. *Nano Lett.* **2006**, *6*, 1812-1816.
65. Reina, A.; Jia, X.; Ho, J.; Nezich, D.; Son, H.; Bulovic, V.; Dresselhaus, M. S.; Kong, J. Large Area, Few-Layer Graphene Films on Arbitrary Substrates by Chemical Vapor Deposition. *Nano Lett.* **2009**, *9*, 30-35.
66. Suk, J. W.; Kitt, A.; Magnuson, C. W.; Hao, Y.; Ahmed, S.; An, J.; Swan, A. K.; Goldberg, B. B.; Ruoff, R. S. Transfer of Cvd-Grown Monolayer Graphene onto Arbitrary Substrates. *ACS Nano* **2011**, *5*, 6916-6924.
67. Song, L.; Ci, L.; Lu, H.; Sorokin, P. B.; Jin, C.; Ni, J.; Kvashnin, A. G.; Kvashnin, D. G.; Lou, J.; Yakobson, B. I. Large Scale Growth and Characterization of Atomic Hexagonal Boron Nitride Layers. *Nano Lett.* **2010**, *10*, 3209-3215.
68. van der Zande, A. M.; Huang, P. Y.; Chenet, D. A.; Berkelbach, T. C.; You, Y.; Lee, G.-H.; Heinz, T. F.; Reichman, D. R.; Muller, D. A.; Hone, J. C. Grains and Grain Boundaries in Highly Crystalline Monolayer Molybdenum Disulphide. *Nat. Mater.* **2013**, *12*, 554-561.
69. Kim, K.; Lee, Z.; Regan, W.; Kisielowski, C.; Crommie, M.; Zettl, A. Grain Boundary Mapping in Polycrystalline Graphene. *ACS Nano* **2011**, *5*, 2142-2146.
70. Bae, S.; Kim, H.; Lee, Y.; Xu, X.; Park, J.-S.; Zheng, Y.; Balakrishnan, J.; Lei, T.; Kim, H. R.; Song, Y. I. Roll-to-Roll Production of 30-Inch Graphene Films for Transparent Electrodes. *Nat. Nanotechnol.* **2010**, *5*, 574-578.

71. Miyamoto, Y.; Rubio, A.; Cohen, M. L.; Louie, S. G. Chiral Tubules of Hexagonal Bc₂n. *Phys. Rev. B* **1994**, *50*, 4976.
72. Lv, R.; Li, Q.; Botello-Méndez, A. R.; Hayashi, T.; Wang, B.; Berkdemir, A.; Hao, Q.; Elías, A. L.; Cruz-Silva, R.; Gutiérrez, H. R.; Kim, Y. A.; Muramatsu, H.; Zhu, J.; Endo, M.; Terrones, H.; Charlier, J.-C.; Pan, M.; Terrones, M. Nitrogen-Doped Graphene: Beyond Single Substitution and Enhanced Molecular Sensing. *Sci. Rep.* **2012**, *2*.
73. Li, X.; Cai, W.; An, J.; Kim, S.; Nah, J.; Yang, D.; Piner, R.; Velamakanni, A.; Jung, I.; Tutuc, E.; K. Banerjee, S.; Colombo, L.; S. Ruoff, R. Large-Area Synthesis of High-Quality and Uniform Graphene Films on Copper Foils. *Science* **2009**, *324*, 1312-1314.
74. Kim, K. S.; Zhao, Y.; Jang, H.; Lee, S. Y.; Kim, J. M.; Kim, K. S.; Ahn, J.-H.; Kim, P.; Choi, J.-Y.; Hong, B. H. Large-Scale Pattern Growth of Graphene Films for Stretchable Transparent Electrodes. *Nature* **2009**, *457*, 706-710.
75. Watanabe, M.; Itoh, S.; Mizushima, K.; Sasaki, T. Electrical Properties of Bc₂n Thin Films Prepared by Chemical Vapor Deposition. *J. Appl. Phys.* **1995**, *78*, 2880-2882.
76. Pint, C. L.; Alvarez, N. T.; Hauge, R. H. Odako Growth of Dense Arrays of Single-Walled Carbon Nanotubes Attached to Carbon Surfaces. *Nano Res.* **2009**, *2*, 526-534.
77. Amama, P. B.; Pint, C. L.; McJilton, L.; Kim, S. M.; Stach, E. A.; Murray, P. T.; Hauge, R. H.; Maruyama, B. Role of Water in Super Growth of Single-Walled Carbon Nanotube Carpets. *Nano Lett.* **2008**, *9*, 44-49.

78. Vlassiouk, I.; Regmi, M.; Fulvio, P.; Dai, S.; Datskos, P.; Eres, G.; Smirnov, S. Role of Hydrogen in Chemical Vapor Deposition Growth of Large Single-Crystal Graphene. *ACS Nano* **2011**, *5*, 6069-6076.
79. Han, T. H.; Huang, Y.-K.; Tan, A. T.; Dravid, V. P.; Huang, J. Steam Etched Porous Graphene Oxide Network for Chemical Sensing. *J. Am. Chem. Soc.* **2011**, *133*, 15264-15267.
80. Luo, D.; Yang, F.; Wang, X.; Sun, H.; Gao, D.; Li, R.; Yang, J.; Li, Y. Anisotropic Etching of Graphite Flakes with Water Vapor to Produce Armchair-Edged Graphene. *Small* **2014**, *10*, 2809-2814.
81. Li, Y.; Kim, W.; Zhang, Y.; Rolandi, M.; Wang, D.; Dai, H. Growth of Single-Walled Carbon Nanotubes from Discrete Catalytic Nanoparticles of Various Sizes. *J. Phys. Chem. B* **2001**, *105*, 11424-11431.
82. Dresselhaus, M. S.; Dresselhaus, G.; Saito, R.; Jorio, A. Raman Spectroscopy of Carbon Nanotubes. *Phys. Rep.* **2005**, *409*, 47-99.
83. Fantini, C.; Jorio, A.; Souza, M.; Strano, M.; Dresselhaus, M.; Pimenta, M. Optical Transition Energies for Carbon Nanotubes from Resonant Raman Spectroscopy: Environment and Temperature Effects. *Phys. Rev. Lett.* **2004**, *93*, 147406.
84. Hata, K.; Futaba, D. N.; Mizuno, K.; Namai, T.; Yumura, M.; Iijima, S. Water-Assisted Highly Efficient Synthesis of Impurity-Free Single-Walled Carbon Nanotubes. *Science* **2004**, *306*, 1362-1364.

85. Dijon, J.; Szkutnik, P.; Fournier, A.; Goislard de Monsabert, T.; Okuno, H.; Quesnel, E.; Muffato, V.; De Vito, E.; Bendiab, N.; Bogner, A. How to Switch from a Tip to Base Growth Mechanism in Carbon Nanotube Growth by Catalytic Chemical Vapour Deposition. *Carbon* **2010**, *48*, 3953-3963.
86. Lin, M.; Ma, Z.; Huang, F.; Fan, Z. F.; Allen, L.; Morkoc, H. Low Resistance Ohmic Contacts on Wide Band-Gap Gan. *Appl. Phys. Lett.* **1994**, *64*, 1003-1005.
87. Dimitrakakis, G. K.; Tylianakis, E.; Froudakis, G. E. Pillared Graphene: A New 3-D Network Nanostructure for Enhanced Hydrogen Storage. *Nano Lett.* **2008**, *8*, 3166-3170.
88. Shahsavari, R.; Sakhavand, N. Junction Configuration-Induced Mechanisms Govern Elastic and Inelastic Deformations in Hybrid Carbon Nanomaterials. *Carbon* **2015**, *95*, 699-709.
89. Jiang, H.; Lee, P. S.; Li, C. 3d Carbon Based Nanostructures for Advanced Supercapacitors. *Energy Environ. Sci.* **2013**, *6*, 41-53.
90. Jorio, A.; Santos, A.; Ribeiro, H.; Fantini, C.; Souza, M.; Vieira, J.; Furtado, C.; Jiang, J.; Saito, R.; Balzano, L. Quantifying Carbon-Nanotube Species with Resonance Raman Scattering. *Phys. Rev. B* **2005**, *72*, 075207.
91. Larjo, J.; Koivikko, H.; Li, D.; Hernberg, R. Atomic-Hydrogen Mapping in Hot-Filament Chemical-Vapor Deposition. *Appl. Opt.* **2001**, *40*, 765-769.
92. Pint, C. L.; Pheasant, S. T.; Parra-Vasquez, A. N. G.; Horton, C.; Xu, Y.; Hauge, R. H. Investigation of Optimal Parameters for Oxide-Assisted Growth of Vertically

Aligned Single-Walled Carbon Nanotubes. *The Journal of Physical Chemistry C* **2009**, *113*, 4125-4133.

93. Chastain, J.; King, R. C.; Moulder, J. *Handbook of X-Ray Photoelectron Spectroscopy: A Reference Book of Standard Spectra for Identification and Interpretation of Xps Data*. Physical Electronics Division, Perkin-Elmer Corporation Eden Prairie, Minnesota: 1992.

94. Yang, Y.; Jeong, S.; Hu, L.; Wu, H.; Lee, S. W.; Cui, Y. Transparent Lithium-Ion Batteries. *Proceedings of the National Academy of Sciences* **2011**, *108*, 13013-13018.

95. Fisichella, G.; Di Franco, S.; Fiorenza, P.; Nigro, R. L.; Roccaforte, F.; Tudisco, C.; Condorelli, G. G.; Piluso, N.; Spartà, N.; Verso, S. L. Micro-and Nanoscale Electrical Characterization of Large-Area Graphene Transferred to Functional Substrates. *Beilstein journal of nanotechnology* **2013**, *4*, 234-242.

96. Choi, H.; Kim, J.; Cho, Y.; Hwang, T.; Lee, J.; Kim, T. Conditioning of Graphene Surface by Co₂ Cluster Jet. *RSC Advances* **2014**, *4*, 41922-41926.

97. Talapatra, S.; Kar, S.; Pal, S.; Vajtai, R.; Ci, L.; Victor, P.; Shaijumon, M.; Kaur, S.; Nalamasu, O.; Ajayan, P. Direct Growth of Aligned Carbon Nanotubes on Bulk Metals. *Nat. Nanotechnol.* **2006**, *1*, 112-116.

98. Cao, A.; Veedu, V. P.; Li, X.; Yao, Z.; Ghasemi-Nejhad, M. N.; Ajayan, P. M. Multifunctional Brushes Made from Carbon Nanotubes. *Nat. Mater.* **2005**, *4*, 540-545.

99. Li, Y.; Luong, D. X.; Zhang, J.; Tarkunde, Y. R.; Kittrell, C.; Sargunaraj, F.; Ji, Y.; Arnusch, C. J.; Tour, J. M. Laser-Induced Graphene in Controlled Atmospheres. From

Superhydrophilic to Superhydrophobic Surfaces. *Adv. Mater.* **2017**, 10.1002/adma.201700496.

100. Lin, J.; Peng, Z.; Liu, Y.; Ruiz-Zepeda, F.; Ye, R.; Samuel, E. L. G.; Yacaman, M. J.; Yakobson, B. I.; Tour, J. M. Laser-Induced Porous Graphene Films from Commercial Polymers. *Nat. Commun.* **2014**, 5, 5714.

101. Peng, Z.; Lin, J.; Ye, R.; Samuel, E. L. G.; Tour, J. M. Flexible and Stackable Laser-Induced Graphene Supercapacitors. *ACS Appl. Mater. Interfaces* **2015**, 7, 3414-3419.

102. Peng, Z.; Ye, R.; Mann, J. A.; Zakhidov, D.; Li, Y.; Smalley, P. R.; Lin, J.; Tour, J. M. Flexible Boron-Doped Laser-Induced Graphene Microsupercapacitors. *ACS Nano* **2015**, 9, 5868-5875.

103. Ye, R.; Peng, Z.; Wang, T.; Xu, Y.; Zhang, J.; Li, Y.; Nilewski, L. G.; Lin, J.; Tour, J. M. In Situ Formation of Metal Oxide Nanocrystals Embedded in Laser-Induced Graphene. *ACS Nano* **2015**, 9, 9244-9251.

104. Li, L.; Zhang, J.; Peng, Z.; Li, Y.; Gao, C.; Ji, Y.; Ye, R.; Kim, N. D.; Zhong, Q.; Yang, Y. High-Performance Pseudocapacitive Microsupercapacitors from Laser-Induced Graphene. *Adv. Mater.* **2015**, 28, 838-845.

105. Mattevi, C.; Kim, H.; Chhowalla, M. A Review of Chemical Vapour Deposition of Graphene on Copper. *J. Mater. Chem.* **2011**, 21, 3324-3334.

106. Wang, S.; Zhang, Y.; Abidi, N.; Cabrales, L. Wettability and Surface Free Energy of Graphene Films. *Langmuir* **2009**, 25, 11078-11081.

107. Lee, Y.; Park, S. H.; Kim, K. B.; Lee, J. K. Fabrication of Hierarchical Structures on a Polymer Surface to Mimic Natural Superhydrophobic Surfaces. *Adv. Mater.* **2007**, *19*, 2330-2335.
108. Bhushan, B.; Jung, Y. C.; Koch, K. Micro-, Nano-and Hierarchical Structures for Superhydrophobicity, Self-Cleaning and Low Adhesion. *Philos. Trans. R. Soc., A* **2009**, *367*, 1631-1672.
109. Bhushan, B.; Nosonovsky, M. The Rose Petal Effect and the Modes of Superhydrophobicity. *Philos. Trans. R. Soc., A* **2010**, *368*, 4713-4728.
110. Hontoria-Lucas, C.; Lopez-Peinado, A.; López-González, J. d. D.; Rojas-Cervantes, M.; Martin-Aranda, R. Study of Oxygen-Containing Groups in a Series of Graphite Oxides: Physical and Chemical Characterization. *Carbon* **1995**, *33*, 1585-1592.
111. Marcano, D. C.; Kosynkin, D. V.; Berlin, J. M.; Sinitskii, A.; Sun, Z.; Slesarev, A.; Alemany, L. B.; Lu, W.; Tour, J. M. Improved Synthesis of Graphene Oxide. *ACS Nano* **2010**, *4*, 4806-4814.
112. Bagri, A.; Mattevi, C.; Acik, M.; Chabal, Y. J.; Chhowalla, M.; Shenoy, V. B. Structural Evolution During the Reduction of Chemically Derived Graphene Oxide. *Nature Chemistry* **2010**, *2*, 581-587.
113. Zhang, W.; Wahlgren, M.; Sivik, B. Membrane Characterization by the Contact Angle Technique: Ii. Characterization of Uf-Membranes and Comparison between the Captive Bubble and Sessile Drop as Methods to Obtain Water Contact Angles. *Desalination* **1989**, *72*, 263-273.

114. Wang, T.; Zheng, Y.; Raji, A.-R. O.; Li, Y.; Sikkema, W. K.; Tour, J. M. Passive Anti-Icing and Active Deicing Films. *ACS Appl. Mater. Interfaces* **2016**, *8*, 14169-14173.
115. Lin, Y.; Ehlert, G. J.; Bukowsky, C.; Sodano, H. A. Superhydrophobic Functionalized Graphene Aerogels. *ACS Appl. Mater. Interfaces* **2011**, *3*, 2200-2203.
116. Zha, D.-a.; Mei, S.; Wang, Z.; Li, H.; Shi, Z.; Jin, Z. Superhydrophobic Polyvinylidene Fluoride/Graphene Porous Materials. *Carbon* **2011**, *49*, 5166-5172.
117. Singh, E.; Chen, Z.; Houshmand, F.; Ren, W.; Peles, Y.; Cheng, H. M.; Koratkar, N. Superhydrophobic Graphene Foams. *Small* **2013**, *9*, 75-80.
118. Li, R.; Chen, C.; Li, J.; Xu, L.; Xiao, G.; Yan, D. A Facile Approach to Superhydrophobic and Superoleophilic Graphene/Polymer Aerogels. *J. Mater. Chem. A* **2014**, *2*, 3057-3064.
119. Chu, F. Sf6 Decomposition in Gas-Insulated Equipment. *IEEE Trans. Electr. Insul.* **1986**, *5*, 693-725.
120. Tsai, W.-T. The Decomposition Products of Sulfur Hexafluoride (Sf6): Reviews of Environmental and Health Risk Analysis. *J. Fluorine Chem.* **2007**, *128*, 1345-1352.
121. Zhao, F.-G.; Zhao, G.; Liu, X.-H.; Ge, C.-W.; Wang, J.-T.; Li, B.-L.; Wang, Q.-G.; Li, W.-S.; Chen, Q.-Y. Fluorinated Graphene: Facile Solution Preparation and Tailorable Properties by Fluorine-Content Tuning. *J. Mater. Chem. A* **2014**, *2*, 8782-8789.
122. Romero Aburto, R.; Alemany, L. B.; Weldeghiorghis, T. K.; Ozden, S.; Peng, Z.; Lherbier, A.; Botello Méndez, A. s. R.; Tiwary, C. S.; Taha-Tijerina, J.; Yan, Z. Chemical

Makeup and Hydrophilic Behavior of Graphene Oxide Nanoribbons after Low-Temperature Fluorination. *ACS Nano* **2015**, *9*, 7009-7018.

123. Gao, L.; McCarthy, T. J. Contact Angle Hysteresis Explained. *Langmuir* **2006**, *22*, 6234-6237.

124. Zhang, X.; Shi, F.; Niu, J.; Jiang, Y.; Wang, Z. Superhydrophobic Surfaces: From Structural Control to Functional Application. *J. Mater. Chem.* **2008**, *18*, 621-633.

125. Li, L.; Zhong, Q.; Kim, N. D.; Ruan, G.; Yang, Y.; Gao, C.; Fei, H.; Li, Y.; Ji, Y.; Tour, J. M. Nitrogen-Doped Carbonized Cotton for Highly Flexible Supercapacitors. *Carbon* **2016**, *105*, 260-267.

126. Sha, J.; Li, Y.; Salvatierra, R. V.; Wang, T.; Dong, P.; Ji, Y.; Lee, S. K.; Zhang, C.; Zhang, J.; Smith, R. H.; Ajayan, P. M.; Lou, J.; Zhao, N.; Tour, J. M. Three-Dimensional Printed Graphene Foams. *ACS Nano* **2017**, 10.1021/acsnano.1027b01987.

127. Chen, Z.; Ren, W.; Gao, L.; Liu, B.; Pei, S.; Cheng, H. M. Three-Dimensional Flexible and Conductive Interconnected Graphene Networks Grown by Chemical Vapour Deposition. *Nat. Mater.* **2011**, *10*, 424-428.

128. Qin, J.; He, C.; Zhao, N.; Wang, Z.; Shi, C.; Liu, E. Z.; Li, J. Graphene Networks Anchored with Sn@Graphene as Lithium Ion Battery Anode. *ACS Nano* **2014**, *8*, 1728-1738.

129. Choi, B. G.; Yang, M.; Hong, W. H.; Choi, J. W.; Huh, Y. S. 3d Macroporous Graphene Frameworks for Supercapacitors with High Energy and Power Densities. *ACS Nano* **2012**, *6*, 4020-4028.

130. Zakhidov, A. A.; Baughman, R. H.; Iqbal, Z.; Cui, C.; Khayrullin, I.; Dantas, S. O.; Marti, J.; Ralchenko, V. G. Carbon Structures with Three-Dimensional Periodicity at Optical Wavelengths. *Science* **1998**, *282*, 897-901.
131. Xu, Y.; Sheng, K.; Li, C.; Shi, G. Self-Assembled Graphene Hydrogel Via a One-Step Hydrothermal Process. *ACS Nano* **2010**, *4*, 4324-4330.
132. Sha, J.; Gao, C.; Lee, S. K.; Li, Y.; Zhao, N.; Tour, J. M. Preparation of Three-Dimensional Graphene Foams Using Powder Metallurgy Templates. *ACS Nano* **2016**, *10*, 1411-1416.
133. Sha, J.; Salvatierra, R. V.; Dong, P.; Li, Y.; Lee, S.-K.; Wang, T.; Zhang, C.; Zhang, J.; Ji, Y.; Ajayan, P. M.; Lou, J.; Zhao, N.; Tour, J. M. Three-Dimensional Rebar Graphene. *ACS Appl. Mater. Interfaces* **2017**, *9*, 7376-7384.
134. Farahani, R. D.; Dube, M.; Therriault, D. Three-Dimensional Printing of Multifunctional Nanocomposites: Manufacturing Techniques and Applications. *Adv. Mater.* **2016**, *28*, 5794-5821.
135. Compton, B. G.; Lewis, J. A. 3d-Printing of Lightweight Cellular Composites. *Adv. Mater.* **2014**, *26*, 5930-5935.
136. Kruth, J.-P.; Froyen, L.; Van Vaerenbergh, J.; Mercelis, P.; Rombouts, M.; Lauwers, B. Selective Laser Melting of Iron-Based Powder. *Journal of Materials Processing Technology* **2004**, *149*, 616-622.
137. Li, X.; Cai, W.; Colombo, L.; Ruoff, R. S. Evolution of Graphene Growth on Ni and Cu by Carbon Isotope Labeling. *Nano Lett.* **2009**, *9*, 4268-4272.

138. Lindahl, N.; Midtvedt, D.; Svensson, J.; Nerushev, O. A.; Lindvall, N.; Isacson, A.; Campbell, E. E. B. Determination of the Bending Rigidity of Graphene Via Electrostatic Actuation of Buckled Membranes. *Nano Lett.* **2012**, *12*, 3526-3531.
139. Inoue, T.; Osatake, H. A New Drying Method of Biological Specimens for Scanning Electron Microscopy: The T-Butyl Alcohol Freeze-Drying Method. *Archives of Histology and Cytology* **1988**, *51*, 53-59.
140. Singh, M.; Kaiser, J.; Hahn, H. Thick Electrodes for High Energy Lithium Ion Batteries. *J. Electrochem. Soc.* **2015**, *162*, A1196-A1201.
141. Sun, H.; Xu, Z.; Gao, C. Multifunctional, Ultra-Flyweight, Synergistically Assembled Carbon Aerogels. *Adv. Mater.* **2013**, *25*, 2554-2560.
142. Wu, Y.; Yi, N.; Huang, L.; Zhang, T.; Fang, S.; Chang, H.; Li, N.; Oh, J.; Lee, J. A.; Kozlov, M.; Chipara, A. C.; Terrones, H.; Xiao, P.; Long, G.; Huang, Y.; Zhang, F.; Zhang, L.; Lepro, X.; Haines, C.; Lima, M. D., *et al.* Three-Dimensionally Bonded Spongy Graphene Material with Super Compressive Elasticity and near-Zero Poisson's Ratio. *Nat. Commun.* **2015**, *6*, 6141.
143. Kim, K. H.; Oh, Y.; Islam, M. F. Graphene Coating Makes Carbon Nanotube Aerogels Superelastic and Resistant to Fatigue. *Nat. Nanotechnol.* **2012**, *7*, 562-566.
144. Dong, X.; Cao, Y.; Wang, J.; Chan-Park, M. B.; Wang, L.; Huang, W.; Chen, P. Hybrid Structure of Zinc Oxide Nanorods and Three Dimensional Graphene Foam for Supercapacitor and Electrochemical Sensor Applications. *RSC Advances* **2012**, *2*, 4364-4369.

145. Zeng, Y.; Hao, R.; Xing, B.; Hou, Y.; Xu, Z. One-Pot Synthesis of Fe₃O₄ Nanoprisms with Controlled Electrochemical Properties. *Chemical Communications* **2010**, *46*, 3920-3922.
146. Worsley, M. A.; Pauzauskie, P. J.; Olson, T. Y.; Biener, J.; Satcher, J. H.; Baumann, T. F. Synthesis of Graphene Aerogel with High Electrical Conductivity. *J. Am. Chem. Soc.* **2010**, *132*, 14067-14069.
147. Liu, F.; Song, S.; Xue, D.; Zhang, H. Folded Structured Graphene Paper for High Performance Electrode Materials. *Adv. Mater.* **2012**, *24*, 1089-1094.
148. Shao, Y.; El-Kady, M. F.; Wang, L. J.; Zhang, Q.; Li, Y.; Wang, H.; Mousavi, M. F.; Kaner, R. B. Graphene-Based Materials for Flexible Supercapacitors. *Chem. Soc. Rev.* **2015**, *44*, 3639-3665.
149. Chen, S.; He, G.; Hu, H.; Jin, S.; Zhou, Y.; He, Y.; He, S.; Zhao, F.; Hou, H. Elastic Carbon Foam Via Direct Carbonization of Polymer Foam for Flexible Electrodes and Organic Chemical Absorption. *Energy Environ. Sci.* **2013**, *6*, 2435-2439.
150. Yuan, C.; Yang, L.; Hou, L.; Li, J.; Sun, Y.; Zhang, X.; Shen, L.; Lu, X.; Xiong, S.; Lou, X. Flexible Hybrid Paper Made of Monolayer Co₃O₄ Microsphere Arrays on RGO/CNTs and Their Application in Electrochemical Capacitors. *Adv. Funct. Mater.* **2012**, *22*, 2560-2566.
151. Wu, J.; Li, C.; Wang, D.; Gui, M. Damping and Sound Absorption Properties of Particle Reinforced Al Matrix Composite Foams. *Compos. Sci. Technol.* **2003**, *63*, 569-574.

152. Banhart, J.; Baumeister, J.; Weber, M. Damping Properties of Aluminium Foams. *Materials Science and Engineering: A* **1996**, *205*, 221-228.
153. Deng, C.; Wang, D.; Zhang, X.; Ma, Y. Damping Characteristics of Carbon Nanotube Reinforced Aluminum Composite. *Mater. Lett.* **2007**, *61*, 3229-3231.
154. Li, Y.; Ruan, G.; Jalilov, A. S.; Tarkunde, Y. R.; Fei, H.; Tour, J. M. Biochar as a Renewable Source for High-Performance CO₂ Sorbent. *Carbon* **2016**, *107*, 344-351.
155. Cox, P. M.; Betts, R. A.; Jones, C. D.; Spall, S. A.; Totterdell, I. J. Acceleration of Global Warming Due to Carbon-Cycle Feedbacks in a Coupled Climate Model. *Nature* **2000**, *408*, 184-187.
156. Solomon, S.; Plattner, G.-K.; Knutti, R.; Friedlingstein, P. Irreversible Climate Change Due to Carbon Dioxide Emissions. *Proc. Natl. Acad. Sci. U. S. A.* **2009**, *106*, 1704-1709.
157. Haszeldine, R. S. Carbon Capture and Storage: How Green Can Black Be? *Science* **2009**, *325*, 1647-1652.
158. Tour, J. M.; Kittrell, C.; Colvin, V. L. Green Carbon as a Bridge to Renewable Energy. *Nat. Mater.* **2010**, *9*, 871-874.
159. He, M.; Sun, Y.; Han, B. Green Carbon Science: Scientific Basis for Integrating Carbon Resource Processing, Utilization, and Recycling. *Angew. Chem. Int. Ed.* **2013**, *52*, 9620-9633.
160. Yang, H.; Xu, Z.; Fan, M.; Gupta, R.; Slimane, R. B.; Bland, A. E.; Wright, I. Progress in Carbon Dioxide Separation and Capture: A Review. *Journal of Environmental Sciences* **2008**, *20*, 14-27.

161. Choi, S.; Drese, J. H.; Jones, C. W. Adsorbent Materials for Carbon Dioxide Capture from Large Anthropogenic Point Sources. *ChemSusChem* **2009**, *2*, 796-854.
162. Rochelle, G. T. Amine Scrubbing for Co₂ Capture. *Science* **2009**, *325*, 1652-1654.
163. D'Alessandro, D. M.; Smit, B.; Long, J. R. Carbon Dioxide Capture: Prospects for New Materials. *Angew. Chem. Int. Ed.* **2010**, *49*, 6058-6082.
164. Dutcher, B.; Fan, M.; Russell, A. G. Amine-Based Co₂ Capture Technology Development from the Beginning of 2013-a Review. *ACS Appl. Mater. Interfaces* **2015**, *7*, 2137-2148.
165. Sevilla, M.; Valle-Vigón, P.; Fuertes, A. B. N-Doped Polypyrrole-Based Porous Carbons for Co₂ Capture. *Adv. Funct. Mater.* **2011**, *21*, 2781-2787.
166. Sevilla, M.; Fuertes, A. B. Sustainable Porous Carbons with a Superior Performance for Co₂ Capture. *Energy Environ. Sci.* **2011**, *4*, 1765-1771.
167. Hwang, C.-C.; Tour, J. J.; Kittrell, C.; Espinal, L.; Alemany, L. B.; Tour, J. M. Capturing Carbon Dioxide as a Polymer from Natural Gas. *Nat. Commun.* **2014**, *5*, 3961.
168. Jalilov, A. S.; Ruan, G.; Hwang, C.-C.; Schipper, D. E.; Tour, J. J.; Li, Y.; Fei, H.; Samuel, E. L. G.; Tour, J. M. Asphalt-Derived High Surface Area Activated Porous Carbons for Carbon Dioxide Capture. *ACS Appl. Mater. Interfaces* **2014**, *7*, 1376-1382.

169. Ashourirad, B.; Sekizkardes, A. K.; Altarawneh, S.; El-Kaderi, H. M. Exceptional Gas Adsorption Properties by Nitrogen-Doped Porous Carbons Derived from Benzimidazole-Linked Polymers. *Chem. Mater.* **2015**, *27*, 1349-1358.
170. Balahmar, N.; Mitchell, A. C.; Mokaya, R. Generalized Mechanochemical Synthesis of Biomass-Derived Sustainable Carbons for High Performance Co₂ Storage. *Adv. Energy Mater.* **2015**, *5*.
171. Coromina, H. M.; Walsh, D. A.; Mokaya, R. Biomass-Derived Activated Carbon with Simultaneously Enhanced Co₂ Uptake for Both Pre and Post Combustion Capture Applications. *J. Mater. Chem. A* **2016**, *4*, 280-289.
172. Chen, J.; Yang, J.; Hu, G.; Hu, X.; Li, Z.; Shen, S.; Radosz, M.; Fan, M. Enhanced Co₂ Capture Capacity of Nitrogen-Doped Biomass-Derived Porous Carbons. *ACS Sustainable Chem. Eng.* **2016**.
173. Phan, A.; Doonan, C. J.; Uribe-Romo, F. J.; Knobler, C. B.; O'keeffe, M.; Yaghi, O. M. Synthesis, Structure, and Carbon Dioxide Capture Properties of Zeolitic Imidazolate Frameworks. *Acc. Chem. Res* **2010**, *43*, 58-67.
174. Sumida, K.; Rogow, D. L.; Mason, J. A.; McDonald, T. M.; Bloch, E. D.; Herm, Z. R.; Bae, T.-H.; Long, J. R. Carbon Dioxide Capture in Metal–Organic Frameworks. *Chem. Rev.* **2011**, *112*, 724-781.
175. Gutov, O. V.; Bury, W.; Gomez-Gualdron, D. A.; Krungleviciute, V.; Fairen-Jimenez, D.; Mondloch, J. E.; Sarjeant, A. A.; Al-Juaid, S. S.; Snurr, R. Q.; Hupp, J. T. Water-Stable Zirconium-Based Metal-Organic Framework Material with High-Surface Area and Gas-Storage Capacities. *Chem. Eur. J.* **2014**, *20*, 12389-12393.

176. An, J.; Geib, S. J.; Rosi, N. L. High and Selective Co₂ Uptake in a Cobalt Adeninate Metal–Organic Framework Exhibiting Pyrimidine-and Amino-Decorated Pores. *J. Am. Chem. Soc.* **2009**, *132*, 38-39.
177. Zeleňák, V.; Badaničová, M.; Halamova, D.; Čejka, J.; Zukal, A.; Murafa, N.; Goerigk, G. Amine-Modified Ordered Mesoporous Silica: Effect of Pore Size on Carbon Dioxide Capture. *Chemical Engineering Journal* **2008**, *144*, 336-342.
178. Drese, J. H.; Choi, S.; Lively, R. P.; Koros, W. J.; Fauth, D. J.; Gray, M. L.; Jones, C. W. Synthesis–Structure–Property Relationships for Hyperbranched Aminosilica Co₂ Adsorbents. *Adv. Funct. Mater.* **2009**, *19*, 3821-3832.
179. Mello, M. R.; Phanon, D.; Silveira, G. Q.; Llewellyn, P. L.; Ronconi, C. M. Amine-Modified Mcm-41 Mesoporous Silica for Carbon Dioxide Capture. *Microporous Mesoporous Mater.* **2011**, *143*, 174-179.
180. Cui, S.; Cheng, W.; Shen, X.; Fan, M.; Russell, A. T.; Wu, Z.; Yi, X. Mesoporous Amine-Modified SiO₂ Aerogel: A Potential Co₂ Sorbent. *Energy Environ. Sci.* **2011**, *4*, 2070-2074.
181. Yong, Z.; Mata, V.; Rodrigues, A. r. E. Adsorption of Carbon Dioxide at High Temperature-a Review. *Sep. Purif. Technol.* **2002**, *26*, 195-205.
182. Yang, R. T. *Adsorbents: Fundamentals and Applications*. John Wiley & Sons: 2003.
183. McCarl, B. A.; Peacocke, C.; Chrisman, R.; Kung, C.-C.; Sands, R. D. Economics of Biochar Production, Utilization and Greenhouse Gas Offsets. *Biochar for environmental management: Science and technology* **2009**, 341-358.

184. Lehmann, J.; Joseph, S. *Biochar for Environmental Management: Science and Technology*. Routledge: 2012.
185. Kinney, T.; Masiello, C.; Dugan, B.; Hockaday, W.; Dean, M.; Zygourakis, K.; Barnes, R. Hydrologic Properties of Biochars Produced at Different Temperatures. *Biomass Bioenergy* **2012**, *41*, 34-43.
186. Parilla, P. A.; Gross, K.; Hurst, K.; Gennett, T. Recommended Volumetric Capacity Definitions and Protocols for Accurate, Standardized and Unambiguous Metrics for Hydrogen Storage Materials. *Applied Physics A* **2016**, *122*, 1-18.
187. Mason, J. A.; Veenstra, M.; Long, J. R. Evaluating Metal–Organic Frameworks for Natural Gas Storage. *Chemical Science* **2014**, *5*, 32-51.
188. Yang, X.; Yu, M.; Zhao, Y.; Zhang, C.; Wang, X.; Jiang, J.-X. Remarkable Gas Adsorption by Carbonized Nitrogen-Rich Hypercrosslinked Porous Organic Polymers. *J. Mater. Chem. A* **2014**, *2*, 15139-15145.
189. Presser, V.; McDonough, J.; Yeon, S.-H.; Gogotsi, Y. Effect of Pore Size on Carbon Dioxide Sorption by Carbide Derived Carbon. *Energy Environ. Sci.* **2011**, *4*, 3059-3066.
190. Sevilla, M.; Parra, J. B.; Fuertes, A. B. Assessment of the Role of Micropore Size and N-Doping in CO₂ Capture by Porous Carbons. *ACS Appl. Mater. Interfaces* **2013**, *5*, 6360-6368.
191. Casco, M. E.; Martínez-Escandell, M.; Silvestre-Albero, J.; Rodríguez-Reinoso, F. Effect of the Porous Structure in Carbon Materials for CO₂ Capture at Atmospheric and High-Pressure. *Carbon* **2014**, *67*, 230-235.

192. Liu, W.-J.; Jiang, H.; Yu, H.-Q. Development of Biochar-Based Functional Materials: Toward a Sustainable Platform Carbon Material. *Chem. Rev.* **2015**, *115*, 12251-12285.
193. Keiluweit, M.; Nico, P. S.; Johnson, M. G.; Kleber, M. Dynamic Molecular Structure of Plant Biomass-Derived Black Carbon (Biochar). *Environ. Sci. Technol.* **2010**, *44*, 1247-1253.
194. Wiedemeier, D. B.; Abiven, S.; Hockaday, W. C.; Keiluweit, M.; Kleber, M.; Masiello, C. A.; McBeath, A. V.; Nico, P. S.; Pyle, L. A.; Schneider, M. P. Aromaticity and Degree of Aromatic Condensation of Char. *Org. Geochem.* **2015**, *78*, 135-143.